



Recognition and tracking of convective flow patterns using Wollaston shearing interferometry

F. Zaussinger*, A. Krebs, V. Travnikov, Ch. Egbers

Department of Aerodynamics and Fluid Mechanics, Brandenburg University of Technology Cottbus-Senftenberg, 03046 Cottbus, Germany

Received 21 February 2017; received in revised form 12 June 2017; accepted 13 June 2017

Available online 21 June 2017

Abstract

The *GeoFlow* experiment on the ISS is designed to study convective flows in a spherical gap under microgravity conditions. The main challenge, however, is the visualization of the fluid flow especially under the safety requirements of the Columbus module. The Wollaston shearing interferometry unit of the Fluid Science Laboratory works by optical means alone and is therefore utilized as measurement device for temperature fluctuations. The resulting interferograms in terms of fringe patterns are the base for the presented advanced post-processing techniques. They are used to identify convective patterns, to track these structures and to reconstruct the inaccessible three-dimensional temperature field. A comparison between experimentally gained results and numerically calculated interferograms is given, too. We show that convective patterns are automatically recognized and tracked accurately in experimental images by means of the generalized structure tensor. Furthermore, generic numerical simulations are used to deduce the internal temperature distribution by comparison with interferograms from the experiment.

© 2017 COSPAR. Published by Elsevier Ltd. All rights reserved.

Keywords: Thermal convection; Spherical shells; Microgravity conditions; Interferometry; Pattern recognition; Generalized structure tensor

1. Introduction

Large-scale structures and mixing times of planetary convective zones have been subject of intensive geophysical research in the past decades (Baumgardner, 1985; Ogawa, 2008; Schubert and Bercovici, 2009). The main driving mechanisms of thermal convection are a thermodynamically unstable vertical temperature profile reaching from the inner core to the surface and the buoyancy force. However, it is challenging to study convective flows in the spherical gap with terrestrial laboratory experiments, since the unidirectional gravitational acceleration of the Earth overlays any artificial radial force field. The most promising solution to overcome this restriction is an experiment under microgravity conditions which allows radial force fields.

The first thermal convection experiment under microgravity conditions was performed by Hart et al. (1986), who placed an experimental container on the Spacelab 3 in the year 1986. The complex half-dome design combined a radial temperature gradient with differentially heating patches. Columnar cells and even spiral waves could be observed. The *GeoFlow* experiment (Egbers et al., 2003; von Larcher et al., 2008; Futterer et al., 2010) on the ISS is designed to investigate convective flows, too. In contrast to Hart's experiment *GeoFlow* studies convection in the *full spherical gap*. Moreover, the captured parameter regime is much larger. In order to visualize convection a Wollaston prism shearing interferometry (WSI) unit is used. The main objectives are the investigation of the basic state and its transition to the turbulent regime in the (non-) rotating spherical shell, the characterization of convective flows and their symmetries, the determination of critical Rayleigh numbers and the occurrence of multi-stability.

* Corresponding author.

E-mail address: florian.zaussinger@b-tu.de (F. Zaussinger).

The visualization of fluid flows in terms of interferometry has a long history. But it was the development of modern lasers and digital cameras which revived this technique in the late 1990s. Interferometry has following advantages compared to other imaging techniques. First, no particles are needed. Particles tend to cluster, settle and need to be replaced regularly. Additionally, they can cause spark overs, if placed in a high voltage field. The WSI is a robust device and insensitive to external disturbances. It responds instantaneously and accurately to small fluctuations which allows for a precise assessment of the temperature field. As a laser optics device the WSI is characterized by adjustable sensitivity, which is obtained by modifying the displacement of the interfering beams. Due to these advantages the measurement of convective flows with a WSI has been carried out by many authors. [Ramesh and Merzkirch \(2001\)](#) used a WSI to investigate the convective heat transfer in an open cavity. They measured the local convective heat transfer coefficient with an overall uncertainty of $\pm 5\%$. Thermo-capillary flows, measured with a WSI, were studied by [Kassemi and Rashidnia \(2000\)](#). Their results are interesting in two respects. The authors combined numerical simulations with measured data to deduce the flow field. Additionally, the results were compared with low-g experiments performed on the TEXUS 33 sounding rocket. However, the low-g experiment utilized particles, instead of a WSI ([Wozniak et al., 1996](#)). In WSI thermal gradients result fringe patterns. The reconstruction of the temperature and the flow field asks for an interpretation of these patterns. Recently, [Feng et al. \(2015\)](#) measured the strain of an illuminated aluminum plate using a WSI. The displacement of the plate exhibits in ‘butterfly fringes’, which are similar to patterns found in the GeoFlow experiment. Numerical simulations helped to interpret their results. However, pattern recognition was not performed. Automatic pattern recognition has become an important issue not only in science, but in daily life. One might think about the recognition of barcodes or finger prints, eye-tracking, face recognition, smile detection in cameras and traffic sign localization in cars. The common factor of these examples is the detection of edges and stripes (cf. [Bigun, 2006](#)) which is the base of the presented algorithm, too. A first computationally efficient recognition of experimentally gained stripe patterns in interferograms has been investigated by [Shapiro \(1995\)](#) using a polar-coordinate transformation. The authors extracted the slopes of fringes by assuming that the fringe patterns have two line symmetries. [Hiby et al. \(2009\)](#) used modern fringe pattern recognition algorithms to identify stripes on tigers. This seems to be far away from our application, however the structures are similar to patterns found in the laminar regime of the GeoFlow experiment. An interesting face recognition algorithm was developed by [Guo and Huang \(2010\)](#). Faces are recognized by individual fringe patterns, which are similar to patterns found in the GeoFlow experiment. Yet, the automated pattern recognition, tracking and numerical

reconstruction has not been carried out for convective flows measured with a WSI. The presented pattern recognition algorithm allows for the detection of generic convective structures in interferograms and may be extended to other applications. Furthermore, this routine can track the identified structures and allows a final numerical reconstruction of the flow field.

This manuscript is structured as follows: Section 2 gives an overview of the experimental set-up, the visualization, the interferometry device and the imaging process. A detailed view on the calculation of numerically based interferograms (hereafter called ‘artificial interferograms’) is given in Section 3. Details of the recognition algorithm as well as applications are presented in Sections 4 and 5. Finally, a comparison between numerical and experimental interferograms is shown in Section 6. A conclusion and discussion of our method is presented at the end of the manuscript. [Appendix A](#) contains geometrical and fluid dynamical properties of the GeoFlow experiment.

2. The GeoFlow experiment

The GeoFlow experiment ([Fig. 1a](#)) was performed between 2008 and 2017 in two missions on the ISS. Both missions used the same experimental container (EC), but with different working fluids. GeoFlow I was performed between 2008 and 2009, GeoFlow II between 2011 and 2017. In the following, we focus on the GeoFlow IIc campaign which is mainly characterized by an acquisition frame rate of 10 Hz. A detailed overview of all missions and campaigns of the GeoFlow experiment is presented in [Appendix A](#). Basically, the GeoFlow experiment consists of a heated inner shell, a cooled concentric outer shell, a fluid filled gap, a high voltage field for the radial force field and an optical unit to visualize the fluid flow. The construction is integrated in a standardized EC of the Fluid Science Laboratory (FSL) which measures $40 \times 28 \times 27 \text{ cm}^3$. The FSL is located in the Columbus module of the International Space Station (ISS), where the influence of any axial force is reduced to microgravity conditions of $g < 10^{-4} \text{ m/s}^2$ and convection develops by the radially implemented force field only. In order to establish this radial component a dielectrophoretic force field is applied on the working fluid ([von Larcher et al., 2008; Futterer et al., 2008](#)). The voltage of $1.8 \text{ kV} \leq V_0 \leq 6.5 \text{ kV}$ induces an acceleration of $g_E = 0.3 \text{ m/s}^2$ at the outer shell which increases by the fifth power of the radius at the inner shell, namely $g_E = 13 \text{ m/s}^2$.

2.1. Geometrical and physical properties

In the following, all reference values (labeled with index ‘ref’) are defined at the outer shell. The radius of the outer shell is $r_o = 27 \text{ mm}$, the inner radius measures $r_i = 13.5 \text{ mm}$. The dimension has been chosen to guarantee a sufficient optical access and a maximum thermal time

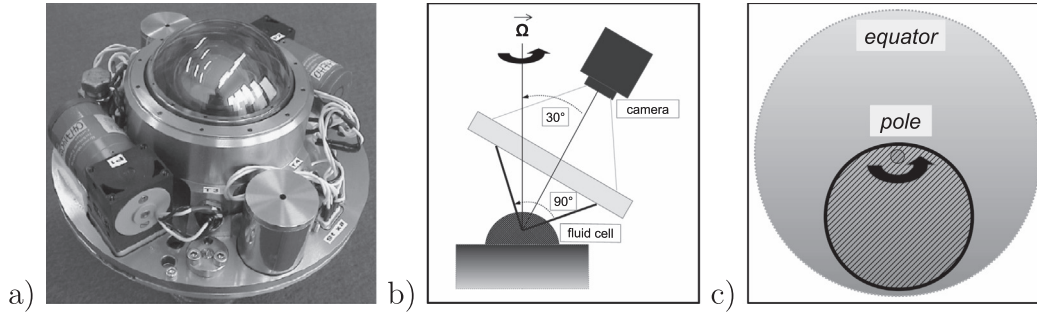


Fig. 1. (a) Breadboard of the GeoFlow experiment as mounted in the FSL on the ISS. (b) Side view of the imaging device, (c) top view of area that is imaged.

scale of $\tau_{\text{visc}} = H^2 / \kappa_{\text{ref}} = 40$ min where $H = r_o - r_i$ denotes the gap width and κ_{ref} the thermal diffusivity. This time is needed to set up a conductive, unbiased initial stratification before an experimental set point is started. Set points are denominated as *rums* which are series of increasing increments of temperature, voltage or rotation. The parametrization of diffusivities is done in terms of the Prandtl number $Pr = \nu_{\text{ref}} / \kappa_{\text{ref}}$, where ν_{ref} is the kinematic viscosity. The Rayleigh number Ra parameterizes the buoyancy and is given by $Ra = \alpha_E \Delta T g_E H^3 / (\nu_{\text{ref}} \kappa_{\text{ref}})$ where α_E names the coefficient of dielectric expansion (comparable with the thermal expansion coefficient) and $g_E = (2\epsilon_0 \epsilon_r / \rho_{\text{ref}}) \cdot (r_i^2 r_o^2 / (4 \cdot (r_o - r_i)^4)) V_0^2 r^{-5} \mathbf{e}_r$ is the acceleration induced by the electric field (comparable with the gravitational acceleration). Moreover, ϵ_0 is the vacuum permittivity, ϵ_r is the relative permittivity, ρ_{ref} is the density, V_0 is the voltage, r is the radius, and \mathbf{e}_r is the radial unit vector. The radial temperature difference ΔT of up to 10 K yields Rayleigh numbers between $5.60 \cdot 10^2 < Ra < 1.43 \cdot 10^7$. The Prandtl number ranges between $64 < Pr < 178$. The values of both non-dimensional numbers depend on the properties of the working fluid and two working environments which are defined by the reference temperatures, $T_{\text{ref}} = 20^\circ\text{C}$ and $T_{\text{ref}} = 30.5^\circ\text{C}$. An interferogram for the conductive state at $T_{\text{ref}} = 30.5^\circ\text{C}$ is depicted in Fig. 3. The GeoFlow I mission was performed with the iso-viscous working fluid M5, the GeoFlow II mission used the thermo-viscous fluid 1-Nonanol, respectively. The viscosity contrast $\gamma = \nu_{\text{ref}} / \nu_{\text{hot}}$ between the cold outer and the hot inner shell parametrizes this property of the fluid.

The experiment itself rotates in its basic configuration slowly at $\Omega = 0.008$ Hz as a stopped tray could result in an unsteady distribution of temperature, since the cooling air would always be blowing on the same location. Additionally, various regions of the fluid cell are captured by the camera when the tray rotates slowly. Further rotation rates range between $0.008 \text{ Hz} \leq \Omega \leq 2 \text{ Hz}$. The details of the experimental parameters, the geometrical properties and the fluid properties of the GeoFlow experiment are presented in Appendix A.

2.2. Interferometry and flow visualization

We utilize the Optical Diagnostics Module (ODM) (cf. Dupont et al., 2004) of the FSL for the visualization of the fluid flow of the GeoFlow experiment. A main diagnostic component of the ODM is the WSI which measures first derivatives of the fluid's refractive index (Fig. 2). The refractive index of the GeoFlow IIC working fluid 1-Nonanol is $n = 1.4338$ at 20°C (source: Merck index) and decreases linearly with the temperature. Due to this dependency a thermal gradient yields phase shifts of adjacent beams of laser light which result in a interferometry fringe pattern.

The camera unit is mounted fixed in a meridional angle of $\varphi = 30^\circ$ relative to the north pole where $\varphi = 0^\circ$. As depicted in Fig. 1b and c the camera captures the experiment with an opening angle of $\varphi = 88^\circ$, ranging from the northern polar region at $\varphi = -14^\circ$ to the equatorial region at $\varphi = 74^\circ$. Six interferograms per turn are recorded for longtime experiments which yields an imaging frame rate of 0.048 Hz. This frame rate is sufficient to capture stationary convective processes accurately. The size of the images is limited by the ODM to 992×992 pixels (GeoFlow I, II, IIB) and 640×480 pixels (GeoFlow IIC). Short time experimental runs with an imaging frame rate of 10 Hz are performed, too. These are more difficult to handle, since the size of the video stream is large compared to the available storage capacity of the hard drive in the Video Monitoring Unit (VMU). The frame rate of 10 Hz makes it possible to follow unsteady, turbulent convective flows precisely, albeit a full rotation at 0.008 Hz results in 1250 images. Lower frame rates, as available in GeoFlow I, II, IIB, are not suited to track turbulent flows. However, only two turns can be recorded at the maximum frame rate until the storage capacity is exhausted.

So far, 1.641.975 images have been recorded. This amount of images calls for an automatization of post-processing. The files are listed in a SQL data base and can be sorted by telemetry data which are available for each image, too. The images are stored as single PNG files or as S-Video streams.

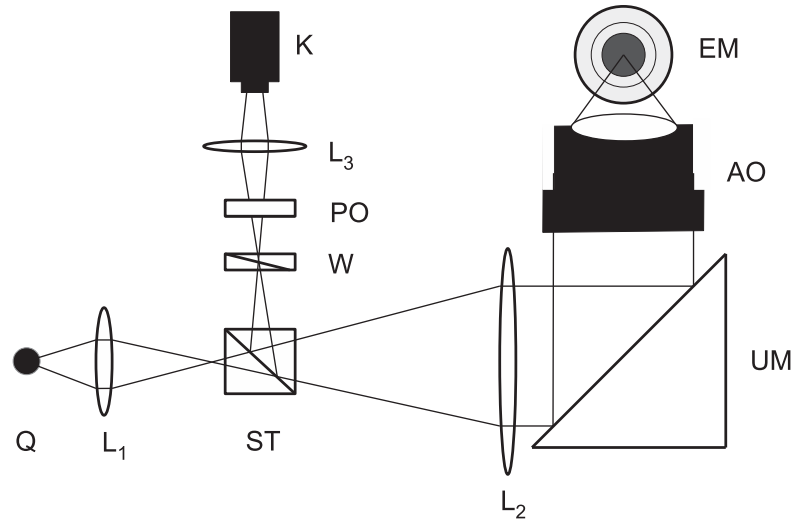


Fig. 2. Wollaston shearing interferometry of the FSL as used to visualize refractive index variations: K the camera, $L_{1,2,3}$ the lenses, PO the polarizer, W the Wollaston prism, ST the beam splitter, Q the light source, UM the mirror, AO the adaption optics and EM the GeoFlow experiment.

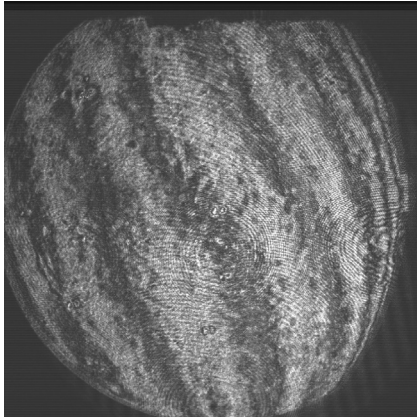


Fig. 3. Fringe pattern of the conductive state at reference temperature $T_{ref} = 30.5^\circ\text{C}$.

3. Artificial interferograms

The experimental interferograms represent an integral value of the radial temperature derivatives which are projected on the plane circle. Hence, it is not possible to reconstruct the full three dimensional flow field or the temperature distribution in the spherical gap directly with the two-dimensional interferograms. This is caused by two mechanisms. First, the mapping from 3D to 2D is surjective by definition. Therefore, it is impossible to calculate a unique reconstruction of the flow based on interferograms alone. Second, the sign of the directional derivative is unknown which makes it difficult to distinguish between cold down-wellings and hot up-wellings. The strategy to determine the temperature distribution in the spherical gap is based on the so called *backward reconstruction*. Three steps are necessary to perform this: (a) a comparable numerical simulation is calculated, (b) an artificial interferometry is performed on the numerical temperature field, (c)

the experimental and the numerical interferograms are compared. The crucial point of this reconstruction is the comparison. Generic interferograms of thermal plumes or laminar sheets have to be known. However, they are achieved with e.g. ground based experiments, numerical simulations or generic analytic functions. Experimental investigations have been carried out by Sitte (2004), Egbers et al. (2003) and von Larcher et al. (2008). These experiments were conducted under the influence of the axial gravitational force field of the Earth. The results of these experiments are very useful, since they show comparable thermal structures as in the μg case. However, the axial gravitational field limits the number of different convective structures. A typical interferogram performed with a ground based experiment is depicted in Fig. 4a. The central plume at the north pole exhibits in a concentric fringe structure which is found as thermal plume in the numerical simulations, too (Fig. 4b). However, analytic functions are needed to verify the assumption, that plumes exhibit as interferometric double ring structures.

3.1. Generic convective structures and their interferograms

As shown in Immohr (2006), interferograms of convective flows show two typical structures: (a) plume-like up- and down-welling regions are characterized by double ring structures, (b) sheet-like up- and down-welling regions exhibit in stripes. Both generic structures can be generated using a one dimensional temperature profile given by the spline $h : \mathbb{R}_{\geq 0} \rightarrow \mathbb{R}_{\geq 0}$ with

$$h(u) := \frac{1}{4} \begin{cases} (2-u)^3 - (4-u)^3 & \text{for } u \leq 1, \\ (2-u)^3 & \text{for } 1 < u \leq 2, \\ 0 & \text{for } 2 < u. \end{cases}$$

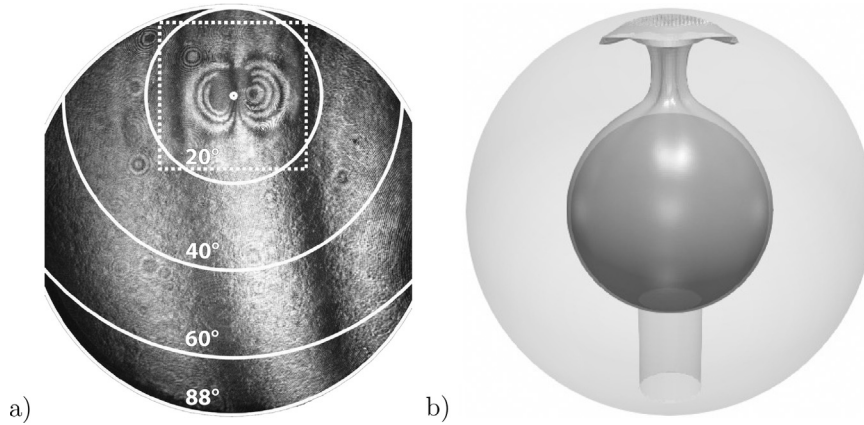


Fig. 4. (a) Typical interferogram conducted under Earth’s conditions (Sitte, 2004). The image shows a ‘double ring’ structure at the north pole for a thermal convection experiment at $Ra = 3.5 \cdot 10^6$ and $Pr = 35$. The degrees from 20° to 88° visualize various opening angles for the camera. (b) In order to interpret the pattern, a numerical simulation at the same Rayleigh number was performed. The temperature iso-surface reveals a rising, convective plume. As presented in this section, this plume can be uniquely assigned to the ring structure in the interferogram. The cylindric structure in the south pole is the shaft surrounding the rotation spindle and the thermal circuits.

We obtain the two-dimensional plume-like temperature field H_P by rotating this cubic spline around the vertical coordinate axis, i.e.,

$$H_P(x, y) := h\left(\frac{\sqrt{x^2 + y^2}}{3}\right),$$

and the corresponding sheet-like temperature field H_S by shifting the profile orthogonal to the x -axis, i.e.,

$$H_S(x, y) := h\left(\frac{1}{3}|x|\right).$$

Both temperature profiles are depicted in Tables 1 and 2, respectively.

The calculation of artificial interferograms is based on the assumption that fringes are generated by a derivative-sensitive oscillating function. Furthermore, the density of fringes (distance between two stripes with the same intensity) should correlate directly with the gradient.

Table 1

(a) Generic sheet-like temperature field H_S (upper row) and corresponding artificial interferogram (lower row). The polarization direction is depicted by the red arrow. Constant regions along the polarization direction generate constant intensities. (b–c) Rotating the polarization plane exhibits in characteristic stripes where the finest stripes are found, when the polarization direction is orthogonal with respect to the maximum of the gradient.

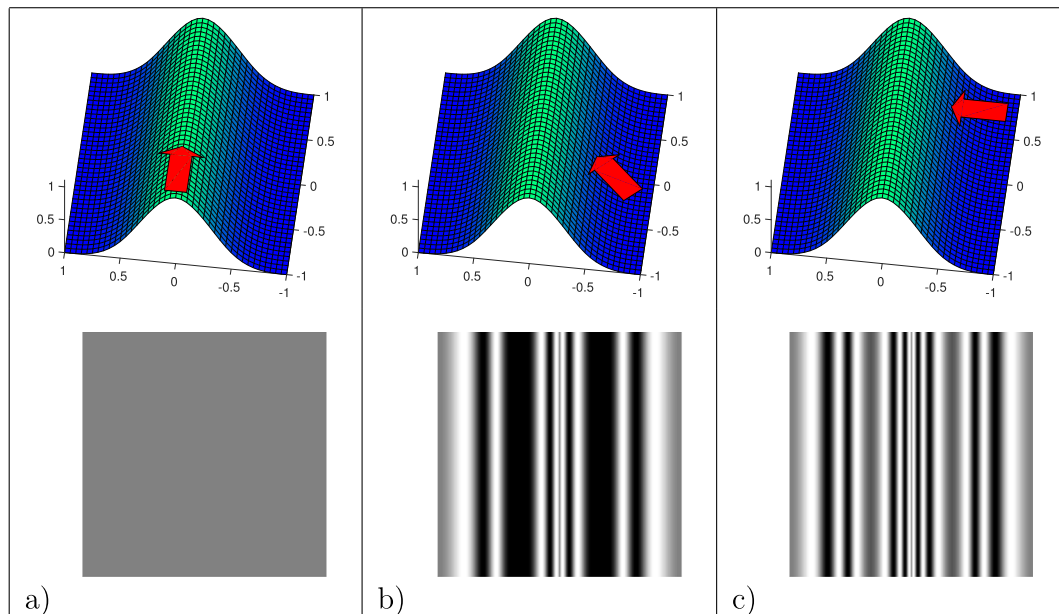
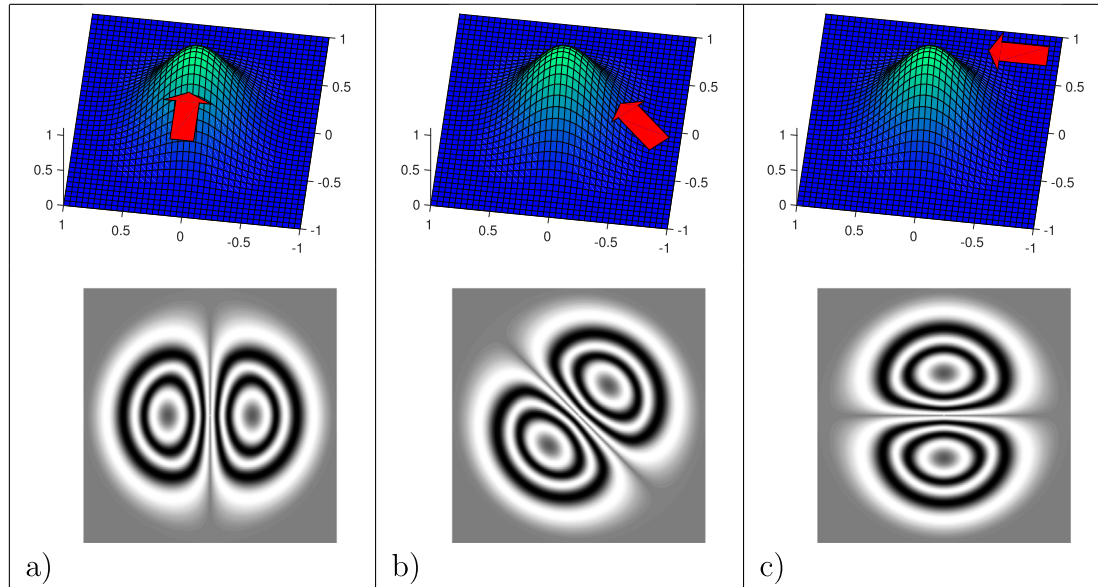


Table 2

(a) Generic plume-like temperature field H_P (upper row) and corresponding artificial interferogram (lower row). The polarization direction is depicted by the red arrow. (b–c) The rotation of the polarization plane by 45° and 90° changes the orientation of the interferogram accordingly.



Trigonometric functions are suitable for this task, as the density can be adjusted by a multiplication factor α_{fringe} with the frequency. We tested the cosine, as this function is smooth and simple to handle. The ability of generating fringes is given by the following example: $\cos(2x)$ with $\alpha_{\text{fringe}} = 2$ is higher frequent and hence produces more fringes as $\cos(x)$ with $\alpha_{\text{fringe}} = 1$. The artificial interferogram $I(\mathbf{x}) \in [-1, 1]$, with $\mathbf{x} = (x, y)$, is finally obtained by the directional derivative of the radially averaged temperature field T_{mean} along the polarization vector \mathbf{s} ,

$$I(\mathbf{x}) = \cos \left(a_{\text{fringe}} \cdot \frac{\partial T_{\text{mean}}(\mathbf{x})}{\partial \mathbf{s}} \right). \quad (1)$$

In practice, this derivative is approximated by a finite difference. The multiplication factor ranges between $1 < a_{\text{fringe}} < 50$ and has to be determined individually for the given temperature field. The choice of taking the cosine function is a compromise on the comparability to the experimental interferograms and the sensibility due to derivatives. The vector \mathbf{s} is defined by the plane of polarization, the optical path and the surface shape. This has to be set individually, too. Table 3 shows the calculation of an artificial interferogram. First, the temperature field (Table 3a) is integrated and weighted radially. We recommend to interpolate the simulation data onto a finer grid, as the numerical derivative gets smoother, (Table 3b). Afterwards, the resulting planar function is derived in direction of \mathbf{s} (Table 3c). Finally, the cosine is applied

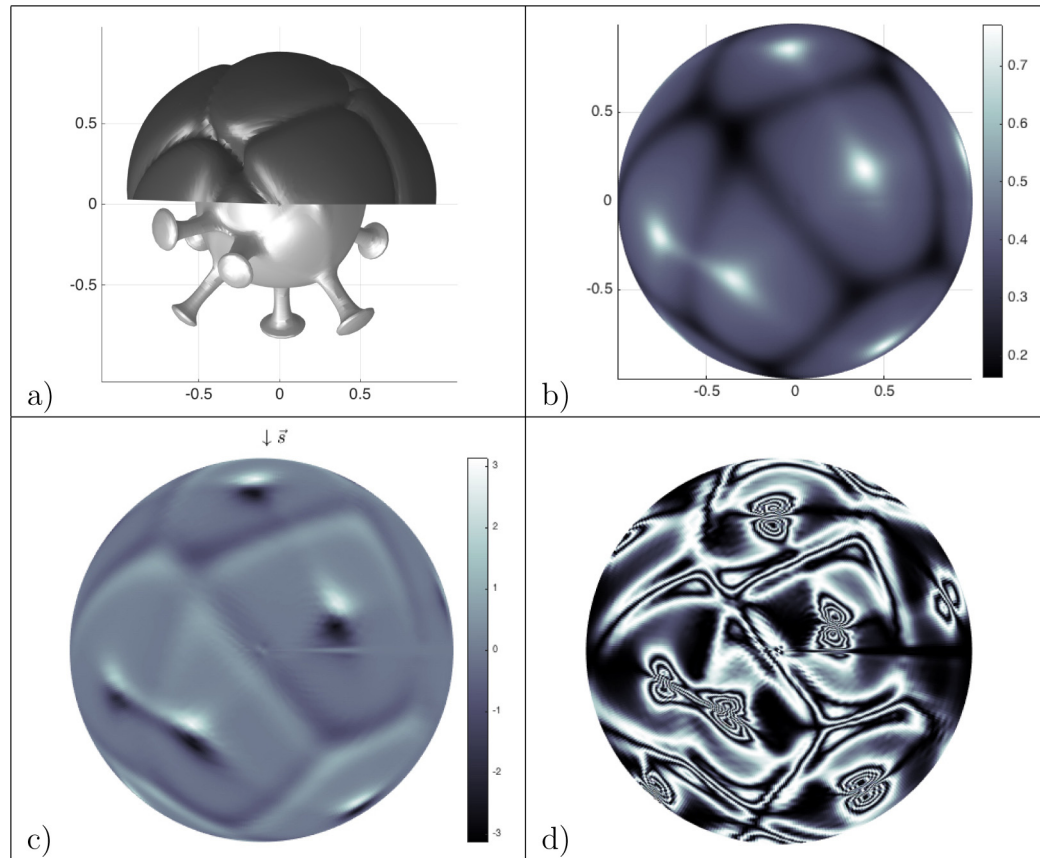
which yields the interferogram (Table 3d). The density of stripes is adjusted by varying the pre-factor which is set to $a_{\text{fringe}} = 12$ in most calculations. We recommend Immohr (2006) for a detailed view on further calculations of artificial interferograms especially for microgravity experiments.

3.2. Comparison of artificial and experimental interferograms

Using the generic example shown in Tables 1 and 2 we obtain the following characterization of sheet- and plume-like structures: the interferogram of a sheet-like flow consists of parallel lines. The black lines intensify when the direction of polarization is orthogonal to the temperature isolines and decreases when the angle between the direction of polarization and the ‘sheet’ direction is lowered. This behavior is obtained by changing the direction of polarization which is depicted in Tables 1 and 2 by the red arrow. Sheets occurring parallel to the direction of polarization are not detectable and show constant intensities (Table 1a). Interferograms of a steep thermal plume are characterized by double ring structures. These patterns are often symmetric with respect to the rings, since the thermal plumes are often rotationally symmetric, too. We find from ground based measurements that the symmetry axis between the ring pair is orthogonal to the direction of polarization. Having this behavior in mind we get a rule of thumb to determine the direction of polarization in unclassified interferograms.

Table 3

(a) Numerical simulation of an unsteady convective flow in the spherical shell with $Pr = 125$, $Ra = 3 \cdot 10^4$ and a viscosity contrast of $\gamma = 32$. The upper hemisphere shows cold down-wellings, colored dark gray. Hot rising plumes are visible in the lower hemisphere as light gray spikes. (b) Radially averaged temperature field T_{mean} . Hot plumes appear as bright spots, cold down-wellings as black lines. (c) The first derivative of the averaged temperature field in direction s of the polarization plane. (d) Artificial interferogram. The frequency of the black-white alterations correspond to the first derivative of the mean temperature field. Plumes correspond to double-ring structures, sheets to stripes.



4. Recognition

It was shown in Section 3 that sheet-like temperature fields correspond to stripes in the interferogram and plume-like temperature fields to double ring structures. The question arises how these two structures are automatically recognized in images. This section presents the mathematical background to answer this. For ease of presentation the section is split into three parts. Firstly, the image processing pipeline (Fig. 5) will guide the reader from the input image and input parameters to the output. Secondly, the mathematical foundations of stripe detection are given in Section 4.2. Thirdly, the mathematics of fringe detection are generalized to double ring structures in Section 4.3.

4.1. Image pipeline

Image primitives such as corners, edges or texture elements may be detected by convolving the image $I(\mathbf{x})$ with

$\mathbf{x} = (x_1, x_2)$ and appropriate filter masks. Granlund and Knutsson (1995) elaborated the fundamentals of this *low-level vision theory*. A related *low-level vision* representation which is closer to our stripes and double ring structures is expanded by Bigun (2006). In image processing it is good practice to start the image processing pipeline with 2D convolutions which modify the spatial frequency characteristics by weighting each pixel within a well defined window. Such convolutions are commonly used to sharpen or blur the image, or – as in our case – to prepare the image for detecting stripes. However, one looks for small filter masks (e.g. smaller than 15×15 pixels), so that the convolution can be efficiently computed in the local space. As a linear operation a convolution secures stability in terms of “Small changes of the filter do not lead to large changes in the output image”. A binary threshold is an example for a nonlinear filter introducing instability – a small change of the threshold can yield a drastic change of the output image. For this reason binary operations are applied at the end of image processing pipelines after corners, edges,

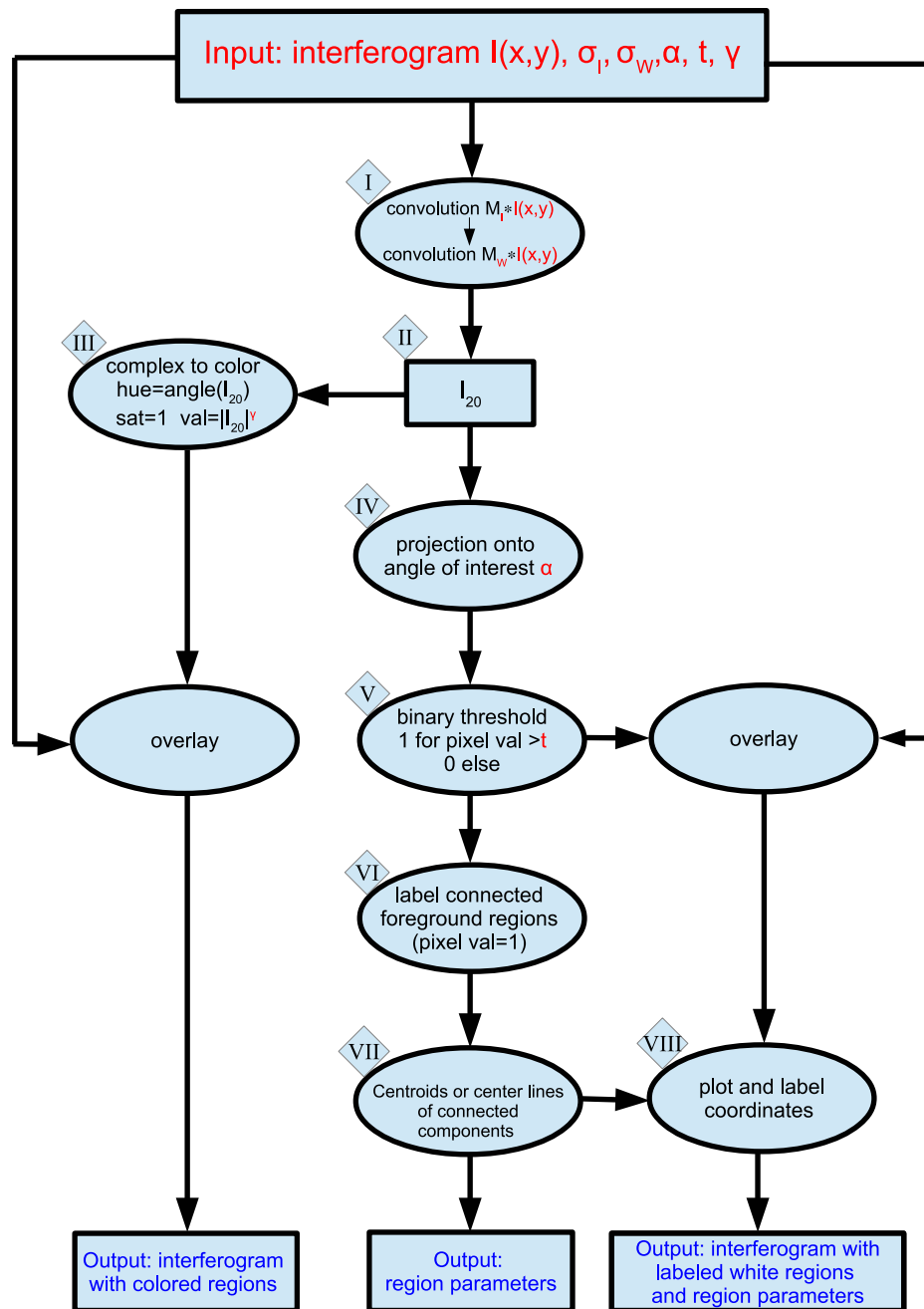


Fig. 5. Image processing pipeline for stripe and double ring detection.

or textures have been identified using the gray value and neighborhood respecting convolutions.

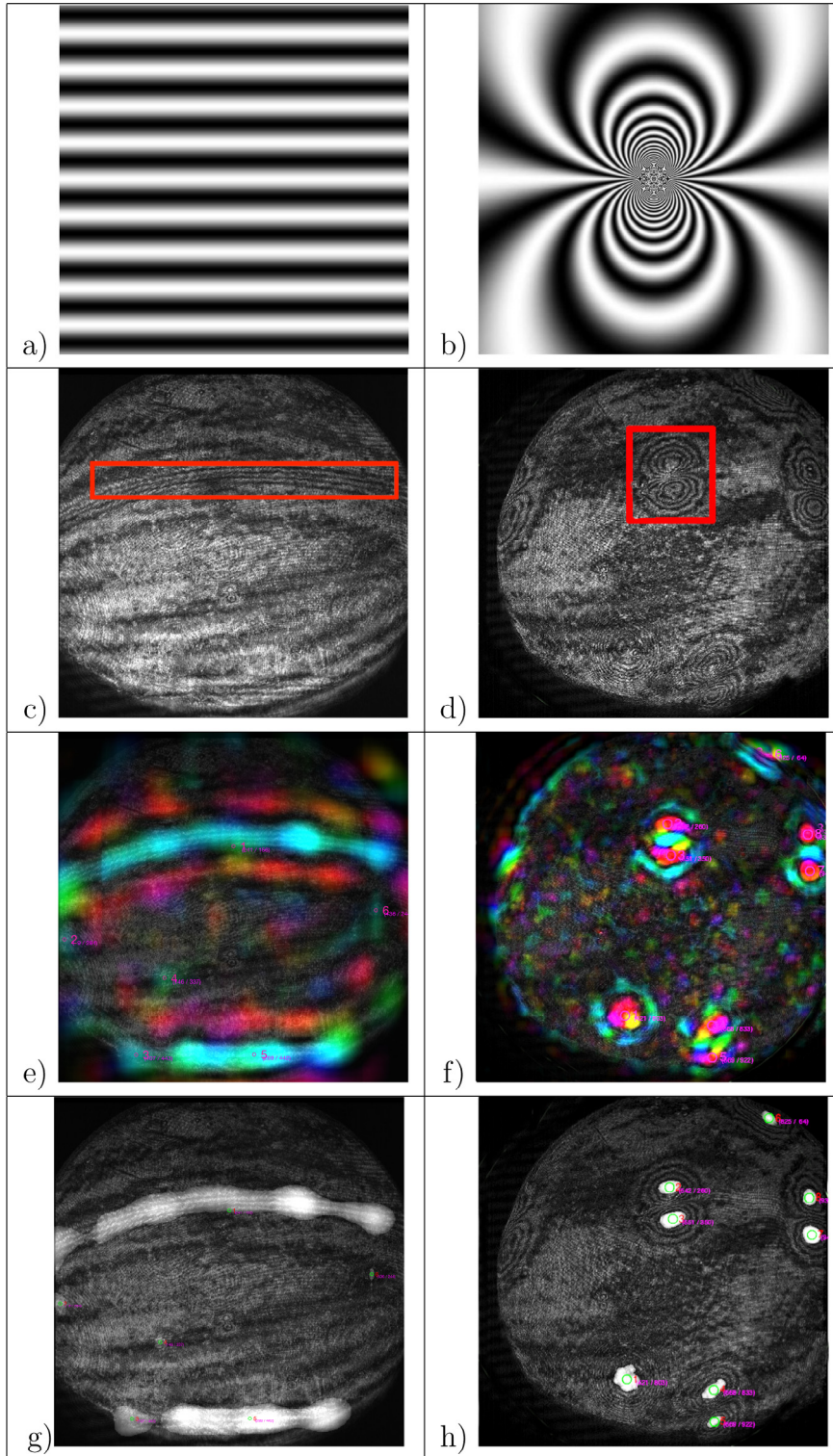
The following recognition process is described by means of the image processing pipeline as depicted in Fig. 5. Roman numerals in the text refer to processes which are labeled with a diamond symbol. The pipeline is used to abstract the stripe regions of image Table 4c and the double ring regions of image Table 4d. However, the same pipeline is applied on both structures. The “magic” for the feature detection (stripes versus double rings) lies in the second 2D convolution M_W , where M_W denotes the structure adapted filter mask, (I). This gives the complex

valued image $I_{20}(\mathbf{x})$ quantifying the occurrence of stripes or double rings, (II). Table 4e and f display the original interferogram overlaid with the color-coded feature indicator I_{20} , (III). The representation of I_{20} may be used for a first inspection of the feature detection, the tuning of the Gaussian interpolation with σ_I and of the window size with σ_W . The stripes light up in blue (Table 4e) whereas the centers of the double rings light up in magenta (Table 4f).

As the color corresponds to the argument $\arg(I_{20})$, the colored regions can be dissected by projecting the complex number I_{20} onto the unit vector $(\cos \alpha, \sin \alpha)^T$, $-\pi \leq \alpha \leq \pi$, where α denotes the color or angle of interest,

Table 4

Recognition algorithm to detect patterns in interferograms. The first row shows the target patterns of (a) stripes and (b) double ring structures. These generic patterns are found in interferograms as (c) sheet-like and (d) plume-like flows. The complex valued tensor entry I_{20} marks best fits (blue) between the original function and the image, as shown in (e) and (f). Local maxima of I_{20} (colored in white) correspond to (g) regions of laminar flows and (h) thermal plume centers.



(IV). The white regions of Table 4g and h are obtained by a binary threshold of the result with using the value t . So, the visual inspection of the color-coded representation of I_{20} allows for the tuning of the input parameters α and t to reach a binarized highlighting of the structures of interest, (V). This binarization may be processed further, (VI). In case of the double rings, the centroids of the whitely presented foreground regions correspond well with the centers of the rings, (VII, VIII).

The following two subsections are devoted to the first filters in the image pipeline, namely M_I and M_W . The two 2D convolutions yield the complex valued feature detector I_{20} . Section 4.2 introduces the concept of the *linear structure tensor* (LST), the mathematical background for the stripe detection.

Harmonic functions pairs can be used to distort lines into double rings. This trick from complex analysis is used to generalize the LST. The concept of the *generalized structure tensor* (GST) is presented in Section 4.3. Our presentation of the LST and the GST follows (Bigun (2006), Chapter 10, 11) tightly. The successful identification of the double ring centers is the basis for applications which are presented in Section 5.

4.2. Stripe detection

In the following, we introduce the mathematics of line detection in the paragraphs (a)–(f). An overview can be found at the end of paragraph (a).

(a) Table 4a shows a stripe image generated by $I(\mathbf{x}) = \cos(\beta x_2)$ where $\beta > 0$ names the parameter to steer the number of stripes in the image. Using the more general rule $I(\mathbf{x}) = \cos(\beta \mathbf{k} \cdot \mathbf{x})$ with $\mathbf{k} = \begin{pmatrix} \cos \gamma \\ \sin \gamma \end{pmatrix}$, the stripes may be rotated counter-clockwise by the angle γ . Replacing $\cos(\beta \cdot)$ by a scalar function g leads to the definition of *linear symmetry*.

Definition 4.1 (cf. Bigun, 2006, Definition 10.1). Let \mathbf{k} be a two-dimensional real unit vector. An image I is called *linear symmetric*, if its isocurves have a common direction, i.e., there exists a scalar function g such that

$$I(\mathbf{x}) = g(\mathbf{k} \cdot \mathbf{x}). \quad (2)$$

Table 4c illustrates an image where the labeled region is approximately linear symmetric. The “common” direction of the stripes in the red frame is not really “common”. It is continuously varying. In the following, we investigate how linear symmetric regions can be quantified based on Definition 4.1. For it, we give an energy formulation of a linear symmetric image in the Fourier domain (b). In the Fourier domain the *linear symmetric energy* of a region in direction \mathbf{k} is characterized by the structure tensor S , a 2×2 matrix. The eigenvector of S corresponding to the largest eigenvalue yields the direction \mathbf{k} of the pattern. The largest

eigenvalue of S quantifies the *linear symmetry energy* of the region (c).

Assuming the particular region of a Gaussian window with center \mathbf{x}_C , this structure tensor S can be approximated for every single pixel with coordinates \mathbf{x}_C of the image by switching back to the spatial domain. The mathematical foundation for this step from the Fourier to the spatial domain is the Parseval-Plancherel theorem (d). The gradient $\nabla I(\mathbf{x})$ needed for computation of S will be approximated by Gaussian interpolation (e). An eigenvalue and eigenvector computation for every Gaussian window corresponding S can be circumvented by a complex valued representation Z of the structure tensor (f).

(b) The linear symmetry of an image I results in a concentration of its 2D Fourier transformation F to a line with direction \mathbf{k} which can be written as

$$F(\boldsymbol{\omega}) = G(\mathbf{k} \cdot \boldsymbol{\omega}) \delta(\mathbf{k}_\perp \cdot \boldsymbol{\omega}). \quad (3)$$

Here, $\boldsymbol{\omega}$ denotes the 2D frequencies. Furthermore, \mathbf{k}_\perp , is orthonormal to \mathbf{k} and δ is the Dirac distribution in 1D. The function G is the one-dimensional Fourier transformation of g . This concentration of the 2D Fourier transformation can be used to identify stripe patterns and their direction \mathbf{k} .

The difference $\mathbf{d}(\boldsymbol{\omega}, \mathbf{k})$ of the frequency vector $\boldsymbol{\omega}$ and its projection on to \mathbf{k} writes as

$$\mathbf{d}(\boldsymbol{\omega}, \mathbf{k}) = \boldsymbol{\omega} - (\boldsymbol{\omega} \cdot \mathbf{k}) \mathbf{k}.$$

The error function

$$e(\mathbf{k}) = \int_{\Omega} |\mathbf{d}(\boldsymbol{\omega}, \mathbf{k})|^2 |F(\boldsymbol{\omega})|^2 d\boldsymbol{\omega} \quad (4)$$

weights the squared Euclidean distances $|\mathbf{d}(\boldsymbol{\omega}, \mathbf{k})|^2$ with the energy $|F(\boldsymbol{\omega})|^2$ and integrates over all 2D frequencies $\boldsymbol{\omega} \in \Omega$. The minimum \mathbf{k}_{\min} of the error function e yields $e(\mathbf{k}_{\min}) = 0$ for linear symmetric images due to (3).

(c) The matrix $S := \begin{pmatrix} s_{11} & s_{12} \\ s_{21} & s_{22} \end{pmatrix}$ defined by the elements

$$s_{ij} = \int_{\Omega} \omega_i \omega_j |F(\boldsymbol{\omega})|^2 d\boldsymbol{\omega} \quad (5)$$

is called the *linear structure tensor of the image I* (LST) (cf. Bigun, 2006, Definition 10.2). S allows to rewrite the error as the quadric form

$$e(\mathbf{k}) = \mathbf{k}^T (\text{trace}(S)I - S) \mathbf{k}.$$

As S is symmetric, there exist real valued eigenvalues and eigenvector pairs $(\mu_{\min}, \mathbf{v}_{\min}), (\mu_{\max}, \mathbf{v}_{\max})$ of S . Using standard calculus, it can be shown the minimum of the error function e defined by (4) is obtained, if $\mathbf{k}_{\min} = \mathbf{v}_{\max}$.

(d) The LST S can be used to look for stripe like structures and their direction \mathbf{k} by applying it to environments of every single point of the image denoted by the coordinates \mathbf{x}_c . Usually these environments are given by a window function centered at \mathbf{x}_c which weights the grayvalues at \mathbf{x} with a factor 0 or close to 0 when the distance

$|\mathbf{x} - \mathbf{x}_c|$ exceeds a certain limit. A prominent example of a window function is the 2D Gaussian $\mu_{\mathbf{x}_c}^{2d}$ defined by $\mu_{\mathbf{x}_c}^{2d}(\mathbf{x}) = \exp\left(-\frac{1}{2\sigma_w^2}|\mathbf{x} - \mathbf{x}_c|^2\right)$ where σ_w determines the size of the window W .

The computational burden combined with the Fourier transformation in Eq. (5) is avoided by applying the Parseval-Plancherel theorem which replaces the integration over the frequency domain Ω by an integration over the spatial domain defined by the window W centered at \mathbf{x}_c

$$s_{ij} = \frac{1}{4\pi^2} \int_W \frac{\partial}{\partial x_i} I(\mathbf{x}) \frac{\partial}{\partial x_j} I(\mathbf{x}) d\mathbf{x}. \quad (6)$$

(e) An image provides values on a discrete domain. To compute the continuous operators $\frac{\partial}{\partial x_i}$, $i = 1, 2$, and $\int_W \cdot d\mathbf{x}$, an approximation of the values on a continuous domain is needed. Let the discrete image I be given on the discrete set of points $\mathbf{x}_{j,l}$. Using the 1D Gaussian interpolator function $\mu(t) = (2\pi\sigma_I^2)^{-1/2} \exp\left(-\frac{t^2}{2\sigma_I^2}\right)$ band-limited signal theory shows that

$$I^C(x_1, x_2) \approx \sum_{j,l} \mu(x_1 - x_{j,l,1}) \mu(x_2 - x_{j,l,2}) I(x_{j,l,1}, x_{j,l,2}) \quad (7)$$

gives a good approximation for a continuous extension of I for $\sigma_I \geq 0.65$ which can be computed efficiently by two successive 2D convolutions due to the tensor product structure $\mu(x_1 - x_{j,l,1})\mu(x_2 - x_{j,l,2})$. As μ decreases rapidly, a sufficient approximation is already obtained using only the j, l with $|x_1 - x_{j,l,1}| < 3\sigma_I$ and $|x_2 - x_{j,l,2}| < 3\sigma_I$. Taking larger σ_I reduces high frequencies and is a common method to reduce noise in images. Detailed analyses of the Gaussian interpolator may be found in (Bigun, 2006, Chapters 6, 8, 9) and (Lindeberg, 1993).

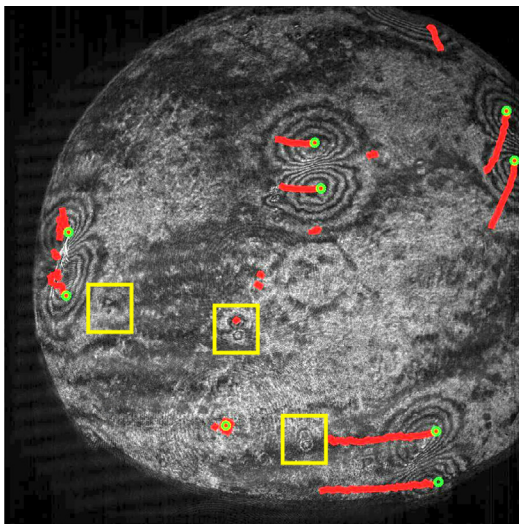


Fig. 6. Tracked paths of automatically identified stationary plumes with a rotation rate of 0.008 Hz. Green dots mark the centers of plumes and the red dots show the covered distance. Yellow squares show stationary dust particles. (For interpretation of the references to color in this figure legend, the reader is referred to the web version of this article.)

With (7) one gets the partial derivatives

$$\begin{aligned} \frac{\partial}{\partial x_1} I^C(x_1, x_2) &\approx \sum_{j,l} \mu'(x_1 - x_{j,l,1}) \mu(x_2 - x_{j,l,2}) I(x_{j,l,1}, x_{j,l,2}), \\ \frac{\partial}{\partial x_2} I^C(x_1, x_2) &\approx \sum_{j,l} \mu(x_1 - x_{j,l,1}) \mu'(x_2 - x_{j,l,2}) I(x_{j,l,1}, x_{j,l,2}). \end{aligned} \quad (8)$$

(f) The computation of the eigenvalues and eigenvectors of S can be circumvented by switching to the following complex representation of the structure tensor

$$Z = \frac{1}{2} \begin{pmatrix} I_{11} & -iI_{20} \\ iI_{20}^* & I_{11} \end{pmatrix} \quad \text{where} \quad \begin{aligned} I_{20} &= s_{11} - s_{22} + i2s_{12}, \\ I_{11} &= s_{11} + s_{22}. \end{aligned} \quad (9)$$

Here, I_{20}^* denotes the complex conjugate of I_{20} . Let $U = \frac{1}{\sqrt{2}} \begin{pmatrix} 1 & -i \\ -i & 1 \end{pmatrix}$ and let U^H its Hermitian transposition. As there holds $U^H U = I$ and $Z = U^H S U$, Z and S are similar. It follows with standard linear algebra that Z and S have the same eigenvalues. Furthermore, straightforward calculation yields

$$I_{20} = (\mu_{\max} - \mu_{\min}) \exp(i2\varphi_{\min}) \quad \text{and} \quad I_{11} = (\mu_{\max} + \mu_{\min}) \quad (10)$$

where $\mathbf{k}_{\min} = \begin{pmatrix} \cos \varphi_{\min} \\ \sin \varphi_{\min} \end{pmatrix}$ minimizes the error function $e(\mathbf{k})$ defined in (4) (cf. Bigun, 2006, Theorem 10.2).

With this, the essential information of the structure tensor S is already contained in the complex number I_{20} . A pixel with ideal linear symmetric neighborhood is characterized by $\mu_{\min} = 0$ and $\mu_{\max} \gg 0$. Therefore, the magnitude $|I_{20}| = \mu_{\max} - \mu_{\min}$ quantifies the occurrence of stripes. Furthermore, the double angle representation $2\varphi_{\min} = \arg(I_{20})$ removes implicitly the ambiguity of the eigenvalue problem that if \mathbf{k} is an eigenvector, then $-\mathbf{k}$ is also an eigenvector. Combining (6) and (9), I_{20} can be rewritten as

$$\begin{aligned} I_{20} &= \int_W \nabla(I)(\mathbf{x}) d\mathbf{x} \quad \text{using the complex differential} \\ &\quad \text{operator} \\ \nabla(I)(\mathbf{x}) &= \left(\frac{\partial}{\partial x_1} I(\mathbf{x}) + i \frac{\partial}{\partial x_2} I(\mathbf{x}) \right)^2. \end{aligned} \quad (11)$$

The above paragraphs (a)–(f) sketched the mathematical background of line detection. We finish this subsection by summarizing the operations needed for the computation of the line detector $I_{20}(\mathbf{x})$. Inspection of (11) makes it clear that the derivatives $\frac{\partial}{\partial x_i} I(\mathbf{x})$, $i = 1, 2$, and the integral $\int_W \nabla(I) d\mathbf{x}$ need to be implemented.

The derivatives are obtained by the two 2D convolutions with the masks M_{I_x} and M_{I_y} realizing the Gaussian interpolation μ with respect to the parameter $\sigma_I \geq 0.65$ according to (8). The tensor structures $(\mu'(\cdot, 1))\mu(\cdot, 2)$ and

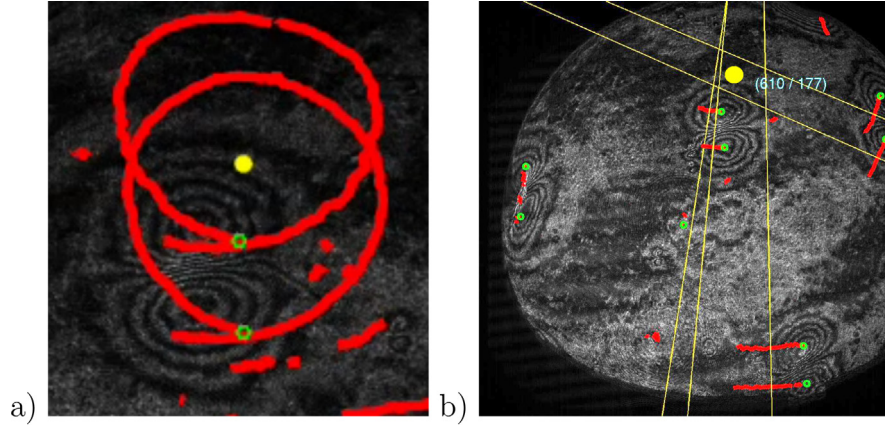


Fig. 7. (a) Elliptical track of a stationary plume in the northern polar region. The piercing point of the rotation axis (yellow point) is found by weighting the centers of the ellipses. (b) Localization of the north pole via the secant method where equatorial plumes are tracked. Both methods yield the same result. (For interpretation of the references to color in this figure legend, the reader is referred to the web version of this article.)

$\mu(\cdot, \cdot, 1)\mu'(\cdot, \cdot, 2)$) allow for the efficient implementation of these convolutions. Increasing σ_I will suppress high frequency structures and noise. Using the complex differential operator ∇ from (11), one sums up the masks and yields the complex valued convolution mask $M_I = M_{I_x} + iM_{I_y}$ indicated in Bubble I of Fig. 5.

According to paragraph (d) the integration $\int_W \nabla(I(\mathbf{x}))d\mathbf{x}$ over a Gaussian window can be realized as the weighted sum of $\nabla(I(\mathbf{x}))$ over all points \mathbf{x} in the neighborhood of \mathbf{x}_C . Here, a neighborhood given by $|\mathbf{x} - \mathbf{x}_C| < 3\sigma_W$ would be sufficiently accurate. Again, this weighted sum can be implemented as a 2D convolution. The entries of the convolution mask M_W indicated in Ellipsis I of Fig. 5 correspond to the window function μ_0^{2d} defined in paragraph (d). The frequency of the detected stripe pattern corresponds inversely proportional to σ_W .

4.3. Detection of double ring patterns

In this section the concept of a *linear symmetric image* is generalized to patterns which can be generated from stripe images by a coordinate transformation. We consider the 2D coordinate transformation $\xi: \mathbb{R}^2 \setminus \{0\} \rightarrow \mathbb{R}^2$ defined by

$$\xi(\mathbf{x}) = \begin{pmatrix} \xi(\mathbf{x}) \\ \eta(\mathbf{x}) \end{pmatrix} = \frac{1}{x_1^2 + x_2^2} \begin{pmatrix} x_1 \\ -x_2 \end{pmatrix}. \quad (12)$$

Table 4b shows a pattern generated by $I(\mathbf{x}) = \cos(\beta\eta(\mathbf{x}))$ where $\beta > 0$ names the parameter to steer the number of black-white alternations. As in Section 4.2 using the more general rule $I(\mathbf{x}) = \cos(\beta\mathbf{k} \cdot \xi(\mathbf{x}))$, the pattern may be rotated counter-clockwise through the angle γ . Analogously to Definition 4.1 replacing $\cos(\beta \cdot)$ by a scalar function g leads us to the following definition.

Definition 4.2 (Bigun, 2006, cf. Definition 11.1). Let \mathbf{k} be a two-dimensional real unit vector. An image I is called *linear*

symmetric in the coordinates $\xi = (\xi, \eta)$, if there exists a scalar function g such that

$$I(\mathbf{x}) = g(\mathbf{k} \cdot \xi(\mathbf{x})).$$

Analogously to the *structure tensor* (6) on the window W , the *generalized structure tensor* (GST) with respect to the ξ coordinates may be defined by

$$S = \begin{pmatrix} \int_W \frac{\partial I}{\partial \xi} \frac{\partial I}{\partial \xi} d\xi & \int_W \frac{\partial I}{\partial \xi} \frac{\partial I}{\partial \eta} d\xi \\ \int_W \frac{\partial I}{\partial \xi} \frac{\partial I}{\partial \eta} d\xi & \int_W \frac{\partial I}{\partial \eta} \frac{\partial I}{\partial \eta} d\xi \end{pmatrix}. \quad (13)$$

Furthermore, the corresponding complex valued representation of the GST Z is defined by (9) with the entries of the real valued GST from (13). The eigenvalues μ_{\min}, μ_{\max} of S and Z , respectively, as well as $\mathbf{k}_{\min} = \begin{pmatrix} \cos \varphi_{\min} \\ \sin \varphi_{\min} \end{pmatrix}$ are again obtained from (10) and the magnitude $|I_{20}|$ quantifies the occurrence of the pattern *linear symmetric in the ξ coordinates*.

Adapting (11) to the ξ coordinates, I_{20} can be rewritten as

$$I_{20} = \int_W \nabla_{\xi}(I)(\xi) d\xi \quad \text{using the complex differential operator} \\ \nabla_{\xi}(I)(\xi) = \left(\frac{\partial}{\partial \xi} I(\xi) + i \frac{\partial}{\partial \eta} I(\xi) \right)^2. \quad (14)$$

Standard calculus allows to switch back to the \mathbf{x} coordinates. We obtain

$$I_{20} = \int_W \frac{\nabla_{\mathbf{x}}^*(\xi)(\mathbf{x})}{|\nabla_{\mathbf{x}}^*(\xi)(\mathbf{x})|} \nabla_{\mathbf{x}}(I)(\mathbf{x}) d\mathbf{x}. \quad (15)$$

where $\nabla_{\mathbf{x}}^*$ denotes the conjugated complex of $\nabla_{\mathbf{x}}$ (cf. Bigun, 2006, Theorem 11.1).

In terms of complex analysis $\xi(\mathbf{x})$ may be rewritten as $\xi(\mathbf{x}) = \text{real}z^{-1}$ with $z = x_1 + ix_2$. Due to the Cauchy-Riemann equations, there holds

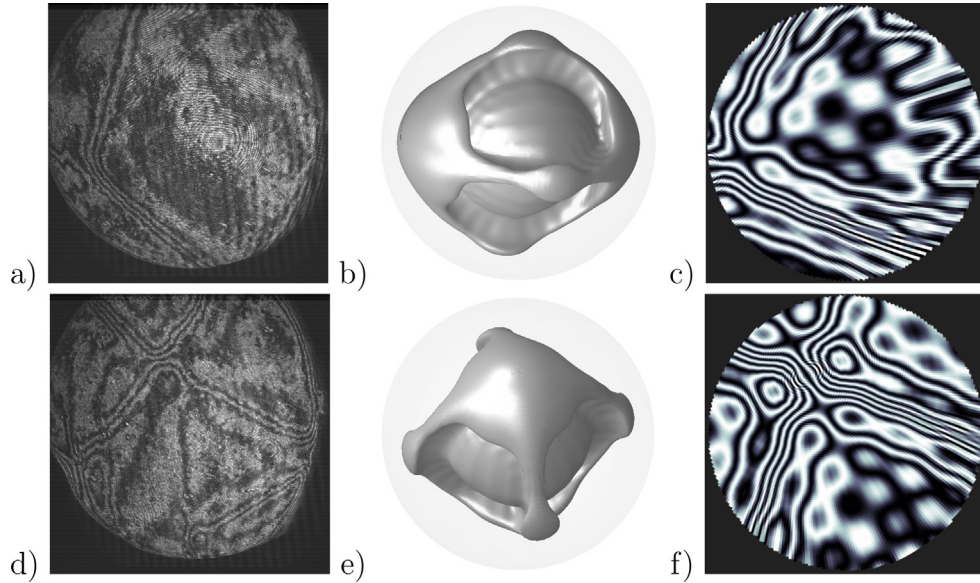


Fig. 8. (a) Interferogram of a laminar convective flow for $Ra = 4000$ and $Pr = 125$. (b) Representative temperature iso-surface of the corresponding numerical simulation (c) artificial interferogram, based on the numerical simulation. (d–f) A shift in the polarization direction lets the central plume in the polar region appear as a cross in the interferogram.

$$\left(\frac{\partial}{\partial x_1} - i \frac{\partial}{\partial x_2}\right)\zeta(x_1, x_2) = \frac{d}{dz}z^{-1} \text{ and further } \nabla_{\xi}^*(\zeta)(\mathbf{x}) = \left(\frac{d}{dz}z^{-1}\right)^2 = z^{-4}.$$

We finish this subsection by specifying a discrete approximation for the GST. Again, as in the case of the *structure tensor* in Section 4.2, the discrete approximation can be computed efficiently using the Gaussian as both the window function and the interpolator. Let

$$\Gamma^{\{0, \sigma^2\}}(\mathbf{x}) = \frac{1}{2\pi\sigma^2} \exp\left(-\frac{1}{2\sigma^2}(|\mathbf{x}|^2)\right)$$

be the ordinary 2D Gaussian. We introduce the n th *symmetry derivative* to the Gaussian by

$$\Gamma^{\{n, \sigma^2\}}(\mathbf{x}) = \left(\frac{\partial}{\partial x_1} + i \frac{\partial}{\partial x_2}\right)^n \Gamma^{\{0, \sigma^2\}}(\mathbf{x}) \quad \text{for } n > 0.$$

As the application of the differential operator $\frac{\partial}{\partial x_1} + i \frac{\partial}{\partial x_2}$ to $\Gamma^{\{0, \sigma^2\}}$ results in the multiplication $-\sigma^{-2}(x_1 + ix_2) \Gamma^{\{0, \sigma^2\}}$, one obtains

$$\Gamma^{\{n, \sigma^2\}} = -\sigma^{-2n}(x_1 + ix_2)^n \Gamma^{\{0, \sigma^2\}}.$$

Let the derivatives $\frac{\partial}{\partial x_1} I$ and $\frac{\partial}{\partial x_2} I$ be approximated using the Gaussian interpolator with σ_I and let the window W be given by the Gaussian with σ_W . Taking this discrete version of $\Gamma^{\{4, \sigma_W^2\}}$ as convolution mask, the discrete approximation of the GST can be written as the two discrete convolutions $*$ on the grid given by the image I , denoted by

$$I_{20} = c \Gamma^{\{4, \sigma_W^2\}} * \left(\Gamma^{\{1, \sigma_I^2\}} * I\right)^2. \tag{16}$$

Here, $\Gamma^{\{*, \cdot\}}$ denotes the complex conjugate of $\Gamma^{\{\cdot, \cdot\}}$ and c a real constant. (cf. Bigun, 2006, Lemma 11.6). With this, the convolution mask $M_I = \Gamma^{\{1, \sigma_I^2\}}$ and $M_W = \Gamma^{\{4, \sigma_W^2\}}$ indicated in Ellipsis I of Fig. 5 determine a double ring indicator.

The coordinate transformation ξ represents a special case of a harmonic function pair (HFP) defined by the complex monomial z^{-1} . As it transforms a stripe image into a double ring like pattern (cf. Table 4b), the generalization

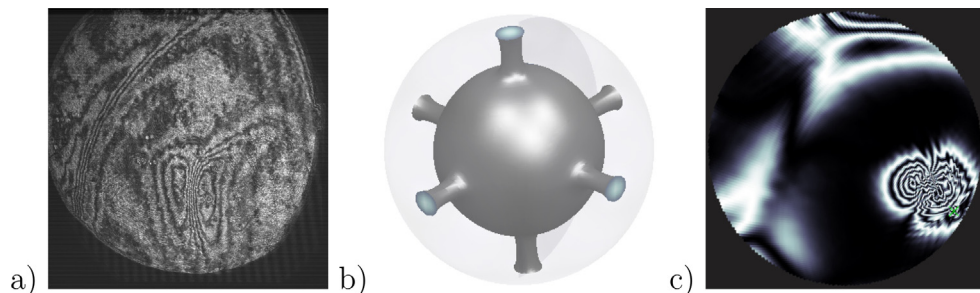


Fig. 9. (a) Transient convective flow for $Ra = 16,000$ and $Pr = 125$. (b) The representative temperature iso-surface of the corresponding numerical simulation (priv. comm. A.-C. Plesa, DLR) reveals an octahedral structure (c) artificial interferogram based on the numerical simulation.

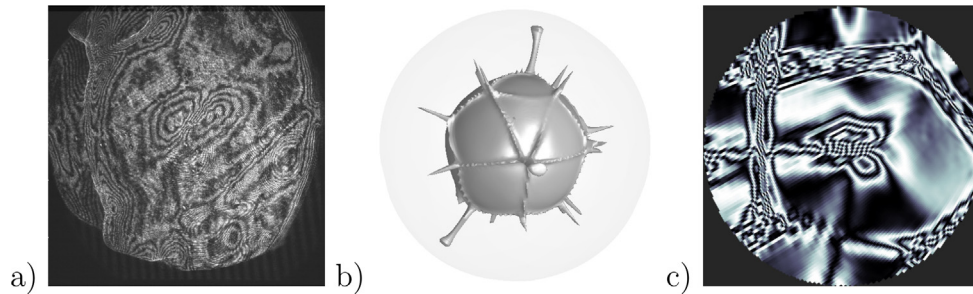


Fig. 10. (a) Turbulent convective flow for $Ra = 64,200$ and $Pr = 125$. (b) The representative temperature iso-surface of the corresponding numerical simulation (priv. comm. A.–C. Plesa, DLR) shows various steep convective plumes, surrounded by cold down-wellings. (c) Artificial interferogram based on the numerical simulation.

of the linear structure tensor with respect to the transformation ξ permits the identification of double ring structures in images. An analytical function $w : \mathbb{C} \setminus X \rightarrow \mathbb{C}$ with a finite set X of exceptions defines a HFP by (real w , imag w). Definition 4.2 works for arbitrary coordinate transformations given by HFPs. A detailed analysis of patterns generated by harmonic monomials z^n , n is integer, as well as of the discrete approximation of the GST for their detection can be found in (Bigun, 2006, Chapter 11).

5. Tracking

Besides recognition, the tracking of the convective structures is one of the aims of this study. This task can be carried out with little effort, if (a) the acquisition frame rate is high with respect to the fluid velocity, and if (b) the convective structures are stable in their shape. The frame rate of the experiment is fixed to two values, namely 0.048 Hz (long term runs) and 10 Hz (short term runs), but only the latter case is suitable for tracking. The plume tracking algorithm starts with the pre-calculated centers $(x(t), y(t))$ of convective plumes which are saved for each image and each time step in an external array. Based on this sequence the paths of convective structures can be extracted. However, this is somewhat superficial, since convective processes underlie merging, vanishing or formation. The plumes are captured and labeled individually, but it is difficult to identify segregated paths. To overcome this problem we analyze the neighborhood of each plume and define a probability radius R , where the plume will most likely appear in the next image. This radius depends on the rotation rate, on the imaging frame rate and on the velocity of the convective structure. For testing purposes we use stationary cells (cf. Section 6.3) with an angle velocity of $\omega = 1.4$ mm/s. The radius is set to a maximum of $R = 6$ px, keeping in mind that the slow rotation moves a stationary plume with about 1 px per frame. This value is obtained from a full rotation with 1250 images and a resolution of 992×992 pixels. The unique tracking of each plume is ensured by introducing the Euclidian norm of the transport vector $\mathbf{v}_t = (x_{i+1} - x_i, y_{i+1} - y_i)$ and fulfilling the inequality,

$$\|\mathbf{v}_t\|_2 < R. \quad (17)$$

The transport vector v_t measures the spatial change of the plume location over two images. This method calculates connected paths for segregated plumes as shown in Fig. 6. The tracking has been applied on the low resolution images of the GeoFlow IIC, too, where connected path could be extracted by adjusting the radius R . We mention this here because the successful low resolution test was mandatory for the start of the campaign. Several applications can be deduced from this type of recognition and tracking, e.g. the calculation of fluid velocities, the measurement of merging time scales or the determination of invariants such as the unknown coordinates of the north pole.

5.1. Identification of reference points

The calibration of the camera is used to quantify the geometrical and optical properties which affect the imaging process. This is essential for the reconstruction of the world model, in our case the flow velocities. Commonly, well defined checkerboard patterns are used to auto-calibrate a camera. This option is not available at the ODM. However, the camera properties can be reconstructed with reference points, too. The GeoFlow experiment rotates slowly which reduces the amount for these markers. Only the north pole is a fixed point in the experiment and the interferogram. The pole is the piercing point of the rotational axis which intersects with the optical axis. As already mentioned, the visualization of the GeoFlow experiment is limited to the northern hemisphere. Therefore, the south pole cannot be captured and does not contribute to the calibration process. The coordinates of the north pole are deduced from closed elliptical tracks. Each plume creates two ellipse-shaped curves which comes from the fact that one single plume appears as double-ring structure with two centers. The tracks form shifted, overlaying curves, where the common center of the structures gives the desired coordinates of the north pole. Two pole-surrounding ellipses as well as the calculated coordinates (colored in yellow) are shown in Fig. 7a. A second way of locating the north pole is utilizing stationary equatorial plumes. These plumes appear as elliptical curves too, but these are not closed (Figs. 6 and 7b). The area bounded by the perpendicular bisectors (yellow lines) approximates the

coordinates of the north pole and are within the uncertainty margin of the coordinates found by the tracking method.

Other markers may be obtained by fixed dust particles in the experimental gap (see yellow squares in Fig. 6). Some of them stick at the shell and move with the rotational velocity. They become noticeable as tiny double ring patterns, which lie on perfect ellipses. However, they have to be tracked manually, as they are too tiny to be recognized automatically by our algorithm. The optical distortion of the interferograms is another source of coordinates. By comparing the image point with the covered area in the experiment, it is possible to obtain enough coordinates for the exact calibration of the camera. This task is planned for future work.

6. Comparison of experimental- and artificial interferograms

The identification of plume-like and sheet-like convective structures by means of generic examples was shown in the previous sections. We are now able to deduce the temperature field from a comparison between experimentally gained interferograms and artificial interferograms based on numerical simulations. This approach bears uncertainties since the interferometric mapping is not unique. However, the basic structures, e.g. octahedral, axisymmetric or n-fold, can be determined. These flows are stationary and unique in their shape. Turbulent, time-depending structures are more difficult to align with numerical simulations. Long simulation times and merged patterns request more post-processing effort. Depending whether the regime is expected to be laminar or turbulent two numerical codes are used. The laminar regime is covered by the spectral code of Hollerbach (2000). Turbulent flows are calculated with the finite element code GAIAA from the DLR (priv. comm. A.-C. Plesa). The spectral solution converges significantly faster in the laminar regime and is therefore more efficient than GAIAA. Otherwise, GAIAA is parallelized and hence faster in the turbulent regime. Currently, a new finite volume code, based on OpenFOAM, is in preparation which will cover both regimes for the dimensional set of equations. The following non-dimensional equations describe the temporal evolution of the three-dimensional flow field \mathbf{u} and the temperature field T . This numerically solved set of equations is scaled with respect to the thermal time scale, the gap width, the diffusion velocity and the temperature difference because as these values are known from the GeoFlow IIc experiment at the reference temperature $T_{\text{ref}} = 30.5^\circ\text{C}$. The resulting non-dimensional numbers are the Rayleigh number Ra and the Prandtl number Pr ,

$$Pr^{-1} \frac{D\mathbf{u}}{Dt} = -\nabla p + \nabla \cdot \left(\frac{\nu(T)}{\nu_{\text{ref}}} (\nabla\mathbf{u} + \nabla\mathbf{u}^T) \right) + \frac{Ra \cdot T}{r^5} \mathbf{e}_r \quad (18)$$

$$\frac{DT}{Dt} = \nabla^2 T \quad (19)$$

$$\nabla \cdot \mathbf{u} = 0. \quad (20)$$

The left hand side of the Navier-Stokes equation (Eq. (18)) describes the advection of the flow field in terms of the material derivative D/Dt . The right hand side models the forces acting on the flow. These are the pressure, the viscosity and the radial dependent buoyancy. The temperature equation (Eq. (19)) is explained analogously. The left hand side is the advection of temperature, the right hand side models the influence of thermal diffusion. Both equations are coupled via the buoyancy force. The incompressible assumption is fulfilled with the divergence-free velocity field, Eq. (20). The temperature dependent viscosity is modeled with the Arrhenius law,

$$\nu(T) = \nu_{\text{ref}} e^{-\ln(\nu_{\text{ref}}/\nu_{\text{hot}})T}. \quad (21)$$

The viscosity contrast is set to $\gamma = 32$ and $Pr = 125$ (see Appendix A for all relevant physical properties). The temperature equation is coupled strongly with the Navier-Stokes equation which might be used to reconstruct the velocity field using the temperature distribution. In the following, we compare the experimental interferograms and the numerical simulations for three representative cases (laminar, transient, turbulent) qualitatively.

6.1. Laminar convective flow

The onset of convection and hence the laminar regime starts at $Ra = 498.15$. This value is independent from the high voltage or the temperature difference, and obtained by a linear stability analysis for $\gamma = 32$. The steady flow regime switches to the transition regime at about $Ra = 10^4$ which is observed in the numerical simulations and the experiment, too. However, the onset itself cannot be studied directly with our experiment, because the resolution of the interferometry unit is too low to capture temperature gradients below $\Delta T = 0.01$ K. The critical Rayleigh number is exceeded for a voltage $V_0 > 10,700$ V at the threshold value of $\Delta T = 0.01$ K, but this voltage is beyond the safety limit of the EC. Evaluable interferograms are obtained for $Ra_{\text{min}} > 4000$. The flow field is dominated by sheet-like, regular, threefold and fourfold structures. While the threefold ($m = 3$) mode is dominant, the fourfold ($m = 4$) mode exhibits in more distinct interferograms. Fig. 8a and d show a fourfold symmetry, which is clearly identified as convective sheet. The numerical simulation confirms this internal structure in the 3D reconstruction (Fig. 8b), as well as in the artificial interferogram (Fig. 8c). Additional structures appear by shifting the polarization direction, which is depicted in Fig. 8d–e. The pattern recognition algorithm localizes the areas of high frequent stripes corresponding to this type of flow precisely.

6.2. Transient convective flow

The transient regime separates laminar from turbulent flows. In terms of the Rayleigh number, we find this region

approximately between $10^4 < Ra < 3 \cdot 10^4$. This regime shows time-dependent structures which are found in both the experiment and simulations. However, the flows are still smooth compared to the turbulent regime. The given range is not defined by clear-cut values, but is based on observations of the GeoFlow experiment and numerical results. The interferogram in Fig. 9a is dominated by ridged structures surrounding single, unconnected plumes. We observe weakly unsteady octahedral structures in the numerical simulation (Fig. 9b), which exhibit as single double rings in the artificial interferogram (Fig. 9c). Again, these structures are accurately found as in the laminar case.

6.3. Turbulent convective flow

The turbulent regime ($Ra > 3 \cdot 10^4$) is characterized by highly unsteady convective flows in most cases. The interferogram in Fig. 10 shows rapidly changing patterns which are difficult to track at high rotation rates. Merging effects and interpenetration dominate this regime which inhibit the recognition with only one harmonic function pair. This gets visible in the top left corner of Fig. 10a, where several plumes merge and form an unclassified new pattern. Interestingly, we found an ‘island of stability’ (Table 4d) in the low turbulent regime ($Ra \approx 5 \cdot 10^4$) which delivers weakly unsteady, but distinct plumes. These interferograms are used to test the presented algorithm. As laminar stripes are not visible, but low fluid flows exist, the recognition is tested under conditions close to reality.

7. Conclusion and discussion

The measurement of convective flows with interferometry is a common and robust experimental technique. Nowadays, fast digital cameras and modern lasers give the opportunity to investigate fluid flows with high spatial and temporal resolution. However, measured interferograms are mostly processed manually. This works for small data sets, but gets exhausting for large series as they occur for time-dependent fluid flows. The presented automatic recognition of patterns in interferograms delivers the chance to reduce the post-processing costs for such flows. Basically, experimentally gained results are compared with artificial interferograms to interpret the convective flows. These artificial interferograms are based on numerical simulations, performed with two different codes. Laminar flows exhibit in symmetric configurations which change to unsteady octahedral structures in the transient regime. Turbulent flows appear as unsteady convective and plume dominated process. The comparison of experimentally gained interferograms and artificial interferograms is only qualitatively, but delivers sufficient indications about the structural processes. So far, we could not test our results against other existing numerical results or experiments. The physical model of GeoFlow IIc, using the r^{-5} depen-

dency and the temperature dependent viscosity, is very specific and not investigated by other authors. However, Feudel et al. (2011) studied iso-viscous convection in the spherical shell with the same radial dependency. Besides a seven-cell and an axisymmetric structure, they found a stable octahedral state for the transient regime. The interferograms at low temperature difference which are only weakly effected by the thermo-viscous influence, show this symmetry, too. The viscosity contrast of $\gamma = 32$ gives reasonable alignments between the experiment and the numerical simulations for the GeoFlow II mission. However, the origin of this high contrast cannot be explained by the physical properties of the fluid alone. It is assumed that the high voltage has a non-linear effect on the relative permittivity ϵ_r . This has to be tested under laboratory conditions and needs further investigations. The thermo-viscous case is covered by codes modeling the Earth’s mantle and similar objects. However, the stagnant-lid convection with infinite Prandtl numbers and viscosity contrasts of $\gamma \gg 10^4$ are far away from our parameter space. Anyhow, the utilized GAIAA code (DLR) and the spectral code of Hollerbach (2000) are consistent in their results and reproduce the experimental interferograms.

The informative value of the interferograms is enhanced by the localization and the tracking of convective plumes. Tracks of stationary plumes are used to determine reference points like the north pole. The coordinates of these points can, for instance, be used to calibrate the camera. This challenge is already in preparation. The aim of this calibration is the correct calculation of plume velocities.

The recognition algorithm can be applied to any interferometric image with patterns generated by the presented class of harmonic function pairs. This class covers many convective fringe patterns. The plume-like interferograms found in experiments of Kassemi and Rashidnia (2000) or Feng et al. (2015) might be tested with our routines. Additionally, these convective processes are unsteady, which could be used to apply our tracking routine, too. The interferometric stripes, as shown in Hiby et al. (2009) or Guo and Huang (2010), have qualitative similarities with patterns found in the laminar regime of the GeoFlow experiment. Again, these images can be used with our algorithm.

The pattern recognition algorithm processes the interferograms also fast. Images with resolutions comparable to ours are processed within several seconds. All steps of the image processing pipeline can be parallelized. The convolutions needed to generate the complex valued tensor can be computed on GPUs, too. With this, real-time applications are feasible.

Limitations of the technique are given by fast changing structures e.g. convective merging processes, and by low acquisition frame rates. In order to capture shape changing, turbulent thermal structures with the algorithm an adaptive exchange of the harmonic function pairs would be required. This is not considered here, but conceivable for future research.

Interferograms deliver information about the temperature field, but the velocity field can only be approximated from the temperature field indirectly. The direct assessment of the flow field requires further techniques, as PIV or LDA. However, particles are needed to determine the fluid flow, but might cause safety problems on the ISS and an unforeseeable working-load for astronauts.

The algorithm was only tested for very low rotation rates. As many GeoFlow experiments were carried out at high rotation, the adaption of the image processing pipeline to interferograms from these runs will be the next step of the GeoFlow evaluation.

Acknowledgements

The GeoFlow research has been funded by the ESA grants AO-99-049 and by the DLR grants 50 WM 0122

and 50 WM 0822. Furthermore the authors thanks the GeoFlow Topical Team (ESA 18950/05/NL/VJ) for fruitful discussions. Sketches and numerical simulations were improved by R. Dawood, P. Haun and F. Schwarzbach. Parallel simulations have been conducted at the Northern German Network for High-Performance Computing (HLRN) and the Heraklit cluster at the BTU Cottbus-Senftenberg.

Appendix A

Tables A1 and A2.

Table A1
Overview of the GeoFlow missions and the parameter space.

	Unit	GeoFlow I	GeoFlow II	GeoFlow IIb	GeoFlow IIc
<i>Execution</i>					
Date		08/2008–01/2009	03/2011–05/2012	12/2012–05/2013	11/2016–02/2017
Scientific time	h	n.a.	1.377	507	639
Performed vs. defined runs		10/30	43/52	12/48	63/63
<i>Variation of experiment parameters</i>					
Working fluid		Silicone oil M5	Alcohol 1-Nonanol	Alcohol 1-Nonanol	Alcohol 1-Nonanol
Viscosity contrast γ	1	$\gamma = 1$	$\gamma = 32$	$\gamma = 32$	$\gamma = 32$
Temp. difference ΔT	K	$0.1 < \Delta T \leq 10$	$0.2 < \Delta T \leq 10$	$0.2 < \Delta T \leq 10$	$0.4 < \Delta T \leq 9.6$
Voltage V_0	kV	10	6.5	$1.8 \leq V_0 \leq 6.5$	$1.8 \leq V_0 \leq 6.5$
Rotation rate Ω	Hz	0.008	0.008	0.008; 0.8; 1.6	0.008; 0.8; 1.6
<i>Imaging</i>					
Frame rate	Hz	0.048	0.048	0.048; 10	10
Images recorded		114.697	273.771	156.466	1.097.041
Telemetry data sets	Lines	342.698	4.810.834	1.736.502	2.219.021
Data	GB	92	263	176	290

Table A2
Physical and geometrical properties of the GeoFlow experiments.

Parameter	Unit	GeoFlow I	GeoFlow II	GeoFlow II
<i>Physical properties</i>				
Environmental temp. T_{ref}	°C	25.0	20.0	30.5
Density ρ_{ref}	kg/m ³	920	820	822
Kinematic viscosity ν_{ref}	m ² /s	$5.00 \cdot 10^{-6}$	$1.42 \cdot 10^{-5}$	$9.73 \cdot 10^{-6}$
Relative permittivity ϵ_r	1	2.70	8.60	8.83
Dielectric expansion α_E	1/K	$1.07 \cdot 10^{-3}$	$2.95 \cdot 10^{-3}$	$2.46 \cdot 10^{-3}$
Thermal conductivity λ	W/(m·K)	$1.16 \cdot 10^{-1}$	$1.63 \cdot 10^{-1}$	$1.58 \cdot 10^{-1}$
Thermal diffusivity κ_{ref}	m ² /s	$7.78 \cdot 10^{-8}$	$7.94 \cdot 10^{-8}$	$7.76 \cdot 10^{-8}$
Prandtl number Pr	1	64	178	125
Ra number Ra	1	$1.43 \cdot 10^5 - 1.43 \cdot 10^7$	$5.60 \cdot 10^2 - 1.75 \cdot 10^5$	$7.15 \cdot 10^2 - 2.24 \cdot 10^5$
Parameter	Unit	Property		
<i>Geometrical properties</i>				
Inner radius r_i	mm	13.5		
Outer radius r_o	mm	27.0		
Gap width H	mm	13.5		
Radius ratio r_i/r_o	1	0.5		
Weight	kg	34		
EC size	m ³	$0.40 \times 0.28 \times 0.27$		

References

- Baumgardner, J.R., 1985. Three-dimensional treatment of convective flow in the earth's mantle. *J. Stat. Phys.* 39 (5), 501–511. <http://dx.doi.org/10.1007/BF01008348>, ISSN 1572-9613.
- Bigun, J., 2006. *Vision with Direction*. Springer.
- Dupont, O., Dewandre, T., Dewandel, J.-L., Claessens, D., 2004. The optical diagnostics of the fluid science laboratory. In: *Proc. of the 5th int. Conference on Space Optics*, pp. 463–469.
- Egbers, Ch., Beyer, W., Bonhage, A., Hollerbach, R., Beltrame, Ph., 2003. The GeoFlow experiment on ISS (part I): experimental preparation and design of laboratory testing hardware. *Adv. Space Res.* 32 (2), 171–180. [http://dx.doi.org/10.1016/S0273-1177\(03\)90248-1](http://dx.doi.org/10.1016/S0273-1177(03)90248-1), ISSN 0273-1177.
- Feng, Z., Gao, Z., Zhang, X., Wang, S., Yang, D., Yuan, H., Qin, J., 2015. A polarized digital shearing speckle pattern interferometry system based on temporal wavelet transformation. *Rev. Sci. Instrum.* 86 (9), 93–102. <http://dx.doi.org/10.1063/1.4929533>.
- Feudel, F., Bergemann, K., Tuckerman, L.S., Egbers, Ch., Futterer, B., Gellert, M., Hollerbach, R., 2011. Convection patterns in a spherical fluid shell. *Phys. Rev. E* 83 (4), 046304. <http://dx.doi.org/10.1103/physreve.83.046304>, Apr ISSN 1550-2376.
- Futterer, B., Gellert, M., von Larcher, Th., Egbers, Ch., 2008. Thermal convection in rotating spherical shells: an experimental and numerical approach within GeoFlow. *Acta Astronaut.* 62 (4–5), 300–307. <http://dx.doi.org/10.1016/j.actaastro.2007.11.006>, ISSN 0094-5765.
- Futterer, B., Egbers, Ch., Dahley, N., Koch, S., Jehring, L., 2010. First identification of sub- and supercritical convection patterns from GeoFlow, the geophysical flow simulation experiment integrated in Fluid Science Laboratory. *Acta Astronaut.* 66 (1–2), 193–200. <http://dx.doi.org/10.1016/j.actaastro.2009.05.027>, Jan ISSN 0094-5765.
- Granlund, G.H., Knutsson, H., 1995. *Signal Processing for Computer Vision*. Kluwer Academic Publishers, Dordrecht, The Netherlands.
- Guo, H., Huang, P., 2010. Face recognition based on fringe pattern analysis. *Opt. Eng.* 49 (3), 037201. <http://dx.doi.org/10.1117/1.3339899>.
- Hart, J.E., Glatzmaier, G.A., Toomre, J., 1986. Space-laboratory and numerical simulations of thermal convection in a rotating hemispherical shell with radial gravity. *J. Fluid Mech.* 173, 519–544. <http://dx.doi.org/10.1017/S0022112086001258>.
- Hiby, L., Lovell, P., Patil, N., Kumar, N.S., Gopalaswamy, A.M., Karanth, K.U., 2009. A tiger cannot change its stripes: using a three-dimensional model to match images of living tigers and tiger skins. *Biol. Lett.* 5 (3), 383–386. <http://dx.doi.org/10.1098/rsbl.2009.0028>, ISSN 1744-9561.
- Hollerbach, R., 2000. A spectral solution of the magneto-convection equations in spherical geometry. *Int. J. Numer. Meth. Fluids* 32 (7), 773–797. [http://dx.doi.org/10.1002/\(SICI\)1097-0363\(20000415\)32:7<773::AID-FLD988>3.0.CO;2-P](http://dx.doi.org/10.1002/(SICI)1097-0363(20000415)32:7<773::AID-FLD988>3.0.CO;2-P), ISSN 1097-0363.
- Immohr, J., 2006. *Sphärische Differentialinterferometrie für Raumfahrtanwendungen - Konvektionsströmungen im Kugelspalt unter dem Einfluss axialer und radialer Kraftwirkung* (PhD thesis). Universität Bremen, VDI-Verlag, Reihe 7, Nr. 485.
- Kassemi, M., Rashidnia, N., 2000. Steady and oscillatory thermocapillary convection generated by a bubble. *Phys. Fluids* 12 (12), 3133–3146. <http://dx.doi.org/10.1063/1.1321263>.
- Lindeberg, T., 1993. Discrete derivative approximations with scale-space properties: a basis for low-level feature extraction. *J. Math. Imag. Vision* 3 (4), 349–376.
- Ogawa, M., 2008. Mantle convection: a review. *Fluid Dyn. Res.* 40 (6), 379–398.
- Ramesh, N., Merzkirch, W., 2001. Combined convective and radiative heat transfer in side-vented open cavities. *Int. J. Heat Fluid Flow* 22 (2), 180–187. [http://dx.doi.org/10.1016/S0142-727X\(00\)00080-1](http://dx.doi.org/10.1016/S0142-727X(00)00080-1), ISSN 0142-727X.
- Schubert, G., Bercovici, D., 2009. *Treatise on Geophysics*, vol. 7. Elsevier.
- Shapiro, V., 1995. Fringe-pattern recognition by using the polar-coordinate transform. *Exp. Mech.* 35 (4), 322–328. <http://dx.doi.org/10.1007/BF02317541>, ISSN 1741-2765.
- Sitte, B., 2004. *Thermische Konvektion in Zentralkraftfeldern* (PhD thesis). Universität Bremen, VDI-Verlag, Reihe 7, Nr. 460.
- von Larcher, Th., Futterer, B., Egbers, Ch., 2008. Geoflow: on the status of experimental preparation of spherical gap flow experiments with central force field on the international space station. *J. Phys: Conf. Ser.* 137, 12–25. <http://dx.doi.org/10.1088/1742-6596/137/1/012025>, Nov. ISSN 1742-6596.
- Wozniak, G., Wozniak, K., Bergelt, H., 1996. On the influence of buoyancy on the surface tension driven flow around a bubble on a heated wall. *Exp. Fluids* 21 (3), 181–186. <http://dx.doi.org/10.1007/BF00191690>, ISSN 1432-1114.

Influence of the temperature-dependent viscosity on convective flow in the radial force field

Vadim Travnikov,^{1,*} Florian Zaussinger,^{1,†} Philippe Beltrame,^{2,‡} and Christoph Egbers^{1,§}

¹*Department of Aerodynamics and Fluid Mechanics, Brandenburg University of Technology Cottbus-Senftenberg, Siemens-Halske-Ring 14, D-03046, Cottbus, Germany*

²*UMR1114, Université d'Avignon–INRA, F-84000 Avignon, France*

(Received 21 March 2017; published 29 August 2017)

The numerical investigation of convective flows in the radial force field caused by an oscillating electric field between spherical surfaces has been performed. A temperature difference ($T_1 > T_2$) as well as a radial force field triggers a fluid flow similar to the Rayleigh-Bénard convection. The onset of convective flow has been studied by means of the linear stability analysis as a function of the radius ratio $\eta = R_1/R_2$. The influence of the temperature-dependent viscosity has been investigated in detail. We found that a varying viscosity contrast $\beta = \nu(T_2)/\nu(T_1)$ between $\beta = 1$ (constant viscosity) and $\beta = 50$ decreases the critical Rayleigh number by a factor of 6. Additionally, we perform a bifurcation analysis based on numerical simulations which have been calculated using a modified pseudospectral code. Numerical results have been compared with the GeoFlow experiment which is located on the International Space Station (ISS). Nonturbulent three-dimensional structures are found in the numerically predicted parameter regime. Furthermore, we observed multiple stable solutions in both experiments and numerical simulations, respectively.

DOI: [10.1103/PhysRevE.96.023108](https://doi.org/10.1103/PhysRevE.96.023108)

I. INTRODUCTION

Buoyancy driven convective flows play a crucial role in geophysical and astrophysical research, and furthermore in the understanding of dynamos in the core of planets. Radial fields induced by means of an artificial electric force field in the spherical gap and coupled with temperature can be used to investigate convective flows in geophysics and astrophysics numerically and experimentally as well. Furthermore, a mechanism of the artificial gravity is useful for the flow control and heat transfer. To trigger such flows the influence of the Earth's gravity must be eliminated and heating source has to be placed to enable the artificial buoyancy force. The first condition can be satisfied by performing the experiment under microgravity conditions, e.g., on the International Space Station (ISS). A possibility to realize the second one is to set a temperature difference between surfaces, say the inner surface is warmer than the outer one ($T_1 > T_2$). The radial force field is created by an electric field \mathbf{E} which induces three forces. The force density generated by \mathbf{E} imposed on a dielectric fluid is obtained by [1]

$$\mathbf{f}_e = \rho_e \mathbf{E} - \frac{1}{2} \mathbf{E}^2 \nabla \epsilon(T) + \nabla \left[\frac{1}{2} \rho \left(\frac{\partial \epsilon}{\partial \rho} \right)_T \mathbf{E}^2 \right], \quad (1)$$

where the first term is the Coulomb force with free charge ρ_e . This force can be neglected as the inherent frequency is several magnitudes higher than characteristic process frequencies found in convective flows. The third one, namely electrostrictive force, is combined with the pressure gradient in the Navier-Stokes equation. The remaining second term corresponds to the dielectrophoretic force \mathbf{f}_{dep} . In principle, the electric permittivity ϵ is a tensor of rank 2, depending on

temperature and frequency. In the case of small temperature fluctuations the electric permittivity is approximated by a linear function

$$\epsilon(T) = \epsilon_0 \epsilon_r [1 - \gamma(T - T_2)]. \quad (2)$$

The force \mathbf{f}_{dep} can be written after small algebra as follows:

$$\mathbf{f}_{\text{dep}} = -\gamma(T - T_2) \mathbf{g}_e, \quad \mathbf{g}_e = \frac{\epsilon_0 \epsilon_r}{2\rho} \nabla E^2, \quad (3)$$

where \mathbf{g}_e is the electric field due to the induced artificial gravity field and γ is the thermal coefficient of the permittivity. The electric field can be found by solving the Gauss equation [2]. An expression for the gravity is simplified for large frequency ω of the applied electric field approximation: $\omega \gg \tau_e^{-1} = \sigma/\epsilon$, with electrical conductivity σ . A period averaged relation for the gravity reads

$$\mathbf{g}_e = -2V_{\text{rms}}^2 \frac{\epsilon_0 \epsilon_r}{\rho} \frac{R_1^2 R_2^2}{(R_2 - R_1)^2 r^5} \mathbf{e}_r. \quad (4)$$

Because the dielectrophoretic force \mathbf{f}_{dep} and the induced artificial gravity have opposite directions the problem can be compared with the classical Rayleigh-Bénard problem.

This specific problem has been considered by many authors in the case of the constant viscosity. The linear stability analysis for the radius ratios $\eta = R_1/R_2 = 0.1-0.7$ has been performed in [3] to investigate the onset of convection. It was found that in the nonrotating case critical Rayleigh number, obtained by means of the linear stability analysis, Ra_{cL} , increases with increasing in η . Moreover, the basic flow becomes unstable with respect to steady perturbations and does not depend on the Prandtl number. Perturbations have been represented in terms of spherical harmonics, Y_ℓ^m , and because of the spherical symmetry the linear stability analysis is performed in terms of the degree ℓ and not of the azimuthal wave number m as it occurs in rotating systems. Therefore, it is particularly important to perform nonlinear three-dimensional calculations to detect which patterns the system prefers. Busse [4] solved the pattern selection problem of the convective

*Vadim.Travnikov@b-tu.de

†Florian.Zaussinger@b-tu.de

‡Philippe.Beltrame@univ-avignon.fr

§Christoph.Egbers@b-tu.de

flow in the nonrotating case *analytically*, in which degree ℓ plays a crucial role. He found solutions with $\ell = 4$ and $\ell = 6$. Recently, the multiplicity of supercritical states has been detected in [5] by means of *numerical simulations*, using a pseudospectral code, developed by Hollerbach [6]. Octahedral and axisymmetric structures have been observed in the interval $2491 < \text{Ra} < 5000$ ($\text{Ra}_{cL} = 2491$), for the radius ratio $\eta = 0.5$ and Prandtl number $\text{Pr} = 64.64$. Further increase in Rayleigh number up to $\text{Ra} = 17450$ leads to the appearance of a seven-cell structure and periodic flow. Experimental investigations of the convective flow under the influence of the artificial gravity in the form of $\mathbf{g}_e \sim r^{-5}$ have been performed in [7] for fluids with constant viscosity like silicon oil. Spatiotemporal irregular structures have been observed for $\text{Ra} = 6.0 \times 10^4$. We expect that the use of working fluids with temperature-dependent viscosity enables the occurrence of new fluid structures which can have an important geophysical application [8,9].

The microgravity experiment GeoFlow is designed to capture convective flows with these properties. This is a motivation for our numerical efforts. First experimental and numerical results [10,11] show that sheetlike flows can be observed for moderate Rayleigh numbers, and that plumelike thermal flows develop if the Rayleigh number increases. Numerical three-dimensional solutions have been obtained by using the finite-volume method. But only recently we have developed a pseudospectral numerical code which is able to perform the linear stability analysis and evaluation of three-dimensional flows as well.

Solomatov [12] characterized convection with temperature dependent viscosity as follows. Isoviscous situations and small contrasts ($\beta < 10^2$) in the viscosity belong to the mobile-lid type. Here, convective plumes reach the colder boundaries. For $10^2 < \beta < 10^4$ the sluggish-lid regime dominates the flow. The viscous boundary layer at the colder side is significantly larger than at the hotter boundaries. This reduces the velocity of convective plumes. Situations where $\beta > 10^4$ develop a stagnant lid. Convective plumes are not able to reach the cold solid boundary. Recently, Curbelo and Mancho [13,14] published results for the transient sluggish lid case. Their simulations showed traveling waves, heteroclinic connections, and chaotic regimes in a two-dimensional setup in the presence of the $O(2)$ symmetry.

This paper is organized as follows. After discussion of governing equations in Sec. II we formulate briefly the numerical method (Sec. III) with which the problem under consideration is solved. Stability of the basic flow has been investigated by means of the linear stability theory in Sec. IV. Some examples of three-dimensional flows are presented in Sec. VA, two bifurcation scenarios and diagrams are discussed in Sec. VB, the behavior of the Nusselt number which describes the heat transfer is shown in Sec. VC, and comparison between numerical calculation and experimental results has been performed in Sec. VI.

II. EQUATIONS

We consider an incompressible viscous dielectric fluid in the spherical gap of width $d = R_2 - R_1$. The inner surface is maintained at the warmer temperature than the outer one

($T_1 > T_2$). Introducing the following scaling $\Delta T = T_1 - T_2$ for the temperature, $\rho_0(\kappa/d)^2$ for the pressure, d for the length, κ/d for the velocity, and $t_k = d^2/\kappa$ for the time, and using the Boussinesq approximation, the Navier-Stokes equation, the energy equation, and the continuity equation can be written in the dimensionless form as follows:

$$\text{Pr}^{-1} \left[\frac{\partial \mathbf{U}}{\partial t} + (\mathbf{U} \cdot \nabla) \mathbf{U} \right] = -\text{Pr}^{-1} \nabla P + \text{Ra} \frac{\eta^2}{(1-\eta)^4} \frac{T}{r^5} \mathbf{e}_r + \nabla \cdot \left[\frac{\nu(T)}{\nu_{\text{ref}}} [\nabla \mathbf{U} + (\nabla \mathbf{U})^T] \right], \quad (5)$$

$$\frac{\partial T}{\partial t} + (\mathbf{U} \cdot \nabla) T = \nabla^2 T, \quad (6)$$

$$\nabla \cdot \mathbf{U} = 0. \quad (7)$$

The flow depends on the radius ratio $\eta = R_1/R_2$, the Prandtl number $\text{Pr} = \nu_{\text{ref}}/\kappa = 125$ (1-Nonanol, GeoFlow II [10]), and the Rayleigh number

$$\text{Ra} = \frac{2\epsilon_0\epsilon_r\gamma}{\rho\nu_{\text{ref}}\kappa} V_{\text{rms}}^2 \Delta T,$$

where ϵ_r is the relative permittivity, γ is the permittivity, $V_{\text{rms}}^2 = V_0^2/2$ is the voltage, ρ is the density, and ν_{ref} is the viscosity on the outer and colder surface. The velocity should obey the no-slip boundary conditions $\mathbf{u} = 0$ and $T = 1$, $T = 0$ for the temperature on the surfaces $r = \eta/(1-\eta)$ and $r = 1/(1-\eta)$, correspondingly. The influence of the temperature-dependent viscosity is the focus of the research presented. The kinematic viscosity varies according to the Arrhenius law

$$\nu(T) = \nu_{\text{ref}} e^{-(\ln\beta)T}, \quad (8)$$

where $\beta = \nu_{\text{ref}}/\nu_{\text{hot}} = \nu_{\text{cold}}/\nu_{\text{hot}}$ is the viscosity contrast that varies between $\beta = 1$ (constant viscosity) and $\beta = 50$ and must be taken into account by solving the Navier-Stokes equation. The equations (5)–(8) with the boundary conditions have to be solved numerically.

III. NUMERICAL METHOD

The fully three-dimensional pseudospectral numerical code for the spherical geometry has been developed by Hollerbach [6] for the case of the constant viscosity. We expanded this tool on the situation when the viscosity varies according to the Arrhenius law Eq. (8). The poloidal-toroidal representation of the velocity field

$$\mathbf{U} = \nabla \times \nabla \times (\Phi \mathbf{e}_r) + \nabla \times (\Psi \mathbf{e}_r) \quad (9)$$

obeys the continuity equation. Separated equations for poloidal Φ and toroidal Ψ potentials are presented in the Appendixes. After performing the mapping $r = \frac{1}{2}[z + \frac{1+\eta}{1-\eta}]$, where $z \in [-1, +1]$ each scalar function can be expanded in terms of Chebychev polynomials $T_{k-1}(z)$ in radial direction and in terms of spherical harmonics $Y_\ell^m(\theta, \phi) = P_\ell^m(\theta) e^{im\phi}$ for the angular dependence. Expressions for poloidal and toroidal

potentials can be written as follows:

$$\Phi(t, r, \theta, \phi) = \sum_{m=0}^{\text{MU}} \sum_{\ell=\ell'}^{\text{LU}} \sum_{k=1}^{\text{KU}+4} (g_{ck\ell m}(t) \cos(m\phi) + g_{sk\ell m}(t) \sin(m\phi)) T_{k-1}(z) P_{\ell}^m(\theta), \quad (10)$$

$$\Psi(t, r, \theta, \phi) = \sum_{m=0}^{\text{MU}} \sum_{\ell=\ell'}^{\text{LU}} \sum_{k=1}^{\text{KU}+2} (f_{ck\ell m}(t) \cos(m\phi) + f_{sk\ell m}(t) \sin(m\phi)) T_{k-1}(z) P_{\ell}^m(\theta), \quad (11)$$

where $\ell' = \max(1, m)$, and KU, LU, and MU are cutoff parameters that vary between 20–30, 30–40, and 20–30, correspondingly. Time-dependent spectral coefficients have been calculated by means of the predictor-corrector method. The smallest time step was $\Delta t = 2 \times 10^{-5}$. Note that four boundary conditions for Φ and two for Ψ are necessary (see the Appendixes).

IV. LINEAR STABILITY ANALYSIS

The system of equations (5)–(8) has basic flow solution $\mathbf{u} = \mathbf{u}_0 = \mathbf{0}$, $T_{\text{cond}} = \frac{\eta}{(1-\eta)^2} \frac{1}{r} - \frac{\eta}{1-\eta}$. In contrast to the Rayleigh-Bénard convection, the artificial gravity is not constant and depends on r according to $g_e \sim r^{-5}$. Stability of the basic flow is investigated by means of linear stability theory, which is used to find such critical Rayleigh numbers, Ra_{cL} , above which the flow becomes unstable with respect to infinitesimal perturbations.

To calculate the critical Rayleigh numbers in frames of the linear stability theory the Navier-Stokes equation as well as the energy equation have to be linearized. Furthermore, the eigenvalue problem for the radius ratios between $\eta = 0.1$ – 0.7 , for different viscosity contrasts $\beta = 1$ – 50 needs to be solved, too. The basic flow is subjected to *small* perturbations $\tilde{\mathbf{u}}(t, r, \theta, \phi)$ for the velocity, $\tilde{p}(t, r, \theta, \phi)$ for the pressure, and $\Theta(t, r, \theta, \phi)$ for the temperature. Substituting the perturbed functions $\mathbf{U} = \mathbf{u}_0(=0) + \tilde{\mathbf{u}}$, $P = p_0 + \tilde{p}$, and $T = T_{\text{cond}} + \Theta$ in Eqs. (5)–(8) and neglecting nonlinear terms results in

$$\text{Pr}^{-1} \frac{\partial \tilde{\mathbf{u}}}{\partial t} = -\text{Pr}^{-1} \nabla \tilde{p} + \text{Ra} \frac{\eta^2}{(1-\eta)^4} \frac{\Theta}{r^5} \mathbf{e}_r + \tilde{\mathbf{f}}_0 + \frac{\nu(T_{\text{cond}})}{\nu_{\text{cold}}} \nabla^2 \tilde{\mathbf{u}}, \quad (12)$$

$$\frac{\partial \Theta}{\partial t} - \tilde{u}_r \frac{\eta}{(1-\eta)^2} \frac{1}{r^2} = \nabla^2 \Theta, \quad (13)$$

$$\nabla \cdot \tilde{\mathbf{u}} = 0, \quad (14)$$

with

$$\tilde{\mathbf{f}}_0 = \begin{pmatrix} \frac{\nu_r(T_{\text{cond}})}{\nu_{\text{cold}}} \tilde{D}_{rr} \\ \frac{\nu_r(T_{\text{cond}})}{\nu_{\text{cold}}} \tilde{D}_{r\theta} \\ \frac{\nu_r(T_{\text{cond}})}{\nu_{\text{cold}}} \tilde{D}_{r\phi} \end{pmatrix},$$

where \tilde{D}_{ij} are components of the rate-of-strain tensor for the perturbed velocity field multiplying by 2. Equations can be formulated in terms of the poloidal-toroidal decomposition. The potential $\tilde{\Phi}$ obeys Eq. (A2) with force $\tilde{\mathbf{F}} = \text{Ra} \frac{\eta^2}{(1-\eta)^4} \frac{\Theta}{r^5} \mathbf{e}_r$.

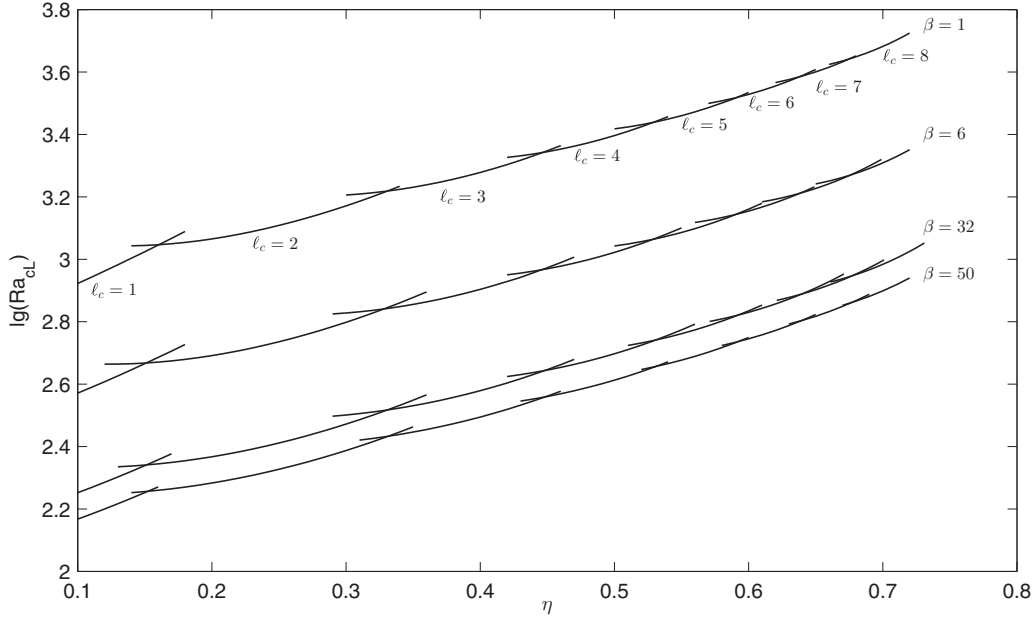
TABLE I. Critical Rayleigh numbers Ra_{cL} .

η	ℓ_c	$\beta = 1$	$\beta = 6$	$\beta = 32$	$\beta = 50$
0.10	1	836.55	372.57	178.72	147.08
0.20	2	1162.12	491.43	232.97	191.55
0.25	2	1283.95	544.15	257.85	212.42
0.30	2	1483.25	628.39	296.49	243.92
0.40	3	1897.87	801.22	379.34	312.33
0.50	4	2491.03	1052.10	498.15	409.96
0.56	5	2967.24	1254.15	594.14	488.79
0.62	6	3591.17	1519.08	719.35	591.59
0.65	7	3984.94	1686.66	799.02	656.92

The right hand side in Eq. (A3) is zero. Therefore, taking into account the boundary conditions for the toroidal potential, we get $\tilde{\Psi} = 0$. Hence we have to solve the system of two equations for $\tilde{\Phi}$ and Θ to derive the critical Rayleigh number. The stability problem has been solved by two methods: the first one by solving a generalized eigenvalue problem [15] and the second one by the time integration of linear Eqs. (12)–(14). Both methods enable the calculation of the leading eigenvalue, σ , which has the largest real part. Numerical analysis shows that the basic flow becomes unstable with respect to steady perturbations, i.e., $\text{Im}(\sigma) = 0$ for all radius ratios and viscosity contrasts considered. Therefore, as in the case of the Rayleigh-Bénard convection, the first instability does not depend on the Prandtl number. The leading eigenvalue is the growth rate in linear regime, calculated according to $\sigma = \frac{1}{\Delta t} \ln \frac{\Theta(t+\Delta t)}{\Theta(t)}$ because the time dependency of perturbation is proportional to $e^{\sigma t}$. The critical Rayleigh number corresponds to $\sigma = 0$. Results of both methods coincide with accuracy much less than 1%. Furthermore, the critical Rayleigh number at the onset of convection does not depend on the azimuthal wave number m . Hence the linear stability equations can be separated for each number ℓ . Summarizing, the critical Rayleigh number obeys

$$\text{Ra}_{cL}(\eta, \beta) = \min_{\ell} \text{Ra}_{\ell}(\eta, \beta). \quad (15)$$

Results of the linear stability analysis are presented in Fig. 1 (note the logarithmic scale for Ra_{cL}) and in Table I. Critical Rayleigh numbers and ℓ_c have been calculated as function on radius ratio for $\eta \in [0.1, 0.7]$ and for viscosity contrasts $\beta = 1, 6, 32, 50$. A stability analysis for the constant viscosity case ($\beta = 1$) has been performed too and discussed in [3]. Note that critical Rayleigh numbers and ℓ_c increase with increasing η for fixed β . But the temperature-dependent viscosity leads to the remarkable decreasing of the critical Rayleigh numbers Ra_{cL} . Indeed, whereas the onset of convection occurs at $\text{Ra}_{cL} = 836.55$ for $\eta = 0.1$ and at $\text{Ra}_{cL} = 2491$ for $\eta = 0.5$ in the case of the constant viscosity, the critical Rayleigh number shifts to $\text{Ra}_{cL} = 147.08$ for $\eta = 0.1$ and $\text{Ra}_{cL} = 409.96$ for $\eta = 0.5$ for the viscosity contrast $\beta = 50$ (Table I). But, generally, shapes of stability curves for temperature-dependent viscosity ($\beta > 1$) and constant viscosity ($\beta = 1$) are similar. Even intervals, in which the number ℓ_c is critical, shift only slightly from one β to the other. The next important feature is that the intervals with higher critical numbers ℓ_c become very narrow if η increases. This provides a multiplicity of the three-dimensional supercritical states.


 FIG. 1. Critical Rayleigh numbers Ra_{cL} as function on η .

V. 3D DYNAMICS SIMULATION

Solutions of the fully three-dimensional nonlinear problem are necessary for the identification of the three-dimensional structure of the flow. Moreover, results obtained in frames of the linear stability theory can be checked by means of three-dimensional calculations. However, only two bifurcation scenarios are analyzed, since the full analysis of the bifurcation branches would go beyond the scope of this study. The analysis of the three-dimensional flow begins with the presentation of slightly supercritical states. Furthermore, we investigate the behavior of the Nusselt number which is important for the description of the heat transfer. Additionally, experimental results allow one to corroborate numerical simulations. A comparison of numerical and experimental results from the GeoFlow experiment for the case $\eta = 0.5$ and $\beta = 32$ is presented in Sec. VI and ends this study.

A. Onset of convection

We present the bifurcated branches of solution near the onset of convection using results of local bifurcation analysis with spherical symmetry and time integration. The spherical symmetry of the problem gives information of the kind of bifurcations near the onset of convection [16]. For generic conditions (codimension-1 bifurcation), the possible bifurcated branches depend only on the ℓ_c critical mode [16]. In particular, the bifurcation is (supercritical or subcritical) pitchfork for odd modes and transcritical for even modes. Because of the spherical symmetry, the solution branch belongs to an orbit of solutions obtained by rotation around the centroid. Moreover, note that the pitchfork bifurcation breaks the antipodal symmetry ($\mathbf{r} \rightarrow -\mathbf{r}$) noted S . However, the solution X and its opposite $S(X)$ belong to the same orbit so, in this paper, we represent only one branch. Moreover, the theory of bifurcation with symmetry allows one to characterize the symmetry of the bifurcated branches at least for $\ell \leq 4$ [17].

The definition of symmetry groups relevant for the paper are given in Appendix B. We list the bifurcated branch for $\ell_c \leq 4$ as follows.

- (i) $\ell_c = 1$. One axisymmetric branch [$O(2)^-$ symmetry].
- (ii) $\ell_c = 2$. One axisymmetric branch [$O(2) \oplus \mathbb{Z}_2^c$]. This branch crosses the bifurcation point and it is unstable.
- (iii) $\ell_c = 3$. Three branches with the symmetries: $O(2)^-$, \mathbf{D}_6^d (threefold rotations), and \mathbb{O}^- (tetrahedron symmetry). The axisymmetric solution is unstable and there is one stable branch among the \mathbf{D}_6^d and \mathbb{O}^- branches.
- (iv) $\ell_c = 4$. Two unstable transcritical branches with the symmetries $O(2) \oplus \mathbb{Z}_2^c$ and \mathbb{O}^- cross the bifurcation point.

Therefore, the direct time integration is required to determine the stable branch for $\ell_c = 3$, on the one hand, and, on the other, for $\ell_c = 2$ or 4 to find the attractor near the onset since all bifurcated branches are unstable. We present two samples of the slightly supercritical three-dimensional flow for radius ratios $\eta = 0.1$ and $\eta = 0.5$ to examine results given by the linear stability analysis. Dynamic features are characterized by the total kinetic energy of the fluid E that can be represented as summation over the energies E_ℓ , corresponding to the wave modes ℓ ,

$$E = \frac{1}{2} \int_V \mathbf{u}^2 dV = \sum_{\ell} E_{\ell} = \sum_{\ell} \sum_{m=0}^{\ell} \varepsilon_{\ell m}. \quad (16)$$

In all cases the conducting state has been used as an initial condition. To produce a three-dimensional flow some spectral coefficients with $m > 0$ [see Eq. (11)] have been perturbed. No symmetry has been assumed. The nonlinear analysis confirms that the basic state [$\mathbf{u}_0 = \mathbf{0}$ and $T_0 = T_{\text{cond}}(r)$] loses stability, if the Rayleigh number exceeds the critical one ($Ra > Ra_{cL} = 147.08$) for $\eta = 0.1$ and $\beta = 50$ (Fig. 2). Calculation of energies E_ℓ show that the degree $\ell = 1$ is dominant (Table II), which is in good agreement with the linear stability (Table I). Modes $\ell = 1, m = 1$ ($\varepsilon_{11} = 0.2968$) and $\ell = 2, m = 2$ ($\varepsilon_{22} = 2.1459 \times 10^{-2}$) have a most significant

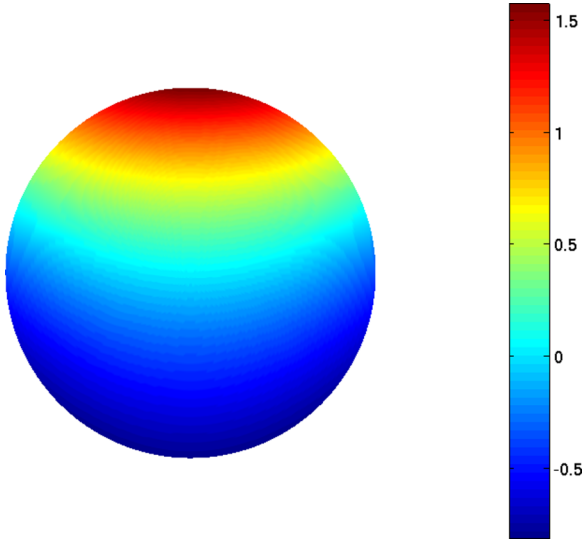


FIG. 2. Radial velocity component for $\eta = 0.1$, $Ra = 150$, $Pr = 125$, and $\beta = 50$ in the middle of the gap.

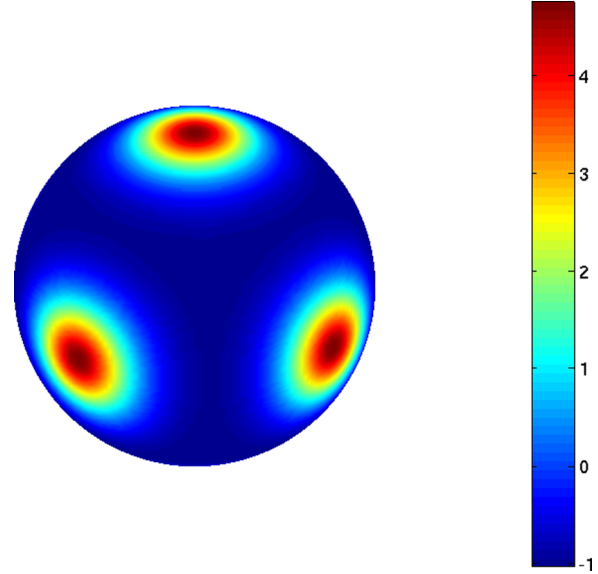


FIG. 3. Radial velocity component for $\eta = 0.5$, $Ra = 412$, $Pr = 125$, and $\beta = 50$ in the middle of the gap.

influence on the three-dimensional structure (Fig. 2). Please note that to make the influence of the mode $\ell = 1, m = 1$ visible the axisymmetric mode has been eliminated.

In case of radius ratio $\eta = 0.5$ nonlinear calculations, performed with small values of the spectral coefficients that have been used as initial conditions, are in very good agreement with linear stability results, too. The radial component of the three-dimensional steady flow obtained just above Ra_{cL} has an octahedral (Fig. 3) form as in the case of constant viscosity $\beta = 1$ [5]. But, in case of the temperature-dependent viscosity, e.g., $\beta = 50$, the flow becomes unstable much earlier at $Ra_{cL} = 409.96$ (Table I). According to the three-dimensional calculations this pattern has two dominant modes (Table III), corresponding to $\ell = 4, m = 0$ ($\epsilon_{40} = 26.6964$) and $\ell = 4, m = 4$ ($\epsilon_{44} = 19.0688$) in qualitative agreement with the analytical result obtained by Busse [4] and Bercovici *et al.* [18].

B. Bifurcation diagrams

Before we start discussion of the bifurcation diagrams, it is useful to introduce some definitions that are important for the description of the system under consideration. Because the basic flow is absent ($\mathbf{u}_0 = 0$) it is convenient to define the value

$$a = \sqrt{E} \tag{17}$$

as the *amplitude* of the flow. The behavior of the amplitude is controlled by the supercriticality, $\delta = (Ra - Ra_{cL})/Ra_{cL}$, or Rayleigh number *control parameter*.

TABLE II. Kinetic energy of the first four modes for $\eta = 0.1$, $Ra = 150$, $Pr = 125$, and $\beta = 50$.

ℓ	E_ℓ	ℓ	E_ℓ
1	0.3151	3	8.631×10^{-4}
2	0.0322	4	3.090×10^{-5}

We present only two bifurcation scenarios occurring in gaps with radius ratios $\eta = 0.1$ and $\eta = 0.5$ and for fixed Prandtl number $Pr = 125$.

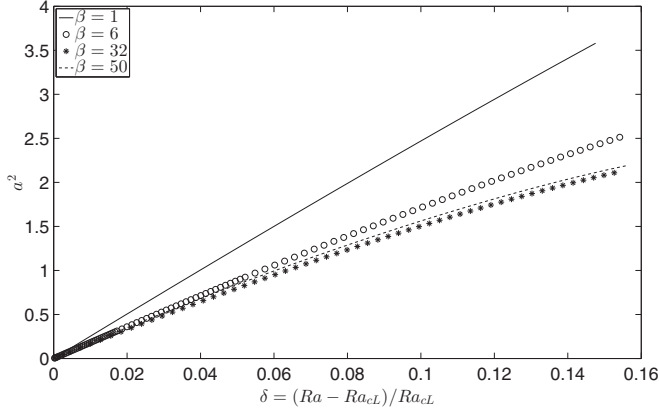
Numerical calculations, performed for wide gap ($\eta = 0.1$), show that critical Rayleigh numbers, given by three-dimensional analysis, coincide with Ra_{cL} , obtained by means of the linear stability analysis for all viscosity contrasts considered. The next confirmation of the linear stability results is that the three-dimensional flow is steady. The bifurcation diagram for this situation is presented in Fig. 4. The Navier-Stokes equation has a stable conductive solution at $\delta < 0$. Convection sets in at the bifurcation point $\delta = 0$. If the Rayleigh number exceeds the critical one, $\delta > 0$, the conductive solution loses its stability with respect to infinitesimal perturbations. The instability sets in as a *pitchfork supercritical bifurcation*, because the conductive solution becomes unstable only at $\delta > 0$. Note that the critical degree is $\ell_c = 1$ in agreement with theoretical results. According to the Landau equation [19] the amplitude at the vicinity of the critical Rayleigh number can be approximated by the expression

$$a = C_a(\beta)\sqrt{\delta}. \tag{18}$$

Values of the constant C_a are located between $C_a = 4$ and $C_a = 5$ (Table IV). It is interesting to note that this kind of bifurcation is usual in the case of the constant viscosity, e.g., in the box with free-slip boundaries [20] and in the cylindrical gap [21,22].

TABLE III. Kinetic energy of the most dangerous modes for $\eta = 0.5$, $Ra = 412$, $Pr = 125$, and $\beta = 50$.

ℓ	E_ℓ	ℓ	E_ℓ
4	45.7652	8	2.5291
6	3.0104	10	0.1732


 FIG. 4. Amplitude of the supercritical flow for $\eta = 0.1$.

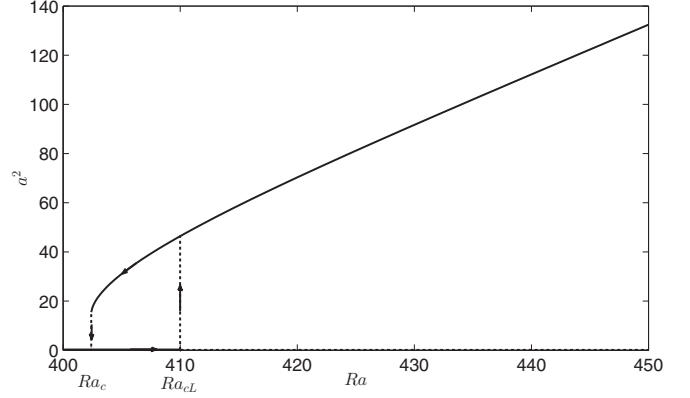
A different bifurcation scenario occurs at $\eta = 0.5$ (Fig. 5). We present the case with $\beta = 50$ in detail. The basic flow loses its stability suddenly at $Ra = Ra_{cL} = 409.96$. A branch where $a = 0$ (dotted line in Fig. 5) becomes unstable with respect to infinitesimal perturbations. The transition occurs with a jump into the branch, corresponding to the convective flow (bold line in Fig. 5). The fundamental difference to the above considered case is that the conductive state becomes unstable in the interval $Ra_G < Ra < Ra_{cL}$ (Ra_G is the Rayleigh number, corresponding to the global stability) if the perturbation is large enough. From the other side, the conductive solution remains stable to infinitesimal perturbations in this region. The transition from the convective branch on the conductive one occurs at $Ra_c = 402.4$ again with a jump. Hence the *subcritical* instability leads to the hysteresis effect. It suggests that the unstable transcritical branch possesses a turning point in the subcritical region for which the branch gains stability as it is observed in the isoviscous case [5,23]. Note that the same bifurcation scenario takes place for other β , too. But whereas the difference $\Delta = (Ra_{cL} - Ra_c)/Ra_{cL} = 0.06\%$ is very small in the case of constant viscosity $\beta = 1$ ($Ra_{cL} = 2491$, $Ra_c = 2489.4$), the hysteresis effect becomes more remarkable in fluids with high viscosity contrast, e.g., for $\beta = 32$ ($Ra_{cL} = 498.15$, $Ra_c = 492.8$) we have numerically found that $\Delta = 1.21\%$ and for $\beta = 50$, $\Delta = 1.84\%$ (Fig. 5).

C. Behavior of the Nusselt number

The Nusselt number is a global characteristic of the heat transfer that is defined as the ratio between the heat flux of the convective flow and the heat flux of the pure conduction regime, $T_{\text{cond}}(r)$. Expressions for the Nusselt number on the inner and outer surfaces can be formulated as follows:

 TABLE IV. Constants C_a and C_{Nu} for $\eta = 0.1$.

β	C_a	C_{Nu}
1	5.02	0.4300
6	4.25	0.3871
32	4.06	0.4037
50	4.19	0.4562


 FIG. 5. Amplitude of the flow for $\eta = 0.5$ and $\beta = 50$.

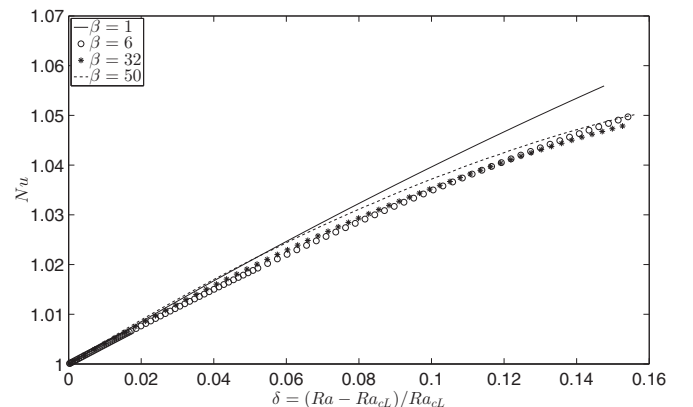
$$Nu_{\text{in}} = -\frac{(1-\eta)^2}{4\pi\eta} \int_{S_{\text{in}}} \left(\frac{\partial T}{\partial r} \right)_{\text{in}} dS_{\text{in}}, \quad (19)$$

$$Nu_{\text{out}} = -\frac{(1-\eta)^2}{4\pi\eta} \int_{S_{\text{out}}} \left(\frac{\partial T}{\partial r} \right)_{\text{out}} dS_{\text{out}}. \quad (20)$$

Beginning with the case $\eta = 0.1$ (supercritical bifurcation), we note that if the Rayleigh number is smaller than the critical one ($Ra < Ra_{cL}$) the Nusselt number is unity and increases if the Rayleigh number exceeds Ra_{cL} (Fig. 6). It is worth noting that according to the linear stability analysis the threshold of convection does not depend on the Prandtl number. Nevertheless, this dependence appears in the nonlinear case. We concentrate on the influence of the parameter β on the flow and heat transfer, because of our interest on the temperature-dependent viscosity in frames of the GeoFlow experiment on the ISS. The behavior of the Nusselt number for slightly supercritical states has a linear shape and changes according to

$$Nu = 1 + C_{Nu}(\beta)\delta. \quad (21)$$

Constants $C_{Nu}(\beta)$ have almost the same value for all β considered (Table IV). Moreover, it is worth noting that the influence of the dielectrophoretic effect on the heat transfer in the wide spherical gap is weaker than in the cylindrical one where $Nu = 1 + 0.92\delta$ for $\eta = 0.1$ [22]. The behavior of the


 FIG. 6. Behavior of the Nusselt number for $\eta = 0.1$.

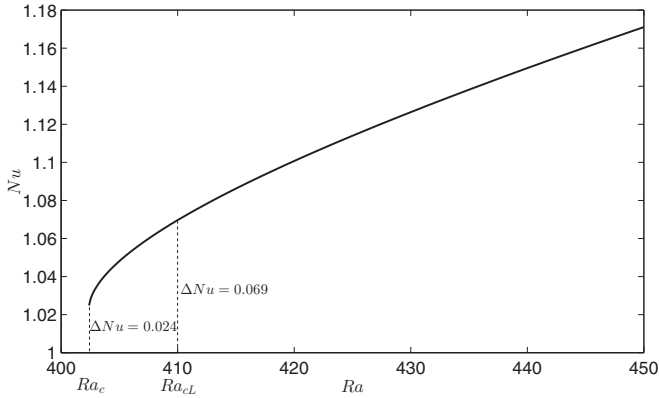


FIG. 7. Behavior of the Nusselt number for $\eta = 0.5$ and $\beta = 50$.

Nusselt number changes drastically for $\eta = 0.5$. A subcritical bifurcation is responsible for the jump of the Nusselt number at $Ra = 409.96$. Furthermore, the Nusselt number undergoes a remarkable increase in comparison to $\eta = 0.1$ (Fig. 7). Indeed, whereas an increase of the Rayleigh number of 10% for the wide gap leads to a change of the Nusselt number solely in 3%–4%, the same growth of the Rayleigh number for $\eta = 0.5$ causes an enhancement of the Nusselt number of 18% which is interesting from a practical point of view for possible technical applications.

VI. COMPARISON WITH EXPERIMENT

The GeoFlow experiment [11,24] on the ISS is designed to study convective flows under the influence of a radial force field. The specific experimental setup follows strictly the spherical gap geometry presented in Sec. I. A gap between two concentric spherical shells is filled with a highly viscous dielectric working fluid, namely the straight chain fatty alcohol 1-Nonanol. The radius ratio of $\eta = 0.5$ is in good agreement with geometrical properties of the Earth’s outer core and even the Earth’s mantle. Convection is triggered by heating the inner shell in steps of $T_{\text{cold}} + \Delta T$, where $(\Delta T)_{\text{min}} = 0.4$ K and the maximum temperature difference is $\Delta T = 10$ K. The experiment is performed at two working environments, $T_{\text{cold}} = 20^\circ\text{C}$ and $T_{\text{cold}} = 30.5^\circ\text{C}$, respectively. The lower working environment has a Prandtl number of $Pr = 179$, whereas the higher temperature level lowers the viscosity and hence the Prandtl number to $Pr = 125$. The Rayleigh number is changed according to the working environment by a factor of about 20% to higher values. The radial force field is established by utilizing the dielectrophoretic effect, which brings radial accelerations between $0.1 \text{ m/s}^2 < g_e < 13 \text{ m/s}^2$. In consequence of the low acceleration at the outer shell it is necessary to perform the experiment under microgravity conditions. The viscosity contrast of $\beta = 32$ exhibits from the temperature dependent relative permittivity of the working fluid.

The visualization of the fluid flow is a crucial point. However, the safety requirements of the Columbus module make it difficult to work with particles in the fluid. Therefore, a Wollaston sharing interferometry unit is utilized which works by optical means alone. The analysis, interpretation, and

postprocessing of these specific interferograms are discussed by various members of the GeoFlow topical team. Depending on the GeoFlow campaign, the interferograms were recorded at different frame rates. In the presented study we use 10 Hz video streams which allow tracking of fluid flows quite accurately. However, this frame rate is more than sufficient for the laminar regime. The recorded period per experimental set point is 2 min, resulting in about 1200 images. In total, 240 parameter variations have been performed during the GeoFlow campaign. The resulting fringe patterns are the base of the following comparisons between numerical simulations and experiments. The experimentally gained Rayleigh numbers are in the range of $10^2 < Ra < 10^6$, but in the following we focus on experiments for $Ra < 1.4 \times 10^4$, which are covered by numerical simulations. This regime is dominated by steady laminar flows and conductive states. Due to limitations of the sensitivity in the Wollaston shearing interferometry it is not possible to visualize the onset of convection itself. The lowest technically reachable Rayleigh number is $Ra = 560$, which is just above the theoretical onset of $Ra = 498.15$. However, evaluable interferograms are achieved for $Ra \geq 4200$. The high voltage is set to $V_{\text{rms}} = 1800$ V and the reference temperature to $T_{\text{cold}} = 30.5^\circ\text{C}$. This gives a Prandtl number of $Pr = 125$, which is used for the numerical simulations, too. Changes in the Rayleigh numbers are only due to temperature variations which are $\Delta T = 1.7$ K. To lower statistical anomalies, we performed all experimental set points twice.

A. Comparison of numerical and experimental results

In order to validate the theoretical results, we compare numerical interferograms with the experimentally gained images (Fig. 8). The numerical interferograms are calculated by means of the temperature field alone. The radially integrated and weighted temperature field needs to be differentiated directionally in the polarization plane. The resulting temperature fluctuations are visualized by applying a cosine on this field. This gives fringe patterns which are similar to the experimental images [25]. Generic analytical interferograms are subsequently used to distinguish between convective rising plumes and sheetlike flows. The parameter regime of time-dependent convective plumes is above $Ra = 1.4 \times 10^4$ and not covered by this study. In principle, we observe only threefold and fourfold symmetries of the m mode in the interferograms. These structures exhibit in regular, star-shaped patterns. The detection of ℓ mode is not unique, since the optical access does not allow one to investigate the whole lateral elongation. However, we can utilize symmetries in the angles between the sheetlike plumes. The angles between the stripes measure theoretically 120° in the threefold case and 90° in the fourfold case. This geometrical property can be used to identify the m modes. Optical distortions lower and raise the observed angles by 20%–30%, depending on the interferometry direction. The angles between the rays are helpful, but not sufficient for the unique identification. As the experiment rotates very slowly (0.008 Hz, Taylor number $Ta < 1$), the fringe lines change their relative shape, too. Only by tracking the structures individually it is possible to identify them. Figure 9, first column, presents four experimental set points, namely $Ra = 3040$, $Ra = 4200$,

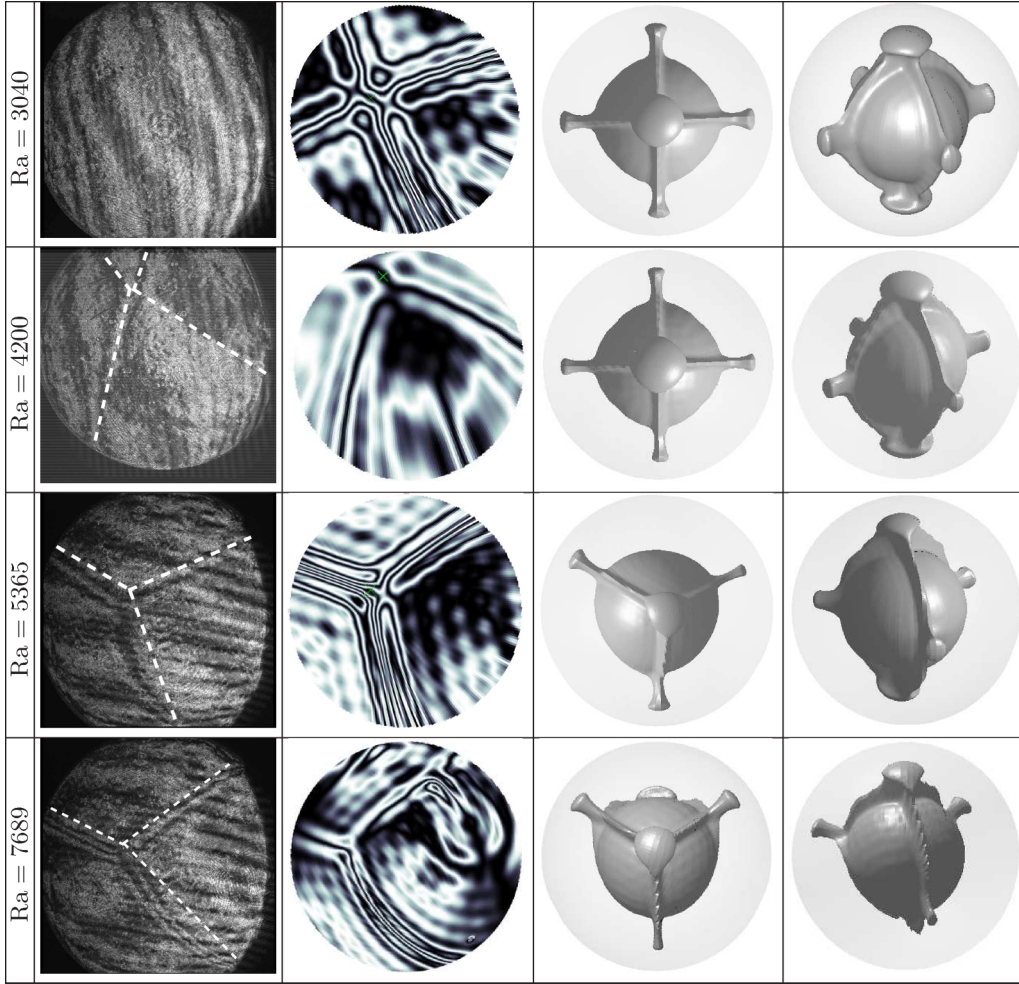


FIG. 8. Comparison of experimental and numerical results for various Rayleigh numbers. From left to right: (1) experimental interferograms from the GeoFlow experiment on the ISS; (2) artificial interferograms calculated by numerical simulations; (3) top view of numerical simulation; (4) side view of numerical simulation. Temperature isosurfaces are calculated at $T = 0.7$. The artificial interferograms show the same modes as the experiments. Even the transition from $(\ell = 4, m = 4)$ at $Ra = 4200$ to $(\ell = 3, m = 3)$ at $Ra = 5365$ is observed. Due to limitations of the interferometry unit, the case of $Ra = 3040$ shows a false conductive solution.

$Ra = 5365$, and $Ra = 7689$. A false (in the sense of interferometry) conductive state is observed: the experimental interferograms do not show significant fringe patterns for $Ra = 3040$, while according to the stability analysis we expect convective flow. The case $Ra = 4200$ displays a fourfold mode $m = 4$ which is in good agreement with the numerical analysis that shows that modes $(\ell = 4, m = 0)$ and $(\ell = 4, m = 4)$ with energies $\epsilon_{40} = 1458.2$ and $\epsilon_{44} = 5900$ are dominant. As found in the numerical simulations, we identify a transition from $m = 4$ to $m = 3$ as the Rayleigh number is increased from $Ra = 4200$ to $Ra = 5365$. Indeed, according to the numerical investigation mode $(\ell = 3, m = 3)$ becomes dominant ($\epsilon_{33} = 7354.52$) for $Ra = 5365$. These patterns are dominant up to $Ra = 1.4 \times 10^4$. Higher values exhibit in transient, time-dependent flows. We summarize that the $m = 4$ and the $m = 3$ modes are predominant in the convective laminar regime for $\eta = 0.5$ and $\beta = 32$ in the GeoFlow experiment. In the following, we analyze the symmetry classes in more detail.

B. Extended analysis of symmetry classes

If the interferometry method allows only identification of the m modes, it is interesting to retrieve the ℓ -spherical mode of these solutions using DNS. Five cases are analyzed in detail and compared with experimental results. For $Ra = 4000$ we found two stable states which differ in the ℓ mode. The cases of $Ra = 3000$, $Ra = 5365$, and $Ra = 7000$ exhibit in unique states. More specifically, we list the symmetry analysis as follows.

(i) $Ra = 3000$ and $Ra = 4000$ ($\ell = 4$). The steady states are a pure $\ell = 4$ mode with the symmetry $\mathbf{D}_4 \oplus \mathbb{Z}_2^c$, i.e., the full group symmetry of a prism with a square basis. This group being a subgroup of the cube symmetry group then, this branch is a secondary branch of the cube symmetric branch (Fig. 5).

(ii) $Ra = 4000$ ($\ell = 3$). The symmetry group is \mathbf{D}_6^d ; this threefold symmetric branch bifurcates from the onset of convection of the mode 3. However, according to our numerical results, it is unstable near the onset of convection. Therefore, the stability of the steady state suggests that at least a

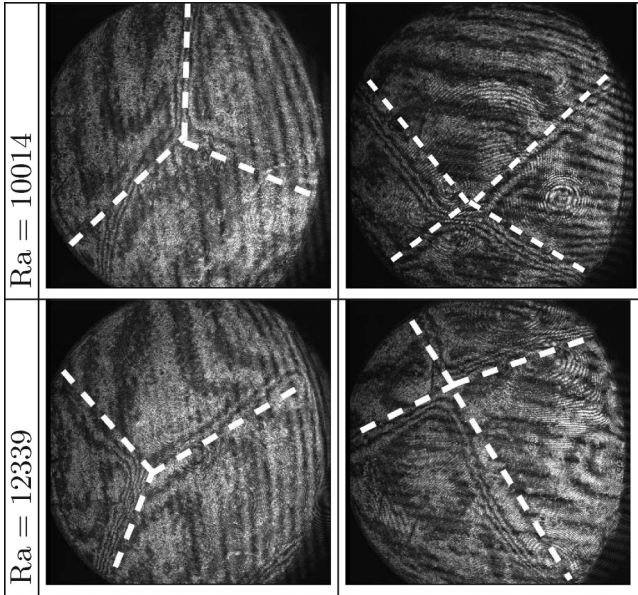


FIG. 9. Hysteresis in the laminar experimental regime: threefold and fourfold symmetries are observed; however, the unstable fourfold symmetry class is more likely in this experiment. In order to lower statistical anomalies, we performed experiments with nonunique patterns several times at different days.

bifurcation occurs and this solution could be a mixed mode (3,4). Therefore, near the bifurcation the mode 4 remains till $Ra = 4000$. Beyond the mode 3 is in competition with the mode 4.

(iii) $Ra = 5365$. Almost symmetries of the steady state are broken except a plane reflexion. It is then the \mathbb{Z}_2^- symmetry. It is easy to recognize approximatively the threefold rotation and other plane reflexion, so the symmetry of the solution is close to the \mathbf{D}_3^z or \mathbf{D}_6^d symmetries. The observed mode can be a secondary branch from \mathbf{D}_6^d or \mathbf{D}_3^z branches. All these solutions are possible steady states of the pure mode $\ell = 3$. However, it is possible that the mode 4 coexists. Moreover, note that this \mathbb{Z}_2^- symmetry was not observed near the onset for the (3,4) mode interaction for the isoviscous case (see [15]).

(iv) $Ra = 7000$. The steady state has the symmetry \mathbf{D}_2^z which corresponds to a twofold reflexion and a plane reflection symmetry. This steady state does not exist for the pure mode $\ell = 3$ but rather for the mode interaction (3,4) (see, e.g., Ref. [15]). Other symmetries are clearly broken, so this steady state is clearly a mixed mode between $\ell = 3$ and $\ell = 4$. The experimental example differs in the Rayleigh number; however, the (3,4) mode is still assumed.

We summarize that the $\ell = 3$ and $\ell = 4$ modes are predominant in the convective laminar regime for $3000 < Ra < 8000$. By increasing the Ra number, we have the main steps of bifurcation scenario: (a) pure mode 4 steady state; (b) almost “pure” mode 3 steady state; (c) mixed modes 3 and 4.

C. Hysteresis effect in experiment

The experiments show the existence of multiple stable patterns. This behavior is restricted to a few experiments for $10^4 < Ra < 1.4 \times 10^4$. At first, the experimental data seemed

to be biased by preceding runs. Therefore, we repeated specific set points randomly which reinforced the suspicion that this parameter space exhibits in multiple stable laminar flows. We found the $m = 3$ and the $m = 4$ wave modes at the same Rayleigh number, but in different set points. First results are displayed in Fig. 9. The angles between the rays as well as the (not presented) time lapse are strong evidence that both modes are stable. However, the flow with wave number $m = 4$ mode is less frequent than the flow with $m = 3$. It is assumed that the basin of attraction of the mode $m = 4$ is smaller than for $m = 3$. Similar results are observed in the numerical simulations, where the initial conditions trigger different dominant modes. The randomly initialized flows are an appropriate way to lower these uncertainties.

VII. CONCLUSION

The presented study deals with the numerical investigation of the convective flow between two spherical surfaces. The inner one is warmer than the outer one. An applied oscillating electrical field produces an artificial radial gravity due to the dielectrophoretic effect. Hence the situation is similar to the Rayleigh-Bénard convection. The influence of the temperature-dependent viscosity has been taken particularly into account. The onset of the convective flow is investigated by means of the linear stability theory that enables one to calculate the critical Rayleigh number, Ra_{cL} , above which the basic flow is always unstable. We found that the temperature-dependent viscosity leads to significant decrease of the critical Rayleigh number. A pseudospectral code developed by Hollerbach [6] and modified for the case of the temperature-dependent viscosity has been used to calculate three-dimensional flows. We present two bifurcation scenarios that occur in spherical gaps with $\eta = 0.1$ and $\eta = 0.5$. Whereas the instability sets in as a supercritical pitchfork bifurcation in the wide gap, if the Rayleigh number exceeds the critical one, the conductive state bifurcates into the convective one with jump, if the gap becomes narrower. The occurring subcritical bifurcation leads to the hysteresis effect. The behavior of the Nusselt number shows that the heat transfer in the wide spherical gap is essentially weaker in comparison to the cylindrical one. Nevertheless the heat transfer grows remarkably if the radius ratio increases. Besides numerical simulations, we compared our results with data from the GeoFlow experiment which is located on the ISS. In order to investigate convection under microgravity conditions, the dielectrophoretic effect is used to maintain an artificial radial force field. The experimental set points reach down to the onset of convection. Evaluable results were found for $Ra > 4020$, where $m = 4$ and $m = 3$ modes are found. Experimental and numerical interferograms are in good agreement in the presented parameter space. Even regimes with multiple stable structures are observed, where both wave numbers ($m = 3$ and $m = 4$) occur at the same Rayleigh number. Especially the experimental validation confirms the theoretical and numerical results presented in this study.

It is planned to extend the presented study to the rotating case. The GeoFlow experiment has been performed for three rotation rates, 0.008 Hz, 0.8 Hz, and 1.6 Hz. The resulting Taylor numbers $Ta = (\Omega d^2/\nu)^2$ are below $Ta = 6 \times 10^4$ for $Ra < 1.4 \times 10^4$, which can be covered by the presented code.

ACKNOWLEDGMENTS

The GeoFlow research has been funded by the ESA Grant No. AO-99-049 and by the DLR Grants No. 50 WM 0122 and No. 50 WM 0822. Furthermore, the authors thank the GeoFlow Topical Team (ESA No. 18950/05/NL/VJ), Prof. U. Harlander (Brandenburg University of Technology Cottbus-Senftenberg, Department of Aerodynamics and Fluid Mechanics), and Prof. H. Kuhlmann (TU Wien, Institute of Fluid Mechanics and Heat Transfer) for fruitful discussions. Parallel simulations have been performed at the Northern German Network for High-Performance Computing (HLRN) and the Heraklit cluster at the BTU Cottbus-Senftenberg.

APPENDIX A: DERIVATION OF EQUATIONS IN THE POLOIDAL-TOROIDAL FORM

In this Appendix we explain how the equations for the poloidal and toroidal potentials in the case of the temperature dependent viscosity can be carried out. Furthermore, we clarify technical details concerning implicit usage of some terms that originally were a part of the friction force. The last term in the Navier-Stokes equation (5) can be written in more useful form. Indeed, introducing the notation $\mathbf{f} = \nabla \cdot \left[\frac{\nu(T)}{\nu_{\text{cold}}} [\nabla \mathbf{u} + (\nabla \mathbf{u})^T] \right]$, we have after small algebra

$$\mathbf{f} = \mathbf{f}_0 + \frac{\nu(T_{\text{cond}})}{\nu_{\text{cold}}} \Delta \mathbf{u} + \mathbf{f}_1 + \frac{\nu(T) - \nu(T_{\text{cond}})}{\nu_{\text{cold}}} \Delta \mathbf{u}, \quad (\text{A1})$$

where

$$\mathbf{f}_0 = \begin{pmatrix} \frac{\nu_r(T_{\text{cond}})}{\nu_{\text{cold}}} D_{rr} \\ \frac{\nu_r(T_{\text{cond}})}{\nu_{\text{cold}}} D_{r\theta} \\ \frac{\nu_r(T_{\text{cond}})}{\nu_{\text{cold}}} D_{r\phi} \end{pmatrix},$$

$$\mathbf{f}_1 = \begin{pmatrix} \frac{\nu_r(T) - \nu_r(T_{\text{cond}})}{\nu_{\text{cold}}} D_{rr} + \frac{1}{r} \frac{\nu_\theta(T)}{\nu_{\text{cold}}} D_{r\theta} + \frac{1}{r \sin \theta} \frac{\nu_\phi(T)}{\nu_{\text{cold}}} D_{r\phi} \\ \frac{\nu_r(T) - \nu_r(T_{\text{cond}})}{\nu_{\text{cold}}} D_{r\theta} + \frac{1}{r} \frac{\nu_\theta(T)}{\nu_{\text{cold}}} D_{\theta\theta} + \frac{1}{r \sin \theta} \frac{\nu_\phi(T)}{\nu_{\text{cold}}} D_{\theta\phi} \\ \frac{\nu_r(T) - \nu_r(T_{\text{cond}})}{\nu_{\text{cold}}} D_{r\phi} + \frac{1}{r} \frac{\nu_\theta(T)}{\nu_{\text{cold}}} D_{\theta\phi} + \frac{1}{r \sin \theta} \frac{\nu_\phi(T)}{\nu_{\text{cold}}} D_{\phi\phi} \end{pmatrix},$$

with $T_{\text{cond}} = \frac{\eta}{(1-\eta)^2} \frac{1}{r} - \frac{\eta}{1-\eta}$. This decomposition of the friction term is useful from the numerical point of view because the first two terms in (A1) can be embraced implicitly which increases the numerical convergence. An application of operations $\nabla \times \nabla \times$ and $\nabla \times$ not only eliminates the pressure but also allows one to obtain separated equations for potentials Φ and Ψ ,

$$\begin{aligned} & \frac{\Delta_s}{r^2} \left[\frac{1}{\text{Pr}} \frac{\partial}{\partial t} \left(\frac{\partial^2}{\partial r^2} + \frac{\Delta_s}{r^2} \right) - \frac{\nu(T_{\text{cond}})}{\nu_{\text{cold}}} \left(\frac{\partial^2}{\partial r^2} + \frac{\Delta_s}{r^2} \right)^2 \right] \Phi \\ & - \frac{\nu_r(T_{\text{cond}})}{\nu_{\text{cold}}} \Delta_s \left[\frac{2}{r^2} \frac{\partial^3}{\partial r^3} - \frac{2}{r^3} \frac{\partial^2}{\partial r^2} + \frac{2}{r^4} \frac{\partial}{\partial r} + \frac{2}{r^4} \Delta_s \frac{\partial}{\partial r} - \frac{4}{r^5} \Delta_s \right] \Phi \end{aligned}$$

$$\begin{aligned} & - \frac{\nu_{rr}(T_{\text{cond}})}{\nu_{\text{cold}}} \Delta_s \left[\frac{1}{r^2} \frac{\partial^2}{\partial r^2} - \frac{2}{r^3} \frac{\partial}{\partial r} - \frac{\Delta_s}{r^4} \right] \Phi \\ & = \nabla \times \nabla \times \mathbf{F}, \end{aligned} \quad (\text{A2})$$

$$\begin{aligned} & - \frac{\Delta_s}{r^2} \left[\frac{1}{\text{Pr}} \frac{\partial}{\partial t} - \frac{\nu(T_{\text{cond}})}{\nu_{\text{cold}}} \left(\frac{\partial^2}{\partial r^2} + \frac{\Delta_s}{r^2} \right) \right] \Psi \\ & + \frac{\nu_r(T_{\text{cond}})}{\nu_{\text{cold}}} \Delta_s \left(\frac{1}{r^2} \frac{\partial}{\partial r} - \frac{2}{r^3} \right) \Psi = \nabla \times \mathbf{F}, \end{aligned} \quad (\text{A3})$$

with

$$\Delta_s = \frac{1}{\sin \theta} \frac{\partial}{\partial \theta} \left[\sin \theta \frac{\partial}{\partial \theta} \right] + \frac{1}{\sin^2 \theta} \frac{\partial^2}{\partial \phi^2}, \quad (\text{A4})$$

$$\begin{aligned} \mathbf{F} &= \text{Ra} \frac{\eta^2}{(1-\eta)^4} \frac{T}{r^5} \mathbf{e}_r \\ &+ \text{Pr}^{-1} \mathbf{u} \times (\nabla \times \mathbf{u}) + \mathbf{f}_1 \\ &+ \frac{\nu(T) - \nu(T_{\text{cond}})}{\nu_{\text{cold}}} \nabla^2 \mathbf{u}. \end{aligned} \quad (\text{A5})$$

There are four boundary conditions for the poloidal potential $\Phi = 0$, $\frac{\partial \Phi}{\partial r} = 0$ and two for the toroidal one $\Psi = 0$ at $r = \frac{\eta}{1-\eta}$ and $r = \frac{1}{1-\eta}$.

APPENDIX B: SYMMETRY GROUPS

In this section we detail the symmetry groups used in this paper. Let us note S the antipodal symmetry $\mathbf{r} \rightarrow -\mathbf{r}$ and $K(\delta)$ the reflection through a plane containing the line δ . Then, we define the following.

(i) The central symmetry group \mathbb{Z}_2^c : generated by S . Note, it acts trivially on the even modes.

(ii) The symmetry of the cube $\mathbb{O} \oplus \mathbb{Z}_2^c$: generated by the direct symmetries of the octahedron and S .

(iii) The symmetry \mathbb{O}^- : generated by the direct symmetries of a tetrahedron and by the reflection $K(\delta)$, where δ is the axis of a threefold rotation of the tetrahedral group.

(iv) Axisymmetric group $\text{O}(2) \oplus \mathbb{Z}_2^c$ (even modes): generated by the rotations about an axis δ and by S .

(v) Axisymmetric group $\text{O}(2)^-$ (odd modes): generated by the rotations about an axis δ and $K(\delta)$.

(vi) n -fold rotation groups (odd modes): \mathbf{D}_n^z , generated by the n -fold rotation about an axis δ and $K(\delta)$; \mathbf{D}_{2n}^d contains the \mathbf{D}_n^z group and additionally it possesses a rotation by π around an axis perpendicular to δ .

- [1] I. Mutabazi, H. N. Yoshikawa, M. T. Fogaing, V. Travnikov, O. Crumeyrolle, B. Futterer, and C. Egbers, *Fluid Dyn. Res.* **48**, 061413 (2016).
- [2] I. Yavorskaya, N. Fomina, and Y. Belyaev, *Acta Astronaut.* **11**, 179 (1984).
- [3] V. Travnikov, C. Egbers, and R. Hollerbach, *Adv. Space Res.* **32**, 181 (2003).

- [4] F. Busse, *J. Fluid Mech.* **72**, 67 (1975).
- [5] F. Feudel, K. Bergemann, L. S. Tuckerman, C. Egbers, B. Futterer, M. Gellert, and R. Hollerbach, *Phys. Rev. E* **83**, 046304 (2011).
- [6] R. Hollerbach, *Int. J. Numer. Meth. Fluids* **732**, 773 (2000).
- [7] B. Futterer, C. Egbers, N. Daley, S. Koch, and L. Jehring, *Acta Astronaut.* **66**, 193 (2010).

- [8] J. Ratcliff, G. Schubert, and A. Zebib, *Physica D* **97**, 242 (1996).
- [9] S. Androvandi, A. Davaille, A. Limare, A. Fouquier, and C. Marais, *Phys. Earth Planet. Inter.* **188**, 132 (2011).
- [10] B. Futterer, N. Daley, S. Koch, N. Scurtu, and C. Egbers, *Acta Astronaut.* **71**, 11 (2012).
- [11] B. Futterer, A. Krebs, A.-C. Plesa, F. Zaussinger, R. Hollerbach, D. Breuer, and C. Egbers, *J. Fluid Mech.* **735**, 647 (2013).
- [12] V. S. Solomatov, *Phys. Fluids* **7**, 266 (1995).
- [13] J. Curbelo and A. M. Mancho, *Phys. Rev. E* **88**, 043005 (2013).
- [14] J. Curbelo and A. M. Mancho, *Phys. Fluids* **26**, 016602 (2014).
- [15] P. Beltrame and P. Chossat, *Eur. J. Mech. B: Fluids* **50**, 156 (2015).
- [16] P. Chossat, R. Lauterbach, and I. Melbourne, *Arch. Ration. Mech. Anal.* **113**, 313 (1990).
- [17] C. Geiger, G. Dangelmayr, J. Rodriguez, and W. Güttinger, in *Pattern Formation: Symmetry Methods and Applications*, Fields Institute Communications, edited by W. L. J. Chadam, M. Golubitsky, and B. Wetton (American Mathematical Society, Providence, RI, 1996), Vol. 5, pp. 225–237.
- [18] D. Bercovici, G. Schubert, and G. Glatzmaier, *Geophys. Astrophys. Fluid Dyn.* **61**, 149 (1991).
- [19] L. Landau and E. Lifshitz, *Electrodynamics of Continuous Media*, 2nd ed. (Elsevier Butterworth-Heinemann, Burlington, MA, 1984), Vol. 8.
- [20] V. Solomatov and A. Barr, *Phys. Earth Planet. Inter.* **165**, 1 (2007).
- [21] H. Yoshikawa, O. Crumeyrolle, and I. Mutabazi, *Phys. Fluids* **25**, 024106 (2013).
- [22] V. Travnikov, O. Crumeyrolle, and I. Mutabazi, *Phys. Fluids* **27**, 054103 (2015).
- [23] P. Beltrame, V. Travnikov, M. Gellert, and C. Egbers, *Nonlin. Process. Geophys.* **13**, 413 (2006).
- [24] J. M. E. Navarro, J. J. Fernández, J. Rodríguez, A. Laverón-Simavilla, and V. Lapuerta, *Microgravity Sci. Technol.* **27**, 61 (2015).
- [25] F. Zaussinger, A. Krebs, V. Travnikov, and Ch. Egbers, *Adv. Space Res.* **60**, 1327 (2017).

Dielectrically driven convection in spherical gap geometry

Florian Zaussinger,¹ Peter Haun,¹ Matthias Neben,¹ Torsten Seelig,¹ Vadim Travnikov,¹
Christoph Egbers,¹ Harunori Yoshikawa,² and Innocent Mutabazi^{3,*}

¹*Department of Aerodynamics and Fluid Mechanics, Brandenburg University of Technology
Cottbus-Senftenberg, Siemens-Halske-Ring 14, 03046 Cottbus, Germany*

²*Laboratoire J.-A. Dieudonné, UMR No. 7351, CNRS, Université Côte d'Azur, Parc Valrose,
06108 Nice Cedex 02, France*

³*Laboratoire Ondes et Milieux Complexes, UMR No. 6294, CNRS, Université du Havre,
Normandie Université, 53 Rue de Prony, CS 80540, 76058 Le Havre Cedex, France*



(Received 4 January 2018; published 5 September 2018)

Dielectric heating occurs in situations where an alternating electric field is applied on an insulating dielectric material. This effect can produce thermal convection in dielectric fluid through the thermoelectric coupling by the dielectrophoretic (DEP) force. The onset and the flow properties of the convection are investigated in a spherical gap geometry. The thermoelectrohydrodynamical equations often adopted in the modeling of the DEP-force-driven thermal convection are extended by an additional source term arising from the dielectric heating in the energy equation. Three-dimensional direct numerical simulations are performed, under microgravity conditions and without any imposed temperature gradient to highlight the effects of dielectric heating. In the conduction state, dielectric heating creates a parabolic temperature profile with a maximum in the interior of the spherical gap. In the convection state, the temperature distribution is more homogeneous with a lower maximum temperature. Numerical results are compared with interferograms from the GeoFlow II experiment performed on the International Space Station to validate the model. For the comparison, a numerical interferogram is applied to temperature fields obtained in the simulation. The onset of convection and basic spatial properties of the resulting internally heated convective zone are in good agreement with the experiment. The computed velocity fields reveal strong downdrafts which lead to recognizable fringe patterns in the interferograms.

DOI: [10.1103/PhysRevFluids.3.093501](https://doi.org/10.1103/PhysRevFluids.3.093501)

I. INTRODUCTION

Heating materials by applying an electric field or by irradiating an electromagnetic field is a common practice in industry. The Ohmic effect and the dielectric loss are often used to generate heat energy inside materials. In the glass industry, electric glass furnaces are more frequently used because of the high efficiency, the smallness of apparatus, and the eco-friendliness [1]. Electric fields of $10\text{--}10^3$ Hz in frequency are applied to glass materials (soda lime and sodium borate glasses) to melt by Ohmic heating. The heating generates temperature gradients to produce the convective motion in the melt. This convection is often modeled as thermal convection driven by the thermal Archimedean buoyancy force. The velocity and temperature fields of the melt are coupled with each other through an Ohmic heat generation term in the energy equation as well as in the thermal variations of fluid properties.

*Corresponding author: innocent.mutabazi@univ-lehavre.fr

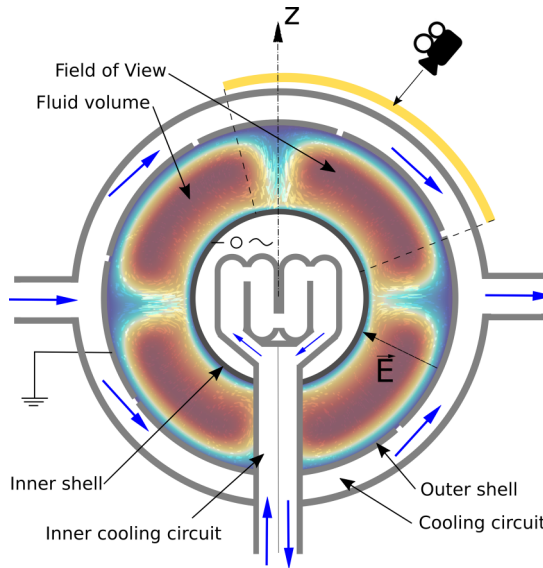


FIG. 1. Sketch of the convection experiment GeoFlow in a spherical geometry performed on the ISS. Red arrows depict the heating circuit and blue arrows the cooling circuit. Interferograms to visualize the temperature field are recorded in the region spanning from the north pole to the equator (yellow area). The depicted temperature field represents a typical convection zone induced by dielectric heating.

Dielectric heating plays an important role in many industrial and chemical applications where materials are thermally processed [2]. The most common application would be the domestically used microwave stove. While the physical process itself has been known since the late 19th century, it has become important with the work of von Hippel [3], which provides a database of properties of dielectric materials. This database was extended in the second half of the 20th century especially for many biological substances which are used in biochemistry and process engineering. The dielectric properties of important aqueous fluids were reviewed in Ref. [4] and more recently for biofuels (e.g., alcohols and their mixtures) in Ref. [5]. Dielectric heating is generated by a high-frequency electric field acting on a dielectric material. The field polarizes nonmotile charges in the material. There are two known types of polarization: (i) induced polarization due to the displacement of electrons inside atoms or molecules and (ii) orientation polarization due to permanent molecular dipoles aligned along the applied field. Heat energy is generated through the second type of polarization when the dipoles cannot respond to the temporal variation of an applied field with a phase delay.

The manifold influence of electric field on a fluid is a subject of thermoelectrohydrodynamics (TEHD). We refer to Refs. [6–9] for the theoretical background. Several laboratory experiments in the scope of TEHD have been reported in the literature. These experiments often use the dielectrophoretic (DEP) force to induce flows under microgravity conditions [e.g., on the International Space Station (ISS) or on parabolic flights]. The GeoFlow experiment (see Fig. 1) on the ISS represents such an experiment in the absence of earth’s gravity field (see Ref. [10]). The main objective of the GeoFlow experiment was the investigation of thermal convection in the spherical gap, which is an analog of convection in planets or stars, under an imposed temperature gradient. However, the experimental setup also allows the study of dielectric heating and the influence of this process on thermal convection.

The investigation of convection induced by dielectric heating has been the object of many experimental and numerical works. Microwave-driven convective flows have been analyzed by different authors. Ayappa *et al.* [11] investigated water in a squared cavity and analyzed the uniformity of heating as a function of the power distribution. Detailed numerical simulations of

the coupled Maxwell and hydrodynamical equations have been performed by Zhang *et al.* [12] and Ratanadecho *et al.* [13]. More recently, Cherbański and Rudniak [14] investigated dielectrically driven convection in water. They showed with three-dimensional (3D) numerical simulations that dielectric heat-driven convection is not able to homogenize the temperature field, but produces temperature peaks. In the present paper, however, dielectric heat-driven convection is investigated in spherical gap geometry.

Natural convection in spherical gap geometries has been studied recently for the GeoFlow project, where centripetal gravity fields are simulated by the DEP force. We refer to Refs. [15,16] for details about the GeoFlow experiment. Theoretical and numerical investigations on the fundamental aspects of the DEP force-driven convection have been performed by Yoshikawa *et al.* [17], Fogaing *et al.* [18], Mutabazi *et al.* [19], Kang *et al.* [20], and Travníkov *et al.* [21] in different geometries. This paper extends these works by including the effects of dielectric heating and explains the occurrence of atypical convective patterns observed in the GeoFlow experiments.

The paper is organized as follows. The theoretical background of dielectric heating and extended TEHD equations are presented in Secs. IA and IB, respectively. The properties of the considered dielectric fluid and the experimental setup of GeoFlow are also given. Section IIA is devoted to the basic conductive state of the system. The full set of TEHD equations is numerically treated in Sec. IIB. A comparison between experimental interferograms and the numerical simulations is given in Sec. III. This paper ends with a detailed discussion and a summary.

A. Dielectric heating

Dielectric materials are electrical insulators with or without permanent molecular dipoles. In the case in which the material is placed in an electric field \mathbf{E} , permanent or induced dipoles are aligned along the electric field lines and can yield a macroscopic body force. In a dielectric fluid, the DEP force is induced by the application of an electric field. The force is proportional to the field squared and to the gradient of the permittivity ϵ :

$$\mathbf{F}_{\text{DEP}} = -\frac{1}{2}\mathbf{E}^2\nabla\epsilon. \quad (1)$$

The permittivity of a dielectric fluid is given by $\epsilon = \epsilon_0\epsilon_r$, where $\epsilon_0 = 8.854 \times 10^{-12}$ F/m is the vacuum permittivity and ϵ_r is the relative permittivity. The permittivity ϵ is in general a decreasing function of the fluid temperature, so a temperature gradient in a fluid leads to a DEP force. A high voltage and a strong thermal variation of ϵ are needed for a DEP force to be comparable to the gravitational force on earth. If a fluid in a spherical capacitor is subjected to a radial temperature gradient, the resulting DEP force is also radial and enables one to investigate thermal convection in a central force field.

Among other fluid properties, the permittivity has the most important influence on TEHD processes. The effects of fluid polarization in an alternating electric field can be treated conveniently in terms of the complex permittivity, which depends on the field frequency as well as on the fluid temperature:

$$\epsilon_r = \epsilon' - i\epsilon''. \quad (2)$$

The real part $\text{Re}[\epsilon_r] = \epsilon'$ is called dielectric constant. The imaginary part $\text{Im}[\epsilon_r] = \epsilon''$ represents the loss rate according to the conductance of the fluid. In an ac electric field \mathbf{E} the electric displacement field is given by $\mathbf{D} = \epsilon_0\mathbf{E} + \mathbf{P} = \epsilon_0\epsilon_r\mathbf{E}$ for a linear isotropic dielectric, with $\mathbf{P} = (\epsilon_r - 1)\mathbf{E}$ the polarization. The polarization current density is $\mathbf{J}_{\text{pol}} = \frac{\partial\mathbf{P}}{\partial t}$. Dielectric heating occurs in situations where the displacement \mathbf{D} has a nonzero phase lag δ to the applied electric field \mathbf{E} . The tangent of δ , called the energy dissipation factor, is expressed as the ratio of the imaginary to real part of the permittivity

$$\tan\delta = \frac{\epsilon''}{\epsilon'}. \quad (3)$$

The power dissipation due to the dielectric loss per unit volume is

$$P = 2\pi f \epsilon_0 \epsilon' \tan \delta |\mathbf{E}|^2, \quad (4)$$

where f is the frequency of the electric field. For a given dielectric the energy loss depends mainly on the electric field strength and the frequency. For convenience, we define the rate of dielectric heating $S_{\text{DH}} = P/\rho C_p$, with C_p the specific-heat capacity at constant pressure:

$$S_{\text{DH}} = \frac{2\pi f \epsilon_0 \epsilon' \tan \delta |\mathbf{E}|^2}{\rho C_p}. \quad (5)$$

The rate of dielectric heating S_{DH} must be included in the law of energy conservation in order to simulate the influence of dielectric heating on a fluid.

B. Theoretical model

An electric field, applied on a dielectric fluid, induces three force densities

$$\mathbf{F} = \underbrace{\rho_V \mathbf{E}}_{\mathbf{F}_C} + \underbrace{\nabla \left[\frac{1}{2} \rho \left(\frac{\partial \epsilon}{\partial \rho} \right)_T \mathbf{E}^2 \right]}_{\mathbf{F}_{\text{es}}} + \mathbf{F}_{\text{DEP}}. \quad (6)$$

The first term, called electrophoretic force, represents the Coulomb forces on free charges in the fluid. In an ac electric field with a frequency higher than all other characteristic frequencies involved in the flow dynamics, this force has no net effect on the fluid motion, since the force averaged over a period of field variation vanishes [17]. The second term is the electrostrictive force density \mathbf{F}_{es} . This force is a gradient force, so it has no effect on the motion of incompressible fluids with no mobile boundary. In the case of free surfaces or moving walls this force has to be taken into account. The dielectrophoretic force density \mathbf{F}_{DEP} [see Eq. (1)] remains as the prevailing force field. It is radially inward oriented and can be compared with a gravitational field. The TEHD equations governing the spatial and temporal evolution of the velocity field \mathbf{u} , the electric field \mathbf{E} , and the temperature field T are [19]

$$\nabla \cdot \mathbf{u} = 0, \quad (7)$$

$$\frac{\partial \mathbf{u}}{\partial t} + (\mathbf{u} \cdot \nabla) \mathbf{u} = -\nabla \Pi + \nabla \cdot \bar{\bar{\tau}} + \rho_0^{-1} \mathbf{F}_{\text{DEP}}, \quad (8)$$

$$\frac{\partial T}{\partial t} + (\mathbf{u} \cdot \nabla) T = \kappa_T \nabla^2 T + S_{\text{DH}}, \quad (9)$$

$$\nabla \cdot \mathbf{E} = 0, \quad (10)$$

where we have adopted the electrohydrodynamic Boussinesq approximation [22]. Equation (7) is the mass conservation for incompressible flows. Equation (8) is the Navier-Stokes equation, with $\bar{\bar{\tau}}$ being the viscous stress tensor. The electrostrictive force \mathbf{F}_{es} is lumped with the pressure [19], resulting in an effective pressure term $\Pi = \frac{1}{\rho_0} [P - \frac{1}{2} \rho (\frac{\partial \epsilon}{\partial \rho})_T \cdot |\mathbf{E}|^2]$. Equation (9) is the energy equation, which describes the evolution of temperature, with κ_T the thermal diffusion coefficient. The rate of dielectric heating S_{sh} is included in this equation for examining the effects of dielectric heating on the flow field. Equation (10) is the Gauss equation. We have assumed that the free charge density of the dielectric is negligible. We have also neglected the thermal variation of the permittivity in the Gauss equation. In a geometry with a large curvature, as considered in the present work, the spatial variation of the electric field arises primarily from the geometry curvature.

The governing equations (7)–(10) are completed by the equation of state for the permittivity ϵ . For a small temperature deviation from a reference value T_0 , it is given by

$$\epsilon = \epsilon_{\text{ref}} [1 - \alpha_E (T - T_0)], \quad (11)$$

where α_E is the dielectric expansion factor and ϵ_{ref} is the permittivity at $T = T_0$ [15,17,19]. We apply Eqs. (7)–(11) to a dielectric fluid in the gap of two concentric electrodes. Each electrode is maintained at a constant temperature and a high-frequency ac electric voltage is imposed over the gap. The temperature field in the conduction state is given [19] by

$$T_b(r) = T_2 + \frac{\eta(T_1 - T_2)}{1 - \eta} \left(\frac{R_2}{r} - 1 \right), \quad (12)$$

where (R_1, T_1) and (R_2, T_2) are the radius and the temperature of the inner and outer electrodes, respectively. The radius ratio is defined by $\eta = R_1/R_2$. In an electric voltage of a frequency higher than the reciprocal of the viscous timescale, only the time-averaged component of the DEP force can affect the fluid motion. This component can be calculated from the effective electric field, which is given in the conduction state [19] by

$$\mathbf{E}_b(r) = -\frac{\eta V_{\text{rms}}}{R_2 - R_1} \frac{B}{\ln(1 - B)} \left(\frac{R_2}{r} \right)^2 \left[1 - B \frac{T_b(r)}{\Delta T} \right]^{-1} \mathbf{e}_r, \quad (13)$$

where $B = \alpha_E \Delta(T_1 - T_2)$ is the thermoelectric parameter, $V_{\text{rms}} = V_0/\sqrt{2}$ is the effective voltage, and \mathbf{e}_r is the radial unit vector. In the present work, we will focus on the case where no temperature gradient is imposed, i.e., $B \rightarrow 0$, and in the electrode geometry of $\eta = 0.5$ ($R_2 = 2R_1$). The effective electric field is then given by

$$\mathbf{E} = \frac{R_1 R_2}{R_2 - R_1} \frac{V_0}{\sqrt{2}} \frac{1}{r^2} \mathbf{e}_r. \quad (14)$$

Neither temperature nor the velocity field influence the electric field (14) in this model. In the case of strong temperature-dependent permittivity or low curvatures $\eta > 0.7$ the coupling between the momentum, energy, and Gauss equation has to be taken into account. The effects of the DEP force are comparable to those of the thermal Archimedean buoyancy force in earth's gravity field. The wording *electric gravity* has been established for the effective acceleration of the dielectric origin,

$$\mathbf{g}_e = \frac{\alpha_E}{\rho_0 \alpha_T} \nabla \left(\frac{\epsilon_0 \epsilon' \mathbf{E}^2}{2} \right). \quad (15)$$

Further, this motivates the electric Rayleigh number as given in [19],

$$\text{Ra} = \frac{\alpha_T \Delta T \mathbf{g}_e (R_2 - R_1)^3}{\nu \kappa_T}, \quad (16)$$

with ν the kinematic viscosity and ΔT a representative value of the temperature variation inside the fluid.

The governing TEHD equations are analyzed in two ways. First, we focus on the conductive base state for a given electric field \mathbf{E} in the spherical capacitor. This gives a rough estimate about timescales and the spatial temperature profiles. Second, the equations are solved numerically in three-dimensional space. Both issues require detailed information about the experimental setup, the geometry, the resulting parameter space, and the fluid properties. These properties are presented in the following.

C. Fluid properties and flow conditions

The present investigation is performed for the flow conditions realized in the GeoFlow experiments, which can provide results for comparison. The GeoFlow experiments were performed in the Fluid Science Laboratory of the Columbus module on the ISS between 2008 and 2017. Two missions have been accomplished. The first mission GeoFlow I (2008) was performed using the isoviscous silicon oil M5, which is a nonpolar liquid. Hence, the fluid is not susceptible for dielectric heating. The second mission GeoFlow II (2011–2017) examined the effects of the

TABLE I. Properties of 1-Nonanol for two reference temperatures at a frequency of 1.0650×10^4 Hz.

Property	$T_0 = 293.0$ K	$T_0 = 303.5$ K
Energy dissipation factor $\tan \delta$	6.12×10^{-2}	7.45×10^{-2}
Relative permittivity ϵ'	9.3	8.44
Density ρ (kg/m ³)	8.29×10^2	8.22×10^2
Specific-heat capacity C_p (J/K)	2.47×10^3	2.47×10^3
Thermal diffusivity κ_T (m ² /s)	7.94×10^{-8}	7.76×10^{-8}

temperature-dependent viscosity on convection with adopting 1-Nonanol as the working fluid. The molecules of the 1-Nonanol have a strong dipole moment due to a hydroxyl group. This makes the fluid susceptible to dielectric heating. All relevant fluid properties are listed in Table I. They are based on measurements of the electrical properties provided by Airbus Defense and Space (formally EADS Astrium). The experiment consists of two concentric shells, which can rotate around a central axis. The inner and outer spherical electrodes have radii of $R_1 = 0.0135$ m and $R_2 = 0.027$ m (radius ratio is $\eta = 0.5$), respectively (see Fig. 1). Electrodes are maintained at constant temperatures. The temperature at the outer shell was considered as the reference value T_0 , adjusted to either 293.0 K or 303.5 K. Electric voltage is limited by a maximum value $V_0 = 6500$ V. The peak value of the electric gravity is reached at the inner sphere, where $g_e \approx 13$ m/s². The lowest value is measured at the outer sphere where $g_e \approx 0.3$ m/s². The Rayleigh number is varied over five magnitudes, $5.6 \times 10^2 < Ra < 1.43 \times 10^7$.

For a given fluid, control parameters are the temperature difference $T_1 - T_2$ between the electrodes, the applied voltage V_0 , and the rotation rate Ω . In the present investigation, we consider only initially isothermal experimental runs ($T_1 = T_2$) with no rotation of the electrodes ($\Omega = 0$). In the GeoFlow II experiment, the maximum electric field strength varies between 1.9×10^5 V/m for

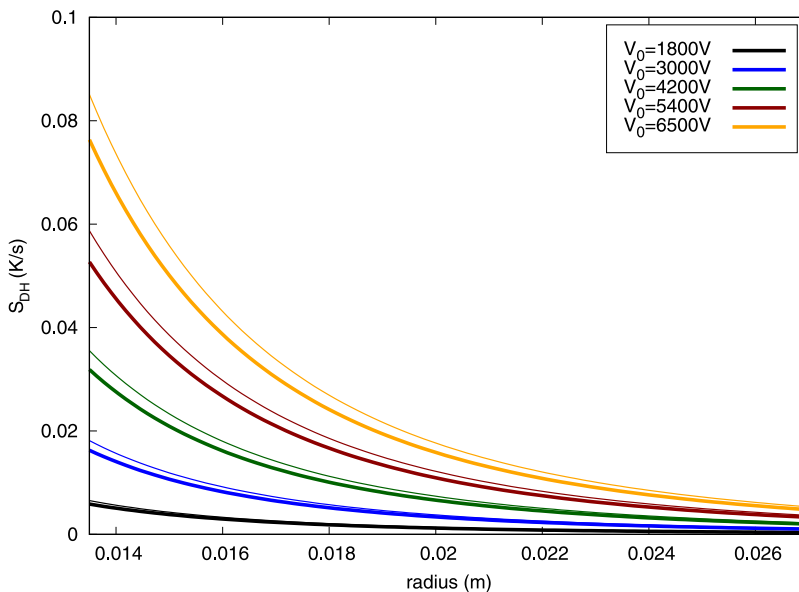


FIG. 2. Radial profiles of the dielectric heating rate S_{DH} [Eq. (5)] for 1-Nonanol at different values of the electric voltage. The fluid properties are listed in Table I. Thin lines correspond to $T_0 = 293.0$ K, and thick lines to $T_0 = 303.5$ K. The highest heating rate is found for $V_0 = 6500$ V at the inner shell.

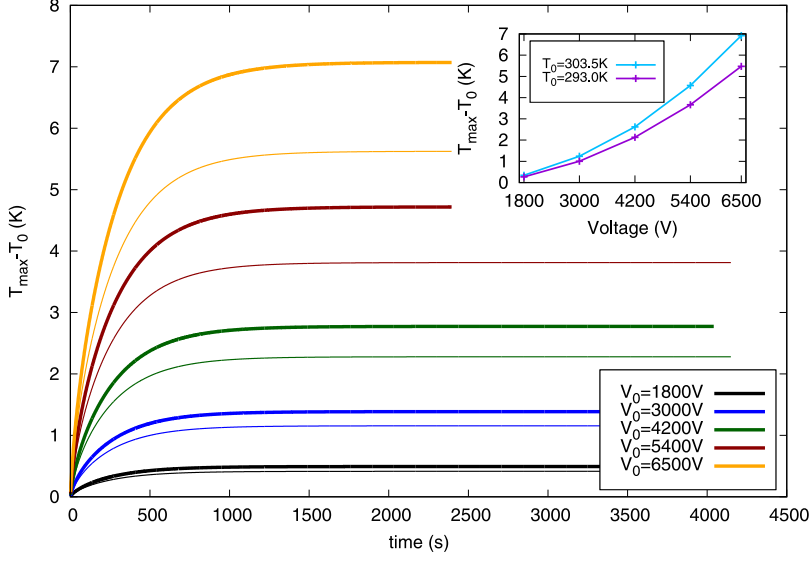


FIG. 3. Temporal evolution of the maximum temperature in the conduction state for $T_0 = 293.0$ K (thin lines) and for $T_0 = 303.5$ K (thick lines). The inset depicts the saturated maximum temperature as a function of the voltage for both reference temperatures.

$V_0 = 1800$ V and 6.9×10^5 V/m for $V_0 = 6500$ V. Figure 2 depicts S_{DH} , calculated from Eqs. (5) and (13), for various voltages and reference temperatures examined in the experiment. A maximum of 0.085 K/s is obtained for $V_0 = 6500$ V at the inner electrode. The resulting temperature profile is obtained by solving Eq. (9) under the boundary condition of constant temperatures at the electrodes.

II. NUMERICAL SIMULATIONS

A. Conductive state

In the conduction state ($\mathbf{u} = \mathbf{0}$), the energy equation (9) reads

$$\frac{\partial T}{\partial t} = \kappa_T \left(\frac{\partial^2 T}{\partial r^2} + \frac{2}{r} \frac{\partial T}{\partial r} \right) + S_{\text{DH}}(\epsilon'(T), V_0, r). \quad (17)$$

The calculation of the source term $S_{\text{DH}}(\epsilon'(T), r)$ is based on the thermal variation of the permittivity and the energy dissipation factor measured in the laboratory (Sec. IC),

$$\epsilon'(T) = -0.51103T + 97.467 + 7.1429 \times 10^{-4}T^2, \quad (18)$$

$$\tan \delta(T) = -4.606 \times 10^{-1}T + 47.37 - 1.594 \times 10^{-6}T^3 + 1.488 \times 10^{-3}T^2, \quad (19)$$

where the temperature is given in kelvins. Equation (17) has been solved by a simple, explicit finite-difference scheme. To guarantee a stable solution a Courant-Friedrichs-Lewy number of 0.25 was chosen for 100 cells. Both reference temperatures $T_0 = 293.0$ and 303.5 K, and five values of V_0 have been tested. The boundaries are kept at the reference temperature $T_1 = T_2 = T_0$. In contrast to the heating rate plotted in Fig. 2, the maximum temperature is not obtained at the inner shell. Within the first thermal timescale $\tau = (R_2 - R_1)^2 / \kappa_T = 2603$ the temperature profile becomes stationary. This is shown for both reference temperatures in Fig. 3, where the difference of the maximum temperature T_{\max} and the reference temperatures is plotted over the thermal timescale.

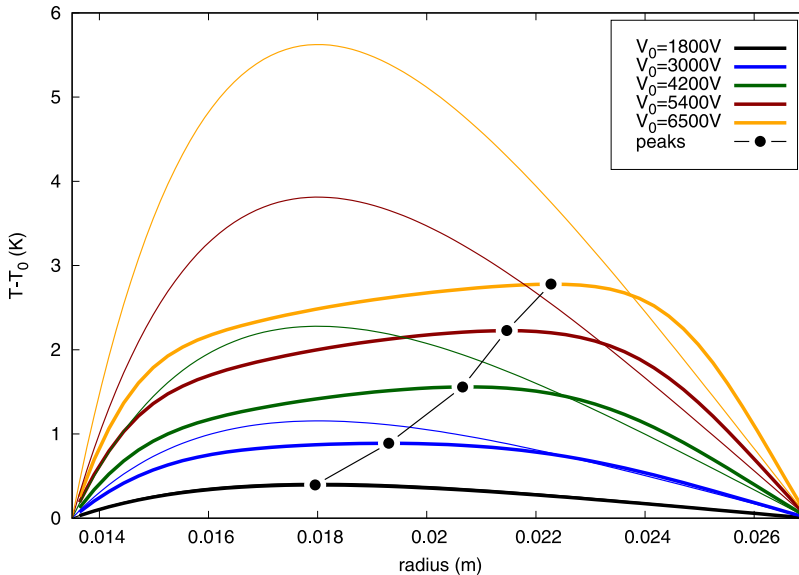


FIG. 4. Radial temperature profiles in the spherical gap with dielectric heating. The conductive solution obtained from Eq. (17) (thin lines) and latitude- and longitude-averaged temperature profiles computed from the 3D simulations (thick lines) are shown for $T_0 = 293.0$ K. The black long-dashed line connects temperature maxima. The profiles for $V_0 = 1800$ V coincide.

The conductive case reveals a paraboliclike temperature profile where the minima are located at the boundaries and the maxima are found in the interior (see Figs. 4 and 5). In all 1D solutions the position of T_{\max} is found at $r_{\max} = 0.0179$ m, or $r_{\max}/R_2 = 0.665$. The slope dT_{\max}/dV_0 increases with the reference temperature (Fig. 3, inset).

B. Three-dimensional simulations

The governing equations (7)–(9), incorporating the electric field given by Eq. (14), are solved numerically with the finite-volume method using the open source software suite OpenFOAM® [23]. A cubed sphere grid is used for all simulations. No-slip boundary conditions are imposed on the velocity field at the electrode surfaces. The thermal boundary conditions are of Dirichlet type, i.e., constant temperatures. The code solves dimensional equations in three dimensions with the PISO algorithm. Time integration is performed with an implicit Crank-Nicolson method. The spatial derivatives are approximated in second order. Subgrid scales are modeled using a one-equation ansatz for the turbulent kinetic energy. The accuracy of the results is given with a maximum residual of 10^{-6} . Several tests have been performed to guarantee converged solutions. A detailed grid study showed that the total energy converges towards a fixed value for 4×10^6 cells. This resolution also resolves the thermal boundary layers with at least five cells. In addition, the latitude- and longitude-averaged temperature profiles are analyzed. These profiles (see Fig. 4) do not change for more than 4×10^6 cells.

The GeoFlow experiment visualizes results as interferograms. They are obtained by a Wollaston shearing interferometry which measures first derivatives of the fluid refractive index. These derivatives are identified as temperature derivatives through nearly identical slopes. Advanced numerical postprocessing techniques are necessary to reconstruct the underlying temperature and velocity field. An approved approach is the backward reconstruction, where numerical interferograms are compared with experimental ones. In the case in which the interferograms match in predefined characteristics (e.g., size, number, and speed of convective plumes), the internal field in the experiment is assumed to be identical to the numerical simulations. To compare simulations and the

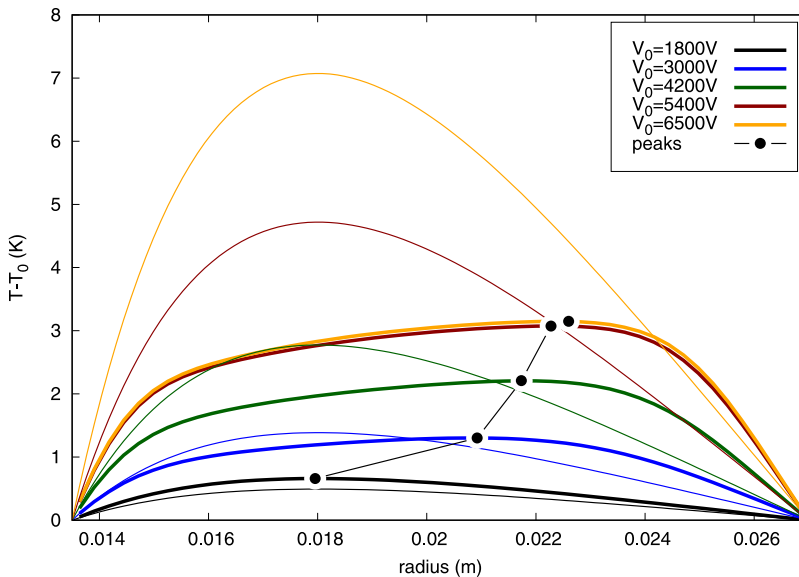


FIG. 5. Radial temperature profiles in the spherical gap with dielectric heating. The conductive solution obtained from Eq. (17) (thin lines) and latitude- and longitude-averaged temperature profiles computed from the 3D simulations (thick lines) are shown for $T_0 = 303.5$ K. The black long-dashed line connects temperature maxima.

experimental images, numerical interferograms $I(x, y)$ are calculated according to the algorithm presented in Ref. [24]. We define the numerical interferometry function

$$I(x, y) = -\cos\left(a_{\text{fringe}} \frac{\partial T_{\text{mean}}}{\partial \mathbf{s}} + bx + cy\right), \quad (20)$$

where a_{fringe} is a control parameter for the density of fringes, T_{mean} is the radially averaged temperature, and \mathbf{s} is the direction of polarization. The interferometric base pattern is implemented by a linear extension of the mean-temperature derivative function with constants b and c . By changing these values, the amount and direction of the base pattern are controlled. For our simulations we use $a_{\text{fringe}} = 0.05$, $b = -200$, and $c = 600$. The numerical interferograms are evaluated in the same area as the experimental interferograms. This is shown in Fig. 6, where the patch of the numerical interferogram is spanned over the outer shell of the experiment. The interferograms show two typical patterns: first, double-ring structures which originate from thermal plumes, and second, parallel lines of fringes which are caused by sheetlike structures. A detailed analysis of these structures is presented in Ref. [24].

All simulations follow the exact timeline of the experiment as shown in Fig. 7. A high voltage and a uniform temperature field at a predefined reference temperature are applied for at least 61 min before the interferograms are recorded. We have also taken into account the initial temperature distribution in the fluid, which is estimated from the ambient temperature of the ISS. Our numerical study covers ten parameter sets, including five voltages $V_0 = 1800, 3000, 4200, 5400, \text{ and } 6500$ V as well as two reference temperatures $T_0 = 293.0$ and 303.5 K.

C. Thermal stratification and heat transfer

The conductive solutions show parabolic profiles at the temperature where the maxima are found in the interior of the gap and the minima are located at the boundaries. This stratification is also found in the 3D simulations. The results of the 1D and 3D calculations are compared in Fig. 4 for

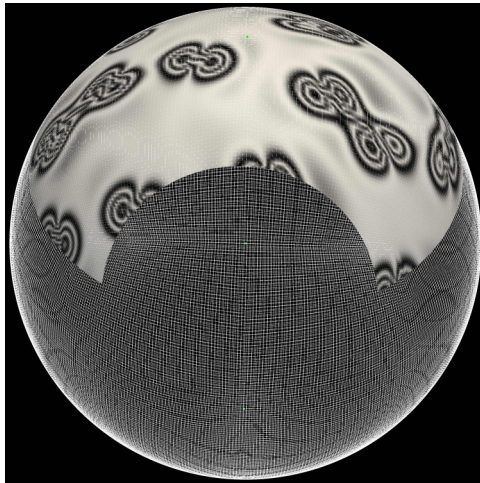


FIG. 6. Area of the numerical interferogram congruent with the experimental interferogram of GeoFlow for $V_0 = 6500$ V and $T_0 = 293.0$ K.

$T_0 = 293.0$ K and in Fig. 5 for $T_0 = 303.5$ K. Thin lines are stationary solutions for the conductive case and thick lines are latitude- and longitude-averaged temperature profiles of 3D simulations. The long-dashed black line connects peak values of the temperature. The location of the temperature peak moves towards the outer shell for increasing voltages, contrary to the conductive case, where the location of the peak is always found at $r_{\max}/R_2 = 0.665$ for both reference temperatures. For $V_0 = 1800$ V and $T_0 = 293.0$ K the 1D and the 3D profiles coincide (black lines). It follows that this case is also conductive in three dimensions, even though the profile shows a negative temperature gradient in the outer half of the gap. The case of $V_0 = 1800$ V and $T_0 = 303.5$ K differs. Here the profile from the 3D simulation is always above the 1D conductive solution. The onset of convection will be found within 1800 V $< V_0 < 3200$ V, where an octahedral convective structure is observed for $V_0 = 3000$ V in the numerical simulations.

The heat transfer is described in terms of the Nusselt number

$$\text{Nu} = \frac{F_{\text{tot}}}{F_{\text{cond}}}, \quad (21)$$

where F_{tot} is the total heat flux, incorporating the convective and the conductive flux. To calculate the total heat flux at the electrodes the temperature field is averaged in the latitude and in the longitude and then differentiated in the radial direction. The conductive flux F_{cond} is given by the solutions of the extended heat (17). Figure 8 shows the Nusselt number calculated at the inner (subscript i) and the outer (subscript o) shells for both reference temperatures and as a function of the voltage.

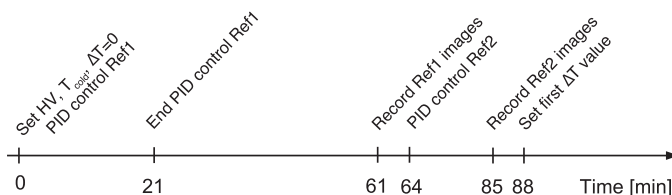


FIG. 7. Time line of experimental runs of GeoFlow II. Two series of reference images (Ref1 and Ref2) are recorded with $\Delta T = 0$ and high voltage V_0 . Ref1 is recorded after 61 min and Ref2 after 85 min. Both reference series are used to measure the influence of dielectric heating on the conductive state.

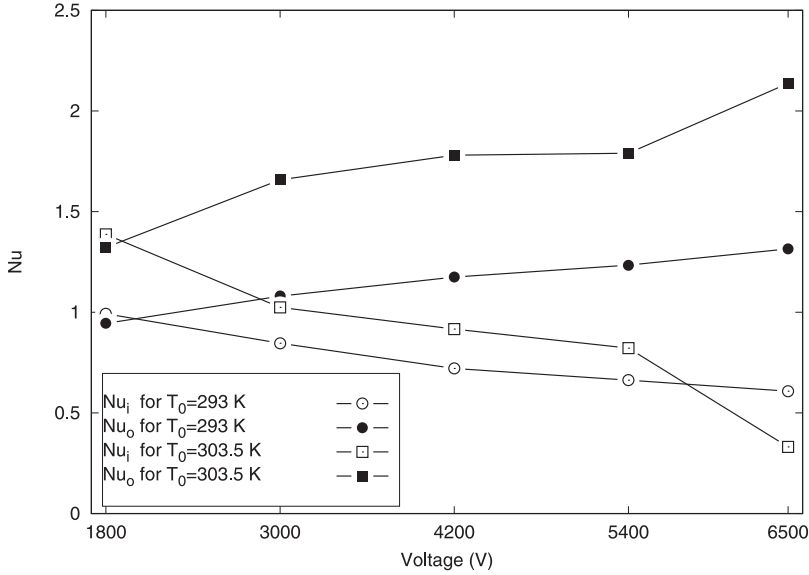


FIG. 8. Nusselt number as a function of the voltage. Closed and open symbols show the Nusselt numbers measured at the outer shell Nu_o and the inner shell Nu_i , respectively.

The value of Nu_i is always decreasing with the voltage, while Nu_o increases with the voltage. The slopes of both graphs are opposite, resulting in a nearly constant averaged arithmetic mean value of Nu (not shown). The Nusselt numbers differ between the reference temperatures. Their values for $T_0 = 303.5$ K are always higher than those for $T_0 = 293.0$ K. Even the assumed conductive case of $V_0 = 1800$ V reveals a Nusselt number of $Nu = 1.5$. In contrast to the classical Rayleigh-Bénard (RB) convection, the Nusselt numbers at the inner shell are also less than unity. This comes from the fact that the convective flux becomes negative in the inner part of the spherical gap. This is a distinctive feature of the TEHD convection under dielectric heating. In the RB convection, the convective flux is always greater than (convection state, $Nu > 1$) or equal to (conduction state, $Nu = 1$) the conductive flux. In the TEHD convection under dielectric heating, therefore, the onset of convection cannot be detected anymore with the criterion $Nu > 1$.

A strong influence of the convective flow on the temperature profile is observed for $V_0 > 3000$ V. The maxima are “eroded” by the velocity field towards the outer shell, where the convective flux is positive and greater than the conductive flux. This explains the differences between the inner and the outer Nusselt numbers. It is observed that convective cells penetrate the stably stratified bottom region, which results in convection cells extending over the whole gap.

III. COMPARISON WITH EXPERIMENT

A. Temperature field

A comparison of experimental interferograms and the numerical results for different values of the voltage is shown in Figs. 9 and 10. The first row depicts the experimental interferograms and the second row the numerical interferograms. The third and fourth rows show the temperature and velocity fields in a meridian plane.

In all experimental interferograms the base pattern of the Wollaston shearing interferometry unit is visible as stripes. This pattern is produced because of the manufacturing tolerance of the shells. The first column ($V_0 = 1800$ V) does not exhibit any convective structures for both reference temperatures. Three explanations are possible: First, the interferometry is not sensitive enough to

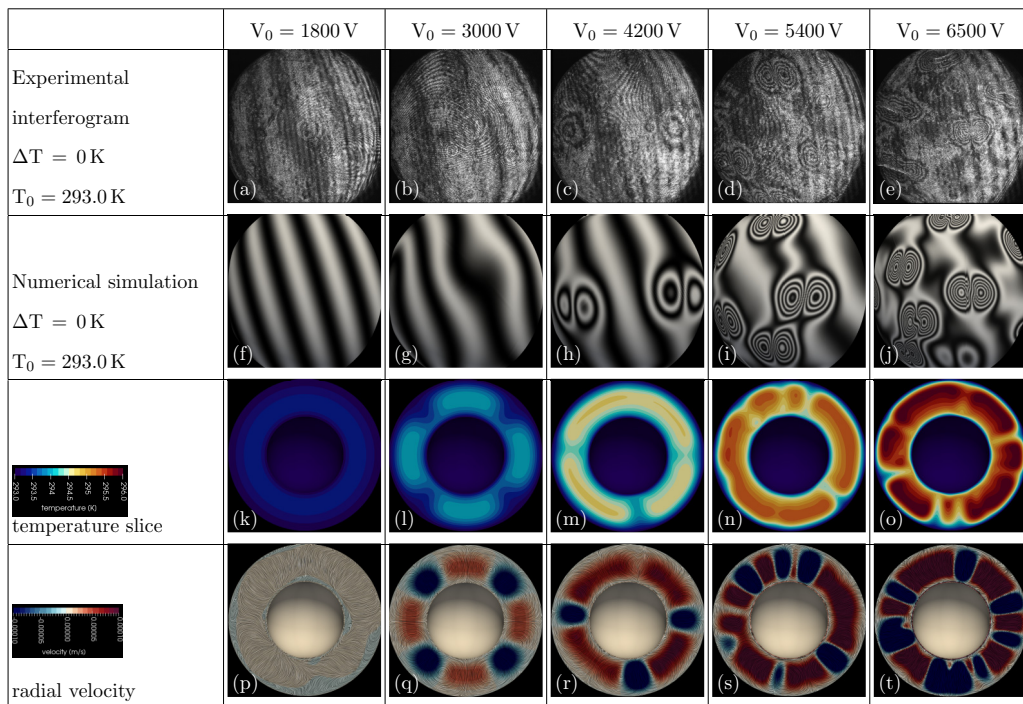


FIG. 9. (a)–(e) Experimental interferograms of the GeoFlow II experiment for $T_0 = 293.0$ K and $\Delta T = 0$. (f)–(j) Numerically calculated interferograms based on 3D simulations. Both rows show interferograms recorded after $t = 2603$ s. Dielectric heating is visible for $V_0 \geq 4200$ V as thermal plumes which exhibit characteristic double-ring structures. Conductive cases (a) and (b) show only the base fringe pattern. (k)–(o) Temperature distribution in a vertical slice. (p)–(t) Streamlines colored by the radial velocity field. Blue regions are downdrafts and red regions are updrafts.

resolve weak temperature gradients; second, the experiment timescale is too short for convective flow to develop; third, the conduction state is stable at this voltage.

Convective plumes at $V_0 = 3000$ V show weak gradients and are hard to identify in the interferograms. They are indicated by slightly distorted fringes. On the other hand, the plumes are visible in the numerical simulations as regular octahedral structures. These structures have also been observed by Zaussinger *et al.* [24] and Feudel *et al.* [25]. For $V_0 \geq 4200$ V convective plumes are visible as double rings in the experiment and in the numerical simulations. The number of rings is positively correlated to the voltage and to the reference temperature. Due to the increased acceleration at higher voltages, the thermal gradients steepen and the frequency of fringes in double-ring packages increases. This holds for both reference temperatures. It may be worth mentioning that sheetlike structures are never observed under the isothermal condition $T_1 = T_2$. The size of convective plumes decreases with increasing voltage. See, for instance, the results for $T_0 = 303.5$ K and $V_0 = 4200$ – 6500 V. The observed behavior of plumes is in good agreement with RB convection, where convective plumes are described as thermal boundary layers separated from walls. The boundary layers get thinner with increasing Rayleigh number. The thermal gradients then become steeper. In addition, the size of the plumes depends on the reference temperature. Plumes are larger for $T_0 = 293.0$ K. By comparing the temperature field [Figs. 9(o) and 10(o)] or the radial velocity field [Figs. 9(t) and 10(t)] observed at different temperatures, one finds steeper plumes at the higher temperature $T_0 = 303.5$ K.

The selected images are representative of the amount of convective cells found. They are obtained by manually counting. For both reference temperatures we find a positive correlation between

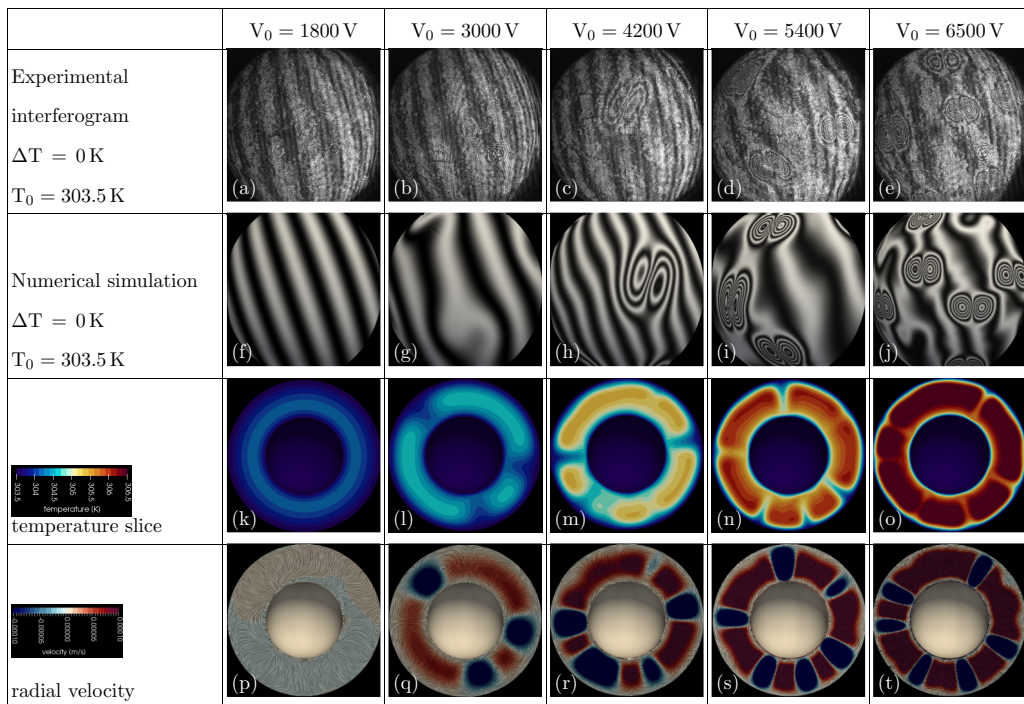


FIG. 10. (a)–(e) Experimental interferograms of the GeoFlow II experiment for $T_0 = 303.5$ K and $\Delta T = 0$. (f)–(j) Numerically calculated interferograms based on 3D simulations. Both rows show interferograms recorded after $t = 2603$ s. Dielectric heating is visible for $V_0 \geq 4200$ V as thermal plumes which exhibit characteristic double-ring structures. Conductive cases (a) and (b) show only the base fringe pattern. (k)–(o) Temperature distribution in a vertical slice. (p)–(t) Streamlines colored by the radial velocity field. Blue regions are downdrafts and red regions are updrafts.

plumes and voltage. Up to 20 plumes are found per hemisphere in the case of $V_0 = 6500$ V. In the statistical mean we find 38% more convection cells in the numerical simulations than in the experiment. This aberration will be discussed in Sec. IV. The numerical simulations reveal that the convective plumes emerge irregularly in the spherical gap. They are not stationary, but are moving and relocated within 10–20 min over the distance of the interferogram. As the experimental interferogram measurement lasts only 3 min, it is not possible to estimate the velocities of plumes for comparisons with the numerical results.

B. Size of double-ring structures

The inner structure of double rings depends on the temperature gradients inside the convective plume. In addition, the temperature distribution in the midgap spherical surface looks Gaussian around a plume. As the interferometry delivers narrower stripes at higher gradients, the two centers of the double rings represent inflection points. These points are located at $\mu \pm \sigma$, where μ is the bisection point of the double-ring centers. The temperature takes its local maximum or minimum there. The length between two centers ($l_c = 2\sigma$) gives a quantitative value for the width of a convective plume which is used to calibrate numerical interferograms. Additionally, l_c depends on the velocity field and the thermal distribution due to dielectric heating. We calculate the mean value of all visible plumes to calibrate the numerical interferograms. The variation of this mean value is within 10%, which indicates that the lateral elongation of the plumes is nearly identical. We find the

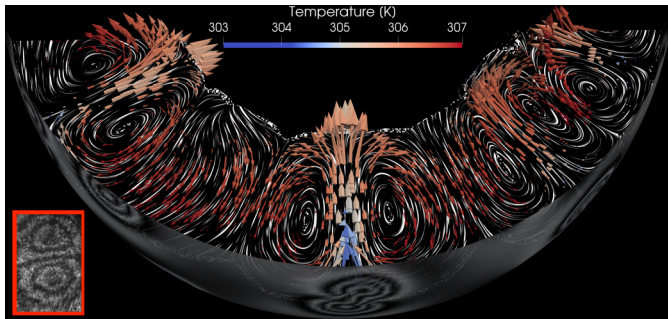


FIG. 11. Velocity vectors and associated streamlines along a convective downdraft. The double-eye pattern occurs from a downward stream, where cold material is transported towards the inner shell. The red box shows an experimental interferogram.

same result in the numerical simulations by analyzing the temperature field in the meridian surface. Double-ring structures at $T_0 = 303.5$ K are generally wider than for $T_0 = 293.0$ K.

C. Velocity field

Interferograms do not deliver direct quantitative information about the velocity field. By careful confrontation of the experimental and numerical interferograms, however, it is possible to deduce some properties of the flow velocities. The simulations show that the convective flow is enhanced by the increase of the applied electric voltage, as expected from the analogy to the classical RB convection. Furthermore, the simulations show peak velocities at the locations of downdrafts, underneath double-ring structures. The mean velocity in updraft regions is about halved. The last rows in Figs. 9 and 10 show this behavior. Blue regions, where the radial velocity points inward, coincide with steep thermal plumes. This observation differs from earlier publications about GeoFlow II, where updrafts were predicted in the same situations. We will discuss this point in Sec. IV. The velocity field in such a downdraft region is shown in Fig. 11 in more detail, where streamlines are superimposed on the velocity vectors. The colors of the vectors indicate the temperature values. One can see that the velocities are larger in the inner half layer than in the outer half layer. This would be a consequence of (i) an increased radial acceleration due to the dielectrophoretic force field and (ii) the channel-like acceleration between the counterrotating vortices. In addition, the fluid could be heated up by passing the middle of the gap (small, deep red colored vectors).

IV. DISCUSSION

Although the GeoFlow experiment delivers only interferograms and hence an integrated value of the mean temperature, we are able to deduce some basic properties of the velocity field with accompanying numerical simulations. We find that cold fluid is transported downward underneath channel-like plumes. This is in strong contrast to earlier publications where steep updrafts have been found. Futterer *et al.* [16] explained the specific convective plumes with a massively increased viscosity contrast of $\nu_{\min}/\nu_{\max} = 32$. Although the numerical simulations reproduced well experimentally determined interferograms, the physical process of the viscosity contrast has never been justified. Travnikov *et al.* [26] also analyzed laminar convection in the same numerical and experimental setup for various viscosity contrasts. Very good alignment of sheetlike structures has been found for $Ra < 14\,000$. The turbulent convective case was not in the scope of this study. Zaussinger *et al.* [24] recognized a “stability island” between the conductive and the convective case. The plumes, now known that they are dielectrically produced, have been studied according to their automatized recognition in images. The presented experimental setup is unique for two

reasons. First, the dielectric properties of 1-Nonanol are user friendly. This means that the frequency of the electric field is reasonable low ($f = 10\,650$ Hz) and the loss rates are high ($\tan \delta \approx 0.07$). Second, the given spherical geometry with radius ratio $\eta = 0.5$ delivers a stationary electric field. This favors the numerical solution [15] as the Gauss equation does not have to be solved in each time step. Although the comparison of numerical and experimental interferograms shows many similarities, it reveals one significant issue. We find 38% more plumes in the simulations than in the experiment. Three reasons could explain this discrepancy. First, the numerical simulations have been performed without the cylindrical shaft. Egbers *et al.* [10] examined the influence of the shaft during the construction phase of GeoFlow and estimated a region of influence of 30° around the shaft in the southern hemisphere. However, the influence of the shaft might extend over a wider zone in convective flows. Second, the experimental interferograms do not show all plumes, as the visibility depends on the polarization plane. Plumes occur and vanish depending on their position according to the polarization plane. This also reduces the amount of actually counted experimental plumes and implies that we find all plumes in the numerical simulations, but only a fraction of them in the experiment. Third, the plumes observed in the simulation are undergoing merging processes (see [25]) and the number of plumes converges towards the experimental amount.

V. CONCLUSION

The behavior of a liquid layer in the gap between two concentric spherical electrodes has been investigated by means of numerical simulations and the microgravity experiment GeoFlow. The liquid was heated internally by dielectric heating, which leads to thermal convection. The isothermal conductive case was analyzed with a simple 1D temperature equation, which involves a source term arising from the dielectric heating. We found that dielectric heating leads to a parabolic-shaped thermal profile, where the maximum was found in the middle of the gap.

Three-dimensional numerical simulation showed that convection does not set in for $V_0 = 1800$ V, but for $V_0 \geq 3000$ V. The onset of convection is expected in between. In addition, we found Nusselt numbers less than unity, which was explained by a negative convective flux in the inner part of the spherical gap. Incorporating the dielectric heating in the equations governing the TEHD convection delivered the best match between numerical and experimental interferograms for GeoFlow II. With increasing voltage, a series of experimental interferograms could be reproduced by numerical simulations.

The GeoFlow experiment does not deliver direct information about the temperature field. Additionally, the velocity field is not accessible, except drift rates of plumes. The temperature distribution is given as an interferogram which represents a radially averaged temperature value and therefore a projection of the full temperature field on the 2D plane. The loss of information is intrinsic owing to the measurement technique. However, the present numerical simulation can complete the experimental measurements. Confronting experimental interferograms with those produced by the simulation, we can deduce basic features of the temperature fields and identify convective plumes and laminar structures in the flow. The simulation also provides associated velocity fields.

Future work could apply the presented TEHD model in situations with an initial temperature contrast. This could explain further inconsistencies in similar experiments. The extension to rotational cases is also in the scope of envisaged work.

ACKNOWLEDGMENTS

The GeoFlow research was funded by the ESA Grant No. AO-99-049, by the DLR Grants No. 50WM0122 and No. 50WM0822, and by the SOKRATES/ERASMUS program LIA-ISTROF (CNRS cooperation). T.S. gratefully acknowledges support from the DFG Grant No. EG 100/20-1. Furthermore, the authors thank the GeoFlow Topical Team (ESA Grant No. 18950/05/NL/VJ) for intensive discussions. In particular, we thank G. Fabricius for the deep insights into the

construction of the GeoFlow experiment and R. Golinske for discussions about dielectric materials. All simulations were performed at the Northern German Network for High-Performance Computing (HLRN) and the Heraklit cluster (BTU Cottbus-Senftenberg).

- [1] J. Staněk, *Electric Melting of Glass* (Elsevier, Amsterdam, 1977).
- [2] A. C. Metaxas and R. J. Meredith, *Industrial Microwave Heating* (Peregrinus, London, 1983).
- [3] A. R. von Hippel, *Dielectric Materials and Applications* (Artech House, Norwood, 1954).
- [4] C. Gabriel, S. Gabriel, E. H. Grant, B. S. J. Halstead, and D. M. P. Mingos, Dielectric parameters relevant to microwave dielectric heating, *Chem. Soc. Rev.* **27**, 213 (1998).
- [5] D. El Khaled, N. Novas, J. A. Gázquez, R. M. García, and F. Manzano-Agugliaro, Alcohols and alcohols mixtures as liquid biofuels: A review of dielectric properties, *Renew. Sust. Energy Rev.* **66**, 556 (2016).
- [6] J. A. Stratten, *Electromagnetic Theory* (McGraw-Hill, New York, 1941).
- [7] T. F. Irvine and J. P. Hartnett, *Advances in Heat Transfer* (Elsevier, Amsterdam, 1979).
- [8] T. B. Jones, *Electrohydrodynamically Enhanced Heat Transfer in Liquids: A Review* (Elsevier, Amsterdam, 1979).
- [9] L. D. Landau and E. M. Lifshitz, *Electrodynamics of Continuous Media* (Elsevier Butterworth-Heinemann, Burlington, 1984).
- [10] C. Egbers, W. Beyer, A. Bonhage, R. Hollerbach, and P. Beltrame, The GeoFlow-experiment on ISS (part I): Experimental preparation and design of laboratory testing hardware, *Adv. Space Res.* **32**, 171 (2003).
- [11] K. G. Ayappa, S. Brandon, J. J. Derby, H. T. Davis, and E. A. Davis, Microwave driven convection in a square cavity, *AIChE J.* **40**, 1268 (1994).
- [12] Q. Zhang, T. H. Jackson, and A. Ugan, Numerical modeling of microwave induced natural convection, *Int. J. Heat Mass Transfer* **43**, 2141 (2000).
- [13] P. Ratanadecho, K. Aoki, and M. Akahori, A numerical and experimental investigation of the modeling of microwave heating for liquid layers using a rectangular wave guide (effects of natural convection and dielectric properties), *Appl. Math. Model.* **26**, 449 (2002).
- [14] R. Cherbański and L. Rudniak, Modelling of microwave heating of water in a monomode applicator—Influence of operating conditions, *Int. J. Therm. Sci.* **74**, 214 (2013).
- [15] V. Travnikov, C. Egbers, and R. Hollerbach, The GeoFlow-experiment on ISS (part II): Numerical simulation, *Adv. Space Res.* **32**, 181 (2003).
- [16] B. Futterer, A. Krebs, A.-C. Plesa, F. Zaussinger, R. Hollerbach, D. Breuer, and C. Egbers, Sheet-like and plume-like thermal flow in a spherical convection experiment performed under microgravity, *J. Fluid Mech.* **735**, 647 (2013).
- [17] H. N. Yoshikawa, M. T. Fogaing, O. Crumeyrolle, and I. Mutabazi, Dielectrophoretic Rayleigh-Bénard convection under microgravity conditions, *Phys. Rev. E* **87**, 043003 (2013).
- [18] M. T. Fogaing, H. N. Yoshikawa, O. Crumeyrolle, and I. Mutabazi, Heat transfer in the thermo-electrohydrodynamic convection under microgravity conditions, *Eur. Phys. J. E* **37**, 35 (2014).
- [19] I. Mutabazi, H. N. Yoshikawa, M. T. Fogaing, V. Travnikov, O. Crumeyrolle, B. Futterer, and C. Egbers, Thermo-electro-hydrodynamic convection under microgravity: A review, *Fluid Dyn. Res.* **48**, 061413 (2016).
- [20] C. Kang, K.-S. Yang, and I. Mutabazi, Thermal effect on large-aspect-ratio Couette-Taylor system: Numerical simulations, *J. Fluid Mech.* **771**, 57 (2015).
- [21] V. Travnikov, O. Crumeyrolle, and I. Mutabazi, Numerical investigation of the heat transfer in cylindrical annulus with a dielectric fluid under microgravity, *Phys. Fluids* **27**, 054103 (2015).
- [22] R. J. Turnbull, Effect of dielectrophoretic forces on the Bénard instability, *Phys. Fluids* **12**, 1809 (1969).
- [23] H. G. Weller, G. Tabor, H. Jasak, and C. Fureby, A tensorial approach to computational continuum mechanics using object-oriented techniques, *Comput. Phys.* **12**, 620 (1998).

- [24] F. Zaussinger, A. Krebs, V. Travnikov, and C. Egbers, Recognition and tracking of convective flow patterns using Wollaston shearing interferometry, [Adv. Space Res. **60**, 1327 \(2017\)](#).
- [25] F. Feudel, N. Seehafer, L. S. Tuckerman, and M. Gellert, Multistability in rotating spherical shell convection, [Phys. Rev. E **87**, 023021 \(2013\)](#).
- [26] V. Travnikov, F. Zaussinger, P. Beltrame, and C. Egbers, Influence of the temperature-dependent viscosity on convective flow in the radial force field, [Phys. Rev. E **96**, 023108 \(2017\)](#).



AtmoFlow - Investigation of Atmospheric-Like Fluid Flows Under Microgravity Conditions

F. Zaussinger¹ · P. Canfield² · A. Froitzheim¹ · V. Travnikov¹ · P. Haun¹ · M. Meier¹ · A. Meyer¹ · P. Heintzmann³ · T. Driebe³ · Ch. Egbers¹

Received: 22 January 2019 / Accepted: 13 June 2019 / Published online: 25 June 2019
© Springer Nature B.V. 2019

Abstract

The main objective of the *AtmoFlow* experiment is the investigation of convective flows in the spherical gap geometry. Gaining fundamental knowledge on the origin and behavior of flow phenomena such as global cells and planetary waves is interesting not only from a meteorological perspective. Understanding the interaction between atmospheric circulation and a planet's climate, be it Earth, Mars, Jupiter, or a distant exoplanet, contributes to various fields of research such as astrophysics, geophysics, fluid physics, and climatology. *AtmoFlow* aims to observe flows in a thin spherical gap that are subjected to a central force-field. The Earth's own gravitational field interferes with a simulated central force-field with the given parameters of the model which makes microgravity conditions of $g < 10^{-3} g_0$ (e.g. on the ISS) necessary. Without losing its overall view on the complex physics, circulation in planetary atmospheres can be reduced to a simple model of a central gravitational field, the incoming and outgoing energy (e.g. radiation) and rotational effects. This strongly simplified assumption makes it possible to break some generic cases down to test models which can be investigated by laboratory experiments and numerical simulations. Varying rotational rates and temperature boundary conditions represent different types of planets. This is a very basic approach, but various open questions regarding local pattern formation or global planetary cells can be investigated with that setup. A concept has been defined for developing a payload that could be installed and utilized on-board the International Space Station (ISS). This concept is based on the microgravity experiment *GeoFlow*, which has been conducted successfully between 2008 and 2016 on the ISS. This paper addresses the scientific goals, the experimental setup, the concept for implementation of the *AtmoFlow* experiment on the ISS and first numerical results.

Keywords Microgravity conditions · Rotating convection · Atmospheric flows · Dielectrophoresis · Dielectric heating

Introduction

In a first approximation planetary atmospheres are confined fluid layers between two spherical shells. Hence, the fluid

flow is determined by the boundaries of the system, which are the inner and outer shell. The inner shell represents the planetary surface or deep, blocking atmospheric layers of e.g. gas giants. The outer shell represents the upper boundary of the climate-relevant atmosphere or, in case of the gas giant, a region, where the gas concentration decreases significantly. This simplified setup makes it possible to break some generic cases to test models, which can be investigated in laboratory experiments and numerical simulations. The main advantage of such an experiment is the reproducibility and the ability to resolve scales, which are parameterized by semi-empirical closure models, see e.g. Scolan and Read (2017).

However, such laboratory experiments are difficult to establish. Earth's gravity field would dominate or at least significantly contribute to any radial force field of a spherical experiment, which makes it very difficult to deduce meaningful results because of the relative

This article belongs to the Topical Collection: Thirty Years of Microgravity Research - A Topical Collection Dedicated to J. C. Legros
Guest Editor: Valentina Shevtsova

✉ F. Zaussinger
florian.zaussinger@b-tu.de

- ¹ Department of Aerodynamics and Fluid Mechanics, Brandenburg University of Technology Cottbus-Senftenberg, Cottbus, Germany
- ² Airbus Defence and Space GmbH, Immenstaad, Germany
- ³ Deutsches Zentrum für Luft- und Raumfahrt e.V., Bonn, Germany

magnitude. The centrifugal force can be used as radial force field to mimic buoyancy. However, this works only for the fast rotating case, see e.g. Busse and Carrigan (1976), and needs an inverted thermal gradient (outer shell heated, inner shell cooled) to establish a convectively unstable system. This setup cannot be used to investigate non-rotating cases and fluid flows with complex boundary conditions. The projection of a hemisphere onto a cylinder is one way to overcome some of the the problems e.g. to make use of a baroclinic wave tank (Borcia and Harlander 2013; Vincze et al. 2015), though various phenomena such as equatorial waves cannot be investigated with this setup. The most promising solution is to set up a spherical gap experiment with a radial force field in a microgravity environment. By applying laterally varying temperature boundary conditions and differential rotation it is possible to simulate a deep planetary atmosphere, where features like planetary waves and complex pattern formation can be studied. Indeed, the main advantage of the experiment proposed in this paper is the full sphere setup, which allows investigating equatorial zonal flows and also allows to distinguish equatorially symmetric and antisymmetric contributions.

Various experiments under microgravity conditions have been performed in the scope of fluid dynamics and convection. The half-dome experiment by Hart et al. (1986) on SpaceLab mission in 1986 was the first microgravity experiment utilizing the dielectrophoretic effect (DEP). Hart's experiment used lateral heating sources, corresponding to planetary atmosphere boundary conditions. Additionally, the experiment was mounted on a rotating table. They investigated columnar cells and their interaction with mid-latitude waves. Even spiral waves and non-axisymmetric convection zones were observed.

Channel flow experiment were conducted by Smirnov et al. (2004), where a Hele-Shaw cell was exposed to microgravity conditions on parabolic flight campaigns. They investigated the displacement of viscous fluid and showed that the increase of the viscosity ratio between two miscible fluids increases the fingering instability. Flow rate limitations in single phase and two phase open capillary channel flows were examined in an experiment setup on the ISS in addition to examining the effect of the geometry of the channel on the stability of the free surface (Canfield et al. 2013; Conrath et al. 2013). The investigators also focused on bubble formation (Canfield 2018), surface-tension driven bubble migration, and passive phase separation (Jenson et al. 2014). The mission lasted multiple months and yielded video material for thousands of data points within a wide range of parameters (Bronowicki et al. 2015).

The first german experiment investigating convective flows in microgravity conditions was conducted on a parabolic flight campaign in 1991, Liu et al. (1992). In the following, similar experiments had been performed on the

TCM Volna ballistic rocket, see e.g. Egbers et al. (1999), Kuhl et al. (2005). During the flight of this rocket the experiment was able to be conducted for about 20 min under microgravity conditions. Based on this first experiment the spherical gap experiment GeoFlow (geophysical flow) was developed in the early 2000s and successfully run on the ISS between 2008 and 2016, (Egbers et al. 2003; Beltrame et al. 2003; Travnikov et al. 2003; Ezquerro Navarro et al. 2015). The GeoFlow experiment was designed to study convective flows whilst applying a radial temperature gradient. Two missions were successfully completed in the scope of this experiment, GeoFlow I (GFI) and GeoFlow II (GFII).

Both experiments have been conducted on the ISS within the Fluid Science Laboratory (FSL) of the Columbus module, but, with differing working fluids. The main advantage of GeoFlow is its full sphere geometry, where basic features of iso-viscous convection (GFI: Futterer et al. (2008); Jehring et al. (2009)) and flows with temperature-dependent viscosity (GFII: Futterer et al. (2013); Zaussinger et al. (2017, 2018b); Travnikov et al. (2017)) have been studied.

Besides the GeoFlow experiments, an experimental setup dedicated to parabolic flight campaigns (PFC) has been developed, too, see Futterer et al. (2016) and Meier et al. (2018). Based on the same physical mechanism, thermo-electric convection is studied inside a cylindrical annulus (Meyer et al. 2017, 2018). Between 2016 and 2018, four campaigns successfully displayed the occurrence of convective instability caused by DEP-force during low gravity phases (22 sec of $10^{-2} g_0$) with different fluids, aspect ratios and control parameters.

While thermo-electric convection in a cylindrical gap is a simplified model for the GeoFlow and AtmoFlow spherical geometries, it has also direct applications such as cylindrical heat exchangers for electronic devices, see e.g. Evgenidis et al. (2011), Lotto et al. (2017).

The proposed experiment AtmoFlow differs much from the previous GeoFlow-setups. First, the inner and the outer boundaries will both be heated/cooled locally. Additionally, a differential rotating unit is foreseen, to simulate deep shells, as they occur in giant planets. Figure 1 depicts such a simplified atmosphere, where incoming radiation and rotation lead to global cell formation. These cells (Hadley cell, Ferrel cell or mid-latitude cell, polar cell) are well known from the Earth and co-responsible for global atmospheric dynamics. In contrast to Hart's experiment, AtmoFlow is designed as a (nearly) full sphere. The advantage of this design is apparent, when equatorial flows and global patterns are investigated. AtmoFlow will be the first experiment under microgravity conditions, which will be able to study simplified global fluid flows, planetary waves and complex patterns in the full spherical shell geometry under atmospheric-like boundary conditions.

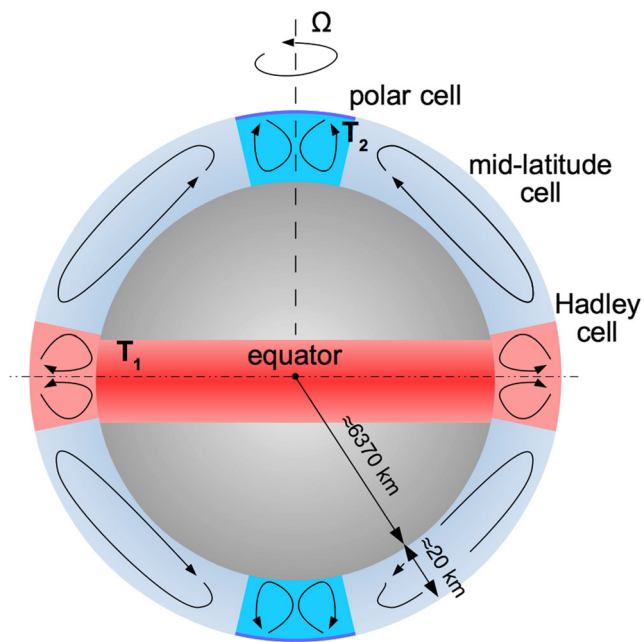


Fig. 1 Simplified planetary atmosphere as found on the Earth. Not to scale.

The empirical study of planetary waves, global cell formation and fluid dynamical instabilities are in the focus of the experiment. The experiment results will provide benchmark data for a rich variety of numerical problems, which are still a challenge for scientific research in various fields.

This paper is structured as follows. Section “**Objectives and Scientific Program**” gives an overview of the objectives and the scientific program of the AtmoFlow experiment. A brief description of the experiment is presented in Section “**Brief Description of the Experiment**”. The experimental methods and diagnostics are presented in Section “**Experimental Methods and Diagnostics**”. This includes a g_0 testing facility on ground, where $g_0 = 9.81 \text{ m/s}^2$. The physics of thermo-electro hydrodynamics and the dielectrophoretic effect are described in Section “**Thermo-Electro Hydrodynamics**”. Results from accompanying numerical simulations are presented in Section “**Numerical Simulations**”. We summarize the content of our findings in Section “**Conclusions and Outlook**”.

Objectives and Scientific Program

The AtmoFlow experiment makes it possible to investigate flows, which are driven by internal heating, boundary temperature difference, rotation or complex boundary conditions. It will enable deep insights into EHD driven fluid flows, which can be used for validating simple convection

models of planetary atmospheres. The extension of semi-empirical parameterizations of unresolved atmospheric processes, e.g. large-scale / small-scale coupling will be investigated, too. Furthermore, precise parametrization of cell formation will be tested with respect of e.g. Rhines scaling, Read et al. (2004); Heimpel et al. (2005). This includes the investigation of the heat transfer from the tropics to the stably stratified mid-latitudes, Scolan and Read (2017). In addition, the findings of AtmoFlow are expected to be of benefit for validation and development of models that deal with climate change. Various initial temperature distributions will be tested to investigate connections between external forcing and climate variability.

The main goal is the elucidation of basic aspects of convection in the rotating spherical shell. This allows the testing of linear stability analysis regarding base flows, convective onsets and bifurcation scenarios in rotating and non-rotating scenarios. Planned applications are presented subsequently:

Non-Rotating Case

The *non-rotating case* is mainly used to test physical models of electro-hydrodynamics. Especially, the role of mixed heating (internal heating and temperature difference across the gap) is not well understood in the spherical gap geometry, see e.g. Vilella and Deschamps (2018). Even though the non-rotating case has no direct geo- or astrophysical counterpart, it is of importance for planned technical applications. The construction of optimized heat exchangers, EHD-based pumps and nozzles will profit from this research. Furthermore, the enhancement of convective heat transfer in absence of gravity (e.g. on space stations or spacecrafts) will benefit from a deeper understanding of EHD driven fluid flows.

Rotating Case

AtmoFlow captures only a small range of realistic geo- and astrophysical parameters. Here, we refer to Section “**Thermo-Electro Hydrodynamics**” where all dimensionless numbers are defined. The size and weight of the payload limits the Rayleigh number to $Ra < 10^6$, the Taylor number to $Ta < 10^7$, the Ekman number to $10^{-2} < Ek < 10^{-3}$, the Prandtl number to $Pr = 8$ and the Rossby number to $|Ro| < 4$. However, many rotating flows can be studied with this setup. In the following, typical applications, limitations and the parameter regimes for proposed research scenarios of rotating AtmoFlow experiments are presented:

- *Convection*, more precisely the convective onset, transitions to the turbulent regime and symmetry-breaking bifurcations (Mamun and Tuckerman 1995;

Feudel et al. 2015) are compared with linear stability analysis and numerical simulations in the super-critical range of $Ra/Ra_{crit} < 20$ and the entire given Taylor number regime. These experiments will be conducted either with internal heating and/or a temperature difference across the gap.

- *Torsional oscillations* and resulting radial equatorial jets (Vorontsov et al. 2002; Hollerbach et al. 2002) can be investigated in the entire parameter range for $Re > 100$. Such experiments depend only on inner sphere dynamics and not on the thermal distribution.
- Several questions arise in the scope of *zonal wind systems* like those found on Jupiter or Saturn. AtmoFlow represents a deep-seated experiment with geometric properties and Ekman numbers comparable to early 3d-simulations by e.g. Christensen (2001) and laboratory experiments e.g. Manneville and Olson (1996). The direction of the jets (super-rotation and retrograde equatorial flows) are found to correlate with the convective Rossby number $Ro_T = \sqrt{Ra/Pr} Ek$. According to definitions by Julien et al. (2012) and Gastine et al. (2013a), the AtmoFlow experiment ranges between $10^{-1} < Ro_T < 10$. The lower limits of Ro_T cover roughly flow regimes as found on planets of our solar system (Wang and Read 2012) e.g. $Ro_T = 0.5$ on Jupiter's surface, (Gastine et al. 2013a). Hence, the basic investigation of zonal winds and the role of Ro_T regarding super-rotation as found on Jupiter or Saturn (Gastine et al. 2013b) as well as retrograde equatorial jets known from Uranus and Neptune (Dietrich et al. 2017) can be conducted by AtmoFlow.

Differential Rotating Case

The basic *spherical Couette flow* consists of a rotating inner shell and a fixed outer shell. In the context of this setup the excitation of inertial modes (Kelley et al. 2010; Rieutord et al. 2012) will be studied for the Rossby number range of $-4 < Ro < 4$. Limitations are only given by high Ekman numbers, which are caused by the small outer radius. In geophysics, *differential rotation* plays an important role, when a solid planetary core rotates with a different rate than the surrounding atmosphere or mantle. It produces internal mixing, which proceeds on dynamical time-scales, Maeder (1995). For instance, the inner core of the Earth is assumed to super-rotate with 1° per year, Waszek et al. (2011). Comparable situations are found in Mercury, Jupiter, Earth's moon and Galilean moons. Hereby, the Richardson criterion ($Ri > 0.25$) parameterizes the condition whether the shear instability is dominant over e.g. buoyancy driven instabilities, or not. For the case of

thermo-EHD this criterion is not tested and still an unsolved problem.

Brief Description of the Experiment

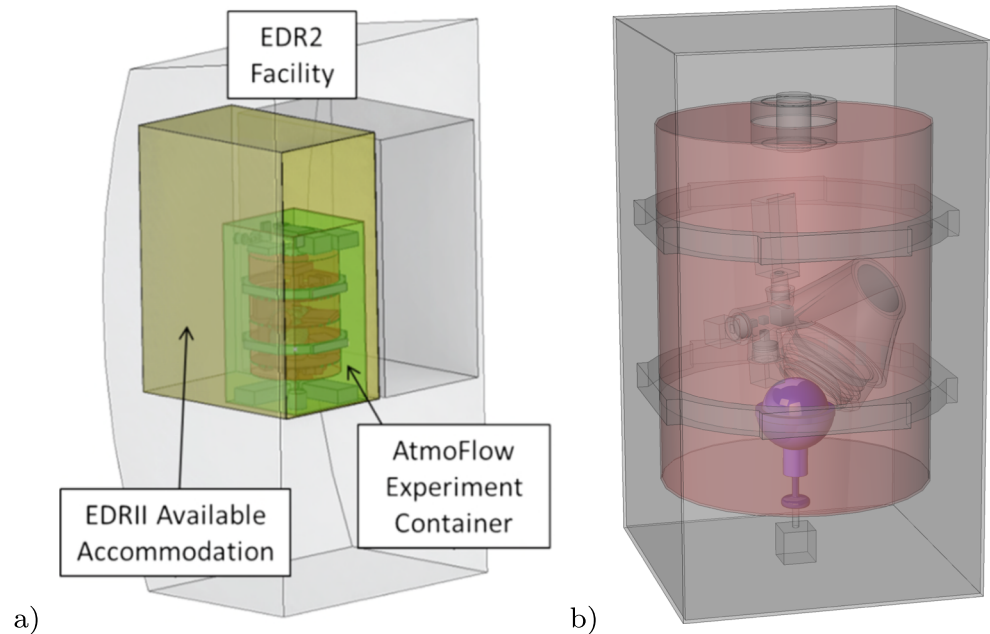
The development of the AtmoFlow experiment benefits from the heritage of the GeoFlow experiments that were performed between 2008 and 2016 in the Fluid Science Laboratory on the ISS. Similarities in the setup are apparent, such as the rotating spherical gap geometry, the central dielectrophoretic force field, and various diagnostic and analytical methods. In particular, AtmoFlow will utilize the same visualization techniques as GeoFlow albeit with some additional and/or modified functionalities. Currently, as of 2018, the AtmoFlow experiment payload is in Phase A/B and the focus of the development work is on the systematic identification and assessment of requirements and consolidation of the concept. The current development baseline assumes accommodation of the payload within the European Drawer Rack Mk II (EDR2, see Fig. 2 and www.esa.int), which should be launched to the ISS and installed in the European Columbus module in the near future.

The ISS provides a microgravity environment that is adequate for the purpose of this experiment. Other microgravity platforms (e.g. drop tower or sounding rockets) are not considered as it is expected that the duration of a single experiment point must last around an hour, which corresponds to the double of a thermal time scale. EDR2 provides interfaces for payloads in terms of mechanical accommodation, access to the stations water cooling loop, various data communication methods, power supply, etc. The concept for the AtmoFlow payload currently consists of a hermetically sealed payload that contains the entire setup including auxiliary systems that are required to perform the experiment. The core of the payload is the fluid cell (see Fig. 3), which is composed of an inner sphere (diameter 0.0378 m), an outer sphere (diameter 0.054 m) and a cooling shell.

The gap between the inner sphere and the outer sphere is filled with the test liquid 3MTMNovocTM 7200 and represents the region of interest for the acquisition of science data. Local temperature boundary conditions are imposed on the poles by cooling plates in the outer shell and at the equator of the inner shell. The mean temperature in the intermediate regions is obtained by a thermalization circuit. Figure 4 depicts the temperature distribution at both shells. A detailed list of all geometrical aspects and the fluid properties is presented in Table 1.

Sensors are located throughout the fluid cell to monitor the temperatures of the thermalization zones and within

Fig. 2 a accommodation of AtmoFlow payload in EDR2, b payload with rotating carousel (red) and spherical gap unit (purple). source: Airbus Defence and Space



the gap between the cooling shell and the outer sphere. The inner sphere and the outer sphere also function as the electrodes for alternating high voltage electrical field, which generates the dielectrophoretic force on the liquid in the spherical gap to simulate a planet's gravity. Here, we refer to Section “[Thermo-Electro Hydrodynamics](#)” where details about the radial force generation are presented. The entire fluid cell is supported by a rotating carousel that imposes the rotational velocity Ω_2 . In addition, the inner sphere can be rotated by a separate drive unit (Ω_1) to impose a differential rotation boundary condition. Visualization of the fluid phenomena is performed using shearing interferometry, see e.g. Zaussinger et al. (2017). The entire optical setup co-rotates with the outer sphere and observes the test section in a circular region between the polar region of the upper hemisphere and the equator of the inner sphere. The field of view stretches across 80° of the northern hemisphere. The metallic surface of the inner sphere acts as a mirror in the optical path while the outer sphere and the cooling shell are transparent in the field of view. Local temperature gradients cause changes in the refractive index of the liquid in the optical path which in turn are visualized as fringes in the resulting interferograms. A dual camera setup including a beam splitter and dedicated Wollaston prisms allows for simultaneous interferometry in perpendicular planes. In addition to the fluid cell, the payload must accommodate all subsystems that are required to perform the experiment such as avionics and power distribution, cooling and thermalization, mechanical structure and mechanisms, optical diagnostics, actuators and

drives, etc. A data downlink function ensures that the images acquired by the interferometer cameras and data acquired by the various sensors within the experiment setup are transferred to ground for analysis.

Geometry and Thermal Boundary Conditions

The experimental cell, depicted in Fig. 3, will rotate as a complete assembly and the inner sphere will be equipped with an additional drive unit to rotate relative to the experimental cell. The geometry and dimensions of the experiment cell are defined to fulfill the objectives stated in Section “[Objectives and Scientific Program](#)”. The radius of the outer sphere R_2 is determined by the size and weight of the optical setup as well as the optical accessibility. This trade-off leads to a radius of outer sphere at $R_2 = 0.027$ m, a radius of inner sphere at $R_1 = 0.0189$ m, resulting in a radius ratio of $\eta = R_1/R_2 = 0.7$. The radius of the inner sphere is further chosen to reach a radius ratio in between thin and thick atmospheres.

The key feature of AtmoFlow is the thermal boundary condition. Realistic atmospheric boundary conditions are very complex, however, it is possible to break them down to follow three regions: a) a solar-heated equatorial region with absorption of re-radiated infrared radiation; b) heat sinks in the upper atmosphere of the poles and mid-latitudes, c.f. Chan and Nigam (2009); c) moderate temperature regions between the polar and the equatorial regions. Imposing these idealized boundary conditions results in a global circulation, which is convectively unstable in the tropics and stable in

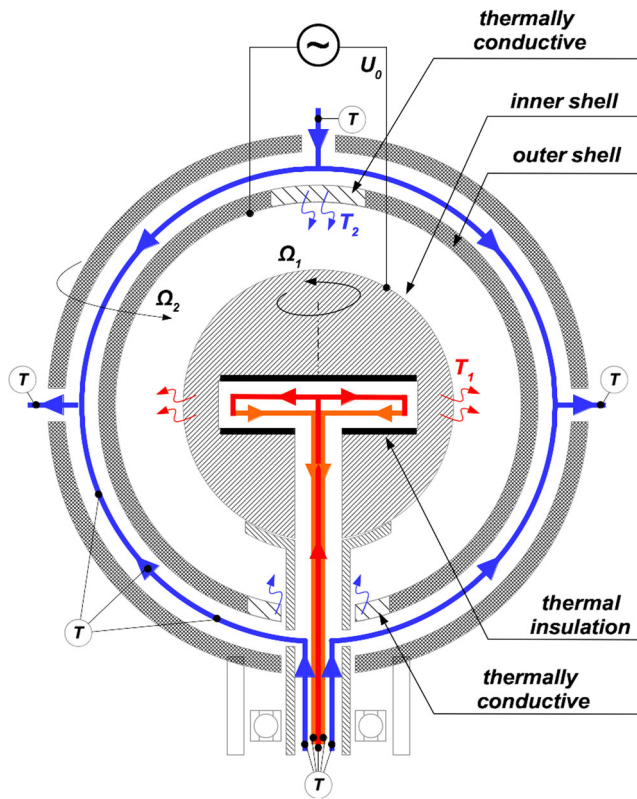
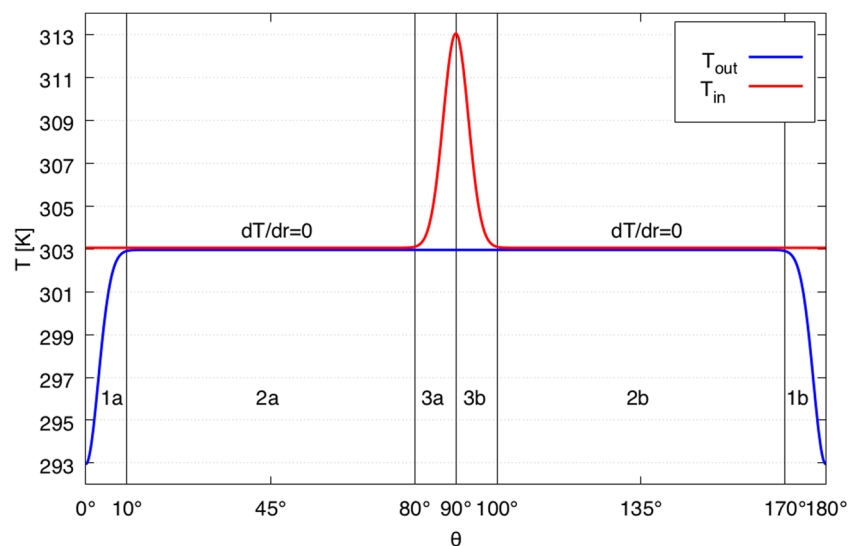


Fig. 3 Vertical cut through the AtmoFlow experiment. Blue lines depict the cooling loop, red lines show the heating circuit. Inner and outer rotation is labeled by Ω_1 and Ω_2 , respectively. The maximum temperature is found at the equator T_1 , the minimum temperature at the poles T_2 .

the mid-latitudes. Hence, the heat transfer from the tropics to the stably stratified mid-latitudes and sub-tropics can be investigated with this setup. A baroclinic wave tank with the same specifications has been investigated by Scolan and Read (2017). They observed the interaction and coexistence

Fig. 4 Imposed thermal boundary conditions used for the numerical simulations of the AtmoFlow experiment for a maximum temperature difference of 20 K. T_{in} specifies the temperature at the inner shell, T_{out} at the outer shell



of convective and baroclinic zones. Hence, this experiment can be used as validator to study equilibrium processes as they occur in planetary atmospheres. For AtmoFlow the thermal boundaries are imposed by heating plates and cooling loops, which results in Dirichlet type boundary conditions as depicted in Fig. 4. Convection is controlled by varying the temperature at the outer shell. Dielectric heating (see Section “Dielectric Heating”) does not change the temperature at the boundaries as it acts only on the fluid in the spherical gap and not in the cooling loops. The temperatures at the boundaries are controlled by thermal sensors. See Section “Temperature Measurement” for a detailed description of the thermal measurements.

The idealized thermal boundary condition used for the numerical simulations represents a conductive solution, when the equator is heated, the upper polar region cooled and the mid-latitudes are insulated. It’s the same approach as found in Scolan and Read (2017). Figure 4 depicts these regions in terms of the temperature as function of the lateral angle θ for the maximum temperature difference between the poles and the equator of 20 K, which are used for the accompanying numerical simulations. The imposed thermal distribution at the surface T_{in} and the upper shell T_{out} can be approximated by,

$$T_{out}(\theta) = \frac{T_{hot} + T_{cold}}{2} + \frac{T_{hot} - T_{cold}}{2} \sin^n(\theta) \quad (1)$$

$$T_{out}(\theta) = T_{cold} + \frac{T_{hot} - T_{cold}}{2} \frac{\cosh(A \cos(\theta)) - \cosh(A)}{1 - \cosh(A)} \quad (2)$$

Here, $\theta = 0^\circ$ is the north pole and $\theta = 180^\circ$ is the south pole. The constant factor $A = 50$ increases the temperature at the poles from T_{cold} to $\frac{T_{hot} + T_{cold}}{2}$ within $\theta = 10^\circ$, see Fig. 4 regions 1a, 1b. In the following, the reference temperature is defined at the equator, $T_{ref} = T_{hot} = 313$ K. All

Table 1 Geometrical parameters and fluid properties for 3MTMNovecTM 7200 (at 313 K, 10⁵ Pa and 10⁴ Hz frequency)

parameter	symbol	unit	value
inner radius	R ₁	m	1.89 × 10 ⁻²
outer radius	R ₂	m	2.7 × 10 ⁻²
radius ratio	η	-	0.7
min. temperature	T _{min}	K	293
max./ref. temperature	T _{max} , T _{ref}	K	313
temperature difference	Δ T	K	(T _{max} - T _{min})/2
rotation rate	Ω _{1,2}	Hz	0-2
max. voltage	U	V	10 ⁴
high voltage frequency	f _{HV}	Hz	10 ⁴
kinematic viscosity	ν	m ² /s	3.68 × 10 ⁻⁷
thermal conductivity	k	W/(mK)	6.61 × 10 ⁻²
spec. heat capacity	c	J/(kg K)	1.241 × 10 ³
thermal diffusivity	κ _T	m ² /s	3.83 × 10 ⁻⁸
thermal exp. coefficient	α _T	1/K	1.6 × 10 ⁻³
electric exp. coefficient@10.000Hz	α _E	K ⁻¹	1.383 × 10 ⁻³
density	ρ	kg/m ³	1.389 × 10 ³
boiling point	T _{boil}	K	349
relative permittivity	ε _r	F/m	7.4
loss factor	tan δ	-	9.73 × 10 ⁻²
refractive index@293K	n	-	1.281

dimensionless numbers refer to this value. The reference length scale is the gap width $d = 0.0081$ m, the reference temperature difference $\Delta T = T_{\text{ref}} - T_{\text{m}}$, where the intermediate temperature is defined as $T_{\text{m}} = \frac{T_{\text{hot}} - T_{\text{cold}}}{2}$. The width of the temperature peak at the equator T_{hot} is controlled by the factor $n=100$ and covers 20° , see Fig. 4 region 3a, 3b. Regions except the poles (outer shell regions 2a, 3a, 3b, 2b) and except the equator (inner shell regions 1a, 2a, 2b, 1b) are thermally insulated ($dT/dr = 0$), see Fig. 4. Due to the insulating regions, the gradient of the permittivity has a non-zero value, which enables the dielectrophoretic force field everywhere in the fluid cell. The specific thermalization of the fluid is realized by two individual cooling/heating circuits, which are integrated in the experimental container.

Working Fluid

The working fluid plays a crucial role and has to fulfill various functions. First, the electric permittivity needs to be as high as possible. This benefits the acceleration based on the dielectrophoretic effect as the voltage can be lowered. Second, the viscosity needs to be low which supports comparisons with realistic atmospheres and water tank experiments. The test liquid requires specific properties especially when used onboard of the ISS in a high voltage environment. It has to be non-flammable, non-toxic, insulating and thermally and chemically stable. Next to silicone oils, per-fluorinated compounds are possible candidates satisfying these requirements. The primary candidate is 3MTM

NovecTM 7200 (ethoxy-nonafluorobutane) C₄F₉OC₂H₅. It is a clear, colorless and low-odor fluid. Furthermore, the viscosity is comparable to water $\text{Pr}(40^\circ\text{C}) = 9.61$. Water would be also a candidate with its much larger permittivity as 3MTM NovecTM 7200. However, it is not suitable for long-duration TEHD-experiments since even small amounts of ions coming from e.g. the fluid loop materials dissolve in the ultra-pure water and increase the electrical conductivity drastically.

Experimental Methods and Diagnostics

Interferometry

The direct data analysis methods will be based on the interferograms (Dubois et al. 1999; Egbers et al. 2003; Zaussinger et al. 2017) and telemetry data (Jehring et al. 2009) and consist of the following aspects:

- Tracking and recognition of convective flow pattern using image processing tools.
- Calculation of the mean temperature field using two perpendicular orientated interferometric images.

The indirect analysis methods are based on a comparison of the experimental results with numerical simulations. Hereby, numerical simulations are performed with identical conditions, whose results can be converted into artificial interferograms. If the interferograms match qualitatively,

the flow state can be analyzed in much more detail with respect to the determination of the temperature field and the three dimensional velocity field, including cell-formation, turbulence, interaction of planetary waves, statistics and extreme value analysis.

The methods described above have already been developed and applied to the GeoFlow experiment data with great success (Egbers et al. 2003; Zaussinger et al. 2017) and is being modified and applied to the AtmoFlow parameters in a separate scientific program funded by DLR Space Administration.

To investigate the flow in the gap between the inner and outer sphere, a Wollaston Shearing Interferometer (WSI) shall be used, which co-rotates with the outer sphere. As minimum field of view, an angular region of 80° between the north pole and the equator is required. To enable measurements of the density gradient in two perpendicular directions simultaneously, the illuminated flow shall be recorded with two cameras each outfitted with a dedicated Wollaston prism. The cameras should have a minimum image acquisition frequency of 1 fps (exposure time $1/500$ s), a minimum image dynamic range of 8 Bit grayscale and a minimum optical resolution of 1024×1024 px, which leads to 10 px per fringe in the interferograms.

The triggering of the cameras will be synchronized with the inner sphere, which therefore would require an image acquisition frequency higher than 1 fps. As the cameras are co-rotating with the outer sphere, markers are required on the inner sphere within the field of view, to determine the relative position of the inner and outer sphere in the recorded images. This allows to track and measure convective structures in post processing tools.

The illumination of the flow shall be realized by a laser light source, whose intensity will be variable by command uplink and whose wavelength has to be optimized for use with the materials in the optical path. A possible solution is a wavelength of 532 nm. Further, the Wollaston prisms will allow to record two interferograms simultaneously. The sensitivity of the interferometer strongly depends on the temperature gradient inside the field of view and has to be determined within ground experiments, see Section “Laboratory Experiments”.

Experimental Runs and Data Handling

To capture the whole parameter space, experimental points are defined. They can be divided into one non-rotating scenario, three rotation scenarios (15 values solid body rotation, 10 values differential rotation at low rotation, 10 values differential rotation at high rotation) and by 20 different electric Rayleigh numbers Ra_E . In total, 12

experimental runs are defined which account for 720 experimental points. Each run has a duration of 60 min which results in $1024^2 \times 1\text{byte} \times 1\text{fps} \times 3600\text{s} \times 720\text{EP} = 2.7\text{TB}$ of image data. The amount of telemetry data is low compared to images and does not contribute much to the total amount of data.

Temperature Measurement

In the AtmoFlow experiment, temperature measurements are needed to monitor the thermal boundary conditions. Therefore, the temperature has to be recorded near the poles of the outer sphere, near the equator of the inner sphere and in the southern or northern half sphere of the cooling liquid volume outside the field of view of the optical diagnostics. In the latter case, three sensors at $\theta = 22.5^\circ$, $\theta = 45^\circ$ and $\theta = 67.5^\circ$ are sufficient. In addition, the temperature is monitored in the outflow region of the cooling liquid volume. The installed temperature sensors will have a temperature range of 283 K – 353 K, an accuracy of 0.2 K (poles and equator), 0.5 K (north or south hemisphere) and a frequency of 1 Hz.

Velocity Measurement

Common techniques to measure fluid velocities are digital holographic velocimeter (Prodi et al. 2006), Particle Image Velocimetry (Meier et al. 2018) and Laser Doppler Anemometry. However, particles for these methods need special treatment or would require the involvement of astronautical staff members. Furthermore, difficulties in connection with tracer based diagnostics in a high voltage environment are assumed. In summary, no direct velocity measurements will be performed. The velocity field will be reconstructed by comparing interferograms with numerical simulations. This has been performed successfully for GeoFlow II as demonstrated in Zaussinger et al. (2018b).

Acceleration Measurement

Long time scale and diffusion driven experiments under microgravity conditions depend on the g-jitter. Trajectories show loops and can cause trembling, see e.g. Shevtsova et al. (2004). To capture these uncertainties acceleration measurements are required. The ISS provides two systems, the Space Acceleration Measurement System II (SAMS-II) and the Microgravity Acceleration Measurement System (MAMS), see e.g. Jules et al. (2004) and Rice et al. (1999), respectively. However, to capture acceleration events near the payload these measurements will be done independently from the mentioned accelerometers near by the experiment in three directions with an accuracy of $10^{-5} g_0$ and an

acquisition rate with at least doubled image acquisition frame rate. Hereby, a frequency range of 5 to 100 Hz is covered. The acceleration amplitude is averaged over a duration of one second. The quality of microgravity shall be better than $10^{-3} g_0$ during the collection of the science data at all experimental data points.

Laboratory Experiments

Within the AtmoFlow project, a laboratory experiment is planned in the so-called ‘baroclinic wave tank’ facility at the BTU Cottbus-Senftenberg, which can give reasonable results for the flow in the mid-latitudes of a spherical shell (Vincze et al. 2015). Thereby, basic flow phenomena like the baroclinic instability can be analyzed on Earth. While the space experiments are restricted to the use of the Wollaston Shearing Interferometry (WSI), in the wave tank setup, we can combine the WSI technique together with Infrared-thermography (IR). Accordingly, the aim of the experiments in the baroclinic wave tank is to characterize specific interference pattern in the parameter space of the AtmoFlow project. Especially interferograms of waves are in the focus of this experiment. So far, only convective patterns like sheet-like upwellings or steep downdrafts can be identified clearly in the with Wollaston shearing interferometry, Zaussinger et al. (2017). The baroclinic wave tank gives the possibility to develop post-processing routines which can be used to identify waves and related wave numbers. Furthermore, interferograms depicting the interaction of convection and waves can be identified clearly using further imaging methods. The tank will also be used to calibrate the interferometry unit for AtmoFlow. Interferograms of the GeoFlow experiment showed many artifacts, which increased the post-processing. Testing the interferometry unit on the baroclinic wave tank will reduce the risk of interferograms with reduced quality.

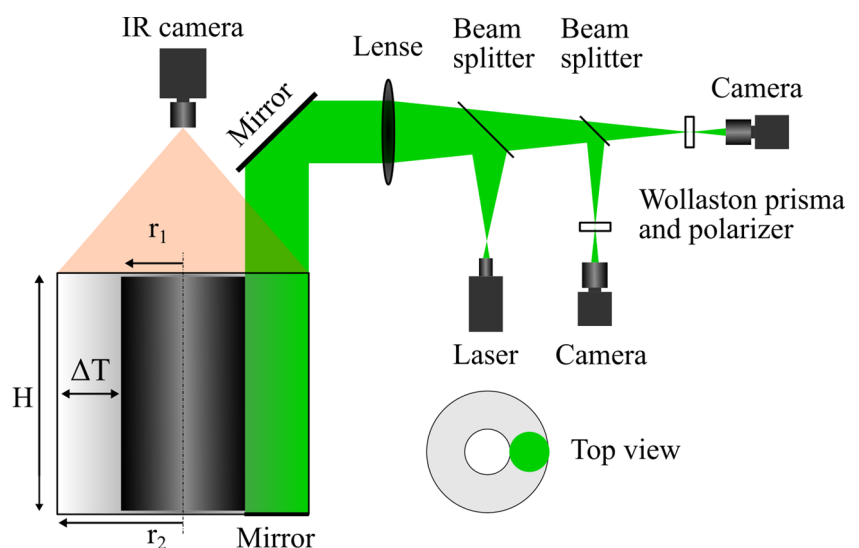
Table 2 Geometrical and experimental parameters of the baroclinic wave tank experiment

parameter	symbol	unit	value
radius inner cylinder	R_{1c}	m	0.45
radius outer cylinder	R_{2c}	m	0.12
fluid height	H	m	0.135
angular velocity	Ω	rpm	0.1-30

A database of common flow patterns consisting of IR images, interferograms and numerical simulations is planned. This database will be the basis for the post-processing phase of AtmoFlow, where machine learning algorithms are trained on reference patterns. Furthermore, an algorithm will be developed to reconstruct the average temperature field from the interference images by use of the additional IR data. The proposed ground experiment is depicted in Fig. 5.

The baroclinic wave tank consists of two concentric cylinders, which are mounted on a rotation table. The measurement gap between the cylinders is filled with distilled water, which has comparable Prandtl number of the AtmoFlow working fluid 3M™ Novec™ 7200. The inner cylinder is made of anodized aluminum and the outer one of borosilicate glass. While the bottom end of the experiment is enclosed by an opaque end plate, the top side has a free surface. The outer cylinder is surrounded by a second borosilicate glass cylinder, which is filled with distilled water and equipped with heating coils. Thus, the outer cylinder can be heated. Further, the inner cylinder features cooling channels and is cooled via a thermostat. Therefore, a radial temperature gradient adjusts with an accuracy of ± 0.1 K/m. The angular velocity of the rotation table as well as the temperatures of the cylinders are controlled by LabView®. The geometrical parameters of the baroclinic wave tank are summarized in Table 2. To enable

Fig. 5 Sketch of the g_0 experiment ‘baroclinic wave tank’ and the planned set up of the measurement technique, which is considered in the AtmoFlow experiment



simultaneous measurements of WSI and IR thermography, the experiment is revised. The upper end of the experimental gap is enclosed by an IR transparent top plate, to prevent possible surface waves, which would distort the interference images. Furthermore, the IR camera as well as the WSI components are mounted with a stiff connection to the turn table of the experiment in order to measure in a co-rotating frame. Data and power supply connections are realized by means of a slip ring.

The WSI set up consists of a laser beam ($\lambda = 532$ nm), which is expanded to cover a circular area of 80 mm^2 , and enters into the measurement gap through the top plate. At the bottom of the experiment the laser beam is reflected and split into two beams. These two light beams are captured by two cameras, each equipped with orthogonal oriented Wollaston prisms and a polarizer. The Wollaston prisms cause an interference of light rays, separated by the distance e . The focal length f of the lens collimating the light beam at the prism and the separation angle of the prism α define the ray distance $f \tan \alpha$. The light intensity distribution I of the interference images is a function of the local gradient of refractive index n in the direction s of the Wollaston prism orientation which is strongly temperature dependent. The intensity variations in s -direction are obtained by

$$\frac{\Delta I}{I} = \cos \left(\frac{2\pi e}{\lambda} \frac{\partial n}{\partial s} \right). \quad (3)$$

In the following, we demonstrate the reconstruction of the temperature field by the usage of two perpendicular WSI

units. This example is based on a temperature measurement of the baroclinic wave tank with a gap width of 0.1 m, at 214 rpm and a temperature difference of 9 K between the inner and outer shell, see Fig. 6. Numerical interferograms are calculated by Eq. 3 for the x -direction and the y -direction, see Fig. 6a and b, respectively. Combining both interferograms reveals the global structures as found in the temperature field, see Fig. 6c, d. The same approach is considered for the AtmoFlow experiment, where two interferograms will be captured simultaneously.

Thermo-Electro Hydrodynamics

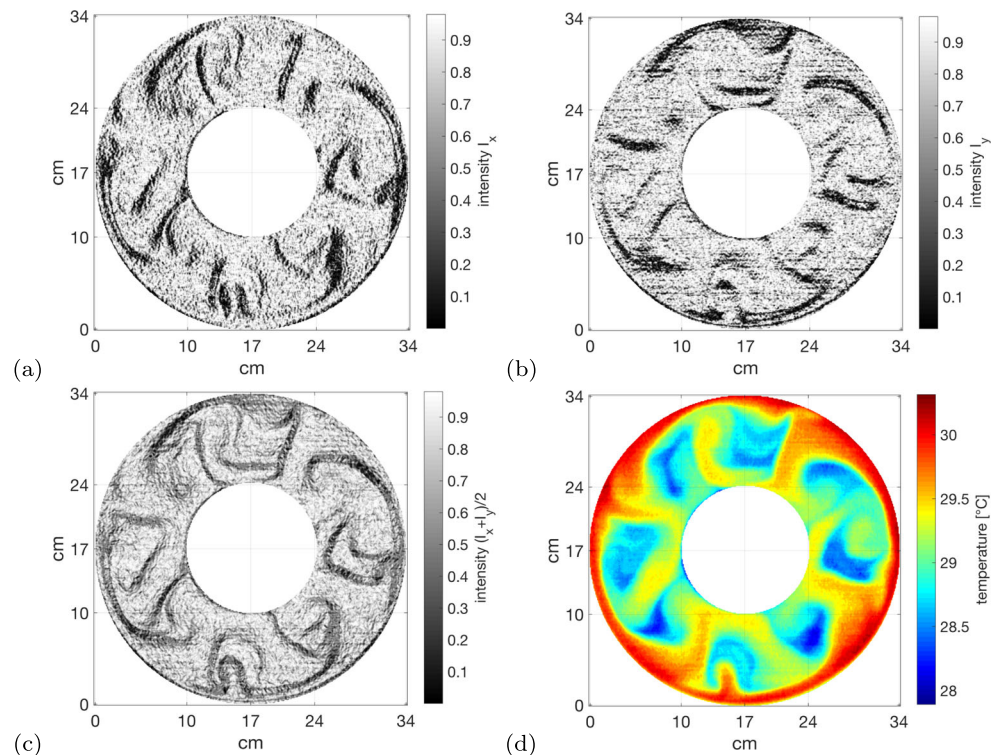
Dielectrophoretic Effect

The force \mathbf{F} of the electric field exerting on the fluid is given by the Coulomb force \mathbf{F}_C , the electro-strictive force \mathbf{F}_{ES} and the dielectrophoretic force \mathbf{F}_{DEP} ,

$$\mathbf{F} = \underbrace{\rho \nabla \mathbf{E}}_{\mathbf{F}_C} + \underbrace{\nabla \left[\frac{1}{2} \rho \left(\frac{\partial \epsilon}{\partial \rho} \right)_T \mathbf{E}^2 \right]}_{\mathbf{F}_{ES}} - \underbrace{\frac{1}{2} \mathbf{E}^2 \nabla \epsilon}_{\mathbf{F}_{DEP}}. \quad (4)$$

The working fluid 3MTM NovecTM 7200 does not carry free charges, resulting in $\mathbf{F}_C = 0$. Furthermore, the electro-strictive pressure force $\mathbf{F}_{ES} = \nabla p_{ES}$ does not contribute to the flow field in the incompressible formulation and is combined with the pressure, Castellanos (1998), Mutabazi

Fig. 6 Numerical interferograms calculated for the temperature distribution in a baroclinic wave tank in **a** the x -direction and **b** the y -direction. **c** combination of both interferograms, **d** experimental temperature distribution used for the calculations. Data provided by Früh (2018)



et al. (2016). The dielectrophoretic force of a spherical capacitor with hot inner shell and cold outer shell is mainly radial directed \mathbf{r} . Horizontal components are about five magnitudes smaller than the radial component and are neglected in the following. This enables a radial acceleration field called *electric gravity*,

$$\mathbf{g_E} = \frac{\alpha_E}{\rho_0 \alpha_T} \nabla \left(\frac{\epsilon_0 \epsilon_r \mathbf{E}^2}{2} \right). \tag{5}$$

For homogeneously thermalized boundaries (T_1 inner shell, T_2 outer shell) it has (or assumes) its maximum $|\mathbf{g_E}| = 3.82 \text{ m/s}^2$ for $U_{\text{rms}} = 5 \text{ kV}$ at the inner shell and its minimum $|\mathbf{g_E}| = 0.15 \text{ m/s}^2$ for $U_{\text{rms}} = 1.0 \text{ kV}$ at the outer shell, respectively, see Fig. 7a. The magnitude of the acceleration $\mathbf{g_E}$ depends on the electric properties of the fluid and the geometry. The direction of the electric gravity is mainly determined by the gradient in the temperature dependent electric permittivity $\epsilon = \epsilon_0 \epsilon_r$, where ϵ_0 is the vacuum permittivity and ϵ_r is the relative permittivity $\epsilon_r(T) = A \cdot T^2 + B \cdot T + C$ and $A = 7.1429 \times 10^{-4}$, $B = -5.1103 \times 10^{-1}$ and $C = 9.7467 \times 10^2$. This function is a second order polynomial approximation to a measurement provided by Airbus Defense and Space. The electric expansion coefficient α_E and the thermal expansion coefficient α_T are available by measurements, too. The direction of the electric gravity coincides with the temperature gradient in the defined temperature regime.

Microgravity conditions are required due to the low acceleration at the outer shell, which is much lower than the Earth’s gravity. The corresponding *electric Rayleigh number* is obtained by,

$$\text{Ra}_E = \frac{\alpha_T g_E \Delta T d^3}{\nu \kappa T}. \tag{6}$$

where $\Delta T = (T_{\text{ref}} - T_{\text{min}})/2$ and $d = R_2 - R_1$. This Rayleigh number is defined for $R_1 = 0.0189 \text{ m}$ at constant equatorial temperature of $T_{\text{ref}} = 313 \text{ K}$. It covers about three magnitudes, $2.47 \times 10^3 < \text{Ra}_E <$

6.17×10^6 , see Fig. 7b. All transitions between conductive, laminar and turbulent flows are observed in this parameter range. Additionally, the parameter range is accessible by accompanying direct numerical simulations.

Furthermore, two dimensionless numbers corresponding to rotation are introduced. The Taylor number,

$$\text{Ta} = \left(\frac{2\Omega d^2}{\nu} \right)^2 \tag{7}$$

ranges between $2 \times 10^1 < \text{Ta} < 2 \times 10^7$, see Fig. 8a. The Rossby number is a dimensionless number parameterizing differential rotation,

$$\text{Ro} = \frac{\Omega_1 - \Omega_2}{\Omega_2} \tag{8}$$

and ranges between $-3.59 < \text{Ro} < 3.59$, see Fig. 8b.

Dielectric Heating

Dielectric heating plays a crucial role for the fluid flow which is under the influence of an a.c. electric field. The microwave stove is based on this physical process causing water molecules to rotate and releasing heat at a frequency of 2.45 GHz. The same situation occurs for the polar working fluid 3M™ Novec™ 7200. The heating as function of the electric field strength is higher at the inner shell than at the outer shell. It scales with the square of the electric field strength and linearly with the frequency of the electric field, see e.g. Zaussinger et al. (2018b). The rate of dielectric heating S_{DH} [K/s] is obtained by,

$$S_{\text{DH}} = \frac{2\pi f_{\text{HV}} \epsilon_0 \epsilon' \tan \delta |\mathbf{E}|^2}{\rho C_p}. \tag{9}$$

where ϵ' is the real part of the relative permittivity and $\tan \delta$ is the dielectric loss rate. Both values are obtained by measurements. In the following, we show the impact of dielectric heating on the temperature distribution in the case where the boundaries are kept isothermally (Fig. 9a), for an

Fig. 7 **a** electric gravity g_E as function of high voltage at the inner shell and out shell, respectively. **b** electric Rayleigh number Ra_E as function of temperature difference

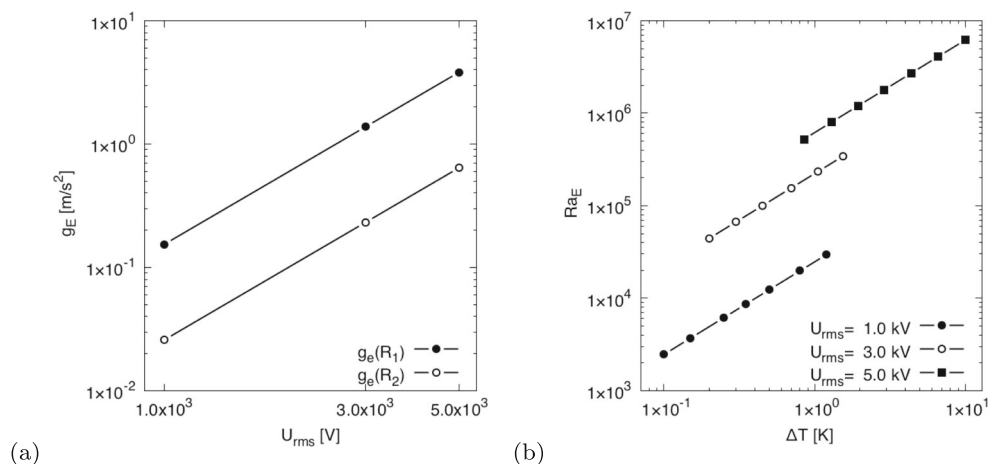
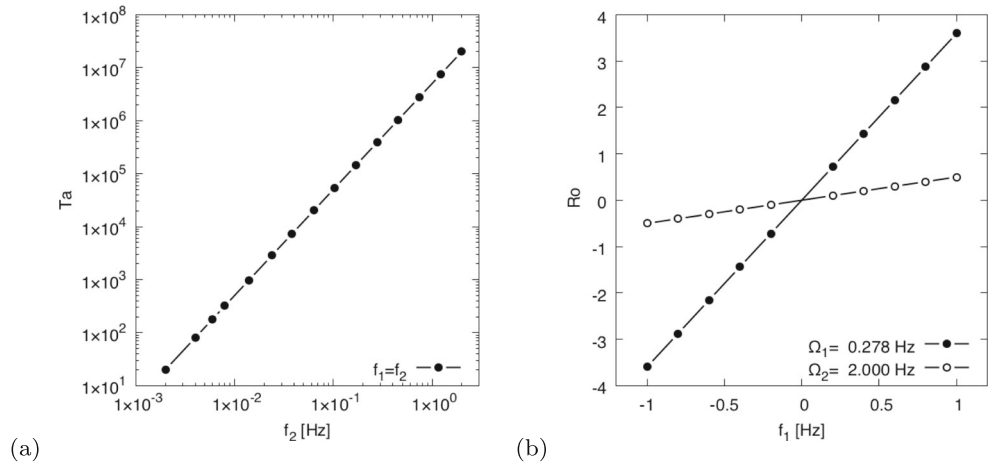


Fig. 8 **a** Taylor number Ta as function of inner shell rotation rate Ω_2 . **b** Rossby number Ro as function of the rotation rates Ω_1 and Ω_2



applied temperature contrast (Fig. 9b) of $\Delta T = 10$ K and various high voltages U_{rms} . The temperature profile in the stationary case can be described by a parabola shape, where the peak value is in the bulk and not at the boundaries. The parabola profile of the temperature distribution reaches its final shape within one thermal time scale ($\tau = 1713$ sec). It is found that the peak value is stationary as depicted in Fig. 10 for various voltages. The boiling point of the working fluid is 349 K. This allows a maximum difference between the reference temperature and the maximum of the temperature due to dielectric heating of $|\Delta T - \Delta T_{ref}| = |249 - 313| = 36$ K. The highest temperature found with dielectric heating is $|T - T_{ref}| = 29$ K for $U_{rms} = 5.0$ kV. This is seven degrees lower than the boiling temperature. In case of isothermally heated boundaries the maximum temperature due to dielectric heating is about 20 degrees below the boiling point. Based on these calculations it is

considered to limit the voltage to $U_{rms} = 5000$ V and the frequency to $f \leq 10^4$ Hz.

Numerical Simulations

Accompanying numerical simulations are performed for the AtmoFlow experiment. They are used to reconstruct the velocity field, which is not accessible by measurement techniques used in AtmoFlow. The reconstruction is based on a comparison of experimental and numerical interferograms. Matching structures in both interferograms correlate with similar temperature and velocity fields. Based on this assumption, the three-dimensional fluid flow gets accessible. However, drift velocities of convective structures are used to support the comparison. Drift rates are calculated directly from interferograms by identifying markers and

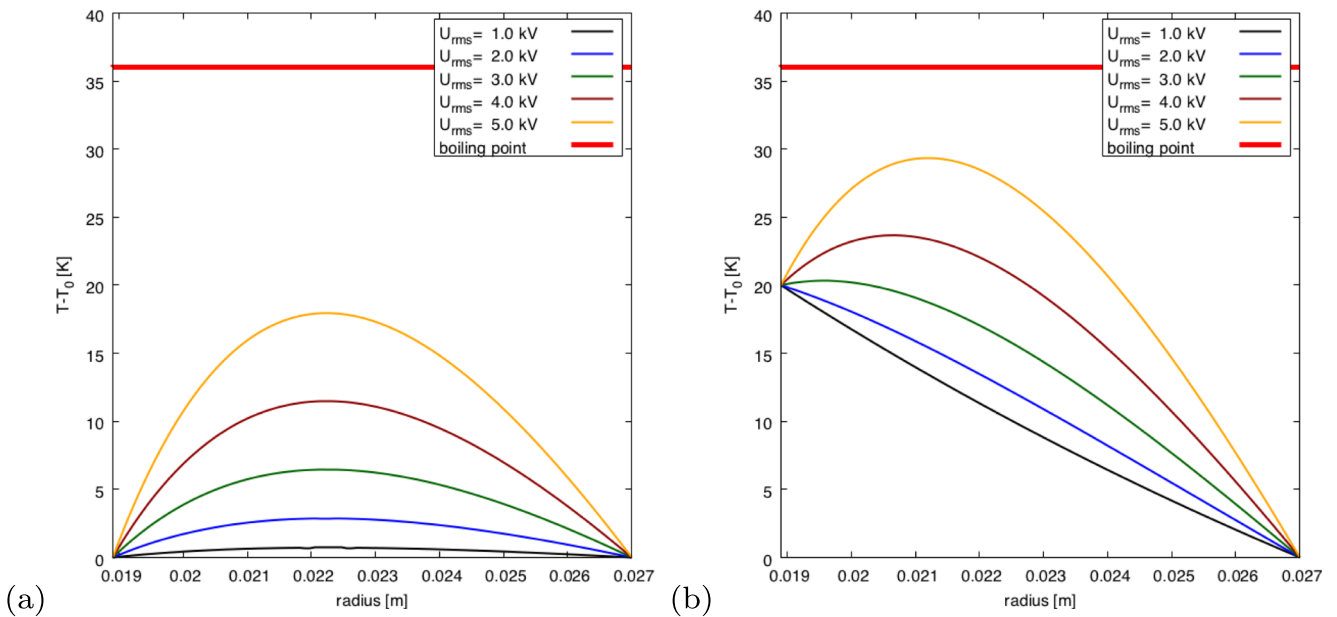
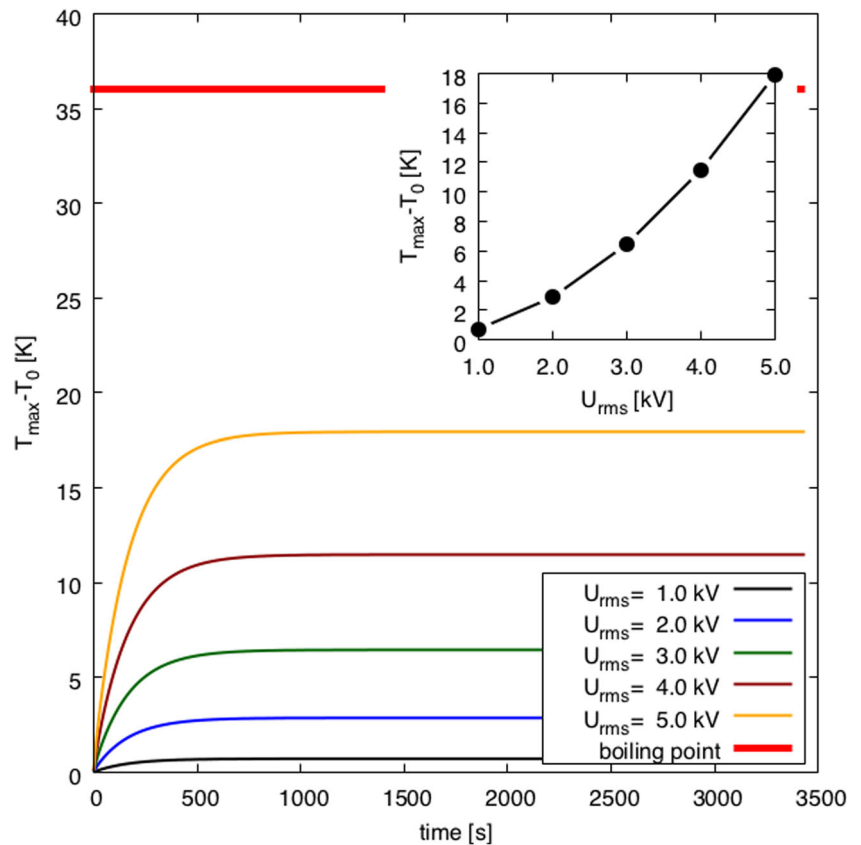


Fig. 9 Conductive thermal distribution in the spherical gap under the influence of dielectric heating for $f_{HV} = 10.000$ Hz and $T_{ref} = 313$ K for the case of **a** an iso-thermal case and **b** a temperature contrast of 20K between the inner and the outer shell

Fig. 10 Temporal evolution of the thermal peak value T_{\max} near the middle of the gap for $f_{\text{HV}} = 10.000$ Hz and $T_0 = 313$ K. (inlet) temperature peak T_{\max} as function of voltage



slowly moving convection cells. They have to be identical in the numerical simulations and in the experiment. In principle, the parameter range of AtmoFlow can be captured by direct numerical simulations. However, they cannot replace the experiment. This is based on the thermo-EHD model, which has still many open questions, Mutabazi et al. (2016). It is e.g. unclear if the Boussinesq approximation is valid for dielectrophoretic driven convection, when temperature differences exceed 3 K. Additionally, dielectric heating has been identified as important term in the model, which is under active research. AtmoFlow shall be used as validator for physical models of EHD regarding convection and internal heating. The governing equations are based on the EHD model presented in Section “Thermo-Electro Hydrodynamics” and the conservation equations of fluid mechanics (Platten and Legros 2012). A comprehensive

Here, \mathbf{u} is the velocity field, Ω is the angular velocity vector, \mathbf{r} is the position vector, p is the pressure, $\bar{\sigma}$ is the viscous stress tensor, $\rho = \rho(T)$, ρ_0 is the reference density, \mathbf{F}_{DEP} is the dielectrophoretic force, T is the temperature, κ_T is the thermal diffusion coefficient, S_{DH} is the dielectric heating term and ϵ is the permittivity. Fluid properties are provided in tabulated form. The electric field is expressed in terms of the scalar potential ϕ , where $\phi(R_1) = 0$ and $\phi(R_2) = U_{\text{rms}}$. This relation results in a non-linear Helmholtz equation which is solved iteratively in each numerical time step,

$$\nabla \cdot (\epsilon(T)\nabla\phi(T)) = 0 \tag{16}$$

The governing equations are solved numerically with the finite volume method (FVM) using the open source software suite OpenFOAM, Weller et al. (1998). A cubed spherical grid with 4×10^6 cells is used for all simulations, where the radial resolution is 60 cells. The velocity boundary conditions are kept no-slip. The thermal boundaries are of Dirichlet type, according Eq. 2. The code solves the governing equations dimensionally in 3D with the PIMPLE algorithm. This algorithm is based on the SIMPLE approach for the solution of incompressible flows, but iterates the pressure loop several times to increase the precision of the solution. The time integration is performed with an implicit Crank-Nicolson method, the space derivatives are approximated in

$$\nabla \cdot \mathbf{u} = 0 \tag{10}$$

$$\rho_0 \frac{\partial \mathbf{u}}{\partial t} + (\mathbf{u} \cdot \nabla)\mathbf{u} = -\nabla p + \nabla \cdot \bar{\sigma} - 2\rho_0\Omega \times \mathbf{u} - \rho(T)\Omega \times (\Omega \times \mathbf{r}) + \rho\mathbf{F}_{\text{DEP}} \tag{11}$$

$$\frac{\partial T}{\partial t} + (\mathbf{u} \cdot \nabla)T = \kappa_T \nabla^2 T + S_{\text{DH}} \tag{12}$$

$$\nabla \cdot (\epsilon(T)\nabla\phi) = 0 \tag{13}$$

$$\nabla\phi = \mathbf{E} \tag{14}$$

$$\nabla \times \mathbf{E} = 0. \tag{15}$$

second order. Turbulent cases in the high Rayleigh number regime are modeled with the one-equation turbulence model ‘dynamic-k’. The accuracy of the results is guaranteed by the velocity residual of $< 10^{-6}$. We refer to Zaussinger et al. (2018b) for a detailed description of the numerical setup. The main numerical study consists of 72 numerical simulations which are located in the $Ra_E - Ta - Ro$ parameter space. In the following, three representative simulations with a temperature difference of 20 K between the equator and the poles are presented. The high voltage is set to $U_{rms} = 2800$ V in all cases. Additionally, all fluid properties are interpolated from the fluid’s data sheet and temperature dependent. Here, the maximum electric gravity $g_E = 1.2$ m/s² is found at the inner sphere and the minimum $g_E = 0.2$ m/s² at the outer sphere. The corresponding Rayleigh number is $Ra_E = 1.9 \times 10^6$. Rotation is applied in the solid-body rotation case with a rate of $\Omega_1 = \Omega_2 = 0.8$ Hz. In case of differential rotation the inner shell rotates with $\Omega_1 = 0.88$ Hz and the outer shell with $\Omega_2 = 0.8$ Hz, respectively. This results in $Ta = 3.2 \times 10^6$ and $Ro = 0.1$. Hammer-Aitoff projections are calculated using the interpolation program TOMS661 (Renka 1988). Hereby, the Cartesian grid of OpenFOAM is interpolated onto a grid in spherical coordinates with the same amount of data points. For reasons of visibility the temperature and radial velocity are averaged along the radius. The artificial interferograms are calculated by superimposing two orthogonal interferograms, one in

x-direction and one in the z-axis, respectively. The intensity I of the interferograms is calculated according Eq. 3 with fluid properties of the working fluid and specifications of the optical path which have been used for GeoFlow.

Non-Rotating Case

The non-rotation case is depicted in Fig. 11. Besides the equatorial up-welling region and the polar down-welling plumes, the overall temperature field is dominated by small, local plumes. These plumes are spread in a band-like structure along the latitudes. The Hammer-Aitoff projection Fig. 11a and especially the thermal contour lines of the radially averaged temperature highlight this global cell formation. Interestingly, the numerical interferogram in Fig. 11b shows these plumes as aligned ‘string of pearls’ structure. A closer look on the velocity field (not depicted) shows many small vortices spread irregularly over both hemispheres. The only up-welling region is found around the equator. This results in a well mixed temperature field with low gradients.

Solid Body Rotation Case

Figure 12 depicts a representative solid body rotation case. This case reveals new fluid structures, which are based on rotational effects. The overall temperature distribution is

Fig. 11 Numerical simulations of the non-rotation case at time stamp $t=5650$ sec for $Ra_E = 1.9 \times 10^6$: **a** radially averaged temperature field as Hammer-Aitoff projection, **b** superposition of two orthogonal artificial interferograms

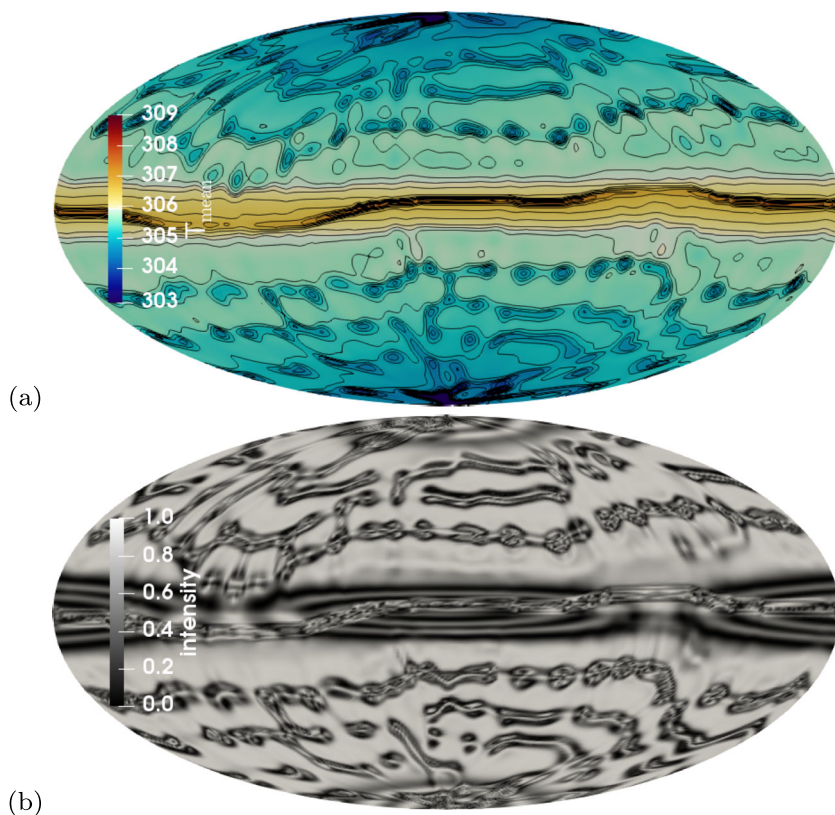


Fig. 12 Numerical simulations of the solid body rotation case at time stamp $t = 2180$ sec for $Ra_E = 1.9 \times 10^6$ and $Ta = 3.2 \times 10^6$: **a** radially averaged temperature field as Hammer-Aitoff projection, **b** superposition of two orthogonal artificial interferograms

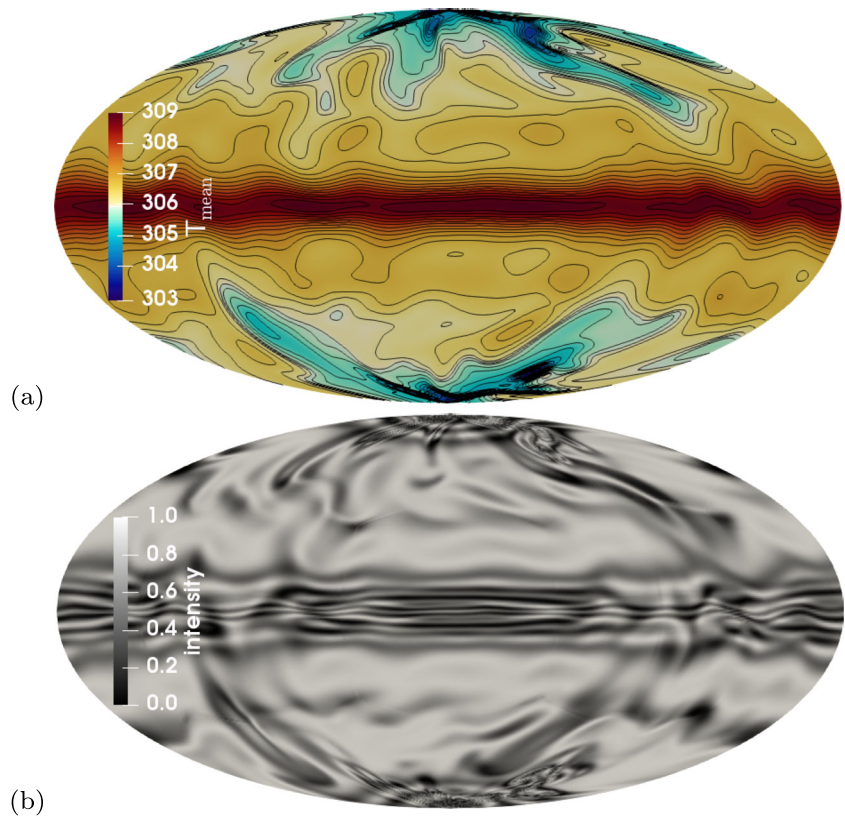
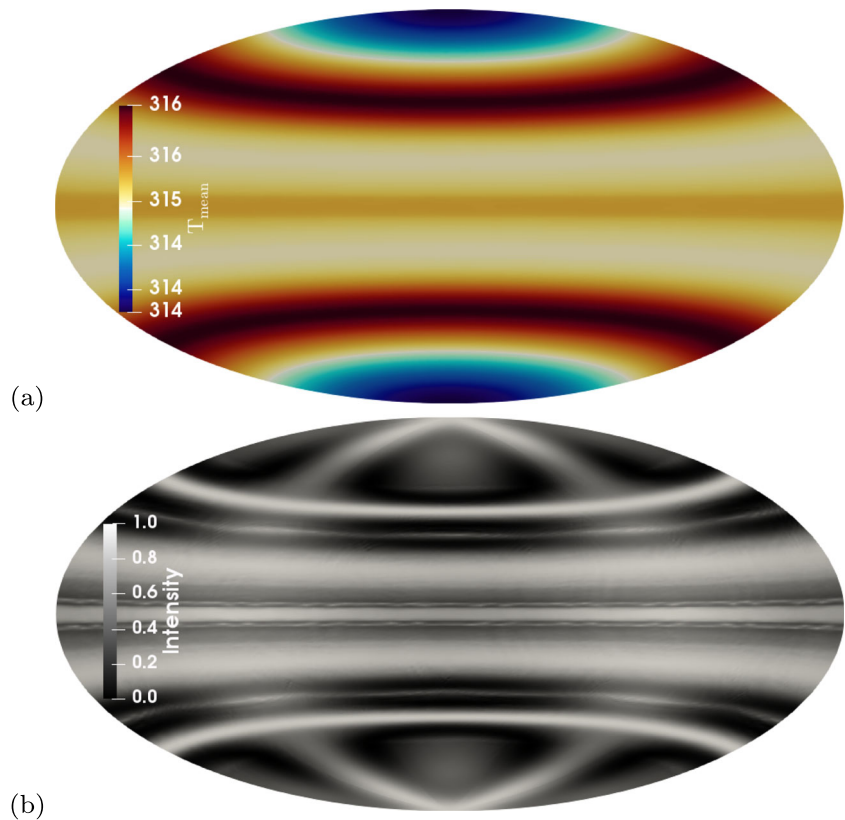


Fig. 13 Numerical simulations of the differential rotation case at time stamp $t=420$ sec for $Ra_E = 1.9 \times 10^4$, $Ta = 3.8 \times 10^5$ and $Ro = 0.72$: **a** radially averaged temperature field as Hammer-Aitoff projection, **b** superposition of two orthogonal artificial interferograms



dominated by broad up-welling and down-welling regions at the equator and the poles, respectively. However, in contrast to the non-rotating case only a few large vortices are visible. Local plumes are not found, except in the polar region. The equatorial region reveals a dominant planetary wave with mode $m = 9$. This wave is visible in the velocity field, the Hammer-Aitoff projection and in the interferogram, too. Hence, this specific simulation can be used as benchmark test for the comparison between the numerical model and the experiment. The poles are characterized by cold fronts reaching deep into the mid-latitudes. These 'fingers' are not symmetrically arranged over both hemispheres, which emphasize the time-dependent and turbulent character of this fluid flow. The interferogram shown in Fig. 12b reveals all mentioned flow structures. Concentric rings at the poles indicate the polar plumes and cold fronts are clearly visible as fringes, too. The equatorial wave can be identified clearly in distorted fringes.

Differential Rotation Case

Figure 13 depicts the case when the inner shell rotates 40% faster than the outer shell. For inner shell rotation $f_1 = 0.278$ Hz and outer shell rotation $f_2 = 0.2$ Hz the Rossby number is $Ro = 0.72$. The temperature difference of $\Delta T = 0.2$ K and the low voltage if $V_{rms} = 2800$ V results in an electric Rayleigh number of $Ra_E = 19400$. Small temperature difference across the gap and low Taylor/Rossby numbers originate in band-like structures and zonal flows as known from gas giants. This specific structure is based on dielectric heating (see temperature legend in Fig. 13a) which dominates the thermal distribution in the bulk. Strong convective flows, aligned with the rotation axis result from the internal heating process. Boundary driven convection is secondary and does not contribute much. The meridional velocity field shows two global thermal plumes in each hemisphere. Furthermore, the interferogram depicted in Fig. 13b reveals these cells. One broad belt in the tropics and one narrow belt in the mid-latitudes.

Conclusions and Outlook

In summary, this paper gives an overview of the current status of the AtmoFlow experiment development. AtmoFlow has been planned for long-term investigation of thermal convection in rotating spherical shells under the influence of a central force field with complex boundary conditions. This setup represents a simplified deep atmosphere as found in giant planets. Microgravity conditions e.g. on the ISS are needed to overcome superpositions of the Earth's gravity and the radial acceleration by the dielectrophoretic

effect. The experiment consists of three main parts: a) two concentric spherical shells filled with the test liquid and thermalized by atmospheric like boundary conditions. b) a rotation tray with two perpendicular co-rotating visualization units, and c) high voltage supply for the radial force field. The payload will be designed for accommodation in the European Drawer Rack Mk II.

Based on the presented parameter space and test matrix, it is intended to investigate approximately 720 individual experiment data points during the scientific test campaign. The data generated from the experiment will be exploited for the following scientific purposes which are related to meteorology, geophysics, astrophysics and engineering:

- The stability of the basic flow states and its transitions with and without rotation
- Interaction of free convection and global wave modes.
- The characteristics of the convective flows and in particular their symmetries.
- Atmospheric cell formation as function of rotation and temperature.
- The critical Rayleigh numbers and wave numbers, which denote linear stability and marks the onset of thermal convection.
- The stability diagram for the different flow states.

The development of AtmoFlow is accompanied by a laboratory experiment and numerical simulations. The baroclinic wave tank experiment is used to evaluate the double interferometry unit and to create a reference database with patterns as they are found in convective fluid flows. Numerical simulations are needed to reconstruct the velocity field, which is not directly accessible by the experiment. Hereby, experimental and numerical interferograms are compared automatically in the post-processing phase of the mission. Stability analysis helps to expound the parameter space, especially the critical dimensionless parameters as the Rayleigh number, the Taylor number or the Rossby number.

Understanding and controlling fluid flow in a spherical geometry under the influence of rotation will be useful in a variety of engineering applications, such as improving spherical gyroscopes, bearings, and centrifugal pumps. Furthermore, study of effects related to the electro-hydrodynamic force, which serves to simulate the central gravity field, will find applications in high-performance heat exchangers, and in the study of electroviscous phenomena e.g. dielectric heating. Even though fluid properties, geometry and boundary conditions differ in industrial applications, the AtmoFlow experiment may provide useful fundamental research in the dynamics of rotating thermo-EHD devices. It will help to understand the motion of liquids in industrial applications, where e.g. injected ions are a source of charge, e.g. in

EHD-pumps, EHD nozzles, electrostatic precipitators or ion-drag pumps. In summary, it is expected that this experiment will deliver results in fluid mechanics, engineering, geophysics, astrophysics, meteorology and fluid transport.

The AtmoFlow experiment payload is currently in development for operation on the ISS.

Acknowledgments The AtmoFlow project is funded by DLR Space Administration under contract numbers 50WP1709 and 50WP1809. The GeoFlow research has been funded by the ESA grants AO-99-049, by the DLR grants 50 WM 0122, 50 WM 0822, 50WM1644 and by the SOKRATES / ERASMUS- program LIA-ISTROF (CNRS-cooperation). Furthermore the authors thank the GeoFlow Topical Team (ESA 18950/05/NL/VJ) for intensive discussions. All simulations have been performed at the Northern German Network for High-Performance Computing (HLRN) and the Heraklit cluster (BTU Cottbus-Senftenberg).

Contents of this manuscript have been presented at the 69th International Astronautical Congress, 01–05 October 2018, Bremen, Germany, www.iafastro.org. We refer to the conference proceedings (Zaussinger et al. 2018a) and Canfield et al. (2018).

Compliance with Ethical Standards

Conflict of interests The authors declare that they have no conflict of interest.

References

- Beltrame, P., Egbers, C., Hollerbach, R.: The geoflow-experiment on {ISS} (part iii): Bifurcation analysis. *Adv. Space Res.* **32**(2), 191–197 (2003). [https://doi.org/10.1016/S0273-1177\(03\)90250-X](https://doi.org/10.1016/S0273-1177(03)90250-X). <http://www.sciencedirect.com/science/article/pii/S027311770390250X>, gravitational Effects in Physico-Chemical Processes
- Borcia, I.D., Harlander, U.: Inertial waves in a rotating annulus with inclined inner cylinder: comparing the spectrum of wave attractor frequency bands and the eigenspectrum in the limit of zero inclination. *Theor. Comput. Fluid Dyn.* **27**(3), 397–413 (2013). <https://doi.org/10.1007/s00162-012-0278-6>
- Bronowicki, P., Canfield, P., Grah, A., Dreyer, M.: Free surfaces in open capillary channels—parallel plates. *Phys. Fluids* **27**(1) (2015)
- Busse, F.H., Carrigan, C.R.: Laboratory simulation of thermal convection in rotating planets and stars. *Science* **191**(4222), 81–83 (1976). <https://doi.org/10.1126/science.191.4222.81>. <http://science.sciencemag.org/content/191/4222/81>
- Canfield, P.: Stability of Free Surfaces in Single-Phase and Two-Phase Open Capillary Channel Flow in a Microgravity Environment. *Cuvillier Verlag, Göttingen* (2018)
- Canfield, P., Bronowicki, P., Chen, Y., Kiewidt, L., Grah, A., Klatte, J., Jenson, R., Blackmore, W., Weislogel, M., Dreyer, M.: The capillary channel flow experiments on the international space station: experiment set-up and first results. *Exp. Fluids* **54**(5), 1519 (2013)
- Canfield, P., Zaussinger, F., Egbers, C., Heintzmann, P.: AtmoFlow - simulating atmospheric flows on the international space station. Part I: experiment and ISS-implementation concept. In: 69th IAC Conference Proceedings, International Astronautical Federation, Vol 18.A2.6.15-69 (2018)
- Castellanos, A.: *Electrohydrodynamics, vol CISM courses and lectures-380*. Springer-Verlag, Wien GmbH (1998)
- Chan, S.C., Nigam, S.: Residual diagnosis of diabatic heating from era-40 and ncep reanalyses: Intercomparisons with trmm. *J. Climate* **22**(2), 414–428 (2009). <https://doi.org/10.1175/2008JCLI2417.1>
- Christensen, U.R.: Zonal flow driven by deep convection in the major planets. *Geophys. Res. Lett.* **28**(13), 2553–2556 (2001). <https://doi.org/10.1029/2000GL012643>
- Conrath, M., Canfield, P., Bronowicki, P., Dreyer, M.E., Weislogel, M.M., Grah, A.: Capillary channel flow experiments aboard the international space station. *Phys. Rev. E* **88**(6), 063,009 (2013)
- Dietrich, W., Gastine, T., Wicht, J.: Reversal and amplification of zonal flows by boundary enforced thermal wind. *Icarus* **282**, 380–392 (2017). <https://doi.org/10.1016/j.icarus.2016.09.013>. <http://www.sciencedirect.com/science/article/pii/S0019103516305759>
- Dubois, F., Joannes, L., Dupont, O., Dewandel, J.L., Legros, J.C.: An integrated optical set-up for fluid-physics experiments under microgravity conditions. *Meas. Sci. Technol.* **10**(10), 934 (1999). <http://stacks.iop.org/0957-0233/10/i=10/a=314>
- Egbers, C., Brasch, W., Sitte, B., Immohr, J., Schmidt, J.R.: Estimates on diagnostic methods for investigations of thermal convection between spherical shells in space. *Meas. Sci. Technol.* **10**(10), 866–877 (1999). <https://doi.org/10.1088/0957-0233/10/10/306>
- Egbers, C., Beyer, W., Bonhage, A., Hollerbach, R., Beltrame, P.: The GeoFlow-experiment on ISS (part I): Experimental preparation and design of laboratory testing hardware. *Adv. Space Res.* **32**(2), 171–180 (2003). [https://doi.org/10.1016/S0273-1177\(03\)90248-1](https://doi.org/10.1016/S0273-1177(03)90248-1). <http://www.sciencedirect.com/science/article/pii/S0273117703902481>, gravitational effects in physico-chemical processes
- Evgenidis, S.P., Zacharias, K.A., Karapantsios, T.D., Kostoglou, M.: Effect of liquid properties on heat transfer from miniature heaters at different gravity conditions. *Microgravity Sci. Technol.* **23**(2), 123–128 (2011). <https://doi.org/10.1007/s12217-010-9206-9>
- Ezquerro Navarro, J.M., Fernández, J.J., Rodríguez, J., Laverón-Simavilla, A., Lapuerta, V.: Results and experiences from the execution of the geoflow experiments on the iss. *Microgravity Sci. Technol.* **27**(1), 61–74 (2015). <https://doi.org/10.1007/s12217-015-9413-5>
- Feudel, F., Tuckerman, L., Gellert, M., Seehafer, N.: Bifurcations of rotating waves in rotating spherical shell convection. *Phys. Rev. E* **92**(053015) (2015)
- Früh, W.G.: Turibase. https://turbase.cineca.it/init/routes/#/logging/view_dataset/14/tabfile (2018)
- Futterer, B., Gellert, M., von Larcher, T., Egbers, C.: Thermal convection in rotating spherical shells: an experimental and numerical approach within GeoFlow. *Acta Astronautica* **62**(4–5), 300–307 (2008). <https://doi.org/10.1016/j.actaastro.2007.11.006>. <http://www.sciencedirect.com/science/article/pii/S0094576507003013>
- Futterer, B., Krebs, A., Plesa, A.C., Zaussinger, F., Hollerbach, R., Breuer, D., Egbers, C.: Sheet-like and plume-like thermal flow in a spherical convection experiment performed under microgravity. *J. Fluid Mech.* **735**, 647–683 (2013). <https://doi.org/10.1017/jfm.2013.507>. <https://www.cambridge.org/core/article/div-class-title-sheet-like-and-plume-like-thermal-flow-in-a-spherical-convection-experiment-performed-under-microgravity-div/32CFFF7061E5F96C8153453826DCFF55>
- Futterer, B., Dahley, N., Egbers, C.: Thermal electro-hydrodynamic heat transfer augmentation in vertical annuli by the use of dielectrophoretic forces through a.c. electric field. *Int. J. Heat Mass Transf.* **93**, 144–154 (2016). <https://doi.org/10.1016/j.ijheatmasstransfer.2015.10.005>. <http://www.sciencedirect.com/science/article/pii/S0017931015010030>
- Gastine, T., Wicht, J., Aurnou, J.: Zonal flow regimes in rotating anelastic spherical shells: an application to giant planets. *Icarus* **225**(1), 156–172 (2013a). <https://doi.org/10.1016/j.icarus.2013.02.031>. <http://www.sciencedirect.com/science/article/pii/S001910351300119X>

- Gastine, T., Yadav, R.K., Morin, J., Reiners, A., Wicht, J.: From solar-like to antisolar differential rotation in cool stars. *Mon. Not. R. Astron. Soc. Lett.* **438**(1), L76–L80 (2013b). <https://doi.org/10.1093/mnrasl/slt162>
- Hart, J.E., Glatzmaier, G.A., Toomre, J.: Space-laboratory and numerical simulations of thermal convection in a rotating hemispherical shell with radial gravity. *J. Fluid Mech.* **173**, 519–544 (1986). <https://doi.org/10.1017/S0022112086001258>. <https://www.cambridge.org/core/article/div-class-title-space-laboratory-and-numerical-simulations-of-thermal-convection-in-a-rotating-hemispherical-shell-with-radial-gravity-div/E5DC65212D6332D9720933F64AC208D4>
- Heimpel, M., Aurnou, J., Wicht, J.: Simulation of equatorial and high-latitude jets on jupiter in a deep convection model. *Nature* **438**(7065), 193–196 (2005). <https://doi.org/10.1038/nature04208>
- Hollerbach, R., Wiener, R.J., Sullivan, I.S., Donnelly, R.J., Barenghi, C.F.: The flow around a torsionally oscillating sphere. *Phys. Fluids* **14**(12), 4192–4205 (2002). <https://doi.org/10.1063/1.1518029>
- Jehring, L., Egbers, C., Beltrame, P., Chossat, P., Feudel, F., Hollerbach, R., Mutabazi, I., Tuckerman, L.: Geoflow: First results from geophysical motivated experiments inside the fluid science laboratory of columbus. American Institute of Aeronautics and Astronautics, pp 1–15. AIAA 2009-960. <https://doi.org/10.2514/6.2009-960> (2009)
- Jenson, R.M., Wollman, A.P., Weislogel, M.M., Sharp, L., Green, R., Canfield, P.J., Klatte, J., Dreyer, M.E.: Passive phase separation of microgravity bubbly flows using conduit geometry. *Int. J. Multiphase Flow* **65**, 68–81 (2014)
- Jules, K., McPherson, K., Hrovat, K., Kelly, E.: Initial characterization of the microgravity environment of the international space station: increments 2 through 4. *Acta Astronaut.* **55**(10), 855–887 (2004). <https://doi.org/10.1016/j.actaastro.2004.04.008>. <http://www.sciencedirect.com/science/article/pii/S0094576504002061>
- Julien, K., Rubio, A.M., Grooms, I., Knobloch, E.: Statistical and physical balances in low rossby number Rayleigh–Bénard convection. *Geophys. Astrophys. Fluid Dyn.* **106**(4–5), 392–428 (2012). <https://doi.org/10.1080/03091929.2012.696109>
- Kelley, D.H., Triana, S.A., Zimmerman, D.S., Lathrop, D.P.: Selection of inertial modes in spherical couette flow. *Phys. Rev. E Stat. Nonlin. Soft. Matter. Phys.* **81**(2 Pt 2), 026,311 (2010). <https://doi.org/10.1103/PhysRevE.81.026311>
- Kuhl, R., Roth, M., Binnenbruck, H., Dreier, W., Forke, R., Preu, P.: The role of sounding rocket microgravity experiments within the german physical sciences programme. In: Warmbein, B. (ed.) 17th ESA Symposium on European Rocket and Balloon Programmes and Related Research, vol. 590, pp. 503–508. ESA Special Publication (2005)
- Liu, M., Egbers, C., Delgado, A., Rath, H.: Investigation of density driven large-scale ocean motion under microgravity. In: Rath, H.J. (ed.), p. 573?581. Springer, Berlin (1992)
- Lotto, M.A., Johnson, K.M., Nie, C.W., Klaus, D.M.: The impact of reduced gravity on free convective heat transfer from a finite, flat, vertical plate. *Microgravity Sci. Technol.* **29**(5), 371–379 (2017). <https://doi.org/10.1007/s12217-017-9555-8>
- Maeder, A.: On the Richardson criterion for shear instabilities in rotating stars. *Astron. Astrophys.* **299**, 84 (1995)
- Mamun, C.K., Tuckerman, L.S.: Asymmetry and hopf bifurcation in spherical couette flow. *Phys. Fluids* **7**(1), 80–91 (1995). <https://doi.org/10.1063/1.868730>
- Manneville, J.B., Olson, P.: Banded convection in rotating fluid spheres and the circulation of the Jovian atmosphere. *Icarus* **122**(2), 242–250 (1996). <https://doi.org/10.1006/icar.1996.0123>. <http://www.sciencedirect.com/science/article/pii/S0019103596901232>
- Meier, M., Jongmanns, M., Meyer, A., Seelig, T., Egbers, C., Mutabazi, I.: Flow pattern and heat transfer in a cylindrical annulus under 1 g and low-g conditions: Experiments. *Microgravity Sci. Technol.* **30**(5), 699–712 (2018). <https://doi.org/10.1007/s12217-018-9649-y>
- Meyer, A., Jongmanns, M., Meier, M., Egbers, C., Mutabazi, I.: Thermal convection in a cylindrical annulus under a combined effect of the radial and vertical gravity. *Comptes Rendus Mécanique* **345**(1), 11–20 (2017). <https://doi.org/10.1016/j.crme.2016.10.003>. <http://www.sciencedirect.com/science/article/pii/S1631072116301000>, basic and applied researches in microgravity – A tribute to Bernard Zappoli’s contribution
- Meyer, A., Crumeyrolle, O., Mutabazi, I., Meier, M., Jongmanns, M., Renoult, M.C., Seelig, T., Egbers, C.: Flow patterns and heat transfer in a cylindrical annulus under 1g and low-g conditions: Theory and simulation. *Microgravity Sci. Technol.* **30**(5), 653–662 (2018). <https://doi.org/10.1007/s12217-018-9636-3>
- Mutabazi, I., Yoshikawa, H.N., Fogaing, M.T., Travnikov, V., Crumeyrolle, O., Futterer, B., Egbers, C.: Thermo-electrohydrodynamic convection under microgravity: a review. *Fluid Dyn. Res.* **48**(6), 061,413 (2016). <http://stacks.iop.org/1873-7005/48/i=6/a=061413>
- Platten, J., Legros, J.: *Convection in Liquids*. Springer, Berlin (2012). <https://books.google.de/books?id=S8buCAAQBAJ>
- Prodi, F., Santachiara, G., Travaini, S., Vedernikov, A., Dubois, F., Minetti, C., Legros, J.: Measurements of phoretic velocities of aerosol particles in microgravity conditions. *Atmospheric Research* **82**(1), 183–189 (2006). <https://doi.org/10.1016/j.atmosres.2005.09.010>. <http://www.sciencedirect.com/science/article/pii/S0169809506000342>, 14th International Conference on Clouds and Precipitation
- Read, P.L., Yamazaki, Y.H., Lewis, S.R., Williams, P.D., Miki-Yamazaki, K., Sommeria, J., Didelle, H., Fincham, A.: Jupiter’s and saturn’s convectively driven banded jets in the laboratory. *Geophys. Res. Lett.* **31**(22). <https://doi.org/10.1029/2004GL020106> (2004)
- Renka, R.J.: Algorithm 660: Qshep2d: Quadratic shepard method for bivariate interpolation of scattered data. *ACM Trans. Math. Softw.* **14**(2), 149–150 (1988). <https://doi.org/10.1145/45054.356231>. <http://doi.acm.org/10.1145/45054.356231>
- Rice, J.E., Fox, J.C., Lange, W.G., Dietrich, R.W., Wagar, W.O.: Microgravity acceleration measurement system for the international space station (1999)
- Rieutord, M., Triana, S.A., Zimmerman, D.S., Lathrop, D.P.: Excitation of inertial modes in an experimental spherical couette flow. *Phys. Rev. E Stat. Nonlin. Soft. Matter. Phys.* **86**(2 Pt 2), 026,304 (2012). <https://doi.org/10.1103/PhysRevE.86.026304>
- Scolan, H., Read, P.L.: A rotating annulus driven by localized convective forcing: a new atmosphere-like experiment. *Exp. Fluids* **58** (6). <https://doi.org/10.1007/s00348-017-2347-5> (2017)
- Shevtsova, V.M., Melnikov, D.E., Legros, J.C.: The study of weak oscillatory flows in space experiments. *Microgravity Sci. Technol.* **15**(1), 49–61 (2004). <https://doi.org/10.1007/BF02870952>
- Smirnov, N.N., Nikitin, V.F., Ivashnyov, O.E., Maximenko, A., Thiercelin, M., Vedernikov, A., Scheid, B., Legros, J.C.: Microgravity investigations of instability and mixing flux in frontal displacement of fluids. *Microgravity Sci. Technol.* **15**(2), 35–51 (2004). <https://doi.org/10.1007/BF02870957>
- Travnikov, V., Egbers, C., Hollerbach, R.: The Geoflow-experiment on ISS (Part II): Numerical simulation. *Adv. Space Res.* **32**(2), 181–189 (2003). [https://doi.org/10.1016/S0273-1177\(03\)90249-3](https://doi.org/10.1016/S0273-1177(03)90249-3). <http://www.sciencedirect.com/science/article/pii/S0273117703902493>, gravitational Effects in Physico-Chemical Processes
- Travnikov, V., Zaussinger, F., Beltrame, P., Egbers, C.: Influence of the temperature-dependent viscosity on convective flow in the radial force field. *Phys. Rev. E* **96**(2) (2017)

- Vilella, K., Deschamps, F.: Temperature and heat flux scaling laws for isoviscous, infinite Prandtl number mixed heating convection. *Geophys. J. Int.* **214**(1), 265–281 (2018). <https://doi.org/10.1093/gji/ggy138>
- Vincze, M., Borchert, S., Achatz, U., von Larcher, T., Baumann, M., Liersch, C., Remmler, S., Beck, T., Alexandrov, K.D., Egbers, C., Fröhlich, J., Heuveline, V., Hickel, S., Harlander, U.: Benchmarking in a rotating annulus: a comparative experimental and numerical study of baroclinic wave dynamics. *Meteorologische Zeitschrift* **23**(6), 611–635 (2015). <https://doi.org/10.1127/metz/2014/0600>
- Vorontsov, S.V., Christensen-Dalsgaard, J., Schou, J., Strakhov, V.N., Thompson, M.J.: Helioseismic measurement of solar torsional oscillations. *Science* **296**(5565), 101–103 (2002). <https://doi.org/10.1126/science.1069190>. <https://science.sciencemag.org/content/296/5565/101>
- Wang, Y., Read, P.: Diversity of planetary atmospheric circulations and climates in a simplified general circulation model. *Proceedings IAU Symposium* **8**(S293), 297–302 (2012). <https://doi.org/10.1017/S1743921313013033>. <https://www.cambridge.org/core/article/diversity-of-planetary-atmospheric-circulations-and-climates-in-a-simplified-general-circulation-model/F06958904E99B92B8B9B208A3E630E0B>
- Waszek, L., Irving, J., Deuss, A.: Reconciling the hemispherical structure of earth's inner core with its super-rotation. *Nat. Geosci.* **4**, 264 EP– (2011). <https://doi.org/10.1038/ngeo1083>
- Weller, H.G., Tabor, G., Jasak, H., Fureby, C.: A tensorial approach to computational continuum mechanics using object-oriented techniques. *Comput. Phys.* **12**, 620–631 (1998). <https://doi.org/10.1063/1.168744>
- Zaussinger, F., Krebs, A., Travnikov, V., Egbers, C.: Recognition and tracking of convective flow patterns using Wollaston shearing interferometry. *Adv. Space Res.* **60**(6), 1327–1344 (2017). <https://doi.org/10.1016/j.asr.2017.06.028>. <http://www.sciencedirect.com/science/article/pii/S0273117717304544>
- Zaussinger, F., Canfield, P., Driebe, T., Egbers, C., Heintzmann, P., Travnikov, V., Froitzheim, A., Haun, P., Meier, M.: AtmoFlow - simulating atmospheric flows on the international space station. Part II: experiments and numerical simulations. In: 69th IAC Conference Proceedings, International Astronautical Federation, vol 18.A2.7.18-69 (2018a)
- Zaussinger, F., Haun, P., Neben, M., Seelig, T., Travnikov, V., Egbers, C., Yoshikawa, H., Mutabazi, I.: Dielectrically driven convection in spherical gap geometry. *Phys. Rev. Fluids* **3**, 093,501 (2018b). <https://doi.org/10.1103/PhysRevFluids.3.093501>. <https://link.aps.org/doi/10.1103/PhysRevFluids.3.093501>

Publisher's Note Springer Nature remains neutral with regard to jurisdictional claims in published maps and institutional affiliations.

Influence of dielectrical heating on convective flow in a radial force field

Vadim Travnikov, Florian Zaussinger , Peter Haun , and Christoph Egbers

Department of Aerodynamics and Fluid Mechanics, Brandenburg University of Technology Cottbus-Senftenberg, Siemens-Halske-Ring 14, 03046, Cottbus, Germany



(Received 15 December 2019; revised manuscript received 6 March 2020; accepted 29 April 2020; published 21 May 2020)

We present results of numerical and experimental investigations of thermal convection induced by internal heating in both a nonrotating and a rotating spherical gap filled with dielectric fluid. The inner and outer surfaces are maintained at constant temperatures T_{in} and T_{out} , respectively. A radial force field is produced due to the dielectrophoretic effect. The buoyancy force in the Navier-Stokes equation and the source term in the energy equation depend on the imposed oscillating electric field according to $V_{\text{rms}}^2 r^{-5}$ and $V_{\text{rms}}^2 r^{-4}$, respectively, where V_{rms} is the root mean squared value of the voltage between spherical surfaces and r is the radial distance. Beginning with the nonrotating case, we perform linear instability analysis in the case of purely internal heating, i.e., both surfaces are maintained at the same temperature $\Delta T = T_{\text{in}} - T_{\text{out}} = 0$. Next, we consider a situation in which there is not only internal heating but also a temperature difference $\Delta T > 0$. While the spherical gap rotated, the occurring two-dimensional steady basic flow was calculated numerically. The stability of the basic flow was investigated by means of linear instability theory. The critical Rayleigh numbers and the critical azimuthal wave numbers are presented in dependence on the Taylor number. We calculate supercritical three-dimensional flows for comparison with experimentally obtained patterns in frames of the GeoFlow experiment on the International Space Station.

DOI: [10.1103/PhysRevE.101.053106](https://doi.org/10.1103/PhysRevE.101.053106)

I. INTRODUCTION

Because of the geophysical relevance the exploration of the convective flows in the spherical gap was the subject of intensive theoretical and numerical studies. If the inner surface is warmer than the outer one and a fluid is influenced by a central force, then the situation occurs that can be compared with the Rayleigh-Bénard convection. The flow patterns occurring in such simplified configuration have been investigated by Busse and his coworkers in both nonrotating and rotating cases. Whereas the flow patterns in the rotating case are defined by the Coriolis force and the critical azimuthal wave numbers m_c can be derived due to the linear instability theory [1,2], we have completely other situation in the nonrotating case because of the symmetry of the problem under consideration. Patterns of the supercritical flow [3–5] and bifurcation scenarios [6] have been formulated in terms of parameter ℓ (degree of corresponding Legendre polynomial) in this case. The next important motivation for the implementation of the numerical analysis of the convective flows under the influence of the radial force field is the world-wide recognized GeoFlow experiment [7] that takes place on the International Space Station (ISS). The most important advantage of this experiment is that the influence of the Earth's gravity can be eliminated. Hence, if the fluid is heated from within and we find the possibility to produce the central force field, then the Rayleigh-Bénard convection in the spherical geometry can be realized under the microgravity conditions. To produce the radial force field the electric field is imposed on a dielectrical incompressible fluid of density ρ and permittivity $\epsilon(T)$, where T is the temperature. The force density, generated by electric

field \mathbf{E} can be expressed as follows [8]:

$$\mathbf{f}_e = \rho_e \mathbf{E} - \frac{1}{2} \mathbf{E}^2 \nabla \epsilon(T) + \nabla \left[\frac{1}{2} \rho \left(\frac{\partial \epsilon}{\partial \rho} \right)_T \mathbf{E}^2 \right], \quad (1)$$

where the first term is the density of the Coulomb force with a free charge ρ_e . The second term represents the dielectrophoretic force density, \mathbf{f}_{dep} . The third term, corresponding to the electrostriction force, can be combined with the pressure gradient. The Coulomb force is negligible if the frequency of the imposed electric field f is much higher than all frequencies that are responsible for the fluid behavior, e.g., the inverse of the charge relaxation time $\tau_e = \epsilon_0 \epsilon_r / \sigma_e$ (ϵ_0 is the vacuum permittivity, ϵ_r is the dielectric constant σ_e is the electrical conductivity), the inverse of the viscous relaxation time $t_v = d^2 / \nu$, and the inverse of the thermal relaxation time $t_k = d^2 / \kappa$, where ν is the kinematic viscosity, κ is the thermal diffusivity, and $d = R_2 - R_1$ is the width of the spherical gap. The next condition that must be satisfied to neglect the Coulomb force is $d \gg \delta_D$, where δ_D is the thickness of the Debye layer on the electrodes [9,10]. Because all these conditions fulfilled only the dielectrophoretic force influences the flow and must be taken into account.

The behavior of the electric permittivity can be approximated by a linear function of the temperature T :

$$\epsilon(T) = \epsilon_0 \epsilon_r [1 - \gamma(T - T_{\text{out}})]. \quad (2)$$

The force \mathbf{f}_{dep} can be written after a little algebra as follows:

$$\mathbf{f}_{\text{dep}} = -\gamma(T - T_{\text{out}}) \mathbf{g}_e, \quad \mathbf{g}_e = \frac{\epsilon_0 \epsilon_r}{2\rho} \nabla \mathbf{E}^2, \quad (3)$$

where \mathbf{g}_e is due to the electric field-induced artificial gravity field, and γ is the coefficient of thermal permittivity. Because the dielectrophoretic force \mathbf{f}_{dep} and the induced artificial gravity have opposite directions, the problem can be compared with the classical Rayleigh-Bénard (RB) problem, with one important difference. Whereas in RB convection the gravity does not change and the flow is controlled due to the temperature gradient, in our case $\Delta T = T_{\text{in}} - T_{\text{out}}$ is maintained at constant value and the flow is triggered by varying the voltage or artificial gravity. Furthermore, volumetric heating is involved in the energy equation due to the source term according to the relation

$$H_E = \frac{2\pi f \epsilon_0 \epsilon_r h_{\text{diss}}}{\rho C_p} \mathbf{E}^2, \quad (4)$$

where h_{diss} is the energy dissipation factor, and C_p is a specific heat capacity. Therefore, we have electric-field-dependent (via voltage) gravity $g_e \sim V_{\text{rms}}^2 r^{-5}$ in the Navier-Stokes equation [11] and source $H_E \sim V_{\text{rms}}^2 r^{-4}$ in the energy equation. In other words, the source term and the gravity are coupled parameters ($H_E \sim g_e$).

This situation completely differs from the situation in which source and the gravity are independent. In our case the gravity is a source. Hence, it is necessary to construct control parameters such that only one depends on the voltage. These specific parameters for the problem under consideration are discussed in the next section.

The work presented is a numerical support for the well-known GeoFlow experiment [12–14] on the ISS. Whereas the GeoFlow I experiment was performed with fluid of constant viscosity (silicon oil M5), a fluid with temperature-dependent viscosity (1-nonanol) was used during the GeoFlow II experiment. Although the temperature-sensitive viscosity plays an important role, we found that the influence of the internal heating is much more significant and becomes crucial if the frequency of the imposed electric field increases from $f = 50$ Hz (GeoFlow I) to $f = 10650$ Hz (GeoFlow II). Thus, the source term Eq. (4) must be involved in the energy equation. This paper is a sequel to Ref. [15], where the problem under investigation was solved numerically in framework of the GeoFlow I experiment in which the effect of the internal heating is negligible.

The paper is organized as follows. After the governing equations are formulated in Sec. II, we present the numerical method in Sec. III. The structure of the basic flow for different Rayleigh numbers and Taylor numbers is discussed in Sec. IV. Linear instability analysis is performed in Sec. V. Nonlinear calculations of the supercritical three-dimensional flows, analysis of the heat transfer and bifurcation analysis in the nonrotating and rotating cases are presented in Secs. VIA and VIB, correspondingly. Experimental results are discussed in Sec. VIC.

II. EQUATIONS

We consider an incompressible viscous dielectric fluid in the Boussinesq approximation in the spherical gap. In the common form, the problem under consideration can be

described due to the Navier-Stokes equation for the velocity

$$\frac{\partial \mathbf{U}}{\partial t} + (\mathbf{U} \nabla) \mathbf{U} = -\nabla p_{\text{eff}} - \gamma(T - T_{\text{out}}) \mathbf{g}_e + \nu \Delta \mathbf{U} - 2\boldsymbol{\Omega} \times \mathbf{U} - \frac{\rho(T)}{\rho_0} \boldsymbol{\Omega} \times (\boldsymbol{\Omega} \times \mathbf{r}), \quad (5)$$

where \mathbf{U} is the velocity field, t is the time,

$$p_{\text{eff}} = \frac{p}{\rho_0} - \frac{\gamma \epsilon_0 \epsilon_r (T - T_{\text{out}}) E^2}{2\rho_0} - \frac{1}{2} \left(\frac{\partial \epsilon}{\partial \rho} \right)_T E^2, \quad (6)$$

$\rho_0 = \rho(T_{\text{out}})$, $\boldsymbol{\Omega}$ is the rotation rate, the energy equation for the temperature

$$\frac{\partial T}{\partial t} + (\mathbf{U} \cdot \nabla) T = \kappa \nabla^2 T + H_E, \quad (7)$$

the continuity equation

$$\nabla \cdot \mathbf{U} = 0, \quad (8)$$

and the Gauss equation

$$\nabla \cdot (\epsilon(T) \nabla v) = 0, \quad (9)$$

where v is the electric potential: $\mathbf{E} = -\nabla v$. Whereas no-slip boundary conditions for the velocity field are used in the study presented, we consider two kinds of boundary conditions for the temperature. If both surfaces are maintained at the same temperature $T_{\text{in}} = T_{\text{out}} = T_b$, then only the internal heating due to the source H_E is responsible for the heat transfer. The situation changes if the inner surface is maintained at a higher temperature than the outer one $T_{\text{in}} > T_{\text{out}}$. In this case the heat transfer is produced not only because of internal heating but also due to conduction. The boundary conditions for the velocity, the temperature and electric potential are

$$\mathbf{U} = 0, \quad T = T_{\text{in}}, \quad v = V_{\text{rms}} \quad (10)$$

on the inner surface $r = R_1$,

$$\mathbf{U} = 0, \quad T = T_{\text{out}}, \quad v = 0. \quad (11)$$

on the outer surface $r = R_2$. Note that real-time-dependent voltage $V(t) = V_0 \cos 2\pi ft$ was replaced by the root mean squared value $V_{\text{rms}} = \sqrt{\langle V^2(t) \rangle} = V_0/\sqrt{2}$ according to the time-averaged relation over a period of the voltage variation $T_e = f^{-1} \langle V^2(t) \rangle = \frac{1}{T_e} \int_0^{T_e} V^2(t) dt$. Conditions of this replacement were numerically derived in [16,17] and can be briefly formulated as follows. First, the Prandtl number of the working fluid must be large ($\text{Pr} \gg 1$). Furthermore, the frequency f must obey two conditions: $f \gg \tau_v^{-1}$ and $f \gg \tau_e^{-1}$. Taking into account that $f = 10650$ Hz, $\text{Pr} = 176$, $\nu = 1.3970 \times 10^{-5} \text{ m}^2\text{s}^{-1}$, $d = R_2 - R_1 = 135$ mm, where R_1 and R_2 are the inner and outer radii, correspondingly, all these conditions are fulfilled (Table I).

Now we have to formulate the governing equations in detail. The first case corresponds to a situation in which only dielectrical heating without rotation ($\Delta T = 0$ K, $\boldsymbol{\Omega} = 0$) is considered. The second one describes not only the effect of dielectrical heating but also a convective effect triggered by the temperature difference between the spherical surfaces and the rotation of the spherical system ($\Delta T > 0$, $\boldsymbol{\Omega} \geq 0$). Because we have different boundary conditions for the temperature, it is useful to formulate two sets of equations to

TABLE I. List of constants.

Nomenclature	$T_{\text{out}} = 293 \text{ K}$
Energy dissipation factor h_{diss}	6.2423×10^{-2}
Volume expansion coefficient $\alpha (\text{K}^{-1})$	8.2343×10^{-4}
Coefficient of thermal permittivity $\gamma (\text{K}^{-1})$	0.010209
AC frequency $f (\text{Hz})$	1.0650×10^4
Permittivity ϵ_r	9.05629
Density $\rho (\text{kgm}^{-3})$	828.16
Specific heat capacity $C_p (\text{JK}^{-1})$	2470
Kinematic viscosity $\nu (\text{m}^2\text{s}^{-1})$	1.3970×10^{-5}
Thermal diffusivity $\kappa (\text{m}^2\text{s}^{-1})$	7.94×10^{-8}

be solved. Beginning with the purely dielectrical heating case and writing the equation for $\epsilon(T)$ in the form

$$\epsilon(T) = \epsilon_0 \epsilon_r [1 - \gamma(T - T_b)], \quad (12)$$

We can introduce the dimensionless temperature T^* using $T - T_b = T_b T^*$. Introducing d for the length, κ/d for the velocity and $t_\kappa = d^2/\kappa$ for the time, $\mathbf{E} = \mathbf{E}^* \frac{V_{\text{rms}}}{d}$ for the electric field the Navier-Stokes equation, the energy equation, and the Gauss equation can be written, dropping stars, in the dimensionless form:

$$\begin{aligned} & \text{Pr}^{-1} \left[\frac{\partial \mathbf{U}}{\partial t} + (\mathbf{U} \nabla) \mathbf{U} \right] \\ &= -\text{Pr}^{-1} \nabla p + \Delta \mathbf{U} - \frac{1}{4} \text{R}_H \cdot T \cdot \nabla [\nabla v_0(r) \\ &+ \nabla v_1(r, \theta, \phi)]^2, \end{aligned} \quad (13)$$

$$\frac{\partial T}{\partial t} + (\mathbf{U} \cdot \nabla) T = \nabla^2 T + \frac{\text{R}_H}{\text{R}_T} [\nabla v_0(r) + \nabla v_1(r, \theta, \phi)]^2, \quad (14)$$

$$\nabla^2 v_1(r, \theta, \phi) = \frac{\gamma T_b}{1 - \gamma T_b T} \nabla T \cdot [\nabla v_0(r) + \nabla v_1(r, \theta, \phi)], \quad (15)$$

where $\text{R}_H = \frac{2\epsilon_0 \epsilon_r \gamma T_b V_{\text{rms}}^2}{\rho \nu \kappa}$ is the Rayleigh-Roberts number, $\text{R}_T = \frac{C_p \gamma T_b^2}{\pi \nu f h_{\text{diss}}}$. Note that it is useful to divide the electric field \mathbf{E} into two parts (θ is polar angle and ϕ is azimuthal angle)

$$\mathbf{E} = \mathbf{E}_0(r) + \mathbf{E}_1(r, \theta, \phi), \quad (16)$$

$$\mathbf{E}_0(r) = -\nabla v_0(r), \quad (17)$$

$$\mathbf{E}_1(r, \theta, \phi) = -\nabla v_1(r, \theta, \phi). \quad (18)$$

Whereas the field $\mathbf{E}_0(r)$, which satisfies an expression $\nabla \cdot \mathbf{E}_0(r) = 0$, can be calculated analytically,

$$\mathbf{E}_0(r) = \frac{\eta}{(1 - \eta)^2} \frac{1}{r^2} \mathbf{e}_r, \quad (19)$$

where $\eta = \frac{R_1}{R_2}$ is a radii ratio, the field $\mathbf{E}_1(r, \theta, \phi)$ has a more complex form because it generally depends on all three coordinates and must be found numerically by solving Eq. (15). The velocity field \mathbf{U} , the temperature T , and the electric

potential v_1 obey

$$\mathbf{U} = 0, \quad T = 0, \quad v_1 = 0 \quad (20)$$

on the both surfaces $r = \eta/(1 - \eta)$ and $r = 1/(1 - \eta)$.

Substituting $\mathbf{E}_0(r)$ in Eq. (3) we obtain the well-known r^{-5} dependence [11]. It is clear that the second field occurs because of the temperature-dependent function $\epsilon(T)$. In the second case, the equation for the permittivity Eq. (2) and the equation of state

$$\rho(T) = \rho_0 [1 - \alpha(T - T_{\text{out}})] \quad (21)$$

have been substituted in the Navier-Stokes equation. The dimensionless temperature T^* can be expressed in the form $T - T_{\text{out}} = \Delta T T^*$, where $\Delta T = T_{\text{in}} - T_{\text{out}}$. If the same scale is retained for the length, for the velocity, for the time, and for the electric field, then the governing equations can be expressed as follows (omitting stars):

$$\begin{aligned} & \text{Pr}^{-1} \left[\frac{\partial \mathbf{U}}{\partial t} + (\mathbf{U} \nabla) \mathbf{U} \right] \\ &= -\text{Pr}^{-1} \nabla p + \Delta \mathbf{U} - \frac{1}{4} \text{Ra}_E \cdot T \cdot \nabla [\nabla v_0(r) \\ &+ \nabla v_1(r, \theta, \phi)]^2 - \sqrt{\text{Ta}} \mathbf{e}_z \times \mathbf{U} + A \cdot T r \sin \theta \mathbf{s}, \end{aligned} \quad (22)$$

$$\frac{\partial T}{\partial t} + (\mathbf{U} \cdot \nabla) T = \nabla^2 T + \frac{\text{Ra}_E}{\text{Ra}_T} [\nabla v_0(r) + \nabla v_1(r, \theta, \phi)]^2, \quad (23)$$

$$\nabla^2 v_1(r, \theta, \phi) = \frac{B}{1 - B \cdot T} \nabla T \cdot [\nabla v_0(r) + \nabla v_1(r, \theta, \phi)], \quad (24)$$

where $\mathbf{e}_z = \cos \theta \mathbf{e}_r - \sin \theta \mathbf{e}_\theta$, $\mathbf{s} = -(\sin \theta \mathbf{e}_r + \cos \theta \mathbf{e}_\theta)$, $\text{Ra}_E = \frac{2\epsilon_0 \epsilon_r \gamma V_{\text{rms}}^2 \Delta T}{\rho \nu \kappa}$ is the Rayleigh number, $\text{Ta} = \left(\frac{2\Omega d^2}{\nu}\right)^2$ is the Taylor number, $\text{Ra}_T = \frac{c_p \gamma \Delta T^2}{\pi \nu f h_{\text{diss}}}$, $A = \frac{\alpha \Delta T}{4} \text{PrTa}$, $B = \gamma \Delta T$. The boundary conditions for the velocity field \mathbf{U} , the temperature T and the electric potential v_1 are

$$\mathbf{U} = 0, \quad T = 1, \quad v_1 = 0 \quad (25)$$

on the $r = \eta/(1 - \eta)$ and

$$\mathbf{U} = 0, \quad T = 0, \quad v_1 = 0 \quad (26)$$

on the $r = 1/(1 - \eta)$. Note that parameters Ra_T and B does not change at fixed ΔT . The parameter A depends only on the Taylor number (for fixed Prandtl number). Hence, we can investigate convective flow that depends on the Rayleigh number (or voltage V_{rms}) and the Taylor number (or rotation rate Ω). We list the values of constants for the working fluid 1-Nonanol in this study used in Table I.

III. NUMERICAL METHOD

The fully three-dimensional pseudospectral numerical code for the spherical geometry was developed by Hollerbach [18]. The poloidal-toroidal representation of the velocity field

$$\mathbf{U} = \nabla \times \nabla \times (\Phi \mathbf{e}_r) + \nabla \times (\Psi \mathbf{e}_r) \quad (27)$$

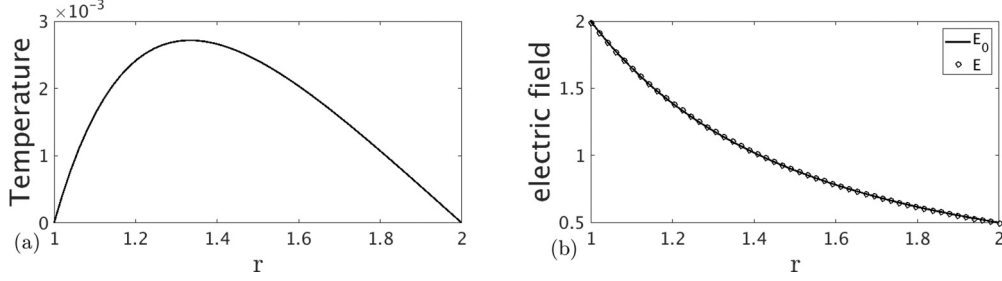


FIG. 1. The base temperature (a) and the base electric field (b) for $\eta = 0.5$, $\Delta T = 0$ K, $R_H = 1.605 \times 10^6$.

automatically obeys the continuity equation. Separated equations for poloidal Φ and toroidal Ψ potentials can be obtained applying operators $\nabla \times \nabla \times$ and $\nabla \times$, correspondingly. After the mapping $r = \frac{1}{2}[z + \frac{1+\eta}{1-\eta}]$ is performed, where $z \in [-1, +1]$, each scalar function can be expanded in terms of the Chebyshev polynomials in the radial direction and in terms of spherical harmonics, $Y_\ell^m(\theta, \phi)$, according to

$$\Phi(t, r, \theta, \phi) = \sum_{m=0}^{\text{MU}} \sum_{\ell=\ell'}^{\text{LU}} \sum_{k=1}^{\text{KU}+4} [f_{ck\ell m}(t) \cos(m\phi) + f_{sk\ell m}(t) \sin(m\phi)] T_{k-1}(z) P_\ell^m(\cos \theta), \quad (28)$$

$$\Psi(t, r, \theta, \phi) = \sum_{m=0}^{\text{MU}} \sum_{\ell=\ell'}^{\text{LU}} \sum_{k=1}^{\text{KU}+2} [e_{ck\ell m}(t) \cos(m\phi) + e_{sk\ell m}(t) \sin(m\phi)] T_{k-1}(z) P_\ell^m(\cos \theta), \quad (29)$$

$\ell' = \max(1, m)$. A similar expression is valid for the temperature

$$T(t, r, \theta, \phi) = \sum_{m=0}^{\text{MT}} \sum_{\ell=m}^{\text{LT}} \sum_{k=1}^{\text{KT}+2} [t_{ck\ell m}(t) \cos(m\phi) + t_{sk\ell m}(t) \sin(m\phi)] T_{k-1}(z) P_\ell^m(\cos \theta). \quad (30)$$

Twenty Chebyshev polynomials ($\text{KU} = \text{KT} = 20$) and 30 Legendre polynomials ($\text{LU} = \text{LT} = 30$) were enough to get the grid-independent solution for the two-dimensional basic flow and linear onset calculations for all Taylor numbers and Rayleigh numbers considered. Whereas the same resolution in the radial direction was used for the fully three-dimensional calculations, a values of LU , LT vary between 30 and 40 and MU and MT alter between 20 and 40. The time-dependent spectral coefficients have been calculated by means of the predictor-corrector method. Because we deal with the oscillating bifurcation the perturbed flow depends on time in contrast to the steady two-dimensional basic flow. Therefore, we use such a time step Δt that for all smaller Δt no changes in critical Rayleigh number and drift velocity occur. This time step depends on the Taylor number and varies between $\Delta t = 10^{-4}$ and $\Delta t = 2 \times 10^{-5}$.

IV. BASIC FLOW

From Eqs. (12)–(19) and Eqs. (2), (21)–(24) it follows that the electric field is coupled *directly* not only with the velocity field due to the buoyancy term in the Navier-Stokes equation but also with the temperature, due to the dielectrical heating in the energy equation. This means that the model

under investigation differs from other cases in the literature where the dielectrical heating or other kinds of heating are negligible. This fact makes it slightly complicated to calculate the basic state. In the case of pure heating ($\Delta T = 0$ K), the basic flow is zero in the nonrotating case. To find the temperature, Eq. (14) must be solved numerically together with the Gauss equation, Eq. (15). The base temperature $T_0(r)$ and the base electric field $\mathbf{E}(r) = \mathbf{E}_0(r) + \mathbf{E}_1(r)$ have a radial one-dimensional structure, see Figs. 1(a) and 1(b),

$$\nabla^2 T_0(r) = -\frac{R_H}{R_T} [\nabla v_0(r) + \nabla v_1(r)]^2, \quad (31)$$

$$\nabla^2 v_1(r) = \frac{\gamma T_b}{1 - \gamma T_b T} \nabla T_0(r) \cdot [\nabla v_0(r) + \nabla v_1(r)]. \quad (32)$$

However, in the case of purely dielectrical heating, an additional field $\mathbf{E}_1(r)$ has such a small value [Fig. 1(b)] that it does not influence the temperature. Therefore, the base temperature can be calculated analytically,

$$T_{0I}(r) = -\frac{1}{2} \frac{R_H}{R_T} \frac{\eta^2}{(1-\eta)^4} \left[\frac{(1-\eta)^2}{\eta} - \frac{(1-\eta^2)}{\eta} \frac{1}{r} + \frac{1}{r^2} \right]. \quad (33)$$

The analytical form of the temperature is particularly useful for calculating the Nusselt number of the basic state, defined as follows:

$$\text{Nu}_{in0}^{\text{analyt}} = \int_{S_{in}} \frac{dT_{0I}(r)}{dr} dS_{in}, \quad (34)$$

$$\text{Nu}_{out0}^{\text{analyt}} = - \int_{S_{out}} \frac{dT_{0I}(r)}{dr} dS_{out}, \quad (35)$$

where $dS_{in,out} = r_{in,out}^2 \sin \theta d\theta d\phi$. After a little algebra, we obtain

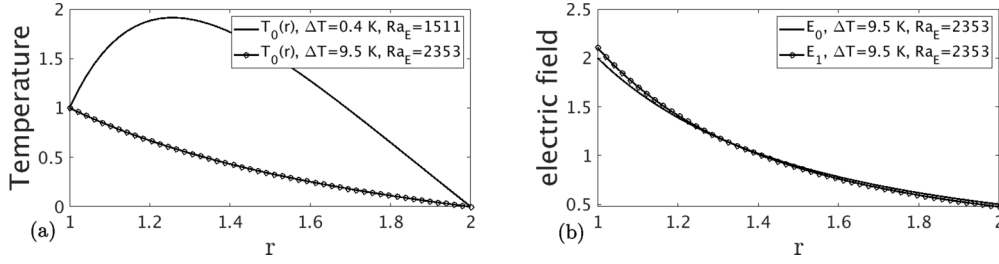
$$\text{Nu}_{in0}^{\text{analyt}} = \text{Nu}_{out0}^{\text{analyt}} = \frac{2\pi\eta}{(1-\eta)^2} \frac{R_H}{R_T}. \quad (36)$$

The energy balance equation in terms of the Nusselt number reads

$$-\text{Nu}_{in0}^{\text{analyt}} - \text{Nu}_{out0}^{\text{analyt}} + \frac{R_H}{R_T} \int_V E_0^2 dV = 0, \quad (37)$$

i.e., the energy is produced due to the dielectrical heating and leaves the domain under consideration through the inner and outer surfaces.

In the second case ($\Delta T > 0$) without rotation ($\text{Ta} = 0$) and neglecting $\mathbf{E}_1(r)$ the analytical solution for the temperature


 FIG. 2. The basic temperature (a) and the electric field (b) for $\eta = 0.5$.

is

$$\begin{aligned}
 T_{0II}(r) = & -\frac{\eta}{1-\eta} + \frac{\eta}{(1-\eta)^2} \frac{1}{r} \\
 & -\frac{1}{2} \frac{\text{Ra}_E}{\text{Ra}_T} \frac{\eta}{(1-\eta)^2} + \frac{1}{2} \frac{\text{Ra}_E}{\text{Ra}_T} \frac{\eta(1+\eta)}{(1-\eta)^3} \frac{1}{r} \\
 & -\frac{1}{2} \frac{\text{Ra}_E}{\text{Ra}_T} \frac{\eta^2}{(1-\eta)^4} \frac{1}{r^2}. \quad (38)
 \end{aligned}$$

Note that the solution can be divided into two parts. The first part occurs because the inner surface is warmer than the outer and is responsible for the energy transport from the warmer inner surface into the volume entirely due to conduction. The second one is associated with dielectrical heating ($\sim \frac{\text{Ra}_E}{\text{Ra}_T}$). Two examples of the base temperature are presented in Fig. 2(a). Whereas the influence of the dielectrical heating is particularly significant for small ΔT ($\text{Ra}_T = 138.28$ for $\Delta T = 0.4\text{K}$), conduction prevails for large ΔT ($\text{Ra}_T = 78\,000$ for $\Delta T = 9.5\text{K}$). Both effects influence heat transfer, which can be expressed in the following form in terms of the Nusselt number:

$$\text{Nu}_{in0}^{\text{analyt}} = -\int_{S_{in}} \frac{dT_{0II}(r)}{dr} dS_{in}, \quad \frac{\text{Ra}_E}{2\text{Ra}_T} \leq 1, \quad (39a)$$

$$\text{Nu}_{in0}^{\text{analyt}} = \int_{S_{in}} \frac{dT_{0II}(r)}{dr} dS_{in}, \quad \frac{\text{Ra}_E}{2\text{Ra}_T} \geq 1, \quad (39b)$$

$$\text{Nu}_{out0}^{\text{analyt}} = -\int_{S_{out}} \frac{dT_{0II}(r)}{dr} dS_{out}. \quad (39c)$$

Hence, whereas the energy flux through the outer surface does not change its sign, the definition of $\text{Nu}_{in0}^{\text{analyt}}$ depends upon which effect is stronger, the dielectrical heating, associated with the imposed electrical field, or the energy transfer because of the conduction. The Nusselt number can be calculated analytically, as in the case of purely dielectrical heating

$$\text{Nu}_{in0}^{\text{analyt}} = \frac{4\pi\eta}{(1-\eta)^2} \left(1 - \frac{1}{2} \frac{\text{Ra}_E}{\text{Ra}_T}\right), \quad \frac{\text{Ra}_E}{2\text{Ra}_T} < 1, \quad (40a)$$

$$\text{Nu}_{in0}^{\text{analyt}} = \frac{4\pi\eta}{(1-\eta)^2} \left(\frac{1}{2} \frac{\text{Ra}_E}{\text{Ra}_T} - 1\right), \quad \frac{\text{Ra}_E}{2\text{Ra}_T} > 1, \quad (40b)$$

$$\text{Nu}_{out0}^{\text{analyt}} = \frac{4\pi\eta}{(1-\eta)^2} \left(1 + \frac{1}{2} \frac{\text{Ra}_E}{\text{Ra}_T}\right). \quad (40c)$$

The energy balance equation in terms of the Nusselt number reads

$$\text{Nu}_{in0}^{\text{analyt}} - \text{Nu}_{out0}^{\text{analyt}} + \frac{\text{Ra}_E}{\text{Ra}_T} \int_V E_0^2 dV = 0 \quad (41)$$

$$\frac{\text{Ra}_E}{2\text{Ra}_T} < 1,$$

$$-\text{Nu}_{in0}^{\text{analyt}} - \text{Nu}_{out0}^{\text{analyt}} + \frac{\text{Ra}_E}{\text{Ra}_T} \int_V E_0^2 dV = 0 \quad (42)$$

$$\frac{\text{Ra}_E}{2\text{Ra}_T} > 1.$$

If $\text{Ra}_E/2\text{Ra}_T < 1$, then the heat flux caused by conduction prevails and the system obtains more energy than it loses because of the internal heating. This situation changes if the Rayleigh number exceeds 2Ra_T (e.g., $2\text{Ra}_T = 276.55$ if $\Delta T = 0.4\text{K}$). Therefore, the Nusselt number has the V-shaped structure.

The influence of $E_1(r)$ becomes important for large values of ΔT , e.g., $\Delta T = 9.5\text{K}$. The difference between $E(r)$ and $E_0(r)$ has a value of 5% at the vicinity of the inner surface [Fig. 2(b)]. Taking $E_1(r)$ into account decreases the critical Rayleigh number from $\text{Ra}_{ECL} = 2487$ (if the field $E(r) = E_0(r)$ is considered) to $\text{Ra}_{ECL} = 2353.29$.

The situation becomes much more complex if the spherical system is rotating ($\text{Ta} > 0$). The centrifugal force causes a two-dimensional axisymmetrical and equatorially symmetrical steady basic flow [$\mathbf{U}_0(r, \theta)$] that must be calculated numerically. Some examples of the basic flow are presented in Fig. 3 in terms of the stream function χ that is connected with velocity components according to $U_{0r}(r, \theta) = \frac{1}{r^2 \sin \theta} \frac{\partial \chi}{\partial \theta}$, $U_{0\theta}(r, \theta) = -\frac{1}{r \sin \theta} \frac{\partial \chi}{\partial r}$. The basic flow is presented for the experimentally relevant radii ratio $\eta = 0.5$, Prandtl number $\text{Pr} = 176$, $\Delta T = 0.4\text{K}$, $\Delta T = 1.7\text{K}$, $\Delta T = 3\text{K}$, and for Taylor numbers $\text{Ta} = 17\,200$ and $\text{Ta} = 68\,800$; see Sec VI C. The first row shows the meridional flow or the stream function, the second one depicts the angular velocity and the third row is the temperature. All flows are presented at the critical Rayleigh number $\text{Ra}_E = \text{Ra}_{ECL}$.

If ΔT increases, then the centrifugal force becomes more and more important and the meridional flow [Figs. 3(a)–3(f), first row] concentrates in the vicinity of the inner surface. The main part of the angular velocity field [Figs. 3(a)–3(f), second row] concentrates near the inner surface, building the boundary layer. The maximum temperature [Figs. 3(a)–3(f), third row] is located within the gap, emphasizing the importance of the internal heating. These features of the basic flow are

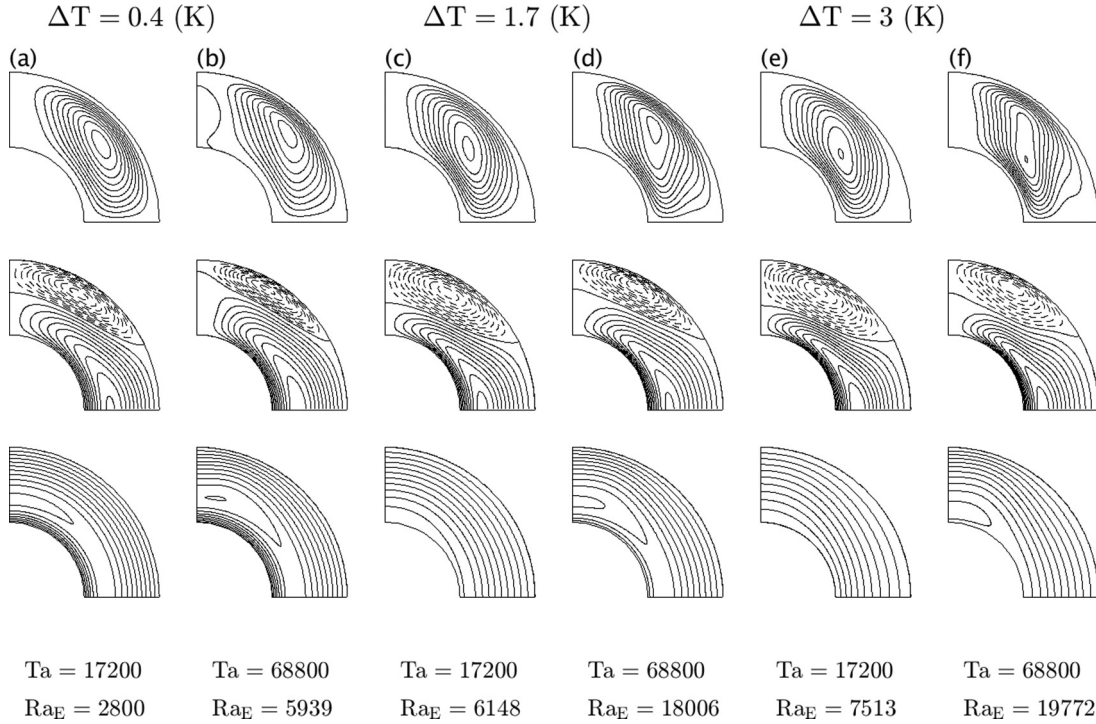


FIG. 3. Basic flow (presented at the critical $Ra_{E,cL}$): first row contours of the meridional circulation χ with (a) $\chi_{\max} = 0.36$, (b) $\chi_{\max} = 0.9$, (c) $\chi_{\max} = 0.48$, (d) $\chi_{\max} = 0.96$, (e) $\chi_{\max} = 0.76$, (f) $\chi_{\max} = 1.2$. Second row contours of the angular velocity with maximal and minimal values (a) $+2.8, -1.2$, (b) $+12.6, -4.8$, (c) $3.6, -2$, (d) $+14, -6.4$, (e) $+5, -3.42$, (f) $+15, -8.0$. Third row contours of the temperature with (a) $T_{\max} = 3.1$, (b) $T_{\max} = 6.4$, (c) $T_{\max} = 1.0$, (d) $T_{\max} = 1.6$, (e) $T_{\max} = 1.0$, (f) $T_{\max} = 1.05$.

crucial for understanding of the origin of the instability as discussed in the next section.

The Nusselt number can be calculated numerically only in the rotating case because of the existence of the basic flow. We present the Nusselt number as a function of Ra_E (Fig. 4) for fixed Taylor number $Ta = 17200$. The shape of the $Nu_{in0}(Ra_E)$, corresponding to the heat transfer through the inner surface in the case of the basic flow (for the fixed $\Delta T = 0.4$ K and $\Delta T = 1.7$ K) is similar to the nonrotating case. Interestingly, the zero-flux point, Ra_{E0} , in which $Nu_{in0} = 0$, i.e., heat fluxes produced due to the imposed electrical field and applied ΔT are the same, almost coincides with $2Ra_T$ for $\Delta T = 0.4$ K ($Ra_{E0} = 276.27$, $2Ra_T = 276.55$) and differs only slightly within a range of 0.5% for $\Delta T = 1.7$ K ($Ra_{E0} = 5016$, $2Ra_T = 4995.27$). Whereas $Nu_{out0}(Ra_E)$ can be approximated by means of linear law [Eq. (40c)] with very good accuracy (less than 0.01%) for $\Delta T = 0.4$ K and

$\Delta T = 1.7$ K, Eqs. (40a) and (40b) can be used to calculate the value $Nu_{in0}(Ra_E)$ only for $\Delta T = 0.4$ K. Detailed analysis shows that numerically obtained Nusselt number, $Nu_{in0}(Ra_E)$, can be approximated by (Fig. 4, left)

$$Nu_{in0}^{\text{approx}} = -0.005025Ra_E + 25.20, \quad \frac{Ra_E}{Ra_{E0}} < 1, \quad (43)$$

$$Nu_{in0}^{\text{approx}} = 0.004989Ra_E - 25.03, \quad \frac{Ra_E}{Ra_{E0}} > 1 \quad (44)$$

for $\Delta T = 1.7$ K.

If the ΔT increases, then the zero-flux point Ra_{E0} does not occur because the heat flux due to conduction through the inner surface prevails over the heat flux caused by the source H_E . Therefore, the Nusselt number for $\Delta T = 3$ K and $Ta = 17200$ must be calculated numerically and the analytically obtained expressions Eqs. (40a)–(40c) are no longer valid.

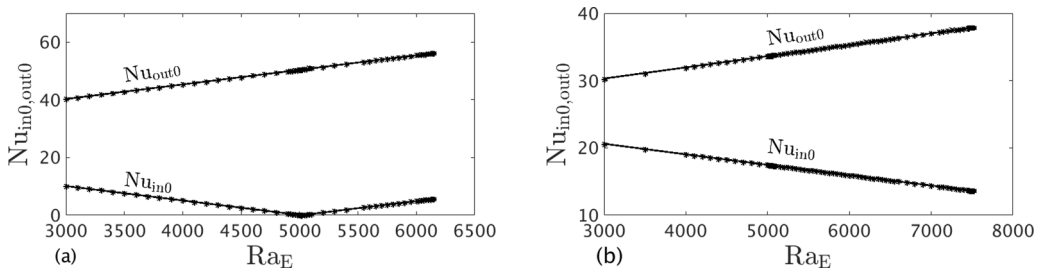


FIG. 4. Nusselt number vs. Rayleigh number for $\Delta T = 1.7$ K (a) and $\Delta T = 3.0$ K (b), $\eta = 0.5$ and $Ta = 17200$. Numerically obtained Nusselt number is presented in solid, the approximated Nusselt number Eqs. (44)–(47) is presented with stars.

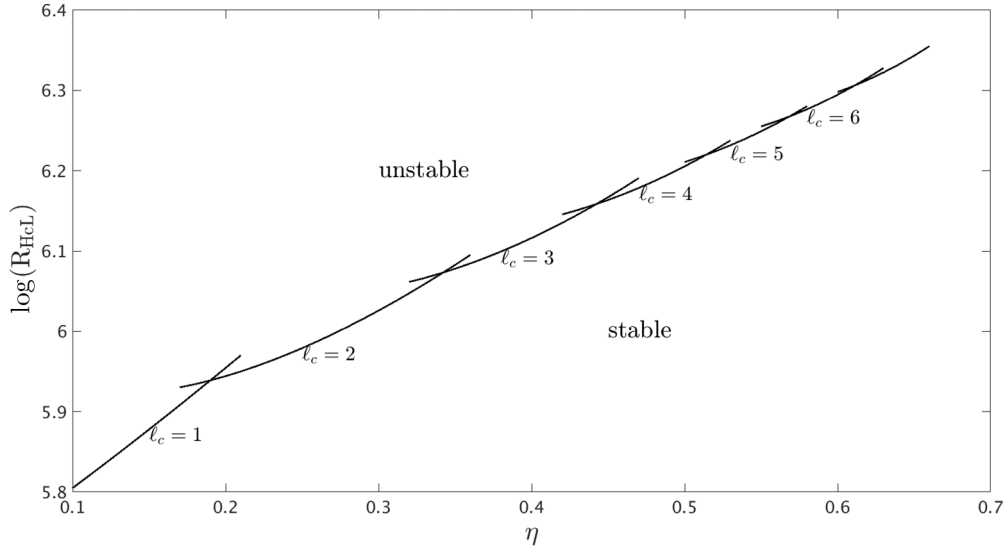


FIG. 5. Critical Rayleigh-Roberts numbers in the case of purely dielectrical heating ($\Delta T = 0$ K).

Nevertheless, numerically obtained Nusselt number can be approximated according to (Fig. 4, right).

$$\text{Nu}_{\text{in}0}^{\text{approx}} = -0.001537\text{Ra}_E + 25.17, \quad (45)$$

$$\text{Nu}_{\text{out}0}^{\text{approx}} = 0.001694\text{Ra}_E + 25.17. \quad (46)$$

V. LINEAR INSTABILITY ANALYSIS

Stability of the basic flow was investigated in frames of linear theory. This is a useful tool to derive such critical Rayleigh-Roberts, R_{HcL} , or Rayleigh number, Ra_{EcL} , above which the basic flow becomes unstable with respect to infinitesimal perturbations \mathbf{u} for the velocity, Θ for the temperature, \tilde{p} for the pressure, and \tilde{v} for the electric potential. Because of the continuity Eq. (8) the poloidal-toroidal decomposition Eq. (27) can be used for the field \mathbf{u} ,

$$\mathbf{u} = \nabla \times \nabla \times (\tilde{\Phi}\mathbf{e}_r) + \nabla \times (\tilde{\Psi}\mathbf{e}_r), \quad (47)$$

too. Furthermore, the expressions Eqs. (28)–(30) are valid for the perturbations in which the spectral coefficients, e.g., $f_{ck\ell m}$ have been replaced by $\tilde{f}_{ck\ell m}$. The eigenvalue problem was solved by means of direct numerical integration. Because the basic flow is steady the temporal structure of the solution of the linearized equation system has form of $e^{\sigma t}$, where $\sigma = \zeta + i\omega$ is the dominant eigenvalue, the real part of the eigenvalue ζ is the growth rate, and ω is the frequency of the perturbation. The goal of the linear analysis is to find such value of the control parameter (R_{HcL} and Ra_{EcL}) at which $\zeta = 0$. Frequency ω defines a kind of bifurcation. If $\omega = 0$, then the basic flow becomes unstable with respect to the stationary perturbations. If $\omega > 0$, then the instability sets in as an oscillating bifurcation.

A. Nonrotating case

Note that the linearized equations, formulated in the spectral space, do not depend on the azimuthal wave number m in the nonrotating case. Furthermore, the linear instability equations can be separated for each number ℓ . Numerical

analysis shows that the basic flow becomes unstable with respect to steady perturbations for all radius ratios considered, i.e., $\omega = 0$. This numerical result is in accordance with the analytical results obtained for the case of the plane and cylindrical geometries [19–21]. The growth rate is calculated according to $\sigma = \frac{1}{\Delta t} \ln \frac{|g_{k\ell}(t+\Delta t)|}{|g_{k\ell}(t)|}$, where $g_{k\ell}(t)$ is the arbitrary spectral coefficient ($\tilde{f}_{c,s}$ or $\tilde{t}_{c,s}$) with fixed subscript k and tested number ℓ . Note that in the linear approach the toroidal potential vanishes $\tilde{\Psi} = 0$ in the nonrotating case. The critical Rayleigh-Roberts number and the critical Rayleigh number, defined as

$$R_{\text{HcL}}(\eta) = \min_{\ell} R_{\text{H}}(\ell, \eta), \quad \text{Ra}_{\text{EcL}}(\eta) = \min_{\ell} \text{Ra}_{\text{E}}(\ell, \eta), \quad (48)$$

obey $\sigma = 0$.

Critical Rayleigh-Roberts numbers for the case of purely dielectric heating are presented in Fig. 5. We see that the critical Rayleigh-Roberts number is $R_{\text{HcL}} = 1.6049 \times 10^6$, which corresponds to the voltage $V_{\text{rms,crit.}} = 1754$ V. The critical wave number is $\ell_c = 4$. The influence of the imposed ΔT is presented in Fig. 6. Although the critical Rayleigh number increases from $\text{Ra}_{\text{EcL}} = 1511.32$ for $\Delta T = 0.4$ K to $\text{Ra}_{\text{EcL}} = 2411.29$ for $\Delta T = 3$ K, the corresponding values of the voltage decrease drastically from $V_{\text{rms,crit.}} = 1456$ V to $V_{\text{rms,crit.}} = 671$ V. Hence, increasing ΔT destabilizes the basic state: A lower voltage is needed for the transition into the three-dimensional flow.

B. Rotating case

If the spherical system rotates with the rotation rate Ω , then the Coriolis force and the centrifugal force must be taken into account. Additionally to the Rayleigh number Ra_E , the flow is characterized by the Taylor number, Ta , and the parameter $A = \frac{1}{4}\alpha\Delta T\text{PrTa}$. As in the nonrotating case, the linearized Navier-Stokes equation, the energy equation and the Gauss equation were solved directly to derive the critical Rayleigh number. The basic feature of the equations, describing the

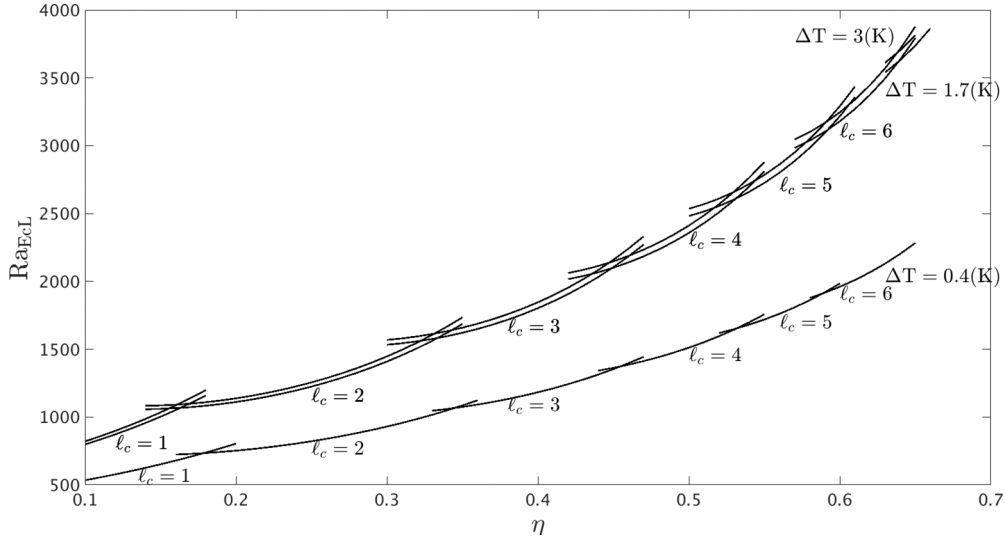


FIG. 6. Critical Rayleigh numbers for the dielectrical heating and $\Delta T > 0$.

stability problem, is that they can be formulated for each azimuthal wave number m . In other words, we have to solve M two-dimensional problems, where M is the maximum of the all wave numbers under consideration. Furthermore, because of the equatorial symmetry of the basic flow, the linear system of equations to be solved can be divided into two sets, corresponding to the two symmetry classes. Perturbations of the first class satisfy the relation

$$\{u_r, u_\theta, u_\phi, \Theta\}(r, \theta, \phi) = \{u_r, -u_\theta, u_\phi, \Theta\}(r, \pi - \theta, \phi), \tag{49}$$

which is symmetric with respect to the equator, and perturbations of the second class,

$$\{u_r, u_\theta, u_\phi, \Theta\}(r, \theta, \phi) = \{-u_r, u_\theta, -u_\phi, -\Theta\}(r, \pi - \theta, \phi), \tag{50}$$

are equatorially antisymmetric.

The *first* class is responsible for the instability of the problem under consideration. The critical Rayleigh number is calculated according to

$$Ra_{EcL}(Ta) = \min_m Ra_E(m, Ta) \tag{51}$$

for the fixed Prandtl number and radii ratio η .

Unfortunately, far more numerical effort is needed to perform the stability analysis in the rotating case in contrast to the nonrotating case considered above. Therefore, we limit the stability investigations to cases with $\eta = 0.5$, $Pr = 176$, $\Delta T = 0.4$ K, $\Delta T = 1.7$ K, and $\Delta T = 3$ K, which are relevant for the GeoFlow experiment. The critical Rayleigh numbers as a function of the Taylor number are presented in Fig. 7. The basic flow becomes unstable with respect to the nonaxisymmetric perturbations with $m_c > 0$: the critical

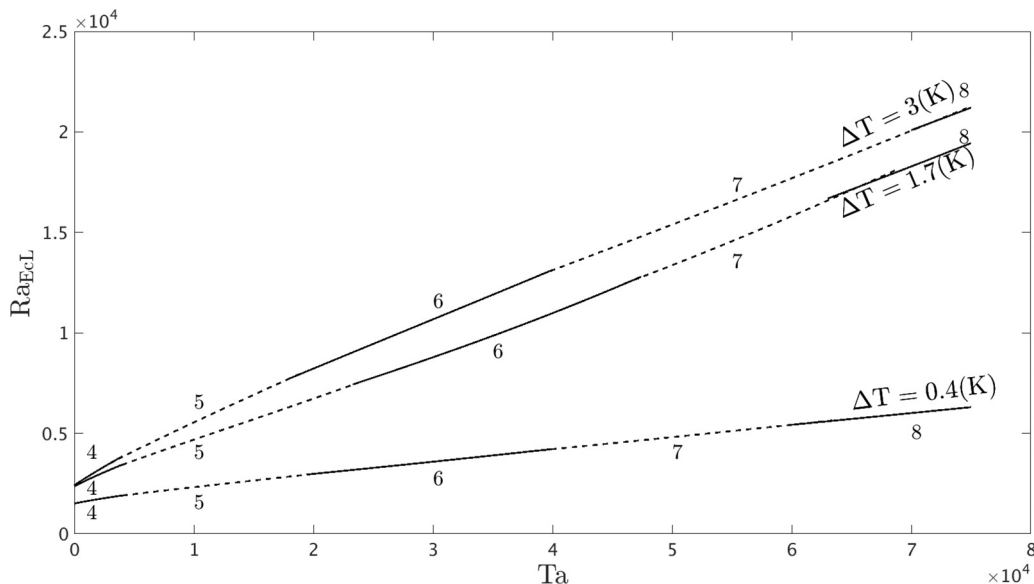


FIG. 7. Critical Rayleigh numbers vs. Taylor number for $\eta = 0.5$ and $Pr = 176$. The numbers in the vicinity of the stability curves are the critical azimuthal wave numbers m_c .

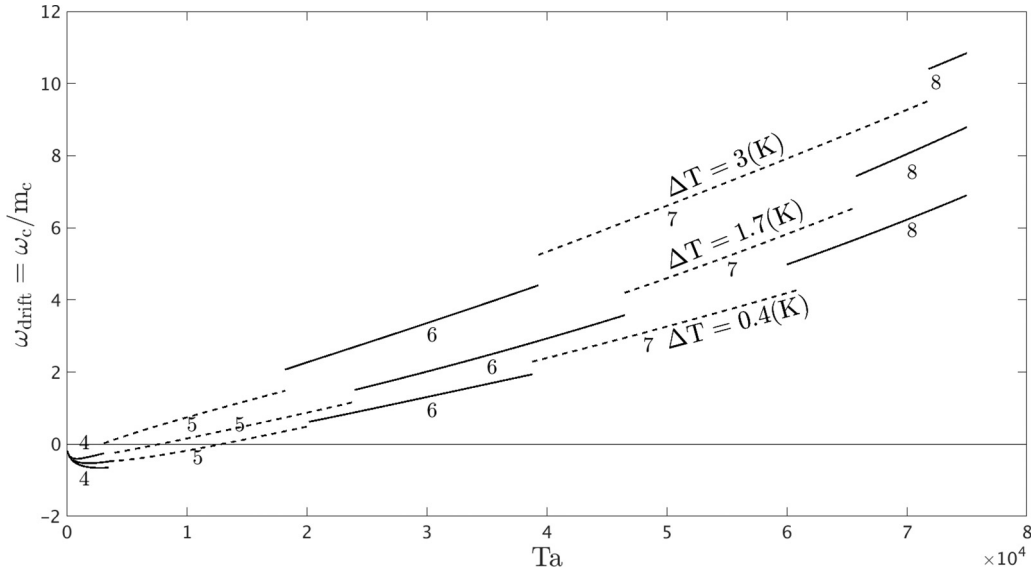


FIG. 8. Drift velocity vs. Taylor number. The numbers in the vicinity of the drift velocity curves are the critical azimuthal wave numbers m_c .

azimuthal wave number varies between $m_c = 4$ for small Taylor numbers and $m_c = 7, 8$ for Taylor numbers in the order of 10^4 . Note that for $Ta > 2.0 \times 10^4$ the critical Rayleigh number can be approximated according to linear law, i.e., $Ra_{EeL} \sim Ta$. The instability sets in as an oscillating bifurcation. The perturbative flow drifts with a velocity (Fig. 8) of $\omega_{drift} = \omega_c/m_c$, where ω_c is the frequency of the dominant perturbation, corresponding to the wave number m_c . An interesting feature of the drift can be detected for small Taylor numbers. Whereas the spherical gap rotates counter-clockwise, the perturbative flow drifts clockwise (Fig. 8). An increase in Ta leads to the change of direction and the higher magnitude of the drift velocity.

It is useful to express the nondimensional parameters such as the Rayleigh number, Taylor number, and drift velocity, ω_{drift} , in terms of the voltage, V_{rms} , rotation rate Ω , and ω_{drift}^{dim} (Table II). This makes it more convenient to compare the results with the GeoFlow experiment. The rotation has a strongly stabilizing effect: If the Taylor number rises, then there is an increase in the critical voltage at which the transition from the basic flow into the three-dimensional flow occurs. The drift velocity of the perturbation ω_{drift}^{dim} is much lower than the rotation rate Ω .

The next issue is to follow why and where the instability occurs. Although the instability can be located by calculating

the eigenvectors, i.e., the velocity field, corresponding to Ra_{EeL} , it can also be located using the azimuthally integrated kinetic energy of the perturbation $e(r, \theta) = \frac{1}{2} \int \mathbf{u}^2 r \sin \theta d\phi$, which is a more convenient tool for analyzing the origin of the instability (Fig. 9). It is important to note that although we deal with the oscillatory bifurcation, the kinetic energy of the perturbative flow remains constant. Therefore, one snapshot is sufficient to determine that there are two regions where the instability concentrates. The first one is the shear instability that appears within the meridional flow (Fig. 9). In the next section we will see that the radial and the longitudinal velocity components of the perturbation are responsible for this instability. The second one occurs in the vicinity of the equator and is associated with the azimuthal velocity component. Although it is impossible to derive amplitudes of the supercritical flow in frames of the linear stability analysis, we are able to predict its patterns. An example of the critical perturbation with $m_c = 5$ is presented in Fig. 10.

VI. THREE-DIMENSIONAL ANALYSIS

Besides the linear instability analysis, we present also simulations of the nonlinear three-dimensional flow. Because the computational effort increases considerably with Ra_E , we consider only slightly supercritical states.

TABLE II. Connection between nondimensional characteristics (Ra_{EeL} , ω_{drift}) of the instability and dimensional characteristics (V_{rms} , ω_{drift}^{dim}). m_c indicate the critical azimuthal wave numbers.

ΔT (K)	Ta	Ω (s ⁻¹)	Ra_{EeL}	$V_{rms,crit}$ (V)	m_c	ω_{drift}	ω_{drift}^{dim} (s ⁻¹)
0.4	17 200	0.8	2 800	1 982	5	0.2901	1.264×10^{-4}
0.4	68 800	1.6	5 940	2 887	8	6.067	2.643×10^{-3}
1.7	17 200	0.8	6 149	1 425	5	0.6670	2.905×10^{-4}
1.7	68 800	1.6	18 006	2 438	8	7.868	3.428×10^{-3}
3	17 200	0.8	7 513	1 186	5	1.394	6.073×10^{-4}
3	68 800	1.6	19 773	1 923	7	9.104	9.325×10^{-3}

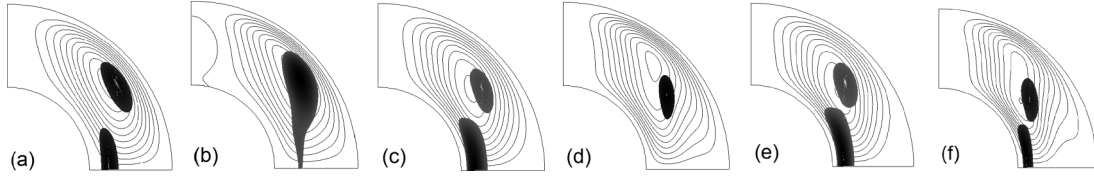


FIG. 9. As in Figs. 3(a)–3(f), the basic meridional circulation is shown. The gray shading indicates the location of the azimuthally integrated kinetic energy $e(r, \theta)$ of the perturbation. Both the basic meridional circulation and $e(r, \theta)$ are shown at the critical Rayleigh number.

The goals of the three-dimensional investigation are as follows. First, we check the results of the linear instability analysis. If the Rayleigh number exceeds the critical value, then the basic flow must become unstable and take on the 3D structure according to the results predicted in the previous section with the same characteristics: ℓ_c in the nonrotating case and m_c and ω_c for $Ta > 0$. Second, we have to investigate whether we are dealing with subcritical or supercritical bifurcation by analyzing the behavior of the amplitude. The third reason, why the nonlinear equilibration is essential, is the possibility to follow how the internal heating influences the heat transfer.

A. Three-dimensional analysis: Nonrotating case ($Ta = 0$)

Beginning with the purely dielectrical heating ($\Delta T = 0$ K) without rotation, we choose a total kinetic energy as a control parameter of the supercritical flow. The amplitude a is defined according to

$$a^2 = E = \frac{1}{2} \int_V \mathbf{U}^2 dV = \sum_{\ell=1}^{LU} E_\ell = \sum_{\ell=1}^{LU} \sum_{m=0}^{\ell} \epsilon_{\ell m}. \quad (52)$$

Introducing expressions

$$\hat{f}_{c,slm}[t, r(z)] = \sum_{k=1}^{KU+4} f_{c,sklm}(t) T_{k-1}(z), \quad (53)$$

$$\hat{e}_{c,slm}[t, r(z)] = \sum_{k=1}^{KU+2} e_{c,sklm}(t) T_{k-1}(z), \quad (54)$$

energies $\epsilon_{\ell m}$ have been calculated analytically,

$$\begin{aligned} \epsilon_{\ell m}(t) = & \left(\ell^2(\ell+1)^2 \int_{\eta/(1-\eta)}^{1/(1-\eta)} \frac{\hat{f}_{\ell m}^2(t, r)}{r^2} dr \right. \\ & + \ell(\ell+1) \int_{\eta/(1-\eta)}^{1/(1-\eta)} \hat{e}_{\ell m}^2(t, r) dr \\ & \left. + \ell(\ell+1) \int_{\eta/(1-\eta)}^{1/(1-\eta)} \hat{f}_{\ell m}^2(t, r) dr \right) C_{\ell m}, \quad (55) \end{aligned}$$

where $\hat{f}_{\ell m}^2(t, r) = \hat{f}_{c\ell m}^2(t, r) + \hat{f}_{s\ell m}^2(t, r)$ [the same relations are valid for $\hat{e}_{\ell m}^2(t, r)$ and $\hat{f}_{\ell m}^2(t, r)$], and $C_{\ell 0} = \frac{2\pi}{2\ell+1}$ for $m = 0$, $C_{\ell m} = \frac{\pi}{2\ell+1} \frac{(\ell+m)!}{(\ell-m)!}$ for $m > 0$.

The behavior of the amplitude $a^2(R_H)$ for $\eta = 0.5$ and $Pr = 176$ is presented in Fig. 11 (left). According to the three-dimensional calculations, the basic flow suddenly becomes unstable with respect to the infinitesimal perturbations if the Rayleigh number exceeds the critical value $R_H > R_{HcL}$ in agreement with the results given by linear instability theory. If $R_{Hc} < R_H < R_{HcL}$, then the basic flow remains stable regarding small perturbations but becomes unstable with respect to the perturbations with finite amplitude. The transition from the convective branch on the branch, corresponding to the basic state $a = 0$, occurs at $R_{Hc} = 1.566 \times 10^6$. The instability sets in as *subcritical* bifurcation, which causes the hysteresis effect.

Let us consider the bifurcation diagram in detail (Fig. 11, left). The conducting state has been used as the initial condition. Furthermore, the mode corresponding to the critical one is perturbed to obtain the three-dimensional flow. If the Rayleigh-Roberts number is less than $R_H < 1.7 \times 10^6$, then

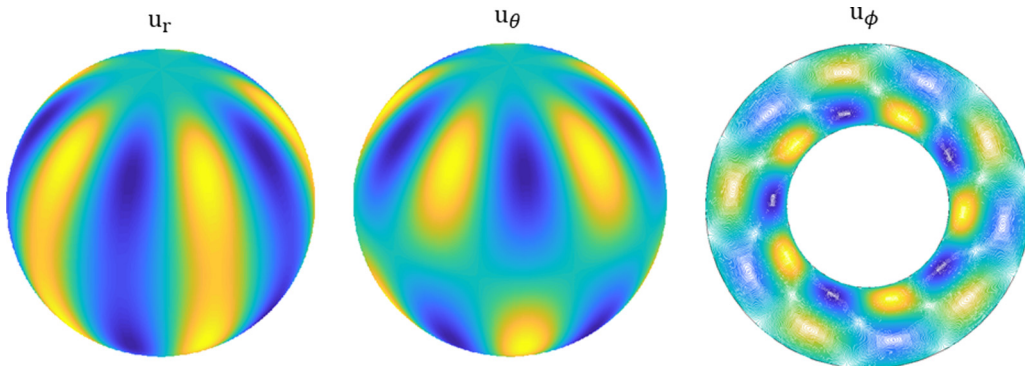


FIG. 10. Velocity components of perturbation u_r , u_θ at $r = 1.6$ and u_ϕ at the equator for $Ra_{EcL} = 2800$, $Ta = 17200$, $\Delta T = 0.4$ K, and $m_c = 5$.

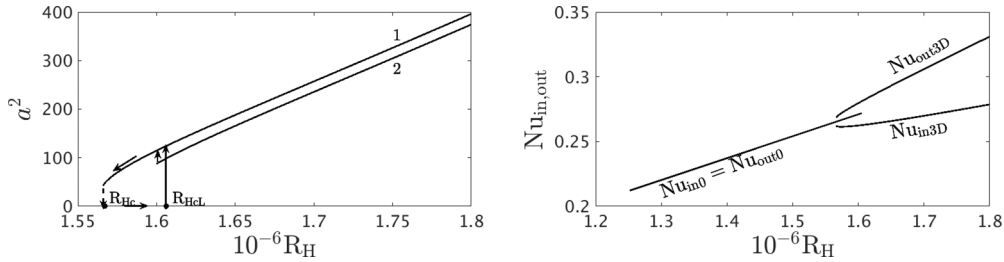


FIG. 11. The bifurcation diagram for the purely dielectrical heating flow is shown left. Arrows detect the hysteresis loop and transition between branches. The Nusselt number behavior is presented right.

we obtain the steady 3D flow in octahedral form (bifurcation branch 1). Starting at $R_H > 1.7 \times 10^6$ we again obtain a steady three-dimensional flow but with a pentagonal structure (bifurcation branch 2). Moving along this branch and decreasing R_H , we jump on the first bifurcation branch at $R_H = 1.6 \times 10^6$. This transition is shown with small arrow. Hence, an important feature of the flow caused by the purely dielectrical heating is the nonuniqueness of the solution. An example of two different flows at $R_H = 1.75 \times 10^6$ is presented in Fig. 12. Energies E_ℓ that make the greatest contribution are listed in Table III.

Note that the mode with $\ell_c = 4$ is dominantly in agreement with linear stability theory. A similar result has been detected in the case of convection ($H_E = 0$) [6].

The heat transfer results are summarized in (Fig. 11, right). Whereas the Nusselt number is the same for the basic flow for both surfaces $Nu_{in0} = Nu_{out0}$, in the three-dimensional case the heat transfer is divided into two branches. Although

the Nusselt number, Nu_{in3D} , increases with Ra_E , the energy flux decreases considerably compared to the basic state. The behavior of the Nu_{out3D} completely differs from Nu_{out0} . The system loses the energy from the outer surface much faster if the flow becomes a three-dimensional structure.

The subcritical bifurcation scenario is detected in the case of convection, also influenced by the dielectrical heating with the applied $\Delta T = 0.4$ K between spherical surfaces (Fig. 13, left). As in the case of the purely dielectrical heating, the basic flow becomes abruptly unstable for $Ra_E > Ra_{EcL} = 1511.32$ in accordance with lines stability theory. The three-dimensional flow is stable with the interval $1507 = Ra_{Ec} < Ra_E < Ra_{EcL}$. The hysteresis effect is much weaker in contrast to the purely dielectrical heating. Indeed, the difference $\Delta = (Ra_{EcL} - Ra_{Ec})/Ra_{EcL} = 0.26\%$ is much smaller than $\Delta_H = (R_{HcL} - R_{Hc})/R_{HcL} = 2.1\%$. In contrast to the purely dielectrical heating case, only one flow structure, the octahedral structure, is found. The similar Nusselt number shape, corresponding to the three-dimensional flow, has been observed in the convective case (Fig. 13, right).

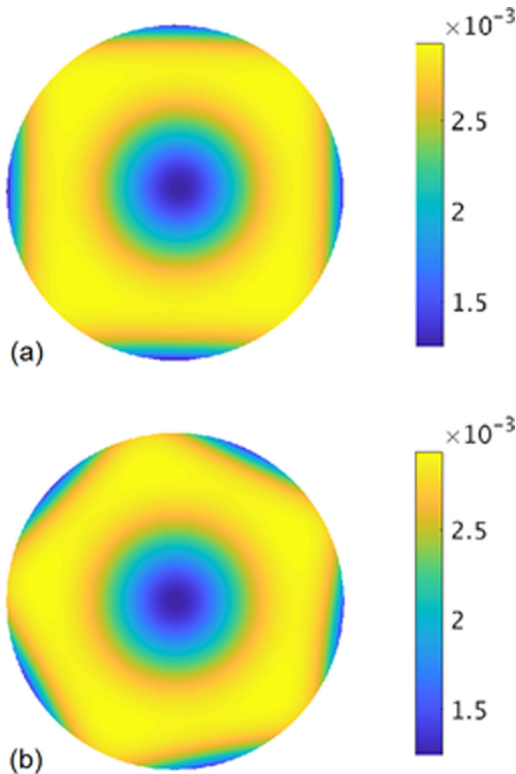


FIG. 12. Nonuniqueness of the solution: the temperature distribution for $R_H = 1.75 \times 10^6$ at $r = 1.5$.

B. Three-dimensional analysis: Rotating case ($Ta > 0$)

We shall now present the results in the rotating case, comparing them with the results given by linear stability theory. Some examples are shown in Figs. 14(a)–14(c). The longitudinal velocity component of the three-dimensional flow, U_θ , with the $m = 8$ structure is presented in Fig. 14 a for a slightly supercritical Rayleigh number ($Ra_{EcL} = 5904$). The flow drifts with $\omega_{drift}^{3D} = 6.1511$, which is in good agreement with stability results ($\omega_{drift} = 6.0672$). The kinetic energy $E(r, \theta) = \frac{1}{2} \int U^2 r \sin \theta d\phi$ [Fig. 15(b) mode $m = 0$, corresponding to the axisymmetric basic flow and nonlinear interactions because of the nonlinear term in the Navier-Stokes equation, is subtracted] is concentrated within the meridional flow, confirming the spatial characteristics of the stability analysis [Fig. 9(b)]. Interestingly, the distribution

TABLE III. Most dominant kinetic energies for $\eta = 0.5$, $R_H = 1.75 \times 10^6$, and $Pr = 176$ for the octahedral structure (left) and the pentagonal structure (right).

ℓ	E_ℓ	ℓ	E_ℓ
4	299.15	4	186.68
6	18.81	5	101.97
8	8.089	7	8.5822
10	0.1724	8	4.7228

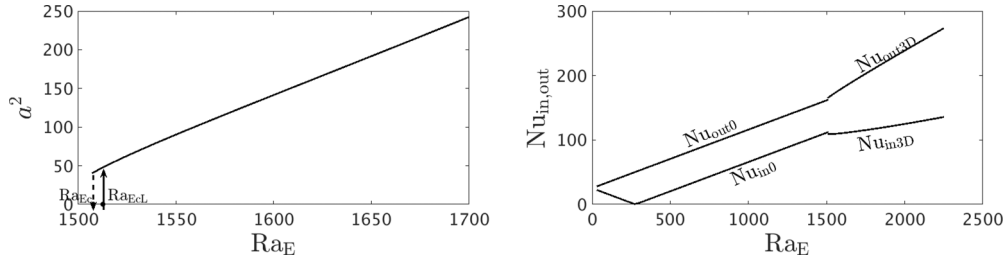


FIG. 13. Left-bifurcation diagram for the flow, caused by the dielectrical heating with convection, right-Nusselt numbers for $\eta = 0.5$ and $\Delta T = 0.4$ K.

of $E(r, \theta)$ ($E_{\max} = 68$) almost coincides with $E_{r\theta}(r, \theta) = \frac{1}{2} \int (U_r^2 + U_\theta^2) r \sin \theta d\phi$ ($E_{r\theta\max} = 66$), emphasizing that the radial and longitudinal velocity components make a most essential contribution into the shear instability.

Two further examples of the supercritical flows are presented in Figs. 14(b) and 14(c). The $m = 5$ and $m = 7$ solutions drift with $\omega_{\text{drift}}^{3D} = 0.6561$ ($\omega_{\text{drift}} = 0.6662$) and $\omega_{\text{drift}}^{3D} = 9.1776$ ($\omega_{\text{drift}} = 9.1044$), correspondingly (Fig. 8). The 3D supercritical solution is symmetrical with respect to the equator and obeys Eq. (50) in accordance with stability results.

The maximum kinetic energy for the $m_c = 5$ solution is now located in the boundary layer in the vicinity of the equator [Fig. 15(c)], which is in accordance with linear stability analysis [Fig. 9(c)]. The instability is associated with the azimuthal component U_ϕ and can be expressed in terms of $E_\phi(r, \theta) = \frac{1}{2} \int U_\phi^2 r \sin \theta d\phi$ ($E_{\max} = 16.5$, $E_{\phi\max} = 14.5$ at the equator).

The kinetic energy for the $m_c = 7$ solution has two maxima [Fig. 15(f)]. Hence, the instability locates in both places described above as linear analysis predicts [Fig. 9(f)]. The corresponding values of the energies are $E_{\max} = 37$, $E_{\phi\max} = 30.5$ at the equator, $E_{\max} = 33.5$, $E_{r\theta\max} = 32.5$ within the meridional flow.

The bifurcation scenario in the rotating case differs from the scenario considered above. Introducing an amplitude according to the expression

$$a^2 = E = \frac{1}{2} \int_V \mathbf{U}^2 dV = \sum_{m=1} E(m) = \sum_{m=1} \sum_{\ell=m} \epsilon_{\ell m} \quad (56)$$

and calculating the amplitude as a function of the supercriticality $\delta = (Ra_E - Ra_{EcL})/Ra_{EcL}$, which is more useful as the control parameter in the rotating case, we note that now we are

dealing with the *supercritical* bifurcation. The basic steady flow loses its stability when $\delta > 0$. The amplitude of the supercritical flow can be expressed according to the Landau equation

$$a^2 = C\delta, \quad (57)$$

with $C(\Delta T = 0.4K) = 2420.64$, $C(\Delta T = 1.7K) = 1624.09$, and $C(\Delta T = 3K) = 1892.25$ [Fig. 16(a)].

The Nusselt number shape undergoes a break in the Ra_{EcL} , confirming that the stability results are correct [Figs. 16(b)–16(d)]. The numerically obtained Nusselt numbers $Nu_{\text{in}3D}(Ra_E)$ and $Nu_{\text{out}3D}(Ra_E)$ can be approximated for the fixed Taylor number $Ta = 17\,200$ and $\Delta T = 0.4$ K, $\Delta T = 1.7$ K, and $\Delta T = 3$ K as follows:

$$\begin{aligned} Nu_{\text{in}3D} &= a_{\text{in}3D} Ra_E + b_{\text{in}3D}, \\ Nu_{\text{out}3D} &= a_{\text{out}3D} Ra_E + b_{\text{out}3D}. \end{aligned} \quad (58)$$

The constants are presented in Table IV.

C. Comparison with experiment

The critical voltages $V_{\text{rms,crit}}$ are compared with outcomes of the GeoFlow experiment (2008–2018). The experimental setup is based on a spherical capacitor with a radius ratio $\eta = 0.5$, where convective flows are investigated under micro-gravity conditions on the ISS [7,22]. By reason of design constraints, the outer radius of the fluid cell measures 0.027 m and the inner radius 0.0135 m. GeoFlow utilizes the dielectrophoretic force to establish a radial force field with voltages between the minimum value of $V_{\text{rms}} = 1272$ V and the maximum value of $V_{\text{rms}} = 4596$ V. Figure 17 depicts a vertical cut through the GeoFlow experiment. A numerical

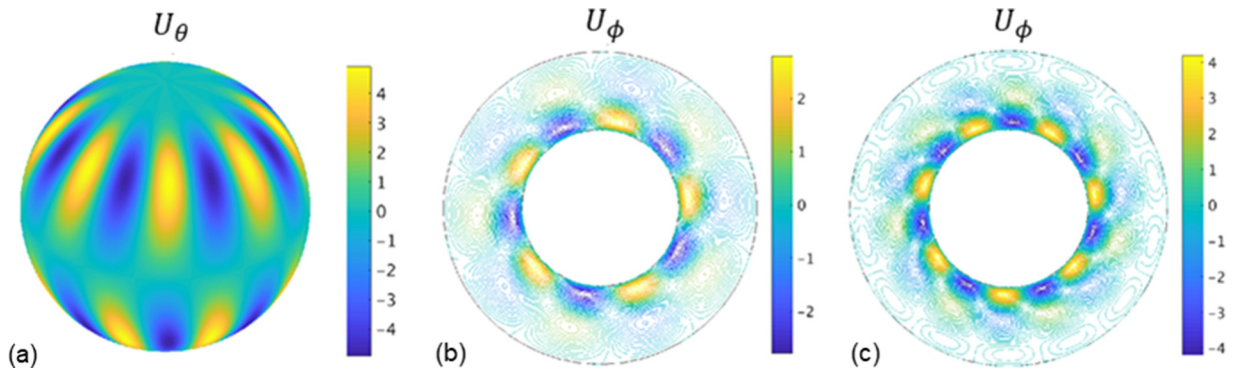


FIG. 14. (a) U_θ at $r = 1.67$ for $\Delta T = 0.4$ K, $Ta = 68\,000$, $Ra_E = 6\,000$; (b, c) U_ϕ at the equator for $\Delta T = 1.7$ K, $Ta = 17\,200$, $Ra_E = 6\,220$ and $\Delta T = 3$ K, $Ta = 68\,800$, $Ra_E = 20\,050$, correspondingly.

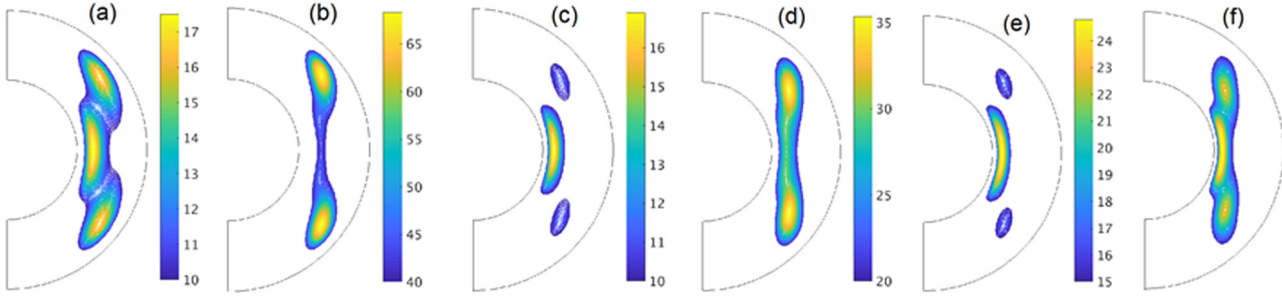


FIG. 15. Azimuthally integrated kinetic energy $E(r, \theta)$ of the three-dimensional flow: (a) $\Delta T = 0.4$ K, $Ta = 17\,200$, $Ra_E = 2\,830$, (b) $\Delta T = 0.4$ K, $Ta = 68\,800$, $Ra_E = 6\,000$, (c) $\Delta T = 1.7$ K, $Ta = 17\,200$, $Ra_E = 6\,220$, (d) $\Delta T = 1.7$ K, $Ta = 68\,800$, $Ra_E = 18\,200$, (e) $\Delta T = 3$ K, $Ta = 17\,200$, $Ra_E = 7\,620$, (f) $\Delta T = 3$ K, $Ta = 68\,800$, $Ra_E = 20\,050$.

simulation visualizes the fluid cell. Heating and cooling circuits thermalize the inner and outer shells, respectively.

The working fluid 1-Nonanol is strongly susceptible to dielectric heating with rates up to 0.1 K/s. The temperature difference across the gap can be adjusted between $0.4\text{ K} \leq \Delta T \leq 10\text{ K}$. In total, 160 experimental points with five different voltages ($V_0 = 1\,800$ V, $3\,000$ V, $4\,200$ V, $5\,400$ V, $6\,500$ V), two reference temperatures ($T_b = 293$ K, 303.5 K) and eight temperature differences ($0.4\text{ K} < \Delta T < 9.5\text{ K}$) were conducted. Each experimental point was repeated for three rotation scenarios. The rotation tray is capable of maintaining rotation frequencies of $f = 0.008$ Hz (in the following denoted as the “nonrotating case”), $f = 0.8$ Hz (medium rotation case) and $f = 1.6$ Hz (high rotation case).

A separate set of experimental points were also conducted without a temperature difference ($\Delta T = 0$ K) across the gap. In these cases $R_T \approx 8.4 \times 10^7$ [cf. Eq. (14)] for both reference temperatures. The Rayleigh-Roberts number which parametrizes internal heating ranges between $8.46 \times 10^5 < R_H < 1.10 \times 10^7$.

In the case of $\Delta T > 0$, the Rayleigh number Ra_E [cf. Eq. (22)] ranges between 1.155×10^3 and 4.471×10^5 . The

convective parameter Ra_T ranges between 1.427×10^2 and 4.962×10^4 . We find 21 experimental points where convection is dominated by the temperature difference across the gap ($Ra_E/(2Ra_T) < 1$) and 139 experimental points where internal heating is dominant ($Ra_E/(2Ra_T) > 1$).

In the following, theoretical values of the onset of convection are compared with experimental data. Interferograms of the GeoFlow experiment are used, which are able to highlight even small deviations in the refractive index and hence in the temperature field. A Wollaston shearing interferometry unit is used to visualize flows. The field of view covers about 90 degrees from the north pole to the equator, cf. Fig. 17 (yellow line and camera icon). Here, we refer to Ref. [23] for a detailed description of the interferometry unit of GeoFlow. The interferograms show a base fringe pattern, cf. Figs. 18(a) and 18(d) in the conductive case. Deviations in terms of distorted lines (highlighted in yellow) indicate convection. Two prevailing structures can be observed: (a) a butterfly pattern as result of steep convective downdrafts and (b) narrow parallel structures from sheetlike up- or downwelling. However, arbitrary combinations of both are omnipresent, especially for high Rayleigh numbers.

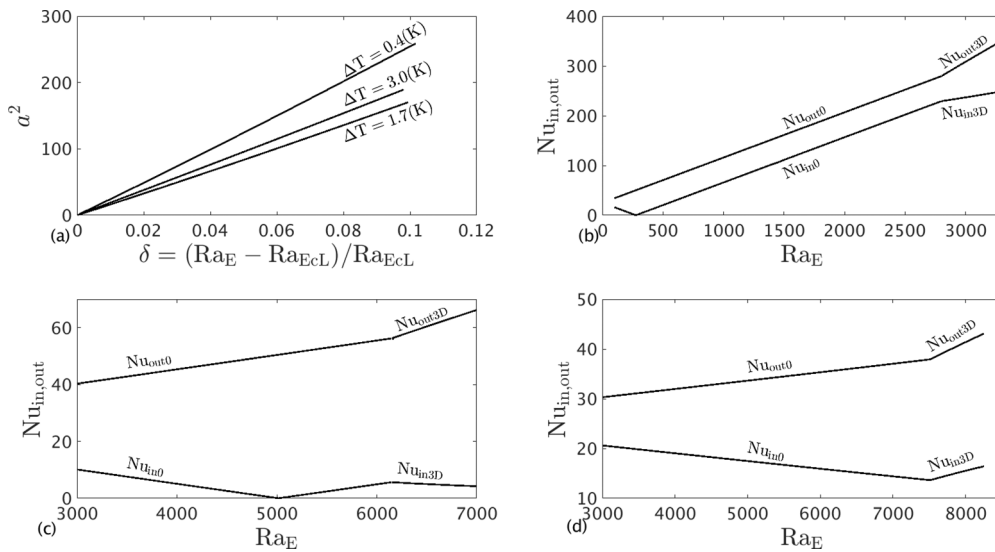


FIG. 16. (a) The amplitude of the supercritical flow and the Nusselt numbers for (b) $\Delta T = 0.4\text{ K}$, (c) $\Delta T = 1.7\text{ K}$, and (d) $\Delta T = 3\text{ K}$ for $\eta = 0.5$, $Ta = 17\,200$.

TABLE IV. Constants for the Nusselt numbers from Eq. (58).

$\Delta T(K)$	a_{in3D}	b_{in3D}	a_{out3D}	b_{out3D}
0.4	0.03905	119.80	0.1427	-119.80
1.7	-0.001760	16.46	0.01181	-16.41
3.0	0.003785	-14.77	0.007052	-15.06

Figure 18 shows interferograms of the nonrotating case with $\Delta T = 0$ K, $\Delta T = 0.4$ K and increasing voltages. The corresponding Rayleigh-Roberts numbers in the first case are $R_H = 8.4 \times 10^5$ for $V_{rms} = 1272$ V, $R_H = 2.3 \times 10^6$ for $V_{rms} = 2121$ V and $R_H = 4.6 \times 10^6$ for $V_{rms} = 2969$ V. The critical value of $R_{HcL} = 1.6 \times 10^6$ takes place between Figs. 18(a) and 18(b), occurring at $V_{rms,crit.} = 1754$ V. Figure 18(b) shows a clear distortion from the base pattern, which changes to a convective plume for higher voltages, cf Fig. 18(c). Accompanying numerical simulations [22] confirm the existence of convective cells for $V_{rms} = 2121$ V.

In the case of $\Delta T = 0.4$ K the onset is predicted at $Ra_{ECL} = 1511$, which corresponds to $V_{rms,crit.} = 1456$ V. The transition from the conductive state to the convective regime is depicted in Figs. 18(d) and 18(e), which capture the onset by experimental points with $Ra_E = 1155$ and $Ra_E = 3208$, respectively. As in the case of pure internal heating, a convective plume is found for higher voltages. The onset of convection in the case of $\Delta T = 3$ K at $V_{rms,crit.} = 671$ V cannot be verified as the lowest voltage available in the experiment is $V_{rms} = 1272$ V.

The theoretical onset of convection in the two rotating cases is validated experimentally using the interferograms presented in Fig. 19 for $\Delta T = 0.4$ K, $\Delta T = 1.7$ K, and $\Delta T = 3$ K.

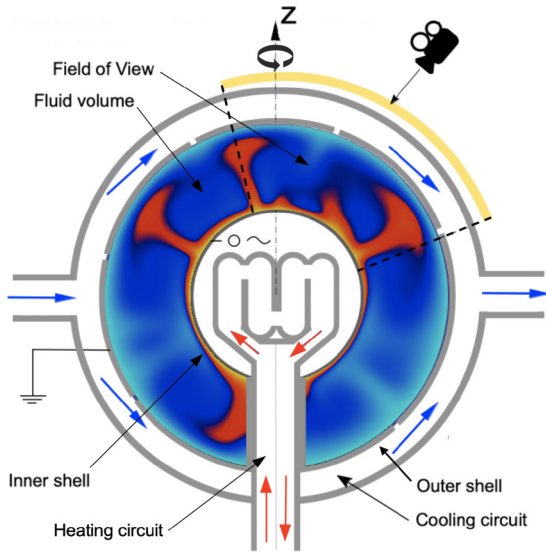


FIG. 17. Sketch of the GeoFlow experiment. The working fluid is thermalized through an inner and outer heating/cooling loop. Interferometry is used to visualize fluid flows (yellow field of view). High voltage is applied to enforce a dielectrophoretic force field, which mimics a radial gravity field. The fluid cell is visualized with a numerical simulation.

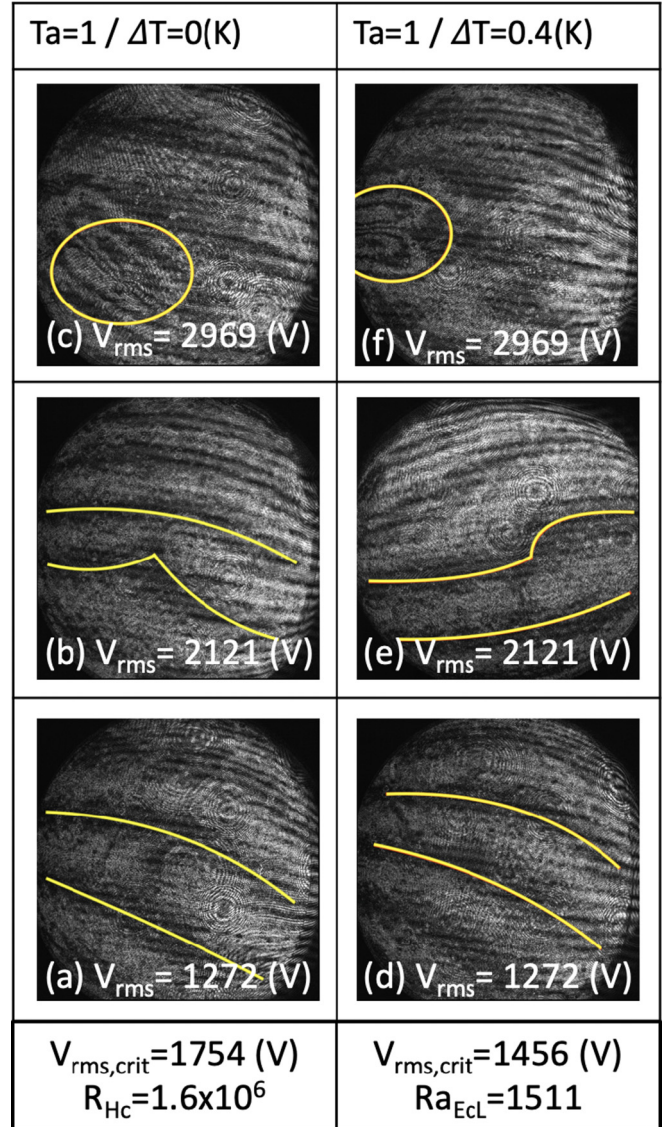


FIG. 18. Experimental interferograms for the nonrotating case for $\Delta T = 0$ K (left-hand column) and $\Delta T = 0.4$ K (right-hand column). The onset of convection is found between (a, b) and (d, e), respectively. While conductive cases show only a base fringe pattern (a, b) the convectively unstable flows appear as butterfly patterns (c, f) for $V_{rms} = 2969$ V and as distorted fringe lines (b, e) for $V_{rms} = 2121$ V. Structures are highlighted in yellow to emphasize the thermal structure.

Figure 19 depicts 12 cases, showing 11 interferograms. For the case $f = 0.8$ Hz, $\Delta T = 3$ K, no conductive experimental point is present. Here, the onset voltage is below the minimum voltage. Over the entire parameter range, the onset of convection is located within the predicted limits. However, the coarse grid of experimental points of GeoFlow makes it difficult to make more accurate statements about the convective onset. This is based on voltage increments of 921 V and temperature increments of 1.3 K. Hence, the onset cannot be captured more precisely with this setup, but with a mean deviation of 177 V. This is based on the investigation of the 42 interferograms used for this study.

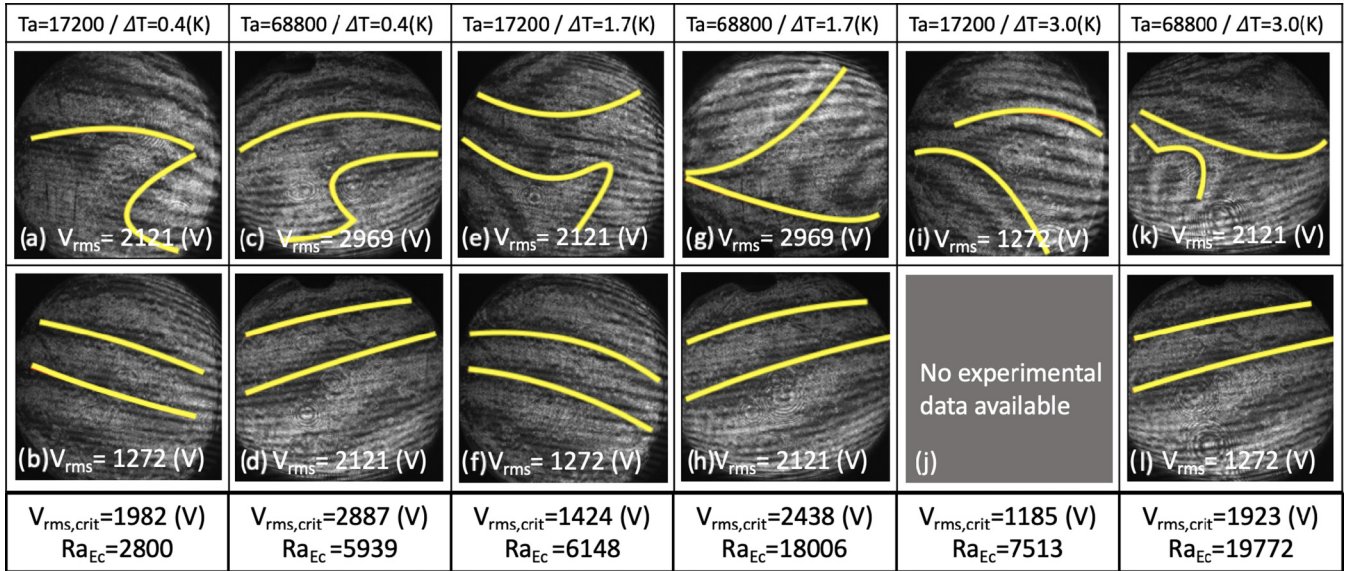


FIG. 19. Experimental interferograms for the rotating case for $\Delta T = 0.4$ K, $\Delta T = 1.7$ K, $\Delta T = 3$ K, $f = 0.8$ Hz ($Ta = 17200$), and $f = 1.6$ Hz ($Ta = 68800$); see Table II. The upper row depicts convectively unstable flows, the lower row depicts conductive cases. The onset of convection is located in between the two rows.

VII. SUMMARY AND CONCLUSIONS

Our purpose in this paper has been to investigate the influence of dielectrical heating on a convective flow under a radial force field in a nonrotating and rotating spherical gap numerically.

First, we consider the base state in the nonrotating spherical gap with $\Delta T = T_{in} - T_{out} \geq 0$. As in the Rayleigh-Bénard convection the basic flow is $\mathbf{U}_0 = 0$ and the temperature is radially dependent. The heat transfer analysis has been performed in terms of the Nusselt number. Whereas in the case of the purely dielectrical heating, i.e., $\Delta T = 0$, the Nusselt numbers or the energy fluxes that leave the domain under consideration through the surfaces are same, the situation is more difficult if the inner surface is warmer than the outer one $\Delta T > 0$. The energy flux that comes from the warmer surface due to the conduction and the energy flux, produced due to the source, have opposite directions that influences the heat transfer.

If the spherical gap rotates (we consider $\Delta T > 0$ only), then the influence of the centrifugal force leads to the formation of a steady, axisymmetric and equatorially symmetrical basic flow that must be calculated numerically. Linear stability theory is used to derive the critical Rayleigh-Roberts number ($\Delta T = 0$ K) and critical Rayleigh number ($\Delta T > 0$) at which the transition from the basic flow into the three-dimensional flow occurs. The first instability does not depend on the Prandtl number in the nonrotating case, as it does in RB convection, because the basic flow becomes unstable with respect to the steady perturbations. In the rotating case, the instability sets in as Hopf bifurcation. Moreover, the basic

flow, loses its stability with respect to the three-dimensional perturbations with positive azimuthal wave numbers $m_c > 0$.

Calculating the three-dimensional flows reveals the different behavior of the amplitude. Whereas the bifurcation is subcritical in the nonrotating case, the supercritical one is responsible for the transition if the system rotates.

The numerical results have been compared with outcomes of the GeoFlow experiment. The critical Rayleigh numbers, more precisely the critical voltages, coincide well with observational data within 177 V. Interferograms are analyzed for convection, which are highlighted as distortions in base fringe patterns.

Both numerical and experimental results show that the internal heating plays a crucial role and must be taken into account if the dielectrical fluid is subjected into the fast oscillated electric field. Further numerical investigations should clarify how the high Taylor numbers $Ta = 10^5 \div 10^7$ influence the flow structure and the heat transfer. This issue has relevance for the geophysical applications.

ACKNOWLEDGMENTS



The GeoFlow research has been funded by the European Space Agency (ESA) Grant No. AO-99-049 and by the DLR Grants No. 50 WM 0122 and No. 50 WM 0822. Furthermore, one of us (V.T.) is supported by Deutsche Forschungsgemeinschaft (DFG, Grant No. TR 986/6-1). Numerical simulations have been performed at the Heraklit cluster at the BTU Cottbus-Senftenberg.

- [1] G. Geiger and F. Busse, *Geophys. Astrophys. Fluid Dyn.* **18**, 147 (1981).
 [2] J. W. M. Ardes and F.H. Busse, *Phys. Earth. Planet. Inter.* **99**, 55 (1993).
 [3] F. Busse, *J.Fluid Mech.* **72**, 67 (1975).

- [4] W. Hirsching and F. Busse, *Geophys. Astrophys. Fluid Dyn.* **72**, 145 (1993).
 [5] D. Bercovici, G. Schubert, and G. Glatzmaier, *Geophys. Astrophys. Fluid Dyn.* **61**, 149 (1991).

- [6] F. Feudel, K. Bergemann, L. S. Tuckerman, C. Egbers, B. Futterer, M. Gellert, and R. Hollerbach, *Phys. Rev. E* **83**, 046304 (2011).
- [7] C. Egbers, W. Beyer, A. Bonhage, R. Hollerbach, and P. Beltrame, *Adv. Space Res.* **32**, 171 (2003).
- [8] L. Landau and E. M. Lifshitz, *Electrodynamics of Continuous Media, Landau Lifshitz Course of Theoretical Physics, Vol. 8, 2nd ed.* (Elsevier Butterworth-Heinemann, Burlington, MA, 1984).
- [9] R. J. Turnbull and J. R. Melcher, *Phys Fluids* **12**, 1160 (1969).
- [10] J. Melcher, *Continuum Electromechanics* (MIT Press, Cambridge, MA, 1981).
- [11] I. Yavorskaya, N. Fomina, and Y. Belyaev, *Acta Astronautica* **11**, 179 (1984).
- [12] B. Futterer, C. Egbers, N. Dahley, S. Koch, and L. Jehring, *Acta Astronautica* **66**, 193 (2010).
- [13] B. Futterer, N. Dahley, S. Koch, N. Scurtu, and C. Egbers, *Acta Astronautica* **71**, 11 (2012).
- [14] B. Futterer, A. Krebs, A.-C. Plesa, F. Zaussinger, R. Hollerbach, D. Breuer, and C. Egbers, *J. Fluid Mech.* **735**, 647 (2013).
- [15] V. Travnikov, C. Egbers, and R. Hollerbach, *Adv. Space Res.* **32**, 181 (2003).
- [16] B. L. Smorodin, *Tech. Phys. Lett.* **27**, 1062 (2001).
- [17] B. L. Smorodin and V. G. Velarde, *J. Electrostat.* **50**, 205 (2001).
- [18] R. Hollerbach, *Int. J. Numer. Meth. Fluids* **732**, 773 (2000).
- [19] P. Roberts, *Q. J. Mech. Appl. Math* **22**, 211 (1969).
- [20] H. Yoshikawa, O. Crumeyrolle, and I. Mutabazi, *Phys Fluids* **25**, 024106 (2013).
- [21] V. Travnikov, O. Crumeyrolle, and I. Mutabazi, *Phys Fluids* **27**, 054103 (2015).
- [22] F. Zaussinger, P. Haun, M. Neben, T. Seelig, V. Travnikov, C. Egbers, H. Yoshikawa, and I. Mutabazi, *Phys. Rev. Fluids* **3**, 093501 (2018).
- [23] F. Zaussinger, A. Krebs, V. Travnikov, and C. Egbers, *Adv. Space Res.* **60**, 1327 (2017).

Rotating spherical gap convection in the GeoFlow International Space Station (ISS) experiment

Florian Zaussinger ^{*}, Peter Haun , Peter S. B. Szabo, Vadim Travnikov, Mustafa Al Kawwas, and Christoph Egbers
*Brandenburg University of Technology Cottbus-Senftenberg,
Department of Aerodynamics and Fluid Mechanics, D-03046 Cottbus, Germany*



(Received 25 March 2019; accepted 27 May 2020; published 19 June 2020)

Thermal convection in a rotating spherical gap is investigated using numerical simulations and compared with results of the GeoFlow ISS experiment. To induce convection, a radial buoyancy force field is established by using the dielectrophoretic effect from a high-frequency alternating electric field. Two heating sources are implemented. One source is a temperature difference across the gap and the other is the internal dielectric heating of the working fluid. To distinguish both heating sources a heating parameter, λ , is introduced that is varied together with the electric Rayleigh number, L , and Ekman number, $Ek \approx 10^{-3}$. The governing thermoelectro hydrodynamic equations are analyzed via a linear stability analysis and by three-dimensional numerical simulations. The results are compared with experimental data of the GeoFlow experiment which show that the threshold of convection and the occurrence of global columnar cells agreed with the theoretical predictions. In addition the observed fluid flow showed non-Gaussian characteristics which are described by the quasinormal approximation. The overall flow phenomena are based on polar plumes and equatorial confined columnar cells and in addition are influenced by internal dielectric heating.

DOI: [10.1103/PhysRevFluids.5.063502](https://doi.org/10.1103/PhysRevFluids.5.063502)

I. INTRODUCTION

Internal heating processes in rotating spherical gaps are of great interest for geophysical and astrophysical applications. Important sources of internal heating are thermonuclear reactions (e.g., in stars), tidal heating, and gravitational heating (e.g., in moons and gas giants) or radioactive decay in terrestrial planets. Internal heating is an important component of hydrostatic equilibrium within stars which establishes the radiative pressure and determines the evolution of the entire body. For example, tidal heating is assumed to increase the heat flux of Jupiter's moon Europa. This leads to the possibility of fluid-filled basins and even of cryovolcanism [1]. The thermal energy release of planets is a key feature which can also be observed in the core of the Earth [2] or Venus [3].

Theoretical and numerical analysis of internal heating in spherical gap geometries has been intensively studied with particular focus on convection in the Earth's mantle [4,5]. However, large Prandtl numbers and large viscosity contrasts render it complicated to capture geophysically relevant convection in laboratory experiments. To overcome these limitations, results are based mainly on fluids with moderate Prandtl numbers ($Pr < 200$) and extrapolated to the geophysically relevant regime of $Pr \rightarrow \infty$ [6–8].

So far, only a few convection experiments have been performed under the influence of internal heating. Limare *et al.* [9] studied highly viscous fluids over three orders of magnitudes of the

*florian.zaussinger@b-tu.de

Rayleigh-Roberts number, Ra_H , and over two orders of magnitudes of Pr . Their work provided the first cross validation of convection with internal heating. Fourel *et al.* [10] improved this experiment by introducing a compositional gradient to study heterogeneities assumed to be in the Earth's lower mantle [11]. The interaction between the two internally heated layers provide a vast variety of convective patterns. Internal heating is not only interesting from an academic point of view, it is also used in several industrial applications such as microwave ovens, mixed convection devices for cooking, to melt glass, process food or even to dry items.

Internal heating-induced convection in the spherical gap geometry has been studied by Zaussinger *et al.* [12] using numerical simulations and experimentally measured data from the GeoFlow IIc experiment [13]. Experimental and numerical interferograms of GeoFlow provided information to test properties of the electrohydrodynamical (EHD) model. They also observed a thermal plume-like distribution and a parabolic mean temperature profile in the radial direction. However, an analysis of rotational effects and a temperature difference between the inner and outer shell were not included in the study. Nonetheless, both of these properties are important for convection in stellar interiors [14] and in planets [15]. An extension to the cylindrical geometry was performed by Travis and Olson [16] that studied a temperature difference across the annulus in the presence of a dielectric internal heating source. A large parameter regime was investigated focusing on fluid flow that was characterized by Ra_H . A scaling law in planar geometry for mixed heating was studied by Vilella and Deschamps [17]. However, these results cannot be directly transferred to the EHD model where the sign of the temperature gradient may change the direction of the buoyancy term.

Thermo-EHD establishes a force field with the dielectrophoretic acceleration as consequence. This acceleration can be used to drive and control fluid motion. The pioneering work on the EHD model in a rectangular cavity was published by Roberts [18] and Turnbull [19] in the late 1960s. Both investigated the stability of the conductive state even in the absence of buoyancy which is an important limitation for space applications. Since then, this theoretical work has been extended and tested by laboratory experiments, see Refs. [20–22]. Heat transfer in a planar EHD system under microgravity conditions was investigated by Yoshikawa *et al.* [23] and Fogaing *et al.* [24]. They compared the heat flux of Rayleigh-Bénard (RB) convection with EHD convection for a large range of Prandtl numbers and explained that differences are due to thermal perturbations induced by the electric field. EHD convection in a spherical capacitor was studied without rotation [12,25] and finally, in the AtmoFlow experiment, with rotation [26]. The GeoFlow experiment was performed over eight years (from 2008 to 2016) on the ISS. The first mission, GeoFlow I, used a silicon oil, M5, to investigate the dynamics of an idealized Earth's core [27]. The second mission, GeoFlow II, operated on the ISS from 2011 to 2018 and studied mantellike dynamics of an idealized Earth with 1-Nonanol as a working fluid. It operated over three scientific campaigns: GeoFlows IIa, IIb, and IIc. However, only the GeoFlow IIc campaign operated with a frame rate of 10 Hz. All other campaigns used 1 Hz or less.

The analogy between the EHD model instability and the RB model instability is violated by two processes: first, the *thermoelectric feedback*, which generates perturbation components in the electric gravity [28]. This feedback is a result of the Gauss equation which couples the temperature-dependent permittivity and the electric field. The second process is *dielectric heating*, a result of the rotation of molecules under a quickly alternating electric field. While dielectric heating occurs in many working fluids, it has not yet been investigated in detail in the EHD models. Dielectric heating is not yet fully controllable and can lead to unpredictable hot spots and damage [29,30].

The main objective of this work is the investigation of convection due to the dielectrophoretic force in a rotating spherical gap with the focus on the influence of dielectric heating. This paper is an extension of the authors' previous work presented by Zaussinger *et al.* [12] which investigated the nonrotating case. For this purpose, the higher statistical moments of numerical simulations are analyzed to reveal the influence of rotation and internal heating. The findings are then compared with the experimental data of the GeoFlow II mission.

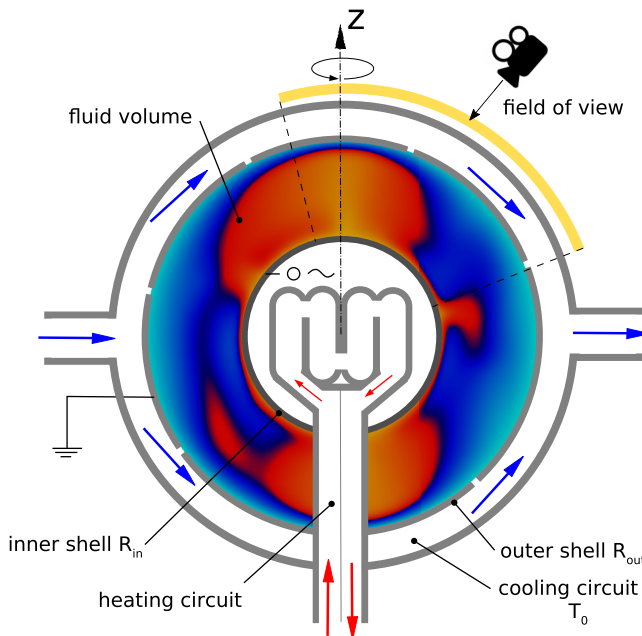


FIG. 1. Schematic cross section of the GeoFlow experimental setup showing a numerically calculated temperature distribution over the gap.

This paper is outlined as follows: The general EHD model and governing equations for the rotating spherical gap are presented in Sec. II, whereas the GeoFlow experiment and numerical methods are described in Sec. III. Analytic results and a detailed statistical description of the fluid flow in the rotating spherical gap are given in Secs. IV and V, respectively. This includes a comparison between numerical simulations and experimental interferograms. A critical discussion of the results and some concluding remarks are given at the end.

II. MODEL FORMULATION

A spherical capacitor with gap width $d = R_{\text{out}} - R_{\text{in}}$, with the same physical specifications as the GeoFlow experiment is filled with a dielectric fluid. The temperature field is imposed (a) with a temperature difference between the inner and outer shell with $\Delta T = T_{\text{in}} - T_0 > 0$ and (b) by an internal heat source which includes dielectric heating. A cross-section schematic of the experiment is shown in Fig. 1. We assume an electrically linear quasielectrostatic field acting on an incompressible dielectric fluid such that the net force on each dipole is given by the *Kelvin polarization force density* $\mathbf{F} = (\epsilon - \epsilon_0)\mathbf{E} \cdot \nabla \mathbf{E}$, where ϵ is the temperature dependent permittivity, ϵ_0 the vacuum permittivity, and \mathbf{E} the electric field.

Thus, the electric *Korteweg-Helmholtz force density* describes the force acting on the fluid and is valid for the given assumptions according to Refs. [12,28,31,32] and written as

$$\mathbf{F}_{\text{KH}} = \rho_f \mathbf{E} - \frac{1}{2} |\mathbf{E}|^2 \nabla \epsilon + \nabla \left(\frac{1}{2} \rho \frac{\partial \epsilon}{\partial \rho} |\mathbf{E}|^2 \right). \quad (1)$$

where ρ is the density. The first term on the right-hand side of the equation represents the Coulomb force, the second term the dielectrophoretic force \mathbf{F}_{DEP} , and the last term the electrostrictive force defining the electrostrictive pressure. A detailed description of the derivation of \mathbf{F}_{KH} is given in Melcher [33].

The fluid is considered to not carry free charges, so that $\rho_f = 0$ and the Coulomb force vanishes. The electrostrictive pressure will be combined with the hydrodynamic pressure in the incompressible momentum equation.

An alternating electric field with potential $\Phi(t) = 2V_{\text{rms}} \cos(2\pi ft)$ is applied at one electrode where f is the ac frequency and V_{rms} the root-mean-square capacitor voltage. This model of the electrostatic equilibrium is justified for $\tau_e^{-1} \ll f \ll d/c$, where τ_e is the charge relaxation time and c is the speed of light [18].

The dielectric loss is given by the power dissipation per unit mass, written as

$$H = \frac{2\pi f \epsilon \tan \delta |\mathbf{E}|^2}{c_p \rho}, \quad (2)$$

where $\tan \delta$ is the ratio between the imaginary and the real part of the permittivity and called the dielectric loss factor [34] and c_p is the specific heat capacity at constant pressure.

A. Governing equations

The equations describing the fluid flow are based on the Oberbeck-Boussinesq approximation (OBA). The OBA assumes low expansion rates with temperature $\alpha \Delta T \ll 1$, where α is the thermal expansion coefficient with a low thermoelectric parameter $e \Delta T \ll 1$, where $e = -\frac{1}{\epsilon} \frac{\partial \epsilon}{\partial T}$ is the thermal permittivity coefficient that decreases with increasing temperature [28]. Under these conditions, the OBA is valid for density $\rho = \rho_0 [1 - \alpha(T - T_0)]$ and permittivity $\epsilon = \epsilon_0 \epsilon_r [1 - e(T - T_0)]$, where ϵ_r is the relative permittivity at reference temperature T_0 .

The problem can now be described with the Navier-Stokes equation by considering the above formulations as

$$\frac{\partial \mathbf{u}}{\partial t} + (\mathbf{u} \cdot \nabla) \mathbf{u} = -\frac{1}{\rho_0} \nabla p - \frac{1}{2\rho_0} |\mathbf{E}|^2 \nabla \epsilon - 2\boldsymbol{\Omega} \times \mathbf{u} - \frac{\rho}{\rho_0} \boldsymbol{\Omega} \times (\boldsymbol{\Omega} \times \mathbf{r}) + \nu \nabla^2 \mathbf{u}, \quad (3)$$

where \mathbf{u} is the velocity, p the pressure, $\boldsymbol{\Omega}$ the rotation vector, \mathbf{r} the position vector, and ν the kinematic viscosity. The temperature equation is

$$\frac{\partial T}{\partial t} + (\mathbf{u} \cdot \nabla) T = \kappa_T \nabla^2 T + H, \quad (4)$$

where T is the temperature and κ_T the thermal diffusivity. Mass conservation is given by the continuity equation $\nabla \cdot \mathbf{u} = 0$. The nonuniform electric field and the thermoelectric feedback is calculated via the Gauss equation [23],

$$\nabla \cdot (\epsilon \mathbf{E}) = 0. \quad (5)$$

Following Eq. (5) above, the direction of the \mathbf{F}_{DEP} is toward the permittivity gradient and is therefore collinear with the electrostatic energy stored in the fluid [28].

We now derive the dimensionless governing equations which are obtained by applying the scaling length $r = r^* d$, velocity $\mathbf{u} = \mathbf{u}^* \kappa_T / d$, time $t = t^* d^2 / \kappa_T$, electric field $\mathbf{E} = \mathbf{E}^* V_{\text{rms}} / d$, temperature difference $T = T^* \Delta T + T_0$, and pressure $p = p^* \rho_0 \kappa_T^2 / d^2$, where the superscript $*$ denotes the value as a dimensionless quantity. The fluid and electric properties are considered constant and taken at the outer shell. Thus, we obtain the dimensionless Navier-Stokes equation,

$$\begin{aligned} \text{Pr}^{-1} \left[\frac{\partial \mathbf{u}^*}{\partial t^*} + (\mathbf{u}^* \cdot \nabla) \mathbf{u}^* \right] &= -\text{Pr}^{-1} \nabla p^* + \nabla^2 \mathbf{u}^* - \frac{1}{4} B \cdot \boldsymbol{\Gamma} \cdot \mathbf{L} \cdot T^* \cdot \nabla |\mathbf{E}^*|^2 \\ &\quad - \text{Ek}^{-1} \mathbf{e}_z \times \mathbf{u}^* + \mathbf{L} \cdot \text{Fr} \cdot T^* r \sin \theta \mathbf{s}, \end{aligned} \quad (6)$$

where $\text{Pr} = \nu / \kappa_T$ is the Prandtl number, $B = e / \alpha$ the ratio of both thermal expansion coefficients, $\text{Ek} = \nu / (2\Omega d^2)$ the Ekman number, r the radial distance, θ the poloidal direction, \mathbf{s} is the unit vector in the equatorial plane, $\text{Fr} = \Omega^2 d / |g_{e,R_{\text{out}}}|$ is the Froude number measuring the relative strength of

TABLE I. Dimensionless parameter range of the GeoFlow experiment. Parameters with asterisks are defined in the Appendix.

Dimensionless parameter	Value
Ekman number (Ek)	2.64×10^{-3} – 7.62×10^{-3}
Froude number (Fr)	5.1×10^{-2} – 2.66
Prandtl number (Pr)	1.24×10^2 – 1.75×10^2
Electric Rayleigh number (L)	3.73×10^2 – 1.59×10^5
Dielectric loss parameter (C_T)*	9.06×10^3 – 2.27×10^6
Convective parameter (C_E)*	2.02×10^{-7} – 3.54×10^{-6}
Expansion ratio (B)	11.20–12.40
Heating parameter (λ)	0.16–60

the centrifugal and the electric gravity force [35], and

$$L = \alpha \Delta T |g_{e,R_{\text{out}}}| d^3 / (\nu \kappa_T) \quad (7)$$

is the electric Rayleigh number given as a ratio of buoyancy to heat diffusion and viscous dissipation. The expression of the electric gravity, g_e , is suitable for substituting gravitational acceleration with the assumption derived in Appendix by neglecting the fluctuation of \mathbf{E} and the electric feedback effect. Hence g_e is defined as

$$g_e(r) = -2V_{\text{rms}}^2 \frac{\epsilon_0 \epsilon_r}{\rho_0} \frac{R_{\text{in}}^2 R_{\text{out}}^2}{(R_{\text{out}} - R_{\text{in}})^2} \frac{1}{r^5} \quad (8)$$

at $r = R_{\text{out}}$. Values of defined dimensionless parameters for the GeoFlow experiment are summarized in Table I.

The dimensionless equation for temperature is

$$\frac{\partial T^*}{\partial t^*} + (\mathbf{u}^* \cdot \nabla) T^* = \nabla^2 T^* + \frac{C_T}{B \Gamma L} |\mathbf{E}^*|^2. \quad (9)$$

We now introduce the heating parameter, λ , written as

$$\lambda = \frac{1}{2} \frac{C_T}{B \Gamma L}, \quad (10)$$

which is used to quantify the heating source in the system. The heating parameter is in fact a result of the energy balance in terms of Nusselt numbers, Nu_{in} and Nu_{out} , evaluated at the inner and outer shells, respectively. Their relationship is written as

$$\text{Nu}_{\text{in}} - \text{Nu}_{\text{out}} + 2\lambda \int_V \mathbf{E}_0^2 dV = 0 \quad \text{for } \lambda < 1, \quad (11)$$

$$-\text{Nu}_{\text{in}} - \text{Nu}_{\text{out}} + 2\lambda \int_V \mathbf{E}_0^2 dV = 0 \quad \text{for } \lambda > 1. \quad (12)$$

The strength of the internal heating is measured by λ , where $\lambda > 1$ indicates strong internal heating and $\lambda < 1$ indicates weak internal heating. For $\lambda = 1$ internal heating increases the fluid's temperature inside the spherical gap geometry until the heat flux through the surfaces is balanced with the internal heating rate. When $\lambda > 1$, the temperature difference across the gap does not contribute significantly to the global energy transport and results in a parabolic mean temperature profile. Figure 2(a) provides an overview of different thermal profiles for various internal heating parameters.

After introducing the internal heating parameter one need also to define a quantitative parameter for the strength of convection. To investigate the flow we therefore define a further dimensionless

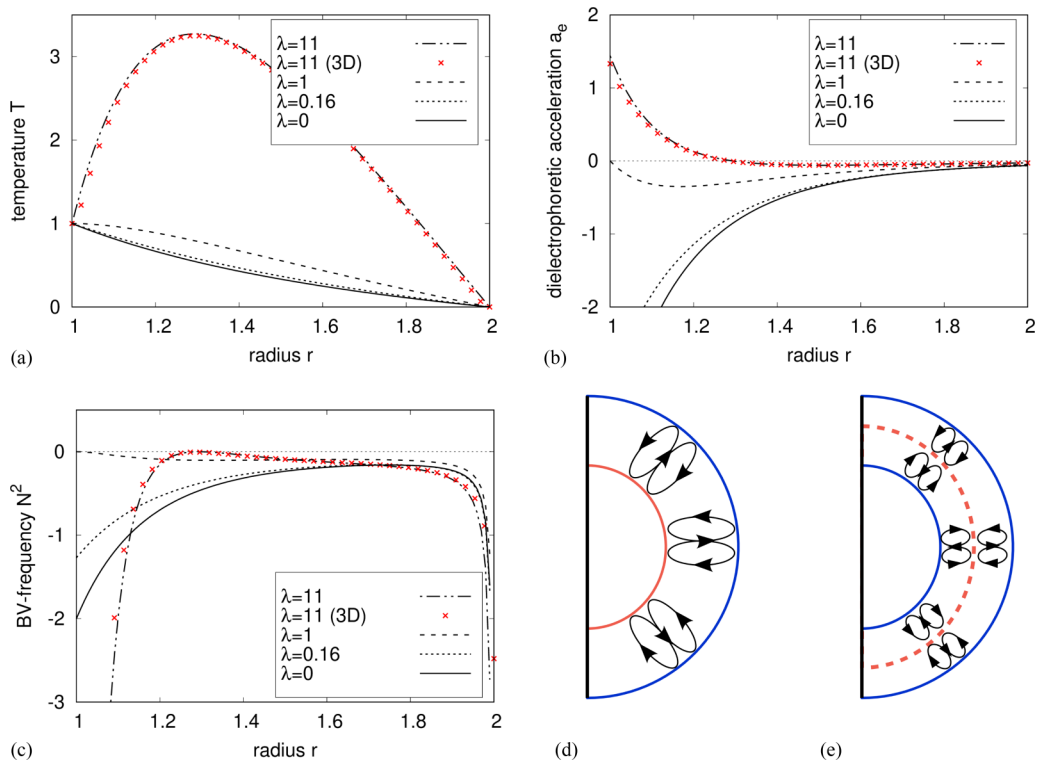


FIG. 2. Analytic solutions for (a) radial temperature distribution, (b) dielectrophoretic acceleration, and (c) Brunt-Väisälä frequency for varying λ in conductive and nonrotating case for $\eta = 0.5$. Red crosses (“x”) present solutions for a three-dimensional numerical simulation with $\lambda = 11$. Values for λ are chosen according to the GeoFlow experiment. (d) Sketch of convection in the spherical gap geometry when $N^2 < 0$ in the complete gap and $\lambda < 1$. (e) Sketch of layered convection in the spherical gap geometry where $N^2 \geq 0$ at the middle of the gap and $N^2 < 0$ elsewhere with $\lambda > 1$.

quantity the dielectrophoretic acceleration, \mathbf{a}_e^* , written as

$$\mathbf{a}_e^* = -\frac{1}{2} |\mathbf{E}|^2 \nabla \epsilon / [d^3 / (V_{\text{rms}}^2 \epsilon_0 \epsilon_r)], \quad (13)$$

which is used to provide an indication of how strong an infinitesimal fluid element is forced at a certain location in the gap. In the next sections dimensionless parameters are used and the asterisk are omitted.

III. METHODS

A. The GeoFlow experiment

The GeoFlow experiment on the ISS consists of a concentric spherical gap capacitor that is used for the investigation of thermal convection. The experimental system has a gap width of 0.0135 m, with an outer radius of $R_{\text{out}} = 0.027$ m resulting in an aspect ratio of $\eta = 0.5$ ($\Gamma = 0.25$). Figure 1 shows a numerically calculated temperature distribution over the spherical gap. Two external temperature controlled fluid circuits established a temperature difference of $0.4 \text{ K} \leq \Delta T \leq 9.5 \text{ K}$ between both shells. To induce a dielectrophoretic forcing and hence a radial buoyancy force a fast alternating electric field is applied. The strength of the force can be controlled by the applied thermal forcing and the amplitude of the electric field. The electric field can be adjusted between 1273 V and 4596 V to study a variety of convection phenomena. To account for rotational forcing, the sphere is

able to rotate with three different angular velocities, Ω , namely with $\Omega = 0.05, 5, \text{ or } 10$ rad/s. The dielectric loss of the working fluid, 1-Nonanol, is caused by the high electric field frequency which generates dielectric internal heating and is also investigated.

The GeoFlow experiment can simulate three different rotation rates, five voltages V_{rms} and eight temperature differences, where two reference temperatures, T_0 , are measured at the outer shell. These input properties define 240 experimental points (EP). The present study includes 160 EPs, summarized in Table I, which presents the full parameter range. However, the weakly rotating case of $\Omega = 0.05$ rad/s with $\text{Ek} \approx 1$ and $\text{Fr} < 10^{-4}$ is excluded in this study. All numerical results presented are based on EPs defined in the GeoFlow *Experimental Scientific Requirements* (ESR) document. A set of eight temperature differences is called a “run” and can be set for a sequential increase of voltages and rotation rates. Five runs are grouped into four clusters. An overview of the each cluster is given in Figs. 4(a)–4(d).

The model formulation in Sec. II suggests that the electric Rayleigh number cannot be chosen independently from C_T as this would lead to inhomogeneous distributed sequences in the λ - L plane, where the heating parameter λ [see Eq. (10)] more intuitively parametrizes the influence of internal heating than C_T . Hence, for the analysis of the dynamics, we group the EPs in such a way that electric Rayleigh number varies only within a predicted dynamical range depending on the critical electric Rayleigh number L_c , but the heating parameter λ remains as strong as possible.

The EPs were visualized by a Wollaston Shearing Interferometry (WSI) system which measures the gradient of the refractive index [13,36]. While the refractive index gradient varies with the thermal distribution within the spherical gap, certain fringe patterns can be observed where the thermal gradient changes the (temperature-dependent) refractive index of the fluid. For example, single convective cells appear as butterfly patterns and sheetlike flows appear as parallel lines [see Fig. 5(c)]. Unfortunately, other visualizations of convective flow could not be performed for ISS safety reasons. The recording plane of the camera of the WSI is mounted at a meridional angle of $\theta = 30^\circ$ with the North Pole located at $\theta = 0^\circ$. Thus, the recorded interferograms cover a range of 88° , ranging from $\theta = -14^\circ$ to $\theta = 74^\circ$, see Fig. 1. From a series of images it is possible to reconstruct the entire northern hemisphere. While the temporal resolution of the images enables a satisfactory analysis for the laminar flow regime, it causes imprecise reconstructions in the transient and turbulent regimes. To overcome these restrictions, only single interferograms are analyzed.

B. Numerical methods

The governing equations are studied using two methods: (a) a linear stability analysis which provides the critical electric Rayleigh numbers L_c and threshold values of the convective onset and (b) three-dimensional large eddy simulations (LES) and interferograms calculated with the software package OpenFoam. The numerical simulations provide the temperature and electric field for the statistical evaluation which are compared with interferograms. For the linear stability analysis, a pseudospectral numerical method is used to solve the dimensionless governing equations [37]. Here the velocity field is decomposed into poloidal and toroidal potentials ψ_1 and ψ_2 ,

$$\mathbf{u} = \nabla \times \nabla \times (\psi_1 \mathbf{e}_r) + \nabla \times (\psi_2 \mathbf{e}_r), \quad (14)$$

obeying the continuity equation. By using the pseudospectral method and applying $\nabla \times \nabla \times$ and $\nabla \times$ to Eq. (6) (which separates the potentials), one can solve the hydrodynamic equations with a high accuracy in the spherical geometry. This results in a fourth-order equation for the potential ψ_1 and a second-order equation for the potential ψ_2 . The critical electric Rayleigh numbers, L_c , are calculated using linearized equations [38]. The corresponding eigenvalue problem is solved by direct numerical integration, where the spectrum is analyzed for growth rates $\sigma = 0$.

For the three-dimensional numerical simulations an incompressible, second-order finite volume, transient buoyancy solver of OpenFoam 4.1 is used which is expanded to include the nonuniform electric field as derived in Appendix. In addition, the solver includes the source terms for the

dielectric heating, H , in the temperature equations and the volumetric body force, F_{DEP} , in momentum equation.

The boundary condition for velocity is no-slip, in a moving reference frame, and Dirichlet for temperature. To mimic the GeoFlow experiment in all aspects, the experimental time scales are set consistent with Zaussinger *et al.* [12]. This included the heating-up periods and the idle periods between each EP. The electric field is defined as a negative gradient of the electric potential and is calculated via the Gauss equation, $\nabla \cdot (\epsilon \nabla \Phi) = 0$, by taking the electrical fluctuations and thermoelectric feedback effect into account. The boundary condition of the electric potential is set at the outer shell with $\Phi = V_{\text{rms}}$ and $\Phi = 0V$ at the inner shell.

The mesh of the spherical gap is generated by radially extruding a spherical two-dimensional (2D) surface grid with 40.950 faces to 1.843.290 honeycomb shaped cells in 3D with a radial resolution of 45 cells. The dimensionless wall distance y^+ is smaller than 0.2 and corresponds to a mesh resolution of at least five cells in the viscous boundary layer. The OpenFoam ‘‘Pimple’’ algorithm solves subsequently the LES model with top-hat filtered versions of Eqs. (3)–(5). The filter width is the cube root volume of each cell. VanDriest damping in distance to the boundary layer ensures that the ‘‘dynamic k’’ turbulence model is applied only in the bulk flow [39].

C. Statistical evaluation

The statistical interpretation is based on snapshots of temperature and dielectrophoretic force. These snapshots are averaged over shells (θ, ϕ) of equidistant radii and over 30 time stamps providing 300 s of the fully developed flow. Hence, the calculated profiles of the first four statistical moments are functions of the radius.

Turbulence and intermittency lead to rare, but intense peaks in the temperature field. As a result, in such intermittent systems especially the higher-order moments depart significantly from the Gaussian distribution. In particular, the evaluation of the third and the fourth statistical moments provide information of rarely occurring events. For convective processes these events are commonly related to thermal plumes.

The first statistical moment, $\langle T \rangle$, is the mean thermal distribution. Temperature fluctuations are described by the variance which is the second statistical moment $\langle T'^2 \rangle$.

An asymmetry of the temperature distribution around the mean value $\langle T \rangle$ is parametrized by the temperature skewness $\langle S \rangle = \langle T'^3 \rangle / (\langle T'^2 \rangle)^{3/2}$. Large positive values of S characterize locally higher values of T which cover a smaller surface area. Hence, the values deviate further from the mean value than locally lower values. The same holds for large negative values of S for cold areas embedded in a hot surrounding [40]. In particular, for $S > 0$ the fluid flow is dominated by strong uprising thermals and for $S < 0$ by strong downdrafts, respectively.

Intermittency is evaluated by the kurtosis (flatness) $\langle K \rangle = \langle T'^4 \rangle / (\langle T'^2 \rangle)^2$. The kurtosis provides a scale of a certain ‘‘tailedness’’ and describes rarely occurring and very spiky events in intermittent systems [41]. For the present study, high values of the kurtosis indicate localized regions with plumes of large magnitude, and large areas with slow ascending and descending flow. However, the direction of the fluid flow in the plumes is given by the sign of the skewness.

The higher statistical moments are very sensitive to rare events. They are indicating in this particular case thermal structures with steep gradients.

IV. BASE FLOW AND THRESHOLD OF CONVECTION

We assume that the toroidal and poloidal components of $\mathbf{E}_1(r, \theta, \phi)$ in the conductive case have only small contributions to the initial electric field $\mathbf{E}_0(r)$. This justifies the assumption of a one-dimensional electric field $\mathbf{E}(r)$. The Gauss equation and the temperature equation are solved analytically for a constant permittivity with the electric field equation presented in Eq. (A6) and the

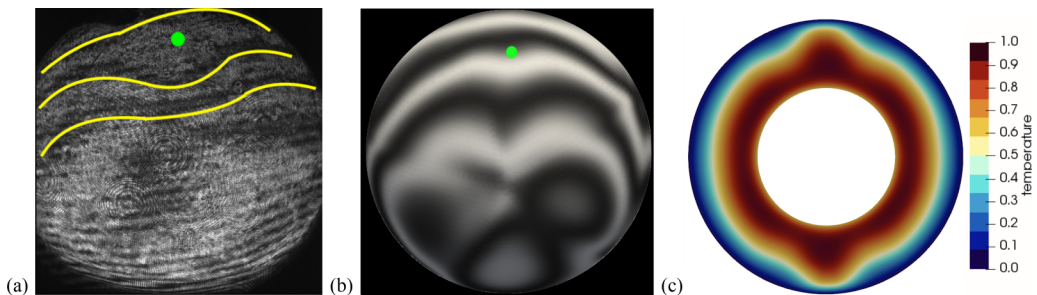


FIG. 3. (a) experimental interferogram for $Ek = 5.2 \times 10^{-3}$ and $\lambda = 1$ for the conductive case. The base flow structures are outlined in yellow, with a sinusoidal distortion around the North Pole labeled with a green dot. The equator is in the lower part of the interferogram. (b) Numerical interferograms with the same parameters evaluated by a three-dimensional simulation. (c) Vertical plane of the temperature distribution through both poles.

temperature condition imposed in the form of

$$T(r) = -\frac{\eta}{1-\eta} + \frac{\eta}{(1-\eta)^2} \frac{1}{r} - \lambda \left[\frac{\eta}{(1-\eta)^2} - \frac{\eta(1+\eta)}{(1-\eta)^3} \frac{1}{r} + \frac{\eta^2}{(1-\eta)^4} \frac{1}{r^2} \right]. \quad (15)$$

This solution is the sum of the base temperature profile, $-\frac{\eta}{1-\eta} + \frac{\eta}{(1-\eta)^2} \frac{1}{r}$, and the contribution from the dielectric heating whose amplitude is λ .

1. Thermal profile

To investigate the base state of the experiment the conductive reference case of run ‘‘C20’’ ($\lambda = 11$) of the GeoFlow experiment is studied. This includes a range of values for the heating parameter, λ , to study the transition state ($\lambda = 1$) where internal and external heating is balanced, where internal heating is absent ($\lambda = 0$), and the smallest achievable value of the GeoFlow experiment ($\lambda = 0.16$). The analytical solutions of the temperature fields are shown in Fig. 2(a) together with the 3D numerical simulation for $\lambda = 11$ indicated by red crosses which present good agreement with the corresponding analytic solution. In the case where $\lambda < 1$, the internal heating is negligible and convection is triggered by ΔT . For $\lambda > 1$, the temperature field reaches a maximum at the inner shell at $r_{\max} = 4\lambda/(1+3\lambda)$. In this case, the stability of the system depends on the interaction of the signs of the dielectrophoretic acceleration that is influenced by the temperature gradient. In the limiting case of $\lambda \gg 1$, the temperature converged to the maximum at approximately $r_{\max} = 4/3$. For $\lambda \leq 1$, the maximum is always found at the inner shell with $r_{\max} = 1$ and radius ratio $\eta = 0.5$. In the absence of rotation ($Fr = 0$) the isothermal surfaces take the form of concentric spheroids with radially dependent temperature distributions. However, for small voltages ($V_{\text{rms}} \leq 2121$ V), the Fr exceeds 0.5 and influences the thermal stratification [42].

In the presence of rotation a two-dimensional axisymmetric and equatorially symmetric steady base flow appears $(u_r, u_\theta, 0)$. Warm fluid is displaced radially outward at the poles whereas cold fluid is transported inward close to the equatorial plane. When the observed flow exhibits such complex motion it cannot be solved analytically and has to be calculated numerically. A meridional flow is observed in a two-cell structure at $Ek, Fr \sim 10^{-3}$ where the temperature maximum is found in the gap for internal heating. However, at the poles there is a radial shift of the temperature maxima toward the outer shell [see Fig. 3(c)]. The base flow of the GeoFlow experiment shows a plumelike structure at the North Pole and wave distortions in the conductive steady state case. Figure 3(a) shows these structures with yellow lines. Numerical simulations and the corresponding numerically evaluated interferograms agreed well with the experimental observation, see Figs. 3(b) and 3(c). However, the numerical reconstruction of the interferograms shows a more pronounced fringe

pattern in the polar region. This, however, is a result of the differently calibrated interferometry unit that is used for the calculation.

2. Dielectrophoretic acceleration and buoyancy

In the conductive case the electric field follows the solution of $\mathbf{E}_0 \sim r^{-2}$ [see Eq. (A6)] where \mathbf{E}_0 is independent of λ . However, the dielectrophoretic acceleration \mathbf{a}_e [obtained from Eq. (A2)] depends on λ and is strictly negative for $\lambda \leq 1$ [see Fig. 2(b)]. The dielectrophoretic acceleration can be calculated by the analytic solution of the temperature by using the OBA for the permittivity and the scaling relation $\beta = e \Delta T \epsilon_r$, the radial component of the dielectrophoretic acceleration is written as

$$a_e(r) = -\frac{1}{2} |\mathbf{E}_0|^2 \frac{d\epsilon}{dr} = -\frac{1}{2} \left(\frac{1}{\Gamma} \frac{1}{r^2} \right)^2 \beta \left[\frac{2}{r^2} + \lambda \left(\frac{6}{r^2} - \frac{8}{r^3} \right) \right] \quad (16)$$

for $\eta = 0.5$. Figure 2(b) depicts the radial component of the dielectrophoretic acceleration $a_e(r)$ for four different values of λ . For $a_e(r) < 0$, the sign of dielectrophoretic acceleration is negative and points radially inward toward the center of the spherical gap. This generates an induced force field comparable to the gravitational force field. However, for $\lambda > 1$, the dielectrophoretic acceleration changes its sign at r_{\max} and can separate the spherical gap into two layers. A deeper insight into the stability of the thermal stratification is given by the Brunt-Väisälä (BV) frequency written as

$$N^2 = -\frac{a_e}{T} \frac{dT}{dr}. \quad (17)$$

An unstable fluid column is observed at $\lambda > 1$ where $N^2 < 0$, except at a region around the temperature maximum where $N^2 = 0$. The absence of buoyancy indicates two convectively unstable layers separated by a stable conductive interface, see Fig. 2(e). While the strong forcing of the dielectrophoretic acceleration is present in the lower shell, a long-time separation is unlikely and a fully mixed spherical gap is expected. When $\lambda < 1$ the entire fluid column is unstable and presents convective patterns reminiscent of an RB cell see Fig. 2(d).

In the rotating case the threshold of the convective onset is characterized by the destabilization of the base flow which is observed by the interferometry unit when the fringe pattern is distorted. For all four clusters [see Figs. 4(a)–4(d)] the onset of convection is observed within a margin of ± 177 V. However, for $L \sim L_c$, ambiguous interferograms are recorded in which a clear distinction between the base flow and the convective flow was not possible.

V. THREE-DIMENSIONAL SIMULATIONS AND COMPARISON WITH THE GEOWFLOW EXPERIMENT

The Geoflow experiment provides only interferograms which show the radially averaged temperature distribution of the gap and not the flow. Thus, we use three-dimensional simulations to reconstruct the flow field and temperature. Numerical results are used to explain the interferograms and to evaluate how significantly the dielectric heating parameter, λ , influences the flow and temperature distribution.

Of 160 analyzed EPs we find 22 (14%) with $\lambda < 1$ and 138 (86%) with $\lambda \geq 1$ with a mean value of $\lambda = 5.6$ and median of $\lambda = 2.1$. The minimum value is $\lambda = 0.16$ at $V_{\text{rms}} = 1273$ V with temperature difference of $\Delta T = 9.5$ K. The maximum value of $\lambda = 60$ is found for the highest available voltage $V_{\text{rms}} = 4596$ V and the lowest temperature difference $\Delta T = 0.4$ K. All cases with $\lambda < 1$ are found at low voltage ($V_{\text{rms}} = 1273$ V) in combination with high temperature differences $\Delta T > 3$ K. All 160 EPs of the GeoFlow experiment are grouped into four clusters with respect to four Ekman numbers and two Prandtl numbers, ($\text{Ek} = 7.6 \times 10^{-3}$, $\text{Pr} = 176$), ($\text{Ek} = 5.2 \times 10^{-3}$, $\text{Pr} = 125$), ($\text{Ek} = 3.8 \times 10^{-3}$, $\text{Pr} = 176$), and ($\text{Ek} = 2.6 \times 10^{-3}$, $\text{Pr} = 125$). Figures 4(a)–4(d) visualize these clusters. To provide an adequate overview, the experimentally recorded interferograms are analyzed

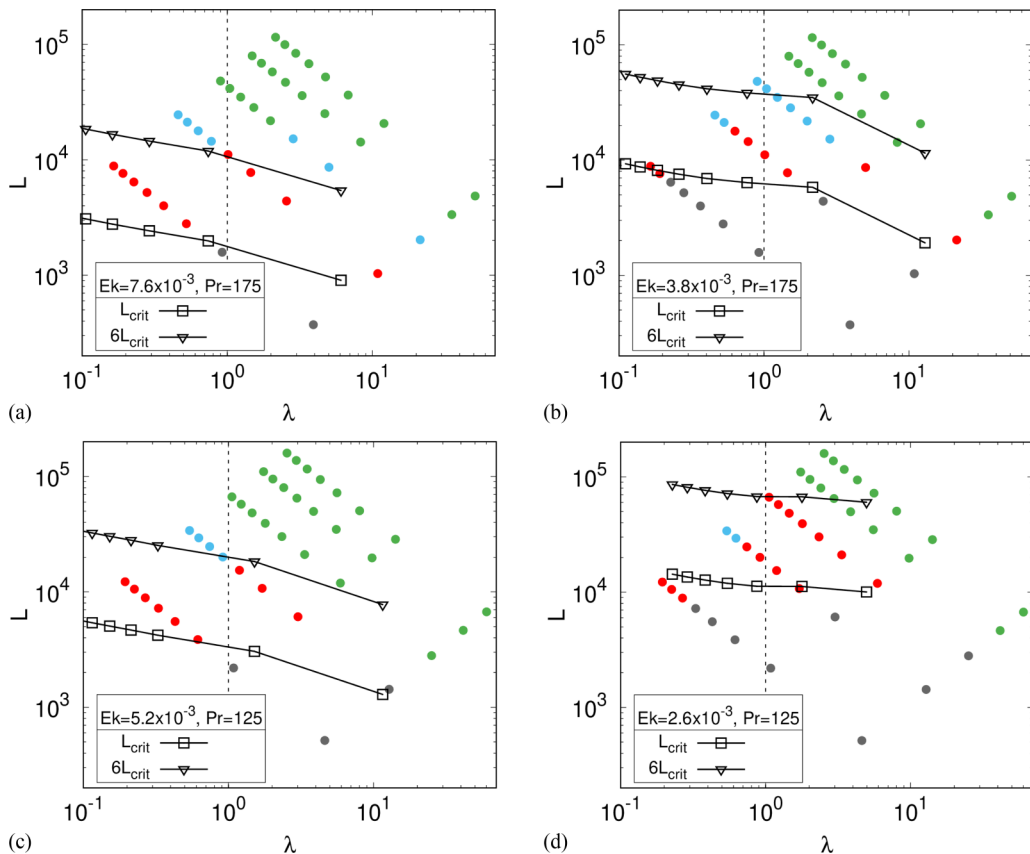


FIG. 4. Experimental points (EP) of the GeoFlow experiment in the λ - L plane for (a) $Ek = 7.6 \times 10^{-3}$, $Pr = 175$; (b) $Ek = 3.8 \times 10^{-3}$, $Pr = 175$; (c) $Ek = 5.2 \times 10^{-3}$, $Pr = 125$; and (d) $Ek = 2.6 \times 10^{-3}$, $Pr = 125$. Dark gray dots represent the conductive cases, red dots the columnar flows, blue dots the transition and green dots the turbulent cases. Black lines with \square symbols mark the onset of convection, and with ∇ symbols the transition to the turbulent regime.

and categorized into several separate cases where the conductive states are colored in dark gray, columnar flows in red, transitional cases with remnants of columnar cells in blue and turbulent cases in green. The black line with \square symbols represents the result of linear stability analysis with the critical Rayleigh number L_c , whereas the black line with ∇ symbols separates the weakly nonlinear regime from the transitional regime. The vertical dashed line represents the transition between convection where the temperature difference across the gap dominates the energy transport ($\lambda < 1$) and the internal heating dominates convection ($\lambda > 1$). In the subsequent section, the dynamics of rotating convection are investigated in more detail, regarding the influence of the heating parameter, λ , the electric Rayleigh number, L . The Prandtl number, Pr , and the Ekman number, Ek , vary only little in the experiment which makes it difficult to deduce meaningful influences on the fluid flow.

A. Weakly nonlinear regime

The weakly nonlinear regime is defined as the region where $L \lesssim 6L_c$ [43]. In this regime, the dynamics follow approximately the Proudman-Taylor (PT) theorem with $\frac{\partial \mathbf{u}}{\partial z} \approx \mathbf{0}$, where z denotes any line parallel to the z axis of rotation. Within this regime, the pressure force is balanced by the Coriolis force and leads to the formation of columnar cells which are aligned with the rotation axis

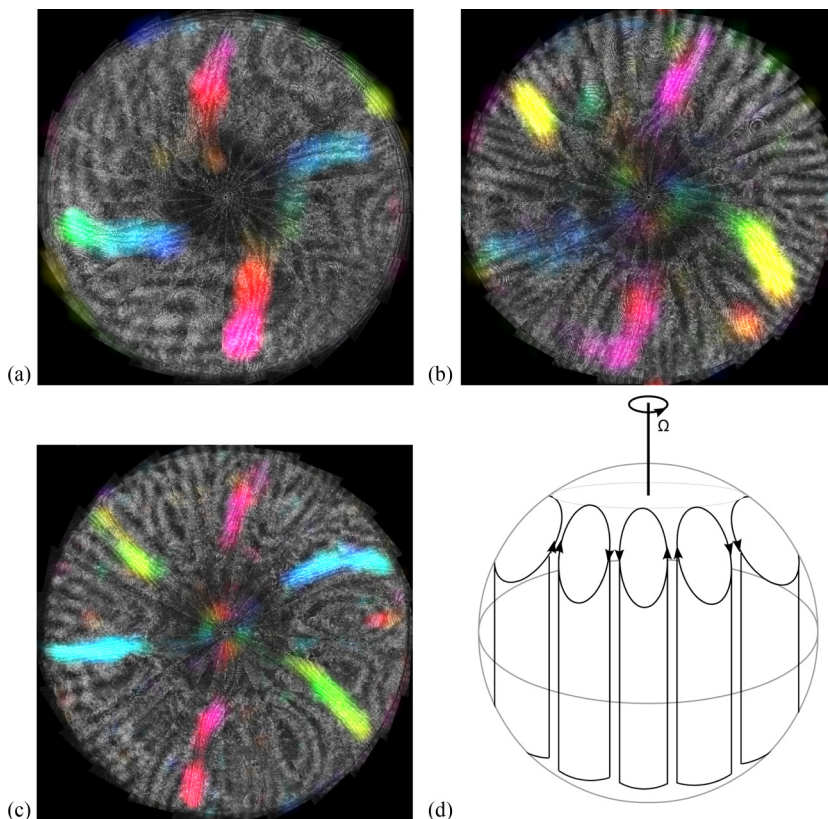


FIG. 5. Columnar cells visualized by automatic pattern recognition, Zaussinger *et al.* [13]. The North Pole is located in the center and the equator at the outline. The colors refer to angles of identified fringe lines. (a) Spiraling columnar cells with $m = 4$ for $L = 8849$, $Ek = 7.6 \times 10^{-3}$, and $\lambda = 0.16$, (b) slightly spiraling columnar cells with $m = 5$ for $L = 7217$, $Ek = 5.2 \times 10^{-3}$, and $\lambda = 0.33$, (c) almost straight cells with $m = 6$ for $L = 12243$, $Ek = 5.2 \times 10^{-3}$, and $\lambda = 0.19$. Animations of all three cases are available as Supplemental Material files in Refs. [46–48]. (d) Sketch of columnar cells aligned with the rotation axis in the spherical shell.

and confined by the tangent to the inner sphere. Spirals occur for impermeable boundaries that tilt the columnar cells. These spirals are well known to occur for moderate Prandtl numbers and are visible in equatorial cuts of the corresponding numerical simulations (see Ref. [44]). The azimuthal wave numbers of the columnar cells are estimated using $m \sim Ek^{-1/3}$ [43,45] which corresponds to $m \sim 5\text{--}7$ for the parameter range of the GeoFlow experiment. Deviations from the theoretical values by one wave number can be explained by the influence of the supply shaft at the South Pole of the experiment (Fig. 1) and by the nonuniform buoyancy force. The regime in which columnar cells occur is delimited by the $6L_c$ criterion, but does not depend on λ , Ek , or Pr .

Figure 5 shows columnar cells with a fourfold, fivefold, and sixfold symmetry. The corresponding experimental points are labeled with wave numbers in Figs. 4(a)–4(d). The starlike structures show steep thermal upwelling and large down-welling regions. Columnar cells can be identified as butterfly patterns which are observed in the upper part of Fig. 5(c). Spiral structures are found for cases as presented in Fig. 5(a) and 5(b).

1. Thermal profile

To analyze the fluid flow in the weakly nonlinear regime of GeoFlow we carried out numerical simulations with the parameters of two representative runs, with $L/L_c = 1.15$ (“C17”) and

$L/L_c = 2.25$ (“C20”). Both runs differ only in the high voltage and cover fairly wide ranges in the heating parameter. Figure 4(a) shows these EPs, where $L/L_c = 1.15$ and $\lambda = 10$ is labeled as “1,” $L/L_c = 1.15$ and $\lambda = 0.5$ is labeled as “2,” $L/L_c = 2.25$ and $\lambda = 2.5$ is labeled as “3,” and $L/L_c = 2.25$ and $\lambda = 0.16$ is labeled as “4.” In all four cases the mean temperature profiles $\langle T \rangle$ do not show strong convective mixing in the bulk of the fluid [see Fig. 6(a)]. This is to be expected as the onset of convection is close to the threshold. When convective mixing appears, the profiles in the bulk flatten and the boundary layers compress toward the shell’s boundaries.

According to the PT theorem columnar cells are expected in the rotating case. Consistent to this, our numerical simulations found columnar cells with wave numbers between $m = 4$ and $m = 8$ which are visible for both heating scenarios, as shown in Figs. 6(g) and 6(h). When $\lambda < 1$, the variance is significantly smaller and shows peaks in the vicinity of the boundaries caused by homogeneously thermalized, rising and/or falling plumes, see Fig. 6(b). The maxima of the thermal fluctuations is observed between $1.5 < r < 1.8$ and coincides with the heating activities in the interior of the polar plumes.

Figures 6(c) and 6(d) shows the averaged skewness and kurtosis in the radial direction. The skewness has a flat profile with values $|S| \leq \sqrt{2}$ and $K \leq 3$ for $1 < r < 1.3$. This region can be described by the quasinormal approximation where the realizability condition [49], $K > 1 + S^2$, provides an upper boundary for the skewness. Furthermore, the observed values of S and K are in good agreement with the elevator model of convective cells which shows a similar sub-Gaussian behavior ($1 < K < 3$). In the upper half of the gap ($r > 1.5$) we found $|S| \geq \sqrt{2}$ and $K > 3$. The positive sign of S and the increase in S and K originates from the centrifugal force. In GeoFlow, the centrifugal force leads to the formation of two dominant up-flows in polar regions.

2. Stability and N^2

The dielectrophoretic acceleration shows behavior similar to that of the conductive case (see Fig. 2). For $\lambda < 1$, the dielectrophoretic acceleration is strictly negative due to the negative radial temperature gradient. A change of sign in the dielectrophoretic acceleration is found for $\lambda > 1$. However, this did not influence the global stability. The BV frequency N^2 is always negative or zero which indicates convective mixing over the entire gap [see Fig. 6(e) and 6(f)]. Far from the boundaries a layering such as two convectively layers separated by a diffusive interface [see Fig. 2(e)] was not observed.

B. Transitional regime for $\lambda \leq 1$

For $L > 6 L_c$ the regular columnar cells disperse and the flow becomes more turbulent. Fig. 10(a) shows a representative EP where the columnar cells are visible, but not regular any more. Consequently, Gastine *et al.* [50] denoted this parameter regime as the “transitional regime.” A set of five representative EPs were analyzed for $L > 6 L_c$ and $\lambda < 1$ and are shown in Fig. 4(a) as four blue circles and the red circle inside the region defined as “set 1.”

1. Thermal profile

The electric Rayleigh number L is in the range of $1.1 \times 10^4 \leq L \leq 2.4 \times 10^4$ which corresponds to values slightly above the weakly nonlinear regime with heating parameters between $0.16 \leq \lambda \leq 1.01$. The averaged temperature field $\langle T \rangle$ and the corresponding variance $\langle T'^2 \rangle$ are shown in Figs. 7(a) and 7(b). For the entire parameter range, the mean temperature shows a well mixed bulk between $r = 1.1$ and $r = 1.7$.

Just as in the weakly nonlinear regime, the centrifugal force leads to a non-Gaussian thermal distribution for $r > 1.5$. Polar plumes are detached toward the upper boundary to form a cell covering the entire gap. Columnar cells confined by the tangent cylinder are only weakly connected to the outer shell. This results in a broad upper boundary layer, but an increase in S and K due to polar plumes, see Fig. 7(c) and 7(d). The skewness is bounded by $\sqrt{2}$ for $r < 1.75$ due to columnar

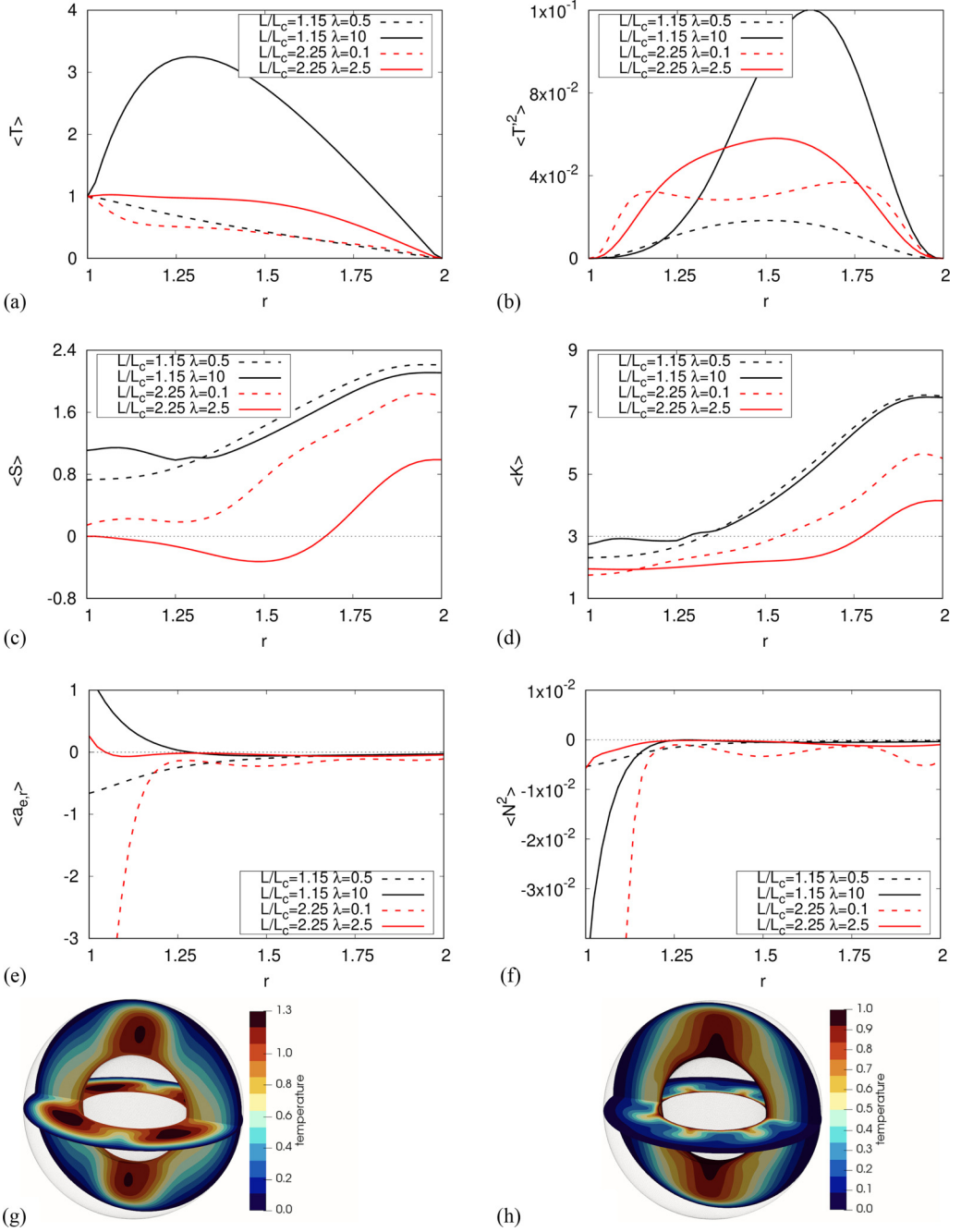


FIG. 6. Averaged thermal properties for simulations with $L/L_c = 1.15$ (black) and $L/L_c = 2.25$ (red), for $\lambda < 1$ and $\lambda > 1$, respectively. (a) The mean temperature, (b) the temperature variance, (c) the skewness of the temperature, (d) the kurtosis of temperature, (e) the dielectrophoretic acceleration, (f) the Brunt-Väisälä frequency, (g) the 3D simulation for $L/L_c = 2.25$ and $\lambda = 2.5$, and (h) a 3D simulation for $L/L_c = 1.15$ and $\lambda = 0.16$.

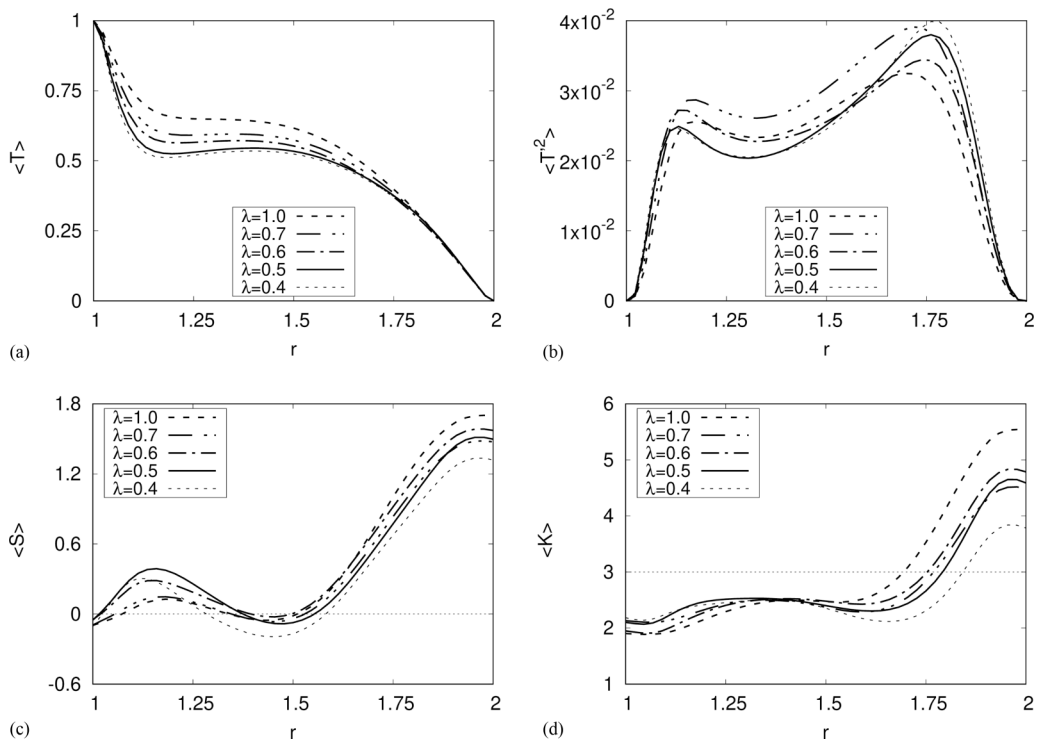


FIG. 7. Averaged (a) temperature, (b) temperature variance, (c) skewness of temperature, and (d) kurtosis of temperature for $\lambda \leq 1$ and $1.4 \times 10^4 < L < 2.4 \times 10^4$.

cells and this leads to a sub-Gaussian ($K \sim 2$) distribution. In contrast to the weakly nonlinear regime, this region is more strongly mixed due to higher convective fluxes.

2. Stability and N^2

Figure 8(a) shows an additional effect of the centrifugal force. A steep gradient exhibits in the dielectrophoretic acceleration, \mathbf{a}_e , at the equatorial region close to the inner shell with $r < 1.1$. The steep gradients at the inner shell are caused by the boundary layers formed by the columnar cells. As shown in Fig. 8(a), the dielectrophoretic acceleration as well as the BV frequency nearly vanish for $r > 1.1$. The confinement of columnar cells by the tangent cylinder and the resulting stable stratification above $r = 1.6$ reduce the thermal gradients and hence the dielectrophoretic acceleration. In summary, the upper boundary regions of the midlatitudes are nearly adiabatically stratified with $N^2 \sim 0$. In the polar regions, the dielectrophoretic acceleration and the BV frequency are nonzero at the outer shell which agree with the results shown in Fig. 2(c). The mean dielectrophoretic acceleration shows a small peak around $r = 1.8$ which is due to the boundary layer. The horizontal components of \mathbf{a}_e does not contribute to the dynamics [see Fig. 8(b) and 8(c)]. The absolute values are two to three orders of magnitudes smaller than the radial component which justifies the use of Eqs. (A8) and (A9) for the parameter range investigated.

C. Transitional regime for $\lambda > 1$

A set of seven representative EPs with $2.0 \times 10^3 < L < 3.5 \times 10^4$ are analyzed for the parameter regime $\lambda > 1$, $\text{Pr} = 175$, and $\text{Ek} = 3.8 \times 10^{-3}$. The heating parameters range between $1.2 < \lambda \leq 21$ and are shown in Fig. 4(a) as four green circles and three blue circles labeled as “set 2.”

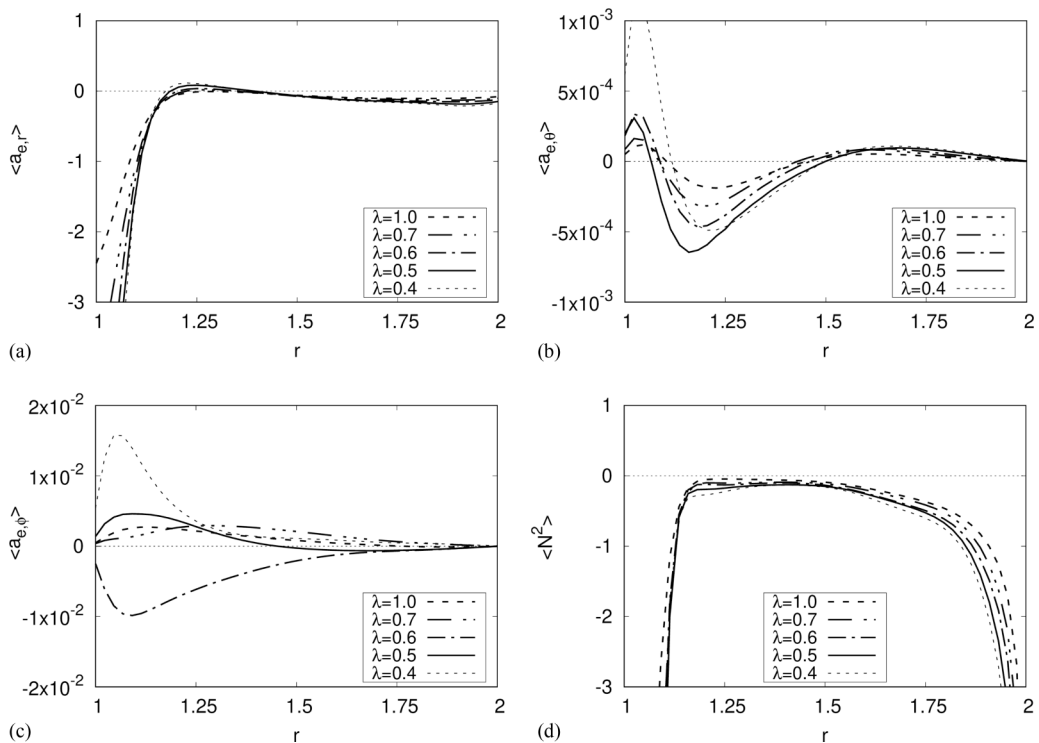


FIG. 8. Averaged (a) radial component of dielectrophoretic acceleration, (b) meridional component of dielectrophoretic acceleration, (c) azimuthal component of dielectrophoretic acceleration, and (d) Brunt-Väisälä frequency for $\lambda < 1$ and $1.4 \times 10^4 < L < 2.4 \times 10^4$.

1. Thermal profile

The maximum of the mean temperature is found in the middle of the gap [see Fig. 9(a)] and shifted toward the outer shell located at $r = 1.5$ which represents a higher value than that of the conductive case $r_{\max} = 4/3$. This shift was also observed in Zaussinger *et al.* [12] and can be explained by an “eroding” convective flow.

The observed thermal fluctuations [see Fig. 9(b)] in the outer gap region are higher than in the case of $\lambda < 1$. This leads to statistical outliers and therefore high values in the kurtosis. This is well observed for the case where $-1 < S \lesssim 0$ and $2 < K \lesssim 3$ and is indicated in Fig. 9(c) and 9(d). In contrast to the cases with low internal heating, the skewness is negative in the lower gap region, but showed a steeper ascent for $r < 1.75$. A closer look to the three-dimensional temperature field reveals the negative sign of S and shows strong pointwise down-welling plumes. Four distinct pointwise plumes are highlighted and occurred as double-eye structures as shown in Fig. 10(b) where white rectangles highlight these structures. However, columnar cells are not observed for $L > 5 \times 10^4$ which is a result of the internal heating process. The columnar cells vanish by the convective flux that reversed the sign of the dielectrophoretic acceleration.

2. Stability and N^2

For $\lambda \geq 5.0$ the dielectrophoretic acceleration is positive between $r = 1.1$ and $r = 1.4$ [see Fig. 11(a)]. However, near the outer boundary, the dielectrophoretic acceleration is small or zero. The inversion of the sign of the dielectrophoretic acceleration would lead to a separation of the flow into two unstable layers separated by a stable, diffusive interface. However, layering is not observed in the numerical simulations. This can be explained by the buoyancy force in the gap.

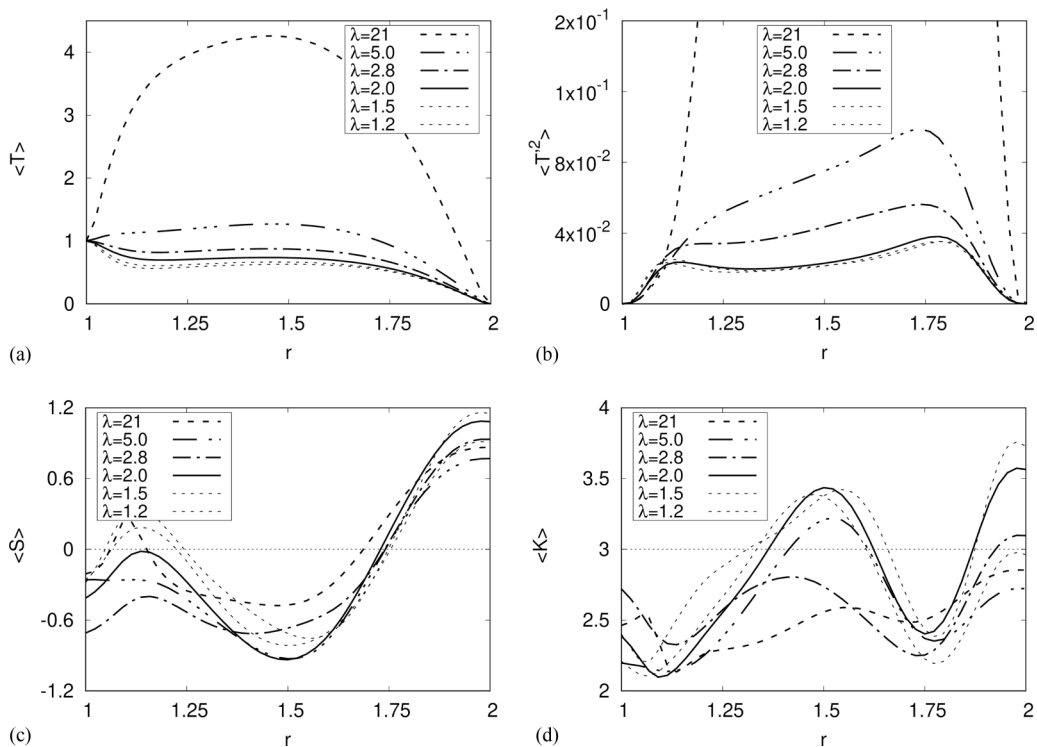


FIG. 9. Averaged (a) temperature, (b) temperature variance, (c) skewness of temperature, and (d) kurtosis of temperature for $\lambda \geq 1$ and $2.0 \times 10^3 < L < 3.5 \times 10^4$.

The dielectrophoretic acceleration is at least an order of magnitude higher at the inner shell than in the bulk or in the upper shell. This destabilized the diffusive interface where the dielectrophoretic acceleration changes sign and is able to form a convection cell which fills the entire gap. The

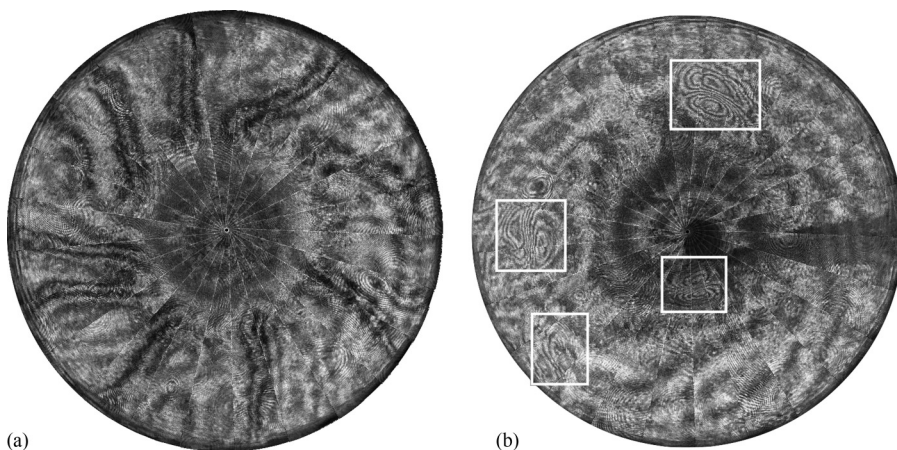


FIG. 10. Interferograms of the GeoFlow experiment with the North Pole at the center of the circle: (a) Remnants of columnar cells for $L = 2.4 \times 10^4$ and $\lambda = 0.7$. (b) Equatorial, pointwise plumes for $L = 6000$ and $\lambda = 60$ with highlighted structures after postprocessing.

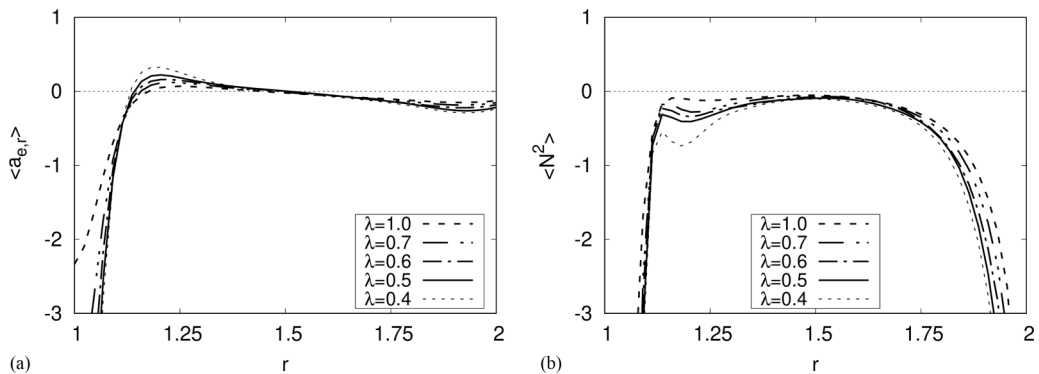


FIG. 11. Averaged (a) radial component of dielectrophoretic acceleration and (b) Brunt-Väisälä frequency for $\lambda \geq 1$ and $2.0 \times 10^3 < L < 3.5 \times 10^4$.

negative sign of the BV frequency over the entire gap confirms this and is shown in Fig. 11. The horizontal components of the dielectrophoretic acceleration are of comparable magnitude to those in the case of $\lambda < 1$ and do not contribute to the flow.

VI. DISCUSSION AND CONCLUDING REMARKS

In contrast to other spherical shell experiments (see Refs. [51,52]) the GeoFlow experiment provides a platform for investigating convection triggered by the dielectrophoretic effect with two heating sources; dielectric heating ($\lambda > 1$) caused by a fast alternating electric field and a temperature difference across the gap ($\lambda < 1$). Furthermore, it is the first study of rotating convection which includes both heating sources and a micro-gravity environment.

We predicted a separation of the flow into two layers in the absence of Earth's gravity. However, we were unable to find evidence of stable flow separation in the experiments or numerical simulations. One reason might be the electric buoyancy force which supports rapid mixing over the entire gap.

Internal heating in rotating RB systems was studied numerically, e.g., by Zhang and Busse [53]. They showed columnar convection for $Pr > 10$ and $Ek < 10^{-3}$, a parameter regime that coincides well with the above-presented results, although a temperature difference ΔT was not included in their work. A direct comparison with their results was difficult as the underlying governing equations differ in many aspects, e.g., the thermoelectric feedback or the centrifugal force term. However, a valid expression of the Taylor-Proudman theorem for the EHD model and columnar cells in the weakly nonlinear regime was found. The case of pure internal heating was analyzed by, e.g., Simitev and Busse [54] and showed results consistent with those found in the GeoFlow experiments in terms of spiral and overlapped columnar convection cells in the weakly nonlinear regime. Deschamps *et al.* [55] investigated volumetrically heated spherical gap convection in the nonrotating case. Numerical simulations showed steep down-welling thermal plumes and broad upwelling regions which agree with the GeoFlow experiments for $\lambda \gg 1$ in the transient regime.

The statistical evaluation showed that the EHD convection in the spherical gap can be described by the quasinormal approximation. Results provided good agreement to studies in the RB cell by Enran and Schumacher [56] where the first four statistical moments showed the same behavior in the plane geometry.

The most limiting feature of the GeoFlow experiment is its inaccessibility regarding visual measurement techniques. Due to safety and weight reasons, it was not possible to use tracer particles or larger adaption optics. Even though the interferograms showed only a projection of the thermal structure it was possible to extract basic properties of the convective flow. The onset of convection and generic convective patterns in the interferometry were compared with the linear stability

analysis and the regimes as defined in Gastine *et al.* [43]. The pointwise plume regime for $\lambda \gg 1$ where internal heating dominates over the centrifugal force was a limiting case in Zaussinger *et al.* [12]. In a first attempt, velocity and drift rates were determined by a machine learning algorithm. However, numerical simulations and measured velocities differed by up to a factor of four. In the future, it is planned to increase the number of measurement points to lower the statistical uncertainty.

Bifurcations and hysteresis effects in the rotating spherical gap were investigated by Feudel *et al.* [57] and Feudel *et al.* [58], respectively. Unfortunately, these effects cannot be confirmed with the experimental points of the GeoFlow IIC mission. The time scales of these experiments were only in the range of a few minutes. However, the GeoFlow IIB mission provided several studies with an experimental time of up to four hours. This data could be used in the future to investigate the above-mentioned bifurcations and hysteresis effects.

The GeoFlow experiment was performed at two reference temperatures, namely 293 K and 303.5 K. This experimental setup resulted in two Prandtl numbers, four Ekman numbers and ten Froude numbers. Each dimensionless value varied between its minimum and maximum by a factor of 1.41, 2.88, and 53, respectively. Differences were mainly found in the onset of convection and the wave numbers of the observed columnar cells. The wave numbers of the columnar cells in the GeoFlow experiment coincide with RB results (see Refs. [43,59]). However, no structural differences between the sets of four different Ekman numbers were found. The influence of the Froude number was not investigated. The complex interaction of all forces made it difficult to focus on this single influence. The weakly rotating case, $Ek \sim 1$, was not included in this study and will be used for future investigations. For the weakly rotating case, regular geometric structures such as tetrahedrons and octahedrons are expected [25]. Unfortunately, the GeoFlow experimental container was withdrawn from service aboard the ISS in December 2018 which makes a resumption of experimental work impossible.

The launch of the follow-up experiment AtmoFlow is planned for 2024. This experiment is designed to investigate atmospheric-like fluid flows [26].

ACKNOWLEDGMENTS

The GeoFlow/AtmoFlow research was funded by ESA Grant No. AO-99-049; by DLR Grants No. 50WM0122, No. 50WM0822, and No. 50WM1841, by the SOKRATES/ERASMUS-program LIA-ISTROF (CNRS-cooperation), and DFG No. TR986/6-1. Furthermore, the authors express their gratitude to the GeoFlow Topical Team (ESA 18950/05/NL/VJ) for constructive discussions. We want to thank Ahmed Oguzhan Erdogan for processing the GeoFlow interferograms. All simulations were performed at the Northern German Network for High-Performance Computing (HLRN) and at the Heraklit cluster (BTU Cottbus-Senftenberg).

APPENDIX: DERIVATION OF DIMENSIONLESS THERMOEHD EQUATIONS

We use the OBA for permittivity ϵ and the identity $\nabla(\epsilon|\mathbf{E}|^2) = \epsilon\nabla|\mathbf{E}|^2 + |\mathbf{E}|^2\nabla\epsilon$, to rewrite the dielectrophoretic force \mathbf{F}_{DEP} as

$$\mathbf{F}_{\text{DEP}} = -\frac{1}{2}|\mathbf{E}|^2\nabla\epsilon = \frac{1}{2}\nabla[|\mathbf{E}|^2\epsilon_r\epsilon_0e(T - T_0)] - \frac{1}{2}\epsilon_r\epsilon_0e(T - T_0)\nabla|\mathbf{E}|^2, \quad (\text{A1})$$

where the first term on the far-right-hand side is a gradient force and is included in the pressure gradient. The remaining term can be written as a electrical thermal buoyancy force, $\mathbf{F} = -\rho_0\alpha(T - T_0)\mathbf{g}_e$ with

$$\mathbf{g}_e = \frac{e}{\rho_0\alpha}\nabla\left(\frac{\epsilon_0\epsilon_r|\mathbf{E}|^2}{2}\right). \quad (\text{A2})$$

This term is known as the *electric gravity* which represents a mean acceleration omitting spatial variations in the permittivity. Hence, \mathbf{g}_e alone is not suitable for the analysis of buoyancy related phenomena. In this study, the corresponding *dielectrophoretic acceleration* $\mathbf{a}_e = \mathbf{F}_{\text{DEP}}/\rho_0$ is instead

used which counts for all spatial variations of the permittivity and the temperature. This includes the consideration of the sign change of the dielectrophoretic acceleration under certain conditions which will also change the sign of the buoyancy term. A comparable approach is used by Mutabazi *et al.* [28] where the electric gravity is split into a base state and a fluctuating part.

Since the electric field has to fulfill the Gauss equation $\nabla \cdot (\epsilon \mathbf{E}) = 0$ or rather the dimensionless formulation Eq. (A3), it is split into two parts and calculated via the gradient of electric potential Φ ,

$$\nabla \cdot \left[(\epsilon_0 \epsilon_r - e T^* \Delta T) \frac{V_{\text{rms}}}{d} \mathbf{E}^* \right] = 0, \quad (\text{A3})$$

$$\mathbf{E}^* = \mathbf{E}_0^*(r^*) + \mathbf{E}_1^*(r^*, \theta, \varphi), \quad (\text{A4})$$

$$\mathbf{E}_0^*(r^*) = -\nabla \Phi_0^*(r^*), \quad \mathbf{E}_1^*(r^*, \theta, \varphi) = -\nabla \Phi_1^*(r^*, \theta, \varphi). \quad (\text{A5})$$

where poloidal and toroidal angles are denoted by θ and φ , respectively. Thus, the field $\mathbf{E}_0^*(r^*)$ satisfies $\nabla \cdot \mathbf{E}_0^*(r^*) = 0$ which can be calculated analytically

$$\mathbf{E}_0^*(r^*) = \frac{1}{\sqrt{\Gamma}} \frac{1}{r^{*2}} \mathbf{e}_{r^*}, \quad (\text{A6})$$

where $\Gamma = (1 - \eta)^4 / \eta^2$ is a geometrical factor for the spherical shell and $\eta = R_{\text{in}} / R_{\text{out}}$ is the radius ratio. The electric potential is calculated via

$$\Delta \Phi_1^* = \frac{C_E \Gamma L}{1 - C_E \Gamma L T^*} \nabla T^* \cdot [\nabla \Phi_0^*(r) + \nabla \Phi_1^*(r, \theta, \varphi)], \quad (\text{A7})$$

with the dielectric loss parameter $C_T = 4\pi f e \epsilon_0^2 \epsilon_r^2 \tan \delta V_{\text{rms}}^4 / (c_p \rho^2 \nu \kappa)$ and the convective parameter $C_E = \rho \nu \kappa / (2\epsilon_0 \epsilon_r V_{\text{rms}}^2)$.

For $|\mathbf{E}_1^*| \ll |\mathbf{E}_0^*|$ [cf. Figs. 8(a)–8(c) where the horizontal components of the dielectrophoretic acceleration are three order of magnitudes smaller than the radial component] the Navier-Stokes equation and the temperature equation read,

$$\begin{aligned} \text{Pr}^{-1} \left[\frac{\partial \mathbf{u}^*}{\partial t^*} + (\mathbf{u}^* \cdot \nabla) \mathbf{u}^* \right] &= -\text{Pr}^{-1} \nabla p^* + \nabla^2 \mathbf{u}^* + B \cdot L \cdot T^* \cdot \frac{1}{r^{*5}} \mathbf{e}_r - \text{Ek}^{-1} \mathbf{e}_z \times \mathbf{u}^* \\ &+ L \cdot \text{Fr} \cdot T^* r^* \sin \theta \mathbf{s} \end{aligned} \quad (\text{A8})$$

and

$$\frac{\partial T^*}{\partial t^*} + (\mathbf{u}^* \cdot \nabla) T^* = \nabla^2 T^* + \frac{C_T}{B \Gamma^2 L} \frac{1}{r^{*4}}, \quad (\text{A9})$$

respectively. Apart from the internal heating term and the geometrical aspects, this set of equations is identical with the governing equations presented in Feudel *et al.* [25] [Eq.(1a)–(1c)] and for the rotating case shown by Curbelo *et al.* [35] [Eqs. (1) and (2)]. This model is not suitable for describing pure internal heating. For completeness, we refer to Travníkov *et al.* [60].

-
- [1] S. A. Fagents, Considerations for effusive cryovolcanism on Europa: The post-Galileo perspective, *J. Geophys. Res.: Planets* **108**, 5139 (2003).
 - [2] T. Lay, J. Hernlund, and B. A. Buffett, Core–mantle boundary heat flow, *Nat. Geosci.* **1**, 25 (2008).
 - [3] S. E. Smrekar and C. Sotin, Constraints on mantle plumes on Venus: Implications for volatile history, *Icarus* **217**, 510 (2012).
 - [4] M. Ogawa, Mantle convection: A review, *Fluid Dyn. Res.* **40**, 379 (2008).
 - [5] G. Schubert and D. Bercovici, *Treatise on Geophysics*, Vol. 7, Mantle Dynamics (Elsevier, Amsterdam, 2009).

- [6] D. J. Tritton, Internally heated convection in the atmosphere of Venus and in the laboratory, *Nature* **257**, 110 (1975).
- [7] Y. Tasaka, Y. Kudoh, Y. Takeda, and T. Yanagisawa, Experimental investigation of natural convection induced by internal heat generation, *J. Phys.: Conf. Ser.* **14**, 168 (2005).
- [8] J. Takahashi, Y. Tasaka, Y. Murai, Y. Takeda, and T. Yanagisawa, Experimental study of cell pattern formation induced by internal heat sources in a horizontal fluid layer, *Int. J. Heat Mass Transf.* **53**, 1483 (2010).
- [9] A. Limare, K. Vilella, E. Di Giuseppe, C. G. Farnetani, E. Kaminski, E. Surducan, V. Surducan, C. Neamtu, L. Fourel, and C. Jaupart, Microwave-heating laboratory experiments for planetary mantle convection, *J. Fluid Mech.* **777**, 50 (2015).
- [10] L. Fourel, A. Limare, C. Jaupart, E. Surducan, C. G. Farnetani, E. C. Kaminski, C. Neamtu, and V. Surducan, The Earth's mantle in a microwave oven: Thermal convection driven by a heterogeneous distribution of heat sources, *Exp. Fluids* **58**, 90 (2017).
- [11] E. Kaminski and M. Javoy, A two-stage scenario for the formation of the earth's mantle and core, *Earth Planet. Sci. Lett.* **365**, 97 (2013).
- [12] F. Zaussinger, P. Haun, M. Neben, T. Seelig, V. Travnikov, C. Egbers, H. Yoshikawa, and I. Mutabazi, Dielectrically driven convection in spherical gap geometry, *Phys. Rev. Fluids* **3**, 093501 (2018).
- [13] F. Zaussinger, A. Krebs, V. Travnikov, and Ch. Egbers, Recognition and tracking of convective flow patterns using Wollaston shearing interferometry, *Adv. Space Res.* **60**, 1327 (2017).
- [14] F. Kupka and H. Muthsam, Modelling of stellar convection, *Living Rev. Comput. Astrophys.* **3**, 1 (2017).
- [15] C. Jaupart, S. Labrosse, F. Lucazeau, and J.-C. Mareschal, 7.06 - Temperatures, heat, and energy in the mantle of the Earth, in *Treatise on Geophysics* (2nd ed.), edited by Gerald Schubert (Elsevier, Oxford, 2015), pp. 223–270.
- [16] B. Travis and P. Olson, Convection with internal heat sources and thermal turbulence in the earth's mantle, *Geophys. J. Int.* **118**, 1 (1994).
- [17] K. Vilella and F. Deschamps, Temperature and heat flux scaling laws for isoviscous, infinite Prandtl number mixed heating convection, *Geophys. J. Int.* **214**, 265 (2018).
- [18] P. H. Roberts, Electrohydrodynamic convection, *Q. J. Mech. Appl. Math.* **22**, 211 (1969).
- [19] R. J. Turnbull, Effect of dielectrophoretic forces on the Bénard instability, *Phys. Fluids* **12**, 1809 (1969).
- [20] P. J. Stiles, Electro-thermal convection in dielectric liquids, *Chem. Phys. Lett.* **179**, 311 (1991).
- [21] P. J. Stiles, F. Lin, and P. J. Blennerhassett, Convective heat transfer through polarized dielectric liquids, *Phys. Fluids A* **5**, 3273 (1993).
- [22] B. L. Smorodin, The effect of an alternating electric field on the liquid dielectric convection in a horizontal capacitor, *Tech. Phys. Lett.* **27**, 1062 (2001).
- [23] H. N. Yoshikawa, M. Tadie Fogaing, O. Crumeyrolle, and I. Mutabazi, Dielectrophoretic rayleigh-bénard convection under microgravity conditions, *Phys. Rev. E* **87**, 043003 (2013).
- [24] M. T. Fogaing, H. N. Yoshikawa, O. Crumeyrolle, and I. Mutabazi, Heat transfer in the thermo-electrohydrodynamic convection under microgravity conditions, *Eur. Phys. J. E* **37**, 1 (2014).
- [25] F. Feudel, K. Bergemann, L. S. Tuckerman, C. Egbers, B. Futterer, M. Gellert, and R. Hollerbach, Convection patterns in a spherical fluid shell, *Phys. Rev. E* **83**, 046304 (2011).
- [26] F. Zaussinger, P. Canfield, A. Froitzheim, V. Travnikov, P. Haun, M. Meier, A. Meyer, P. Heintzmann, T. Driebe, and Ch. Egbers, AtmoFlow—Investigation of atmospheric-like fluid flows under microgravity conditions, *Micrograv. Sci. Technol.* **31**, 569 (2019).
- [27] C. Egbers, W. Beyer, A. Bonhage, R. Hollerbach, and P. Beltrame, The GeoFlow experiment on ISS (Part I): Experimental preparation and design of laboratory testing hardware, *Adv. Space Res.* **32**, 171 (2003), Gravitational effects in physico-chemical processes.
- [28] I. Mutabazi, H. N. Yoshikawa, M. T. Fogaing, V. Travnikov, O. Crumeyrolle, B. Futterer, and C. Egbers, Thermo-electrohydrodynamic convection under microgravity: A review, *Fluid Dyn. Res.* **48**, 061413 (2016).
- [29] K. G. Ayappa, S. Brandon, J. J. Derby, H. T. Davis, and E. A. Davis, Microwave driven convection in a square cavity, *AIChE J.* **40**, 1268 (1994).

- [30] R. Cherbański and L. Rudniak, Modelling of microwave heating of water in a monomode applicator—Influence of operating conditions, *Int. J. Therm. Sci.* **74**, 214 (2013).
- [31] A. Castellanos, *Electrohydrodynamics*, Vol. CISM courses and lectures-380 (Springer-Verlag Wien GmbH, Wien, 1998).
- [32] M. Zahn, Derivation of the korteweg-helmholtz electric and magnetic force densities including electrostriction and magnetostriction from the quasistatic poynting’s theorems, in *Proceedings of the 2006 IEEE Conference on Electrical Insulation and Dielectric Phenomena* (IEEE, Los Alamitos, CA, 2006), pp. 186–189.
- [33] J. R. Melcher, *Continuum Electromechanics*, (MIT Press, Cambridge, MA, 1981).
- [34] C. Gabriel, S. Gabriel, E. H. Grant, E. H. Grant, B. S. J. Halstead, and D. Michael P. Mingos, Dielectric parameters relevant to microwave dielectric heating, *Chem. Soc. Rev.* **27**, 213 (1998).
- [35] J. Curbelo, J. M. Lopez, A. M. Mancho, and F. Marques, Confined rotating convection with large prandtl number: Centrifugal effects on wall modes, *Phys. Rev. E* **89**, 013019 (2014).
- [36] O. Dupont, T. Dewandre, J.-L. Dewandel, and D. Claessens, The optical diagnostics of the fluid science laboratory, in *Proceedings of the 5th International Conference on Space Optics, Toulouse, France*, edited by B. Warmbein (ESA Publications Division, Netherlands, 2004), pp. 463–470.
- [37] R. Hollerbach, A spectral solution of the magneto-convection equations in spherical geometry, *Int. J. Numer. Methods Fluids* **32**, 773 (2000).
- [38] V. Travnikov, C. Egbers, and R. Hollerbach, The Geoflow-experiment on ISS (Part II): Numerical simulation, *Adv. Space Res.* **32**, 181 (2003).
- [39] W.-W. Kim and S. Menon, A new dynamic one-equation subgrid-scale model for large eddy simulations, in *Proceedings of the 33rd Aerospace Sciences Meeting and Exhibit* (American Institute of Aeronautics and Astronautics, Reston, Virginia, 1995).
- [40] F. Kupka, F. Zaussinger, and M. H. Montgomery, Mixing and overshooting in surface convection zones of DA white dwarfs: First results from ANTARES, *Mon. Not. R. Astron. Soc.* **474**, 4660 (2018).
- [41] J. D. Scheel and J. Schumacher, Global and local statistics in turbulent convection at low prandtl numbers, *J. Fluid Mech.* **802**, 147 (2016).
- [42] J. Curbelo and A. M. Mancho, Symmetry and plate-like convection in fluids with temperature-dependent viscosity, *Phys. Fluids* **26**, 016602 (2014).
- [43] T. Gastine, J. Wicht, and J. Aubert, Scaling regimes in spherical shell rotating convection, *J. Fluid Mech.* **808**, 690 (2016).
- [44] K. Zhang, Spiralling columnar convection in rapidly rotating spherical fluid shells, *J. Fluid Mech.* **236**, 535 (1992).
- [45] F. H. Busse, Thermal instabilities in rapidly rotating systems, *J. Fluid Mech.* **44**, 441 (1970).
- [46] See Supplemental Material at <http://link.aps.org/supplemental/10.1103/PhysRevFluids.5.063502> for animation of columnar cells with $m = 4$.
- [47] See Supplemental Material at <http://link.aps.org/supplemental/10.1103/PhysRevFluids.5.063502> for animation of columnar cells with $m = 5$.
- [48] See Supplemental Material at <http://link.aps.org/supplemental/10.1103/PhysRevFluids.5.063502> for animation of columnar cells with $m = 6$.
- [49] V. M. Gryanik, J. Hartmann, S. Raasch, and M. Schröter, A refinement of the millionshchikov quasi-normality hypothesis for convective boundary layer turbulence, *J. Atmos. Sci.* **62**, 2632 (2005).
- [50] T. Gastine, J. Wicht, and J. M. Aurnou, Turbulent rayleigh–bénard convection in spherical shells, *J. Fluid Mech.* **778**, 721 (2015).
- [51] F. H. Busse and C. R. Carrigan, Laboratory simulation of thermal convection in rotating planets and stars, *Science* **191**, 81 (1976).
- [52] J. E. Hart, G. A. Glatzmaier, and J. Toomre, Space-laboratory and numerical simulations of thermal convection in a rotating hemispherical shell with radial gravity, *J. Fluid Mech.* **173**, 519 (1986).
- [53] K.-K. Zhang and F. H. Busse, On the onset of convection in rotating spherical shells, *Geophys. Astrophys. Fluid Dyn.* **39**, 119 (1987).
- [54] R. Simitev and F. H. Busse, Patterns of convection in rotating spherical shells, *New J. Phys.* **5**, 97 (2003).

- [55] F. Deschamps, C. Yao, P. J. Tackley, and C. Sanchez-Valle, High rayleigh number thermal convection in volumetrically heated spherical shells, *J. Geophys. Res.: Planets* **117**, E09006 (2012).
- [56] M. S. Emran and J. Schumacher, Fine-scale statistics of temperature and its derivatives in convective turbulence, *J. Fluid Mech.* **611**, 13 (2008).
- [57] F. Feudel, L. S. Tuckerman, M. Gellert, and N. Seehafer, Bifurcations of rotating waves in rotating spherical shell convection, *Phys. Rev. E* **92**, 053015 (2015).
- [58] F. Feudel, L. S. Tuckerman, M. Zaks, and R. Hollerbach, Hysteresis of dynamos in rotating spherical shell convection, *Phys. Rev. Fluids* **2**, 053902 (2017).
- [59] P. H. Roberts, On the thermal instability of a rotating-fluid sphere containing heat sources, *Philos. Trans. R. Soc. Lond. A* **263**, 93 (1968).
- [60] V. Travnikov, F. Zaussinger, P. Haun, and Ch. Egbers, Influence of the dielectrical heating on the convective flow in the radial force field, *Phys. Rev. E* **101**, 053106 (2020).